



**UNIVERSIDAD DE INVESTIGACIÓN DE
TECNOLOGÍA EXPERIMENTAL YACHAY**

Escuela de Ciencias de la Tierra, Energía y Ambiente

**TÍTULO: MELT INCLUSIONS CHARACTERIZATION IN
OLIVINE PHENOCRYSTS USING NANOTOMOGRAPHY
ANALYSIS FROM THE SOUTHERN PORTION OF THE
NORTH ANDEAN VOLCANIC ZONE (ECUADOR)**

Trabajo de integración curricular presentado como requisito para
la obtención del título de Geólogo

Autor:

Bolaños Mosquera Francisco Xavier

Tutores:

M.Sc. Torres Ramírez Raisa Ivanova

Ph.D. Weller Derek James

Urcuquí, diciembre 2023

AUTORÍA

Yo, **BOLAÑOS MOSQUERA FRANCISCO XAVIER**, con cédula de identidad 1727409714, declaro que las ideas, juicios, valoraciones, interpretaciones, consultas bibliográficas, definiciones y conceptualizaciones expuestas en el presente trabajo; así como, los procedimientos y herramientas utilizadas en la investigación, son de absoluta responsabilidad de el/la autora (a) del trabajo de integración curricular. Así mismo, me acojo a los reglamentos internos de la Universidad de Investigación de Tecnología Experimental Yachay.

Urcuquí, septiembre 2023.



Francisco Xavier Bolaños Mosquera

CI: 1727409714

AUTORIZACIÓN DE PUBLICACIÓN

Yo, **BOLAÑOS MOSQUERA FRANCISCO XAVIER**, con cédula de identidad 1727409714, cedo a la Universidad de Investigación de Tecnología Experimental Yachay, los derechos de publicación de la presente obra, sin que deba haber un reconocimiento económico por este concepto. Declaro además que el texto del presente trabajo de titulación no podrá ser cedido a ninguna empresa editorial para su publicación u otros fines, sin contar previamente con la autorización escrita de la Universidad.

Asimismo, autorizo a la Universidad que realice la digitalización y publicación de este trabajo de integración curricular en el repositorio virtual, de conformidad a lo dispuesto en el Art. 144 de la Ley Orgánica de Educación Superior

Urcuquí, septiembre 2023.



Francisco Xavier Bolaños Mosquera

CI: 1727409714

DEDICATORY

I dedicate this to my family, my father Mauricio, my mother Margarita, my sisters Cinthya and Lia, my father's wife Evelyn, my nephews Rafaela and Sebastian, and my aunt Geovanna. Plus, my best friend Diego and a special person in my life, Andrea.

Thank you for your support and encouragement.

Bolaños Mosquera Francisco Xavier

ACKNOWLEDGMENTS

I want to express my gratitude to every faculty member of the university that acted as my professors in all my time in the university. Specially, to the past and present faculty members of the School of Earth Sciences, Energy and Environment that inculcated their knowledge and passion for this field with particular mention to: Elisa Piispa, Céline Mandon, Anna Foster, Elizabeth Mariño, and Germán Martin.

I want to thank my tutor and mentor Derek Weller, without his guidance, help and encouragement nothing of this could have been possible. He showed me that science can be also a tool to grow as a person.

To my other tutor Raisa Torres, which advice, help, and encouragement led to this to happen. Along with other people that were involved through this process: laboratory technicians Sebastian Gallegos, Miguel Larrea, Cristian Panchana, and Julio Chacón.

Bolaños Mosquera Francisco Xavier

RESUMEN

Los procesos magmáticos pueden generar productos volcánicos con características morfológicas y químicas únicas, por lo tanto estos productos volcánicos pueden ser utilizados para inferir las propiedades del sistema magmático. Ecuador es un país con constante actividad volcánica producto de su contexto geológico (sistema de subducción), y por ello el estudio de los diferentes sistemas magmáticos en su área es crítico, en especial la porción sur de la Zona Volcánica Norandina, esta presenta varios edificios volcánicos, entre ellos los conos de escoria Licto (Tulabug y Loma Bellavista). Se investigó su vulcanismo y evolución magmática aplicando diferentes técnicas petrológicas/geoquímicas con énfasis en las inclusiones fluidas. Estas técnicas fueron: muestreo de campo y preparación de depósitos de escoria, observación petrológica de minerales de olivino y clastos, visualización espacial y mediciones de minerales y sus partes utilizando nanotomografía, espectroscopia Raman para estimar composiciones químicas de minerales, análisis de elementos mayores de minerales e inclusiones fluidas y análisis vesicular de clastos volcánicos. Se determina que las morfologías predominantes de olivino hospedantes de inclusiones de fundido son poliédricas y poliédricas dendríticas (depósitos de escoria de Tulabug). Estas morfologías y los datos químicos (Fo% 81,79) muestran que el olivino se formó a velocidades de enfriamiento lentas (0,17 °C/min o 10,38 °C/hora). La zonación química normal en los olivinos muestra una posible cristalización fraccionada de sistema simple/cerrado en el sistema magmático. La mezcla de magmas se infiere debido al análisis de núcleo a borde en los olivinos. Una mezcla de litologías ultramáficas fue probablemente la roca madre de los magmas. El tamaño de las burbujas dentro de las inclusiones de fundido es un signo de magma rico en volátiles. La variación de la composición química de las inclusiones fundidas (59,3 wt% de SiO₂) determinó que la cristalización de un conjunto mineral de olivino + plagioclasa + clinopiroxeno + espinela fue un proceso importante en el sistema magmático. La contaminación de la corteza como asimilación magmática se produjo en el sistema magmático debido a la posible interacción entre los magmas y la granodiorita de Pungalá. El análisis vesicular de los clastos determina signos de desgasificación con cambios en los mecanismos de crecimiento de las burbujas desde la maduración a la coalescencia. La información anterior nos permitió crear un modelo de evolución magmática que infiere dos cámaras magmáticas bajo Licto. Licto sondea ser un sistema magmático complejo, el cual es un ejemplo de las interacciones magmáticas en esta porción de la Zona Volcánica Norandina y su importancia.

PALABRAS CLAVE: Conos de escoria de Licto, inclusiones de fundido, análisis geoquímico, análisis petrológico, evolución magmática, olivino y depósitos de escoria.

ABSTRACT

Magmatic processes can produce volcanic products with unique morphological and chemical characteristics. These volcanic products can be used to infer the properties of the magmatic system. Ecuador is a country with constant volcanic activity product of its geological setting (subduction system), and by that the study of the different magmatic systems in its area is critical. The southern portion of the North Andean Volcanic Zone has various volcanic edifices, between them the Licto cinder cones (Tulabug and Loma Bellavista). Its volcanism and magmatic evolution was researched by applying different petrological/geochemical techniques with emphasis on melt inclusions. These techniques were: field sampling and preparation of scoria deposits, petrological observation of olivine minerals and clasts, spatial visualization and measurements of minerals and its parts using nanotomography, Raman spectroscopy to constrain chemical compositions of minerals, major element analysis of minerals and melt inclusions, and vesicular analyses of volcanic clasts. It is determined that the predominant olivine morphologies of host minerals for melt inclusions are polyhedral and dendritic polyhedral (scoria deposits from Tulabug). These morphologies and chemical data (Fo% 81.79) shows that the olivine were formed at slow cooling rates (0.17 °C/min or 10.38 °C/hour). Normal chemical zoning in olivines show a possible simple/close-system fractional crystallization in the magmatic system. Magma mixing is inferred due to the core to rim analysis in olivines, where a mix of ultramafic lithologies likely were the source rock for magmas. Size of bubbles within melt inclusions are a sign of volatile-rich magma, and melt inclusions chemical composition variation (59.3 SiO₂ wt%) determined that an olivine + plagioclase + clinopyroxene + spinel mineral assemblage crystallization was an important process in the magmatic system. Crustal contamination as magma assimilation occurred in the magmatic system due the possible interaction between magmas and the Pungalá granodiorite, while the vesicular analysis of clasts determine signs of degassing with changes in the bubble growth mechanisms from ripening to coalescence. The previous information allowed us to create a magmatic evolution model that infers two magmatic chambers under Licto, where this volcanic area probe to be a complex magmatic system, which is an example of the magmatic interactions in this portion of the North Andean Volcanic Zone and its importance.

KEY WORDS: Licto cinder cones, melt inclusions, geochemical analysis, petrological analysis, magmatic evolution, olivine, and scoria deposits.

Table of Contents

DEDICATORY	iv
ACKNOWLEDGMENTS	v
RESUMEN	vi
ABSTRACT	vii
List of Figures.....	x
List of Tables	xiv
1. Introduction	1
1.1 Melt inclusions.....	1
1.2 Melt inclusions and space-time trends.....	5
1.3 Olivine growth and melt inclusions link.....	6
1.3.1 Olivine morphology	7
1.4 Inclusions from a homogeneous fluid: primary and secondary inclusions.....	10
1.5 Basaltic melt inclusions	11
1.6 Evolution of basaltic melt inclusions after trapping	14
1.6.1 Post-Entrapment Crystallization and re-equilibration of melt inclusions	14
1.7 Spatial distribution of melt inclusions	16
1.8 Chemical composition of melt inclusions and their use to understand magmatic processes	17
1.9 Volatile content of melt inclusions	17
1.10 Subduction zone system.....	19
1.11 Purpose of the study.....	20
2. Geologic Background and Tectonic Setting.....	21
3. Methodology.....	24
3.1 Sampling/Geological Setting	24
3.2 Scoria processing and selection of olivine crystals	26
3.3 First identification of suitable melt inclusions in olivine crystals	26
3.4 Melt inclusion identification/selection.....	27
3.5 Textural analysis of melt inclusions and orientation of the crystal using computed nanotomography (polyhedral olivines).....	29
3.6 Thin section of olivine crystals (polyhedral morphology).....	30
3.7 Raman spectroscopy (polyhedral olivines).....	30
3.8 Olivine composition estimation with a mathematical model.....	32
3.9 EPMA analysis	33
3.10 Core to rim analysis	36

3.11 Post-entrapment crystallization correction	37
3.12 Textural correlation with chemistry composition	41
3.13 Fractional crystallization modeling and melt liquidus association	43
3.14 Vesicular analysis	47
3.15 Use of FOAMS to calculate estimations of volumes of melt inclusions using results from nanotomography	49
4. Results	51
4.1 Olivine Morphology	51
4.2 Melt inclusion description using computed x-ray nanotomography.....	53
4.3 3D models of olivine crystals	55
4.4 Internal features within the olivine crystal.....	57
4.5 Olivine composition estimation using Raman spectroscopy	59
4.6 EPMA analysis	62
4.7 Olivine zonation.....	64
4.8 Post-entrapment corrections results and implications.....	66
4.9 Basic textural analysis and its possible link with change in chemical composition	73
4.10 Fractional crystallization modeling and melt liquidus association	78
4.11 Vesicular analysis	85
4.12 Volume estimations of melt inclusions in polyhedral olivines.....	91
5. Discussion.....	94
5.1 Polyhedral olivine morphology and chemical composition.....	94
5.2 Melt inclusions morphology and chemical analysis	101
5.3 Textural analysis of clasts from the Tulabug cinder cone	112
5.4 Theory of magmatic evolution and eruption at Licto	116
6. Conclusions and Future Work	119
References	122
Appendix	129
Appendix 1: Section Images from the nanotomographer	129
Appendix 2: Glass slides images	142
Appendix 3: Foams results in diagrams for all the clasts analyzed	151
Appendix 4: Pungalá Granodiorite Sample whole rock composition.....	155

List of Figures

Figure 1: Different mechanisms of postentrapment modification of melt inclusions, modified figure (Wallace, 2005).....	3
Figure 2: Example of a rapid growth olivine morphology, development of embayments within the crystalline structure allow for the formation of melt inclusions.....	4
Figure 3: SEM images and micro-photographs of different experimental olivine morphologies for context. A: Polyhedral, B: Tabular, C: Skeletal, D: Dendritic, E: Feather shape. Modified figure (Faure et al., 2003).....	8
Figure 4: Modified SEM image as an example of a dendritic olivine showing the development of rods from experimental results (Faure et al., 2007)	10
Figure 5: Modified general cross-section in Ecuador showing the subducting tectonic setting (Cajamarca-Zuniga et al., 2022).....	20
Figure 6: Images of two of the cinder cones at Licto. A: Loma Bellavista, B: Tulabug. Licto, Chimborazo (Ecuador).....	23
Figure 7: Location Map of the Tulabug Cone, as a reference of the city of Riobamba (Chimborazo).	23
Figure 8: Location Map of the Tulabug Cone, as a reference of the city of Riobamba, Satellite Imagery (Chimborazo).....	24
Figure 9: Sampling site 1 in Tulabug. A: Layer of lavas, B: Scoria layers.....	25
Figure 10: Sampling site 2 in Tulabug. A: Scoria layer, B: Cangahua	26
Figure 11: Mounting procedure of olivine phenocrysts. A: 76 olivines mounted in a circular vessel, B: Epoxy resin used to maintain the crystals together, C: Hot plate to ensure the solidification of the epoxy, D: Epoxy crystallized with olivines.	27
Figure 12: Example of Raman Spectra taken from olivine samples (Breitenfeld et al., 2018)..	31
Figure 13: Images of the mounts created for EPMA analysis.....	34
Figure 14: Measurement procedure for distance from edge of the crystal to the melt inclusion.	41
Figure 15: Example of nested approach in FOAMS, using binary generated images from BSE images of clasts (VBr/6).....	48
Figure 16: Crystal configuration of olivines. Image modified. (Deer et al., 2013).....	51
Figure 17: Polyhedral olivine with possible skeletal features.....	52
Figure 18: Example of the usual crystallographic structure of olivines observed in Licto.....	52
Figure 19: Different angle of an olivine from Licto covered by volcanic glass.....	53
Figure 20: Different orientation of an olivine from Licto, other features of the usual orthorhombic configuration are seen.	53

Figure 21: Section image from olivine sample LS2-MSL-1835-1/1301 taken from the nanotomographer. A large melt inclusion is seen with its associated bubble.	54
Figure 22: Section image from olivine sample LS2-MSL-1835-5-3/1862 and Binary image of a melt inclusions	55
Figure 23: 3D models from olivine sample LS2-MSL-1835-1, left: model with no internal features, right: model with visible internal features.	56
Figure 24: 3D models from olivine sample LS2-MSL-1835-3, left: model with no internal features, right: model with visible internal features.	56
Figure 25: 3D model from olivine sample LS2-MSL-1835-5	57
Figure 26: General image of the glass slide 3 from olivine sample (reflected light).	58
Figure 27: Left: close look to internal features within glass slide 1 (reflected light), Right: melt inclusions observed within the olivine in glass slide 1 (reflected light).....	58
Figure 28: Volcanic glass entrapped within an olivine sample from glass slide 2 (reflected light).	59
Figure 29: Close look to the melt inclusions identified in glass slide 6 (reflected light).	59
Figure 30: Raman spectra results from the 11 glass slide samples of olivines	60
Figure 31: Raman spectra of targeted melt inclusion in glass slide 6	61
Figure 32: Raman spectra of targeted melt inclusion in glass slide 6, showing range wavenumber 3100 cm ⁻¹ to 3200 cm ⁻¹	62
Figure 33: BSE image of olivine crystal which measurements are taken in a line from rim to core.	64
Figure 34: Zoom in the path measurements taken from specific locations of the olivine crystal.	64
Figure 35: Diagram of distance from the rim in μm vs the Fo % and Ni wt % of the measurements from the olivine from rim to core.	65
Figure 36: SiO ₂ vs FeO ^t diagram showing corrected melt inclusions for post-entrapment crystallization when it reaches equilibrium (first output) compared with a few glass compositions measured in EMPA	67
Figure 37: SiO ₂ vs FeO ^t diagram for uncorrected melt inclusions, whole rocks compositions, glass compositions (glass: glass within the olivine crystal, glass clasts: glass in the clasts of the scoria), and PEC and corrected Fe-loss melt inclusions.	68
Figure 38: MgO vs FeO ^t diagram melt inclusions uncorrected, whole rocks compositions, glass compositions, and PEC and Fe-loss corrected melt inclusions.	69
Figure 39: Harker diagrams for various major elements plotted against SiO ₂ (wt%), PEC and Fe-loss corrected melt inclusions, whole rocks, a few selected matrix glasses are represented (this study). Melt inclusions obtained from a lava sample from Tulabug, green dots (D. Narváez, 2021).	70

Figure 40: Rock classification diagram (Peccerillo & Taylor, 1976) for the PEC and Fe-loss corrected melt inclusions, whole rocks, and a few selected matrix glasses.	71
Figure 41: Major element variation depending on the shortest distance between the melt inclusion and the crystal host edge.	74
Figure 42: Images of olivine crystals obtained by BSE images. A: Example of polyhedral morphology, B: Example of dendritic polyhedral morphology (arrows showing stair like texture).	75
Figure 43: Frequency diagram of the different interpreted morphologies for host olivines of melt inclusions.....	75
Figure 44: A: Shortest distance between melt inclusions and crystal host edge for A) MgO, B) Al ₂ O ₃ and C) CaO (wt%) concentrations.	76
Figure 45: CaO wt % vs Al ₂ O ₃ wt %, liquid line of descent (LLD) of 1 st phase model (olivine + spinel) and cotectic model (olivine + plagioclase + clinopyroxene) that could crystallize at the set conditions.	77
Figure 46: Calculated models of fractional crystallization for major element content plots (wt %) versus SiO ₂ , PEC and Fe-loss corrected melt inclusions, whole rocks, glass matrix, and fractional crystallization models developed are showed. ol: olivine, spl: spinel, plg: plagioclase, cpx: clinopyroxene.....	78
Figure 47: Small microlites or microphenocrysts of plagioclase in the matrix glass of a clast. ol: olivine, spl: spinel, plg: plagioclase, cpx: clinopyroxene.....	80
Figure 48: Forsterite % vs Fayalite % for melt liquidus association (MLA) from PEC and Fe-loss corrected melt inclusions, glasses, whole rocks, with results obtained from EMPA and fractional crystallization models. All EPMA olivines correspond to host olivines of melt inclusions.	81
Figure 49: Triangular classification diagram for spinel for melt liquidus association from melt inclusions, glasses, whole rocks, with results obtained from EMPA and fractional crystallization models.	82
Figure 50: Triangular classification diagram for clinopyroxene for melt liquidus association from melt inclusions, glasses, whole rocks, with results obtained from EMPA (type of material and core/rim measurement) and fractional crystallization models. Mic: microlite sample, Phen: phenocryst sample.....	83
Figure 51: Triangular classification diagram for plagioclase for melt liquidus association from melt inclusions, glasses, whole rocks, with results obtained from EMPA and fractional crystallization models.....	84
Figure 52: Images from the different clasts from the scoria layer samples at Licto. ol: olivine	85
Figure 53: Major element variation diagrams (in wt%) for the different types of scoria clasts.	86
Figure 54: Modified reference diagrams for basic textural vesicle interpretation. (Shea, Houghton, et al., 2010).....	87

Figure 55: Left: VVD plots for dense black clast samples, Right: CVVD plots for dense black clast samples.....	88
Figure 56: Left: VSD plots for dense black clast samples, Right: CVSD plots for dense black clast samples.....	89
Figure 57: Left: Representative VVD plots for vesicle black and vesicle brown clast samples, Right: CVVD plots for vesicle black and vesicle brown clast samples.	90
Figure 58: Left: VSD plots for vesicle black and vesicle brown clast samples, Right: CVSD plots for vesicle black and vesicle brown clast samples.	91
Figure 59: Left: Fo % vs Ca (ppm) of selected olivines measured by EMPA and estimated chemical compositions using mathematical models, Right: Fo % vs Mn (ppm) of selected olivines measured by EMPA and estimated chemical compositions using mathematical models.	97
Figure 60: Mn/Fe vs Ni/Mg ratios of EMPA measured olivine compositions compared to olivines created under different tectonic settings and parental source.....	98
Figure 61: Modified image where ideal conditions olivines were created under specific conditions of degree of undercooling and cooling rate (Faure et al., 2003).....	101
Figure 62: Section taken from the nanotomographer of one olivine crystal, a larger bubble is seen compared to its associated glass phase.....	102
Figure 63: Section taken from the nanotomographer of one olivine crystal, smaller bubbles compared to its associated glass phase.....	103
Figure 64: Comparison between melt inclusions from artificially created polyhedral olivines (left) and melt inclusions observed in olivine samples at Licto (right) (Faure & Schiano, 2005).	104
Figure 65: Plot of CaO vs Al ₂ O ₃ of melt inclusions compositions from specific morphology olivines created in ideal conditions (Faure & Schiano, 2005).	105
Figure 66: Top: SiO ₂ wt % vs TiO ₂ wt % of PEC and Fe-loss corrected melt inclusions, identified lava samples (whole rocks from Tulabug and Bellavista), glass from clasts, the composition of the Pungala granodiorite (Guerrero & Vallejo, 2020), and the possible mixing line between the most primitive magma observed and the granodiorite. Bottom: SiO ₂ wt % vs MgO wt %, same measurements as before.	109
Figure 67: Comparison between dense black clast and a vesicular black clasts. Similar mineral assemblages with larger olivines in dense black clasts. Microphenocrysts of plagioclase, clinopyroxene, and olivine occur in the matrix glass of both samples. ol: olivine	113
Figure 68: Theory of vesicularity evolution of clast during the explosive eruption of Licto inferred from texture analysis.	115
Figure 69: Theory of magmatic evolution at Licto based on the chemical information, olivine + melt inclusion morphology and textural analysis of the scoria clasts.	118

List of Tables

Table 1: Accepted values for the San Carlos olivines (SC), and Juan de Fuca glasses (JDF). n/a corresponds to values not reported or not relevant for calculations of error. (JAROSEWICH et al., 1980; Straub et al., 2004)	36
Table 2: Results from estimation of Fo % using Raman spectra.	60
Table 3: Average values of measurement done with EPMA of host olivines (olv), olivines from clasts, clinopyroxene from clasts (Cpx), plagioclase from clasts (Plg), spinel from clasts (Spl), melt inclusions (MI), and matrix glasses from clasts. n/a (not measured), *** not possible to calculate since reference does not report values. All values in wt %	63
Table 4: Measured shortest distances from crystal (host) edge to melt inclusions (SDE). ID: grain number/associated melt inclusion if applicable, n/a: not possible to measure	74
Table 5: Range of Fo% values for olivines measured by EPMA, created using melt liquids association with glass compositions (MLA glass), created using melt liquids association with melt inclusions PEC compositions (MLA MI PEC), created using melt liquids association with whole rocks compositions (MLA whole rocks), created using fractional crystallization model 1 st Phase, and created using fractional crystallization model cotectic.....	81
Table 6: Range of Fe ³⁺ values for spinel measured by EPMA, created using melt liquids association with glass compositions (MLA glass), created using melt liquids association with melt inclusions PEC compositions (MLA MI PEC), created using melt liquids association with whole rocks compositions (MLA whole rocks).....	82
Table 7: Range of Wo (wollastonite) values for clinopyroxene measured by EPMA, created using melt liquids association with 1) glass compositions (MLA glass), 2) melt inclusions PEC compositions (MLA MI PEC), 3) whole rocks compositions (MLA whole rocks), 4) fractional crystallization model cotectic, and using fractional crystallization model 54%, 55%, and 56%. En: Enstatite, Fs: Ferrosilite.....	83
Table 8: Range of An (anorthite) values for plagioclase measured by EPMA, created using melt liquids association with glass compositions (MLA glass), created using melt liquids association with melt inclusions PEC compositions (MLA MI PEC), created using melt liquids association with whole rocks compositions (MLA whole rocks), created using fractional crystallization model cotectic, created using fractional crystallization model 54%, created using fractional crystallization model 55%, and created using fractional crystallization model 56%. Ab: Albite, Or: Orthoclase.	84
Table 9: Results of volume estimation of melt inclusions using FOAMS.	92
Table 10: Ratios of volume estimation between glass and associated bubble of melt inclusions using FOAMS.	93

1. Introduction

1.1 Melt inclusions

Magmas are a complex network of atoms and compounds that exist in a liquid state due to their high temperature. When the temperature drops below a threshold, crystallization starts to occur which lead to the formation of certain minerals, during this process magma and crystals coexist in the same space. Crystallization process is not perfect, meaning that due the heterogeneous conditions of the surroundings, perfect crystalline structures are uncommon in nature. For example, crystal growth rate can be enhanced in certain parts while others not. This can produce imperfections within the crystal lattice that allow certain materials to become trapped within the growing crystal, these materials are called inclusions. These inclusions can be fluids, silicate melts or minerals. Particularly of interest are silicate melts because they are the most studied type of inclusions to understand magmatic processes (Barth & Plank, 2021; Frezzotti, 2001; Lowenstern, 1995; Roedder, 1984; Schiano, 2003; Sobolev, 1996).

Melt inclusions are a term used to describe a small droplet of magma that has become trapped within the crystal and solidified during cooling of magma during transport and eruption. Upon cooling of the crystal during an eruption and exposure to surface temperatures, melt inclusions will quench and it will form a volcanic glass. Melt inclusions can vary in size and shape, however usually they can reach a maximum size of 1 mm.

Melt inclusions, specifically the ones hosted in olivines, are one of the most valuable sources of information of the pre-eruptive history of magmas during their storage that erupt to form volcanic rocks (Wallace et al., 2021). Melt inclusions can be used to obtain information on the physical characteristics of magmas during their entrapment such as entrapment pressure, temperature and chemical composition of melts within magma storage regions. The study of fluid inclusions can provide details on the fluids transporting metals responsible for forming ore deposits, this is because often in ore deposition not only the ore constituent is part of the melt, but also volatiles and salts (Roedder, 1984). In many occasions the only trace of volatiles and salts presence in a sample is located in melt inclusions, hence certain patterns of volatiles or salts included in melt inclusions can be clear indicators of ore deposition (Roedder, 1984). The most important characteristics

of magmas that can be ascertained from studying melt inclusions are temperature during the entrapment of the inclusion within the host crystal, the pressure when the inclusion was entrapped, and the magma density and composition.

Other possible information that can be obtained from melt inclusion studies is the amount of water vapor and CO₂ during initial magma formation and also the velocity of magma ascent, this information can be constrained using water diffusion models between melt inclusions and the host crystal (Barth & Plank, 2021; L. R. Moore et al., 2015). One of the principles for the use of melt inclusions as geothermometers is based on differential shrinkage between the host mineral and the melt inclusions. The melt entrapped in the inclusions shrinks more than the host mineral so when cooling starts a bubble forms in the inclusions, the temperature then is obtained by heating of the rock sample until the bubble absorbs into the melt obtaining an approximation of temperature at which the melt inclusion was formed, this is the principle of rehomegenization experiments. Pressure is primarily estimated using the volatile content in melt inclusions where the most used volatiles are H₂O and CO₂. Pressure controls the concentration of these volatiles due to the strong relationship between volatile solubility and magma pressure (Iacovino et al., 2021; Newman & Lowenstern, 2002). Density can be considered as an important parameter to take into account if it can be used to give a general idea of the composition of vapor and daughter phases within the melt inclusion. The overall density of a melt inclusion can be determined by obtaining the density of each of the phases, compositions, and individual volumes of each of the phases present in the inclusion, then the average density is calculated, this is important because density differences are the main driver of movement of melts within the earth crust (Roedder, 1984). The different procedures to determine the composition of melt inclusions requires the characterization of the different phases present in the inclusion, the procedures can be destructive or non-destructive. Procedures considered as destructive either can alter the original composition of the sample being analyzed or change it completely after the procedure is carried out. In the other case, non-destructive procedures do not affect the composition of the sample because the techniques do not damage the analytical area or affect the original composition (Roedder, 1984).

Ideal melt inclusions in volcanic rocks occur as a homogenous silicate glass. However, the melt inclusion can experience processes after their entrapment that can modify the original melt composition. Commonly, melt inclusions contain an exsolved vapor bubble

or shrinkage bubble, and possibly daughter phases that crystallized within the melt inclusion upon cooling. An example of the different processes affecting melt inclusions are summarized in Figure 1.

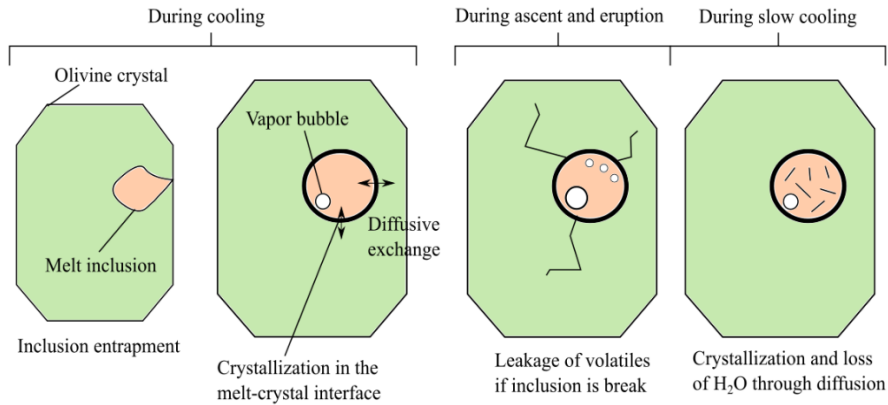


Figure 1: Different mechanisms of postentrapment modification of melt inclusions, modified figure (Wallace, 2005).

Depending on the rate of cooling and the residence time of the host crystal within the magma reservoir, the inclusion may be a silicate glass, a silicate glass with daughter phases, and in extreme cases a crystalline inclusion that if formed are now called mineral inclusions, the last one complicates the study of melt inclusions because they can equilibrate with host crystal and entrapped melt during post-entrapment crystallization (Roedder, 1984).

Silicate melt inclusions are usually composed of glass, vapor bubbles, and daughter phases (Frezzotti, 2001). In some cases, vapor bubbles and daughter phases can be present or not. Another characteristic to notice in melt inclusions are the size of the bubbles, because they are directly related to the composition, cooling behavior and the content of volatiles of the inclusions (Frezzotti, 2001; L. R. Moore et al., 2015). The presence of volatiles inside the bubbles also can be estimated by establishing the percentage volume of the bubble compared to the glass of the inclusion (Frezzotti, 2001). The principal way for melt inclusions to form is irregularities during crystal growth, specifically in olivine crystals it seems that inclusions are trapped in a more random way probably due to the different morphologies for crystal growth, which morphologies are related to growth kinetics (Frezzotti, 2001; Shea et al., 2015; Shea, Gurioli, et al., 2010; Shea, Houghton, et al., 2010). These are some of the general characteristics to take into account while studying melt inclusions.

Melt inclusions are still one of the main sources of information to understand magmatic processes on earth because they preserve information about pre-eruptive magma storage conditions; petrological information obtained by different techniques of melt inclusions ranges from volatile concentration of parent magma to the chemical composition of the magmas at depth. However, one of the most remarkable features of melt inclusions is that during their formation they preserve the conditions of a specific time and space variation in magma evolution (Sobolev, 1996).

Isolation of melt inclusions or entrapment of melt inclusions occur due to several characteristics of the magma; one of them, is the rate of volume diffusion which describes elemental movement in a crystal lattice, the other one is the rate of volume diffusion that also depends on the difference in concentration in the mineral and the diffusion concentrations. According to this, elements that are considered as incompatible in the host mineral have a limited capability of diffusion transport so they will be better isolated in the melt inclusion, this is the opposite to compatible (Sobolev, 1996). Inclusions can be formed when certain characteristics of the magma like temperature, pressure or composition changes, the rate of crystal growth also affects the formation of melt inclusions (Wallace et al., 2021). Crystal growth is driven by the undercooling which is the difference in temperature between the liquidus and the temperature when crystallization starts (Wallace et al., 2021). Rapid crystal growth which is caused by higher levels of undercooling promotes hopper, skeletal and dendritic morphologies; these morphologies can promote the entrapment of magma (Wallace et al., 2021) (Figure 2).

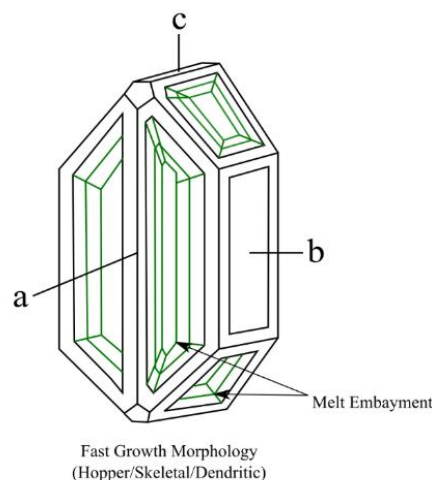


Figure 2: Example of a rapid growth olivine morphology, development of embayments within the crystalline structure allow for the formation of melt inclusions.

The number of inclusions in a sample usually is inverse to the melt inclusion size, meaning that if there is a large number of inclusions, the inclusions will be small in size. If the number of inclusions is small, the size of inclusions tends to be larger. The studies of melt inclusions usually select inclusions of 10-100 μm size range (Roedder, 1984).

Melt inclusions form at the interface of melt and crystalline phases that are characterized by regions of slow crystal growth. The most relevant mechanisms for melt inclusions formation in basaltic magmas are crystallization and textural equilibration (being textural equilibration the changes in crystal growth morphology for example between rapid hopper, dendritic, or skeletal growth), differential dissolution of the host crystal, and localized slow crystal growth due to defects. If the mechanism of melt inclusion formation is determined, several pieces of information related to the magmatic conditions can be ascertained. For instance, in the case of rapidly growing skeletal crystals, inclusions are trapped by the intersection of melt in rod crystal, hopper or swallowtail morphologies. The inclusions created under this mechanism are usually small and irregular with orientations based on the crystallographic orientation (Kent, 2008).

1.2 Melt inclusions and space-time trends

Melt inclusions provide a unique perspective to understand magmas and their evolution. This is because naturally magmas evolve with time and in space due to processes like magma mixing, crustal assimilation, or fractional crystallization. However, when products that erupt from volcanoes are typically evolved andesites, dacites, and rhyolites, very little remains of the earlier history of the magmas to understand magmatic processes that occur during early stages of magmatic evolution. It is advantageous to focus on minerals that tend to form early in the crystallization sequence such as olivine crystals. Olivine is one of the first minerals that form during the initial stages of cooling of a mafic magma according to the Bowen series (Bowen, 1922). Then, if the idea is to study the properties of the magma in the primitive state, melt inclusions entrapped within this mineral can provide insight into this information. Highly mafic rocks usually contain a considerable amount of olivine crystals. An important characteristic of mafic magmas is that they are sufficiently hot and typically cool slowly which allows the crystals to grow to a sufficient size and thus melt inclusions are more likely to develop. Researchers that utilized melt inclusions focus on olivine-hosted melt inclusions within mafic magmas

because they provide one of the only ways to constrain the primitive characteristics of magmas. Thus, the focus of this work is going to be olivine-hosted melt inclusions that crystallized from mafic magmas.

Melt inclusions, in theory, should be a perfect representation of the magma characteristics during the formation of the crystal. Although due to chemical/geological processes their composition can vary after entrapment Figure 1. Mechanisms that modify the properties of the melt inclusions after they are trapped within a crystal are termed post-entrapment processes. One of the processes that cause changes in the composition is the crystallization of the host phase that occurs at the walls of the inclusion (Danyushevsky et al., 2004). From this example it is important to emphasize that the study of melt inclusions does not stop when melt inclusions in samples of olivine phenocrysts are characterized, to determine the true conditions at which the inclusions were formed further analyses are required. Some of these analyses are reheating of melt inclusions (rehomogenization) or to create numerical models that describe crystallization after entrapment (Danyushevsky et al., 2004).

1.3 Olivine growth and melt inclusions link

The first step to understand the distribution of melt inclusions within an olivine crystal is to determine which model of olivine growth applies to the samples examined in this study. Olivine composition usually is explained as a solid solution between two endmembers of the olivine group, these members are forsterite and fayalite (Cressey & Howie, 2005). Forsterite is the magnesium rich endmember of olivine (Mg_2SiO_4), and fayalite is iron rich endmember (Fe_2SiO_4), Olivines with different forsterite content are found in different igneous rocks. For instance, olivines with Fo (forsterite) wt% 96 – 82 are found in ultramafic rocks like dunite and peridotite that compose the mantle, olivines with Fo wt% 91 – 86 are found in mantle derived ultramafic nodules present in some basalts, and olivines with Fo wt% 80 – 50 are common in basalts and gabbros (Cressey & Howie, 2005). So olivines are common in rocks ultramafic to mafic in composition.

As explained, olivines have a mafic composition, it is possible to determine magmatic processes that occurred during the formation of the magmas in equilibrium with mantle peridotite. This is especially true when olivines have a more mafic composition (> 80 Fo) (Salas et al., 2021). If chemical zoning is present within the crystal, the growth of the

crystal can occur in a sequence, where the innermost part of the crystal (the core) is the oldest part, and the outermost part of the crystal (the rims) is the youngest part. One of the most common growth patterns of olivines is an early dendritic growth which then is followed by infilling in of the dendritic system of the crystal, this type of growth pattern is important for the formation of olivine melt inclusions (Salas et al., 2021; Shea et al., 2015).

Another common crystal morphology of olivines in arc-systems are olivines with a polyhedral morphology. The changes in olivine crystal morphology during growth is linked with olivine maturity and the stage of the melt of which they are derived from.

In other words, as the magma evolves as it migrates to the surface, the different environments the olivines encounter can influence the overall morphology of the olivine. Thus, the nature of mineral growth patterns that represent changes in the geological conditions and careful observation of these complex patterns allows for the interpretation of the processes that formed those features. In order to determine with more precision how the crystallization of olivines changed during magma evolution it is required to compare a growth model with chemical data of the crystal. That is because chemical composition of the melt from where the olivine is formed changes with time, and also mineral and melt interaction determines changes in composition, usually as the olivine is formed the melt around it is depleted in iron and magnesium, and the crystal is enriched with these elements. Furthermore, the core of the crystal that is formed usually has a higher forsterite concentration compared to the rims. Also, as melt reaches the surface the forsterite concentration in the olivines also decreases (Salas et al., 2021).

1.3.1 Olivine morphology

Olivine morphology mainly varies due to two parameters that vary during crystal growth, these are cooling rate and the degree of undercooling. The cooling rate is the decrease in temperature in a certain period of time. Undercooling is one of the most important parameters that determine a certain crystal morphology as well as the rate of growth of the crystals. The rate of growth appears to be largest when the degree of undercooling is small, this is possibly explained by long-range diffusion which is a mechanism for the crystal to lose latent heat and is more common at small rates of undercooling (Conte et al., 2006). In the case of cooling rate, it also affects crystal growth and by that the melt

fraction within the crystal (fraction of melt inside the crystal), this is because with increasing cooling rate the crystal size decreases and a smaller crystal size has a smaller melt fraction and vice versa. The temperature at which cooling starts also affects several characteristics especially crystal morphology (Conte et al., 2006). The most common morphologies of olivine crystals are polyhedral, tabular, skeletal, dendritic, and feather shape (Faure et al., 2003) (Figure 3).

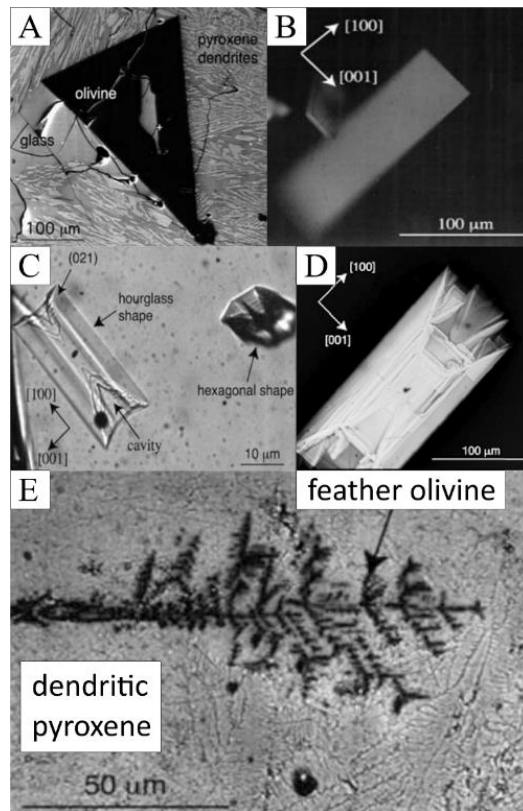


Figure 3: SEM images and micro-photographs of different experimental olivine morphologies for context. A: Polyhedral, B: Tabular, C: Skeletal, D: Dendritic, E: Feather shape. Modified figure (Faure et al., 2003).

Polyhedral shapes (Figure 3/A) are common and are characterized by having well defined crystal faces, it is common also to encounter melt inclusions with certain shapes such as spherical or elongated. Tabular shape is often associated with polyhedral or hopper olivine crystals (Figure 3/B). The skeletal morphology of olivine or hopper crystals shows a hexagonal shape or an hourglass shape usually depending on the orientation of observation of the crystal (Figure 3/C). The step morphology (formation of regular steps in the interface of the crystal and the glassy pockets) also develops when the skeletal morphology is present, it is influenced directly by the cooling rate. If the cooling rate is low, the step morphology is preferred. Dendritic morphology shows certain shapes called swallowtail and rod, characterized by overgrowth in certain areas of the crystal with

irregular crystal faces (Figure 3/D). Feather morphology is characterized by the presence of fine fibers that develop near the dendritic fibers (near the shallow tail crystals) (Figure 3/E) (Faure et al., 2003).

At certain ranges of undercooling and cooling rate, specific crystal morphologies are developed. If the degree of undercooling and the cooling rate are low, the preferred morphology is polyhedral. As the cooling rate increases the morphology preference is shifted to tabular or skeletal (hopper). The boundary between these morphologies can be described as the change from a steady state crystal growth to a rapid crystal growth (where the polyhedral morphology does not occur). Up to this point, if the cooling rate changes the morphology is not affected. However, if the degree of undercooling changes this can lead to changes in the morphology, which can develop dendritic shapes. Dendritic shapes seem to develop as the repetition of a three-dimensional shape (the skeletal/hopper morphology). The size of the crystals, as they repeat, decrease (Conte et al., 2006).

The thermal and physical conditions of magmas that end up creating olivine crystals are often studied using chemical zonation in olivines which is a result of change in the chemical and physical conditions within the magmatic system. The crystal habit of olivine is a direct consequence of the geological conditions that led to its formation (Faure et al., 2007). The importance of changes in morphology of polyhedral olivine crystals are because they can be used to determine magmatic conditions of formation. During slow cooling episodes, polyhedral crystals are formed. If the cooling rate increases, small crystals start to nucleate along preexisting crystal faces. This particular change is clear due to the appearance of large cavities in the crystals with a stair-like shape, which is typical of olivine with a skeletal morphology. In hopper polyhedral crystals it is possible to find elongated glass inclusions parallel to some faces of the crystal. The inclusions also can be connected to the exterior of the crystal forming an embayment or reentrant. The next change in morphology of the crystal at rapid cooling rates is from a skeletal (hopper) polyhedral crystal to a dendritic polyhedral crystal. The host polyhedral crystal structure (faces of the crystal) controls the formation of dendritic rods in the crystal cavities (Faure et al., 2007).

Rapid cooling events are related with dendrites, while slow cooling events show polyhedral shapes, this is one of the main tools to determine at which cooling rates the olivine crystals were formed. The presence of parallel rods also is an indication that two different stages of cooling formed the final crystal shape of the olivines (Figure 4).

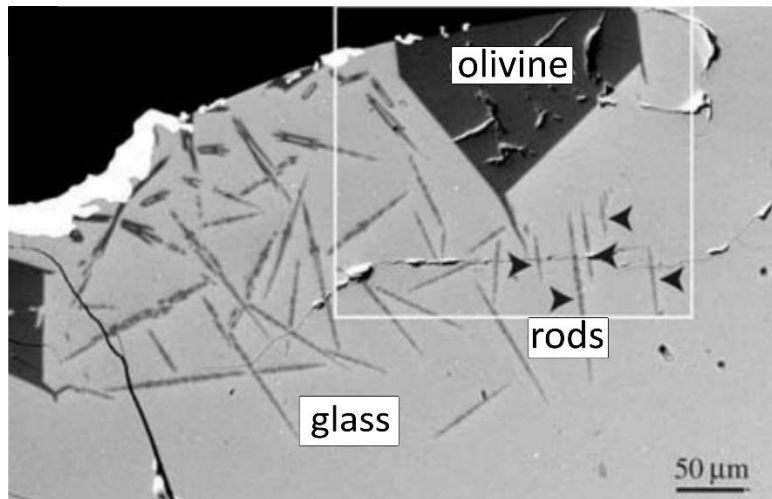


Figure 4: Modified SEM image as an example of a dendritic olivine showing the development of rods from experimental results (Faure et al., 2007)

Screw dislocation mechanism (type of irregularity within the crystal structure that describes a sudden change in the arrangement of atoms) is the main explanation for the growth of polyhedral crystals, especially when the degree of undercooling is low. This mechanism also in this particular crystal shape is supported by the appearance of melt inclusions that are irregular and curvilinear in shape (Faure et al., 2007).

Microtextural information observed in volcanic products can be used to infer crystallization histories and provide insight into processes leading up to volcanic eruptions (Conte et al., 2006; Donaldson, 1976; Jones et al., 2014; Salas et al., 2021). Mean crystal size and number density of magnetite microlites that can be present on olivines is another method applied to study growth histories of phenocrysts from volcanic rocks. Genareau et al. (2010) demonstrated that these observations can be used to determine the amount of time that it took to form a crystal. The surface of a phenocryst olivine also changes depending on certain crystal growth conditions; crystals that have growth in a free melt environment show smooth surfaces, compared to other crystal growth environments that can alter the surface of the crystal (Jones et al., 2014).

1.4 Inclusions from a homogeneous fluid: primary and secondary inclusions

In order to understand why a melt inclusion may be primary or secondary first it is important to understand the common form for creation of melt inclusions. Growth irregularities happen when a crystal grows or recrystallizes, these irregularities can result in the tapping of small portions of the melt in the solid crystal. These irregularities are

sealed off during the growth of the host crystal, these sealed portions are called primary melt inclusions. Such distinction between primary and secondary melt inclusions is necessary in order to make a reconstruction of events that lead to the formation of the sample, in this case olivine crystals in volcanic rocks. The most important types of primary inclusions are called intracrystalline inclusions and intercrystalline inclusions. Intracrystalline inclusions are the most studied and they are inclusions that are within single crystals. The formation of this type of primary inclusions heavily depends on the crystal growth. Crystal growth may depend on the concentration of constituents in the melt. The most straightforward principle is that certain minerals (with specific crystalline structures) require specific elements for their formation. If there are not enough elements to form these minerals, its formation is interrupted leading to more or less perfection in the growth process. By this explanation, primary inclusions are irregularities that formed in a crystal. Intercrystalline inclusions are less studied, but they have importance in certain applications, these are inclusions that are formed at the contact between crystals (Roedder, 1984).

Secondary inclusions are the ones that are formed by any process that occurs after the host has been crystalized. The usual way that these inclusions are formed is by the fracture of a crystal in the presence of a fluid. The fluid will enter in the fracture which will cause the dissolution and recrystallization of the host crystal. The crystal surface will change which eventually will result in the trapping of new secondary inclusions, the usual result of this process is the creation of a plane of sharply faceted negative crystal inclusions. This type of inclusions is more common in minerals that have suffered alterations post formation, like metamorphosed quartz (Roedder, 1984).

1.5 Basaltic melt inclusions

Volcanic rocks of basaltic composition are defined as rocks that have been erupted as lavas or tephra, their main chemical composition is SiO₂ between 45 to 52 wt%, the rocks contain a considerable amount of MgO and FeO, and minerals in the form of phenocrysts like orthopyroxene, clinopyroxene, anorthite-rich plagioclase, forsterite-rich olivine and a spinel phase (Kent, 2008). The process that originates basaltic magmas and their evolution allows for the formation of melt inclusions regardless of the conditions and the environment of formation. Hence melt inclusions occur in most of the different tectonics

settings that occur on earth, from subduction related magmatic process, to the ones generated in environments where the melt generation processes is adiabatic decompression (Kent, 2008) such as mid-ocean ridge, mantle plumes, and rifting environments. Studies of melt inclusions in basaltic magmas have several advantages compared to traditional whole rock analyses. One of the advantages is that because melt inclusions can form at higher pressures, the volatile concentrations are higher, and volatile oriented studies have more information available. At low pressure environments volatiles begin to exsolve out of the magma, so the products that later erupted from these low-pressure environments will never contain the original volatile concentrations. That is why melt inclusions are useful for volatile studies, because crystal limits the exchange between the inclusion and the host magma regardless of the pressure environment of the magma. Thus, volatile information of primary magmas as measured from melt inclusions can be used to infer magma degassing upon ascent and eruption. Volatile information is also important for understanding other information about volcanic rocks like, the possible viscosity of the magma from which the rocks are generated, and volatiles also influence mineral stability. Specially in subduction zones, volatiles play an important role in magma generation, so primitive volatile information can be used to understand magmatic generation processes. The other advantage of melt inclusion studies in basaltic rocks is that melt inclusions usually show more variety in melt compositions. This can be explained due to the mixture of different magmas located at different locations in the magmatic plumbing system. The melt inclusions entrapped within crystals before a magma mixing event preserve a snapshot of the previous compositional history of the original melt.

Variations in magma composition obtained from melt inclusions studies is one of the primary methods to constrain the generation and evolution of basaltic rocks. Furthermore, melt inclusions can be the only possible way to understand the original characteristics of the magma that formed a rock that has been highly altered and are thus useful for studies of ancient and altered basaltic lavas (Kent, 2008).

Mineral hosts of melt inclusions are a fundamental part to consider due to the influence on inclusion characteristics and formation. The most commonly used host minerals in basaltic rocks are olivine, spinel, plagioclase, orthopyroxene, and clinopyroxene. Usually, the most preferred mineral to study melt inclusions is olivine. This is because olivine is one of the earliest minerals that forms during magma cooling, the melt inclusions that

form during olivine formation preserve the earliest characteristics of the melt. In other words, the early stages of magma evolution. Furthermore, olivine is translucent so the observer can identify the inclusions. Olivine crystal structures are fairly incompatible with the most trace elements (REE (rare earth elements) like La, Ce, Eu and others). So, olivine fractionation does not alter the trace element characteristics of primitive magmas. The small mineral-melt distribution coefficients do not lead to fractionation of incompatible elements during crystallization of the mineral host (Kent, 2008) and thus post-entrapment processes are less likely to modify the trace element contents of olivine-hosted melt inclusions. Furthermore, the rate of diffusive equilibration of the melt inclusion within the host crystal is low due to the very low mineral-melt distribution coefficients (caused by the incompatibility of these elements in the crystal and thus their preferential incorporation in the liquid phase and not the crystalline phase). This is important because trace elements are commonly used to determine for example the tectonic environments where magmas are formed (subduction zone, mid-ocean ridge, rift, etc.), and for variations in the petrogenesis of arc magmas.

Melt inclusion information sometimes is constrained using experimental petrology methods that generally involves taking a sample and heating/applying pressure until it reaches similar conditions of a magma at depth, then olivines are artificially grown, the olivines are observed and conclusions like the abundance of inclusions in isothermal conditions are documented. Isothermal growth is a condition that provides insight in melt inclusion formation. For example, when isothermal conditions are present, inclusions are significantly more abundant in each individual crystal. If a sample of olivine crystal shows an abundance of melt inclusions, it is possible that the formation of them was under isothermal conditions. The experiments where this information of melt inclusion formation mechanisms was obtained usually are a fair approximation of natural/real conditions thought to exist in magmatic systems (Kent, 2008).

Changes in the composition during melt inclusion formation is one of the major concerns with basaltic magmas. Under certain circumstances, the inclusion formation can promote changes in the composition of the melt that is trapped. For instance, as previously explained, during the formation of melt inclusions the melt is incorporated from the boundary layers at crystal-liquid interfaces.

The problem is if the composition of the melt trapped at the boundary is an acceptable representation of the overall melt at the time of trapping. Experiments showed that the

rate of crystal growth and the mechanism of inclusion trapping are important characteristics to consider in order to understand the true composition of natural melt inclusions.

This is because the diffusion rate of elements within the melt are closely related to the rate of crystal growth. Thus, elements can become depleted or enriched during the growth of the host crystal and complete entrapment so the melt inclusion composition may differ from the original melt (Kent, 2008).

1.6 Evolution of basaltic melt inclusions after trapping

It has been pointed out that melt inclusions are a remarkable way to measure melt conditions at the moment of entrapment. However, different processes can affect melt inclusions after trapping, altering the composition of the inclusion. Melt after being trapped does not follow the same compositional evolution as the host magma. This is because the composition evolves following temperature within the inclusion. At the moment of formation, the inclusion has the same temperature and pressure of the melt around it. Since the volume of the inclusion is small compared with the host, the temperature of the inclusion will be the same as the melt around it. Nonetheless, the parameter that varies significantly is the pressure in the inclusion compared to the melt. Changes in pressure are small within the melt inclusions compared to the changes that the overall melt experiences during ascent and decompression. The pressure change of the melt inclusion is considered to be at least less than 30% and even below 10% of the total pressure change that the host mineral and the melt experiences. Particularly, this difference in pressure between the inclusion and its surroundings can cause ruptures in the mineral host. Decompressing the melt inclusion can lead to changes in the composition of the inclusion. These compositional changes are caused because pressure is a factor that influences mineral formation and volatile solubility. If pressure changes due to a sudden rupture, minerals can begin to crystallize within the melt inclusions that are stable in the lower pressure environment (Kent, 2008).

1.6.1 Post-Entrapment Crystallization and re-equilibration of melt inclusions

Right after the inclusion is formed and the temperature decreases, crystallization of the host phase will start in the wall of the inclusion. Nucleation sites are abundant at the

margin of the inclusions and this is why crystallization is preferred at these locations. Mineral growth will have a fractional behavior (meaning that as olivine crystallizes along the wall of the inclusions, elements necessary for its growth (Mg, Fe, etc.) are removed from the melt changing its composition) if there is no significant re-equilibration between the crystal that is growing (or also called the new rim along the margin of the inclusion) and the mineral host. In the case of olivine, the new crystal will be new olivine (an increment) that has higher concentration of magnesium compared to the entrapped melt because the olivine structure can contain 30 - 45 % of MgO and mafic magmas typically have 3 - 12 MgO. Because the initial rim of olivine is Mg-rich, the resulting melt will have a higher Fe content and FeO/MgO. So, the subsequent rim of olivine to form at the interface of the melt and the host crystal will be more Fe-rich. This process creates a zone of Fe-rich olivine around the melt inclusion, the melt inclusions also will be depleted in Mg and other elements compatible in the olivine such as Ni and P. This process also causes an increase in concentration of olivine-incompatible elements (Kent, 2008). This process is called Post-Entrapment Crystallization (PEC).

Melt inclusions have been studied because it is the only possible window for studying original magmatic compositions that have not been altered due to magmatic evolutionary processes. However, the interpretation of melt inclusion data is complicated because melt inclusions may be altered by post-entrapment re-equilibration. The rate of inclusion equilibration will determine if the inclusion will reflect the initial conditions of the magma when it was entrapped. the inclusion will not exchange completely with the external melt if the rate of equilibration is slow. In contrast, if the rate is fast the melt will only reflect conditions of the most recent melt that the mineral host interacted with (Kent, 2008). The rate of inclusion equilibration can be determined by the diffusivity of the species in the host crystal. The timescales for equilibration of a melt inclusion have been constrained by observing diffusion profiles of specific chemical species such as H₂O and knowing the diffusivities of these species in the host crystal. Timescale information can be constrained by modeling the diffusive exchange of the species with host crystal and matching the measured diffusion profile with those calculated using the diffusion equation (Qin et al., 1992). The difference in size between the inclusion and the host, the partition coefficient of the species (numerical value that determines the ratio between elements using chemical compatibility between them in two different phases), the cooling rate, and the degree of

initial disequilibrium between the inclusions and the host are also data necessary for determine the rate of equilibration in the mathematical models (Kent, 2008).

The most important re-equilibration process for melt inclusions in olivine is concerned with iron loss; this is a case that involves the re-equilibration of the inclusion and the host of the Fe^{2+} content (Danyushevsky et al., 2002). This process is also affected by the cooling rate. If cooling rates are slower than the rate of crystallization, diffusive equilibration can increase significantly and lead to the loss of Fe from the melt inclusion (Kent, 2008).

1.7 Spatial distribution of melt inclusions

The purpose of studying the tridimensional distribution of melt inclusions inside crystals is to determine the different shapes of the inclusions and the volumetric proportions of the different phases (glass, vapor, or daughter minerals) (Richard et al., 2019).

The spatial distribution of the melt inclusion and their properties are important because the different properties can be used for different purposes. For example, the relative size of the vapor bubbles. The size of the bubbles will depend on three characteristics of the inclusion: melt composition, volatile content, and cooling behavior. Just based on the size of the bubble, preliminary characteristics of the melt inclusion can be studied (Frezzotti, 2001). How crystal growth may affect the distribution of melt inclusions is also an important feature to be studied, an example of this is that irregularities of growth can control the distribution of inclusions in other host phases such as quartz crystals. Olivine and pyroxene crystals have a tendency to trap melt inclusions in random manners. The shapes of the inclusions can vary between each other inside a crystal. However very often have smooth rounded, oblate and even elongated morphologies and even can follow the external morphology of the mineral host (Frezzotti, 2001).

Possible chemical trends of melt inclusions which depend on the distance of them from the edge of the crystal are still a subject of study, which can provide a possible insight in the relationship between minerals and parent melts as they evolve.

1.8 Chemical composition of melt inclusions and their use to understand magmatic processes

In order to determine the melt composition for major and trace elements, silicate-melt inclusions in olivine are chemically analyzed. The chemical composition regarding major and trace elements in melt inclusions can be used to infer several important magmatic processes that create the inclusions. Some of them are to create reconstructions of primary melt composition and formation conditions. They can be used to make fractional crystallization models, and how much assimilation and or magma mixing actually affected the resultant magma composition (Frezzotti, 2001). An example of the use of major and trace elements measurements/variability in melt inclusions in olivine phenocryst is that they were used to determine the origin of the sample from distinct parental magma sources. In the case of trace and light element measurements in melt inclusions, they can be used to determine different stages of melting and extraction of melts that are formed at mantle conditions (Frezzotti, 2001).

Melt inclusions chemical measurements focuses on the following chemical elements: Si, Ti, Al, Cr, Fe, Mn, Mg, Ca, Ni, Na, K, P which are called major and minor elements in silicate liquids because they have relatively high concentrations and can be measured using an Electron Probe Microanalyzer (EPMA). It is also possible to use an EPMA to determine F, Cl, and S which are volatile chemical elements (Kent, 2008). Their concentrations are typically high enough where they can be accurately measured using this technique in contrast to the other volatile elements described below. One of the disadvantages of EPMA analysis is that it cannot distinguish between different iron cations (ferrous Fe^{2+} and ferric Fe^{3+}), and it is reported as only FeO (Fe^{2+}), however stoichiometric approaches can be applied to estimate the proportions of each chemical species.

1.9 Volatile content of melt inclusions

Magmatic volatile contents can be studied using silicate-melt inclusions, these can be used to determine volatile content before and during crystal growth. Melt inclusions, specifically silicate melt inclusions, can retain high concentrations of volatiles that may be lost during magma degassing. The melt inclusion containing abundant volatile content (in some cases between 7 to 8 wt% H_2O) is supported in the idea that they trapped their

original volatile content because the volatiles would begin to degas at low pressures (Barth & Plank, 2021; G. Moore, 2008; L. R. Moore et al., 2015). The usual volatiles that are measured in melt inclusions are H₂O, CO₂, F, Cl, and S. Measurement of these species can be used to infer the pre-eruptive volatile contents and if melt inclusion entrapment occurred in many different stages and thus the evolution and behavior of volatiles in the magmatic system can be inferred. However, diffusion processes can affect the original content of volatiles in the melt inclusions too so corrections must be taken into account (Bucholz et al., 2013).

H₂O diffusion between the olivine bearing melt inclusion and the changing magma can change significantly, from rates of re-equilibration of days to even hours/minutes (Lloyd et al., 2013). Besides the usual processes that can lead to H₂O re-equilibration like magma mixing and magma ascent, post-eruptive processes like cooling rates at surface temperature can also induce re-equilibration (Lloyd et al., 2013).

The investigation of these post-eruptive processes and H₂O re-equilibration have established that melt inclusions may be affected by H₂O loss in these processes, and melt inclusion H₂O concentrations may not be affected significantly by other usual mechanisms like open-degassing (magmatic systems with open connections) and mantle derived H₂O variations (mantle water content determine the final content of water in melt inclusions) (Lloyd et al., 2013). The size of melt inclusions also seems to be a significant factor that determines rates of water loss. This is possibly because a larger size of the inclusion means that the melt inclusion reaches the most external portion of the mineral host which increases the chemical gradient and thus enhances re-equilibration. For instance, the same study concludes that melt inclusions with a diameter between 40 – 100 µm and a mineral host (olivines) with a range between 400 – 1000 µm can lose H₂O in a range of 1 to 30 wt% (Lloyd et al., 2013). Usually, tephra samples with a diameter < 2 cm can have the best glassy melt inclusions due to their equilibrium with the mineral host (olivine), preserving the original H₂O content. However, if ascent rates are low and diffusive rates are fast, the inclusions can experience a significant H₂O loss (Lloyd et al., 2013).

On average, silicic melt inclusions usually contain around 4 wt% of H₂O and thus the parent magmas are also believed to have this average water content. Based on the measurements obtained from volatile analyses of the content of melt inclusions, it is

possible to infer the primitive volatile content of the magma that was entrapped in the inclusion (Lowenstern, 1995).

Not only the glass phase within the melt inclusion carries a major proportion of the volatile budget. Vapor bubbles which are common in melt inclusions are thought to carry significant volatile portions, specifically CO₂. Volatile concentration analyses carried in vapor bubbles and glass in melt inclusions have shown that most of the CO₂ is carried in the bubble (L. R. Moore et al., 2015). Especially in volcanic systems, melt inclusions contain vapor bubbles consisting of both H₂O and CO₂. So, if a volatile budget is estimated without taking into account the volatile composition of the bubble, the estimates will largely underestimate CO₂ content of the whole melt inclusion. The major concern is that if the volatile budget is wrong, estimated degassing trends will be off, which are important to understand open or closed magmatic systems (L. R. Moore et al., 2015).

It is important to express that there have been advances in the procedures to determine volatile content of magma that was entrapped in the inclusion, both volatile content of solid and liquid phases in vapor bubbles should be quantified to access the original volatile composition of the magma (Lowenstern, 1995).

1.10 Subduction zone system

A subduction zone is defined as where the convergence of two tectonic plates occur, the oceanic lithosphere of one of the tectonic plates plunge below the continental/oceanic lithosphere of the other plate reaching the mantle (Schellart, 2023). The most important characteristics of subduction zones are the formation of a deep sea trench (plate boundary between the two tectonic plates), the Wadati-Benioff zone which is a planar zone of seismicity that extends from the trench to approximately 700 km in depth to the mantle (marks the location of the subducted lithospheric slab), and a magmatic arc above the overriding plate which forms due to partial melting in the mantle wedge (partial melting is enhanced by the presence of fluids liberated by the subducted slab) (Schellart, 2023), the usual mantle sources in the subarc that melt in this tectonic setting are: peridotite, pyroxenites, and other metasomatized ultramafic lithologies. The last characteristic is the one of interest for this study, since magmatism in continental Ecuador is driven by this

type of process as all volcanism in an arc setting (Chiaradia et al., 2009). A representation of the subduction zone functioning in Ecuador is shown (Figure 5).

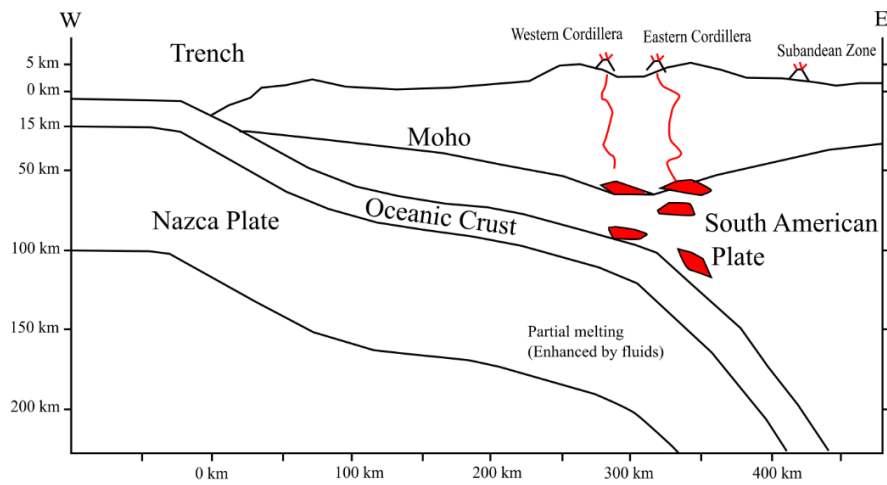


Figure 5: Modified general cross-section in Ecuador showing the subducting tectonic setting (Cajamarca-Zuniga et al., 2022).

1.11 Purpose of the study

This thesis will address three topics related to volcanism at a small volume mafic system in a continental arc setting and the application of olivine-hosted melt inclusions to study magmatic processes.

- Application of olivine hosted melt inclusions
 - Evaluate if there is a systematic variation in the melt inclusion properties based on the special arrangement of the melt inclusion within the host olivine
- Petrogenesis of magmas at the Tulabug and Bellavista cones of the Licto volcanic complex
 - Constrain the potential mantle source characteristics in the subarc mantle beneath Licto
 - Evaluate for potential causes for magma diversity and melt evolution within the shallow plumbing system at Licto
- Eruption dynamics and magma ascent processes
 - Constrain details of vesicle nucleation and growth mechanism during magma ascent through the conduit system at Licto

2. Geologic Background and Tectonic Setting

Several locations were considered from Ecuador, due to its position in an active convergent margin. This margin is located between the subduction of the oceanic Nazca plate under the South American continental plate. The Ecuadorian volcanic arc forms part of the “North Andean Volcanic Zone”. This study will focus on the volcanic products collected from the Licto cones (Tulabug and Bellavista), located in the southern segment of the Ecuadorian volcanic arc. Furthermore, the cinder cones are located south of the Grijalva Fracture Zone and in the volcanic arc located in the Interandean Valley (Bablon et al., 2019). This is due to the likelihood of the material to represent early stages of magma evolution in this area (mafic composition), the type of volcanic material encountered in this cones (scoria) quenches rapidly when exposed to surface conditions helping to preserve magmatic properties, and the southern location due to be likely located outside the influence zone of the Carnegie subduction. The chemical variations in the composition of the volcanic deposits found in Ecuador could be associated with changes in the inputs derived from the subducting slab or the petrological interactions occurred between magma and crust (Ancellin et al., 2017; Chiaradia et al., 2020). The quaternary volcanic arc width in Ecuador has a range of around 60 to 150 km caused by geometry changes in the subducting slab, this could influence compositional changes in the crust (a wider magma generation zone) (Bablon et al., 2019).

The development of the southern portion of the north Andean volcanic arc presumably started with the construction of the andesitic Huisla volcano, located in the Interandean valley at approximately 600 ka. The increase in the volcanic activity on the area of interest in the period of time between 300 ka to 100 ka is shown by the construction of the volcanic edifices of Carihuarizo and Tungurahua followed by the formation of the Licto cones, Mulmul volcano and Puyo cones (Bablon et al., 2019). It is suggested that the Quaternary volcanism in Ecuador migrated southward due to the presence of older volcanoes in the northern portion of the southern segment compared to the younger ones to the south. The edifices of the southern segment are located approximately 105-110 km above the dipping plate (subduction zone). At these depths temperature and pressure conditions are met for the melting of mantle wedge and the production of magma (Bablon et al., 2019). Clusters of volcanism are identified separated by segments with scarce Quaternary volcanic activity, Licto (Tulabug cone) is identified to be a product of the last southernmost cluster of volcanic activity. This particular arrangement of volcanic clusters is thought to be the

product of thermal anomalies in the mantle wedge which increases the range of melting and the production of magma, where these clusters show a change in orientation from north to south, with a NW trend orientation in the south (Bablon et al., 2019). The seismic interpreted flexure of the slab at depth identified in Ecuador seems to play an important role in the Quaternary volcanic activity. This relationship is especially evident in the southern termination since the volcanoes at this location are located above this flexure (Bablon et al., 2019). In summary, the volcanic activity at the southernmost portion of the volcanic arc in Ecuador is related with a change in the dip of the slab (geometry of the slab), where the northern portion of the arc is located above a slab with a shallower dip, and the southern portion with a steeper dip. These changes in the tectonic geometry in Ecuador promoted changes in volcanism in the area, which affected the volcanism in Licto (Bablon et al., 2019).

The most important deposits that are going to be analyzed comes from scoria beds at Tulabug, these deposits are on top of lava beds. The deposit comes from a group of volcanoes named “Licto” cinder cones, which are located near the city of Riobamba (Chimborazo province). The Licto scoria cones, Tulabug and Bellavista, have a basaltic andesite and andesite composition respectively (Schiano et al., 2010), and the Riobamba basin, where the Licto cones are located, is composed of Pleistocene sedimentary deposits (Lavenue et al., 1995) (Figure 6).

In the area of study, different lithostratigraphic units are encountered. For instance, Sicalpa volcanics are composed of fine-grained tuffs with clasts of medium size (white to gray in color), and agglomerates which have an intermediate to acidic composition. These volcanics are estimated to have a Pleistocene age (Hoffstetter, 1956). Altar volcanics (old name, now Pisayambo volcanics) are mainly composed of pumices and andesitic fragments. Very thick Cangahua is present across the area. The Pungalá intrusive is a granodiorite composed of orthoclase, albite, and andesitic-oligoclase (Hoffstetter, 1956) and is exposed just north of the Licto cones.

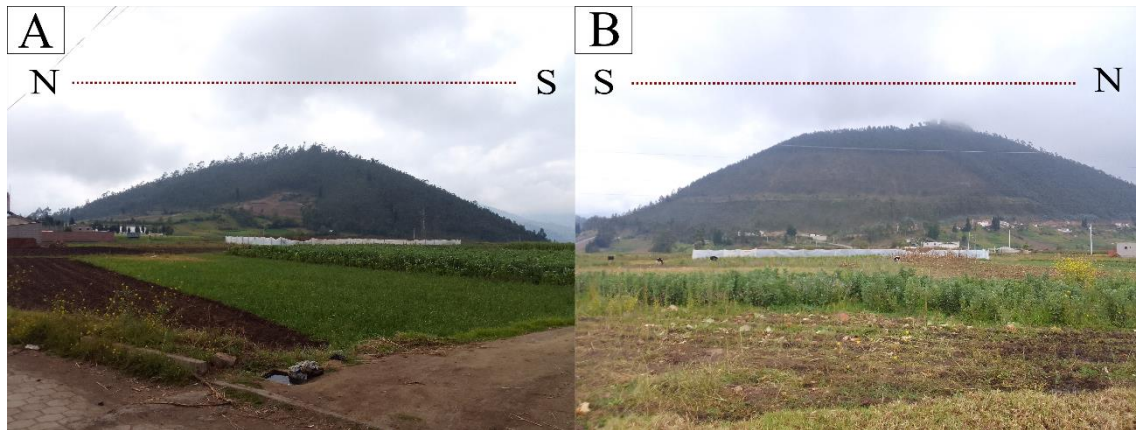


Figure 6: Images of two of the cinder cones at Licto. A: Loma Bellavista, B: Tulabug. Licto, Chimborazo (Ecuador).

There are two main eruptive centers that belong to the Licto cinder cones (Figure 7 and Figure 8). This study, is focused on the Tulabug cone based on the composition of the erupted products. The cone erupted basaltic andesite magmas and it shows a more primitive composition compared to the main volcanic arc (Ancellin et al., 2017; Bablon et al., 2019; Schiano et al., 2010).

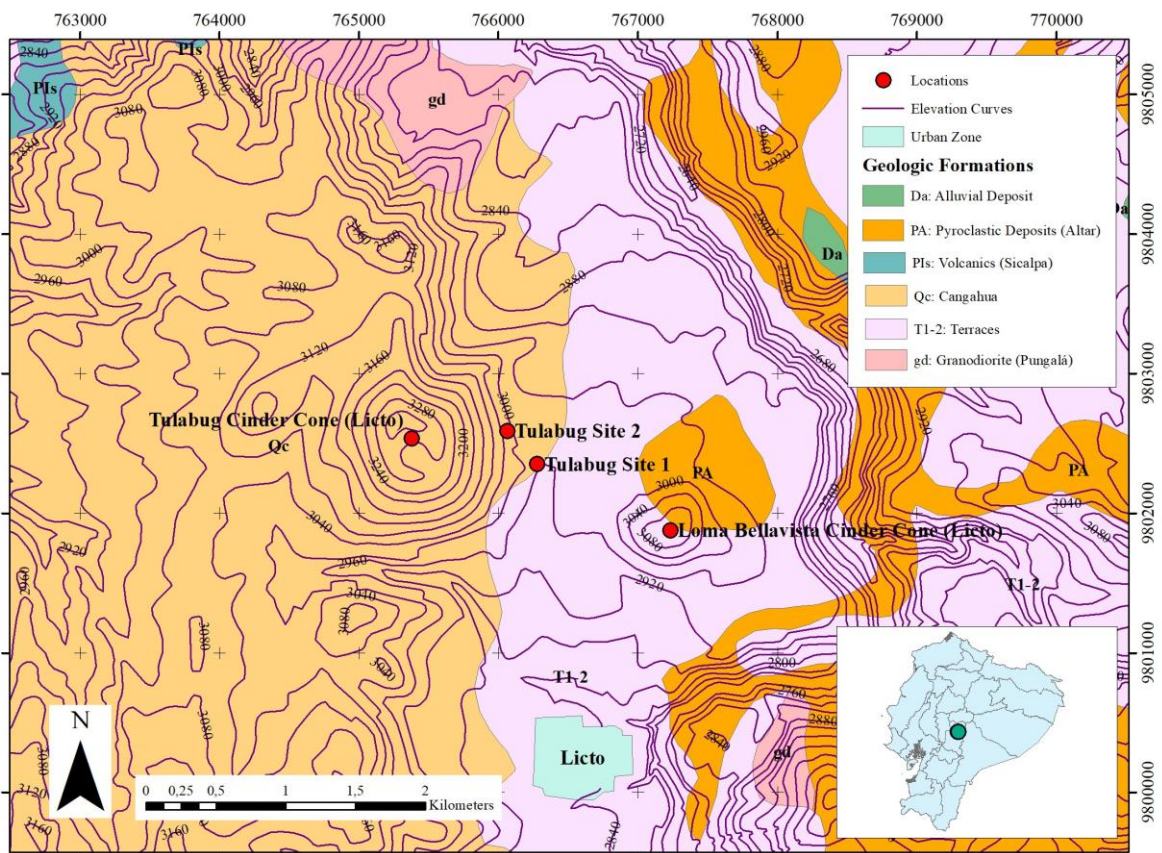


Figure 7: Location Map of the Tulabug Cone, as a reference of the city of Riobamba (Chimborazo).

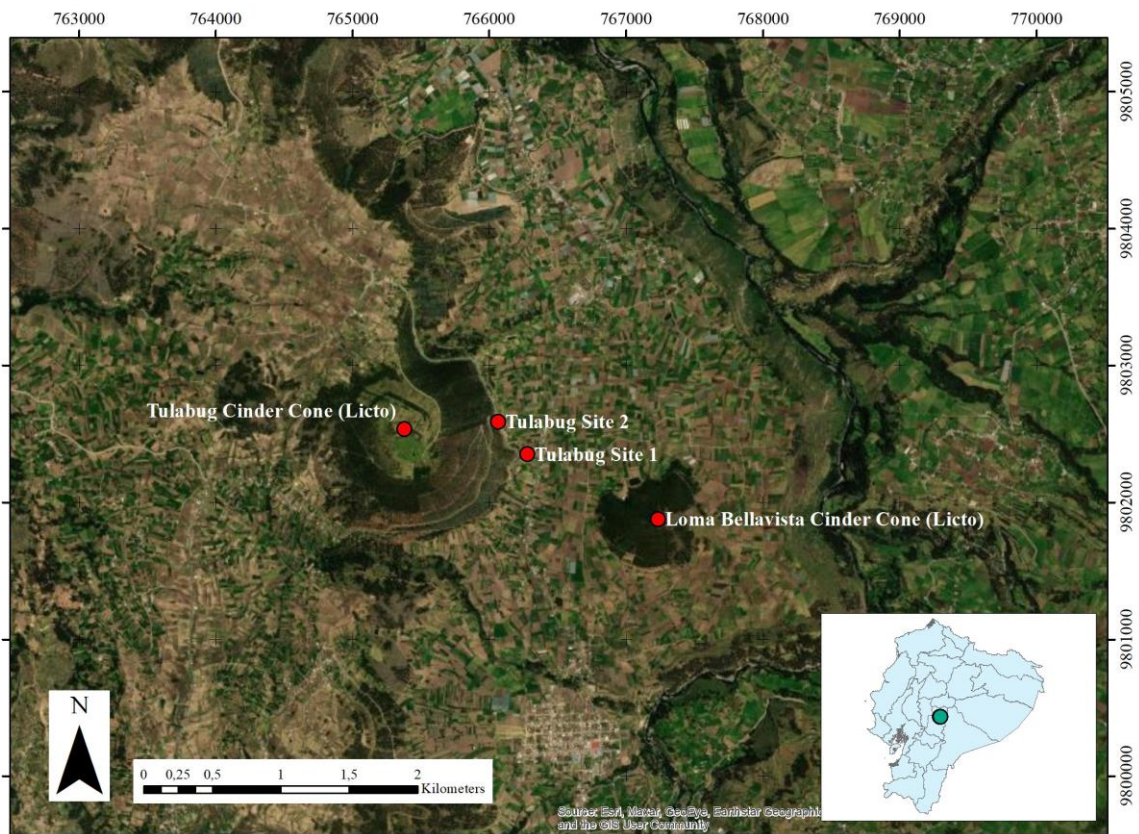


Figure 8: Location Map of the Tulabug Cone, as a reference of the city of Riobamba, Satellite Imagery (Chimborazo).

The age approximation of the Tulabug cone (the lava flow) is 183 ± 9 ka, obtained through K-Ar method, considering geological time scales it can be considered a recent eruption (Bablon et al., 2019).

3. Methodology

3.1 Sampling/Geological Setting

Melt inclusions that can be studied under the conditions of this project, which generally are no additional laboratory procedures such as rehomogenization, require certain characteristics of the material where they come from (see section 1). The former additional procedure is essential in heavily altered melt inclusions. Another important condition is that the crystals cooled rapidly during an eruption. That is why volcanic tephra is usually the desired deposit from which the olivine samples will be extracted from in this type of study. This is because volcanic tephra is a product of explosive eruptions, and under this type of eruptions the material quenches rapidly when exposed to surface conditions, preserving magmatic properties.

Licto site 1-1 is located at the base of the Tulabug cone (Figure 7), the volcanic material at this site is composed of layers of lava flows and scoria fall deposits. The base of the sequence consists of a 2-m thick lava flow, thin layers of scoria falls are directly overlaying this lava flow alternating with finer ash deposits. The scoria layers were selected for sampling. These layers have an estimated thickness of around 10 to 15 cm, particular layers of scoria fall are unconsolidated, more consolidated material makes up the lava layers. Planar bedding is the general sedimentary structure of the outcrop likely caused by air fall along the flanks of the volcano, the planar beds conform to the original topography of the landscape when they were deposited which form a small trough shaped structure in the outcrop, and there is no internal layering in the scoria deposits (Figure 9).

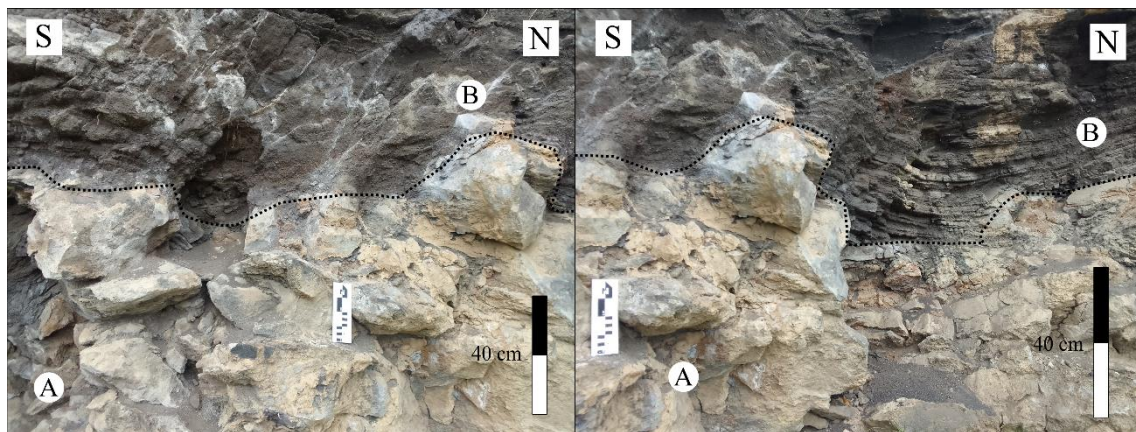


Figure 9: Sampling site 1 in Tulabug. A: Layer of lavas, B: Scoria layers

The collected material corresponds to scoria clasts belonging to one of the layers of the deposit. Licto site 2-1 has similar characteristics as the upper part of Licto site 1-1 (Figure 7). The thickness of the bed goes from 1 to 2 meters, the material has a black/gray color, the material is volcanic scoria with a grain size of around 10 mm, however is not homogenous, there is a clear variation of grain size in the deposit which can be inferred through sieving. The deposit is characterized by faint parallel bedding with an average grain size between 10 to 1 mm. A closer look to the samples collected show that the main lithological composition is volcanic glass, olivine crystals, and plagioclase. The dark coloration of the collected material could be an indicator of the mafic composition of the volcanic material. There is not internal layering (Figure 10)

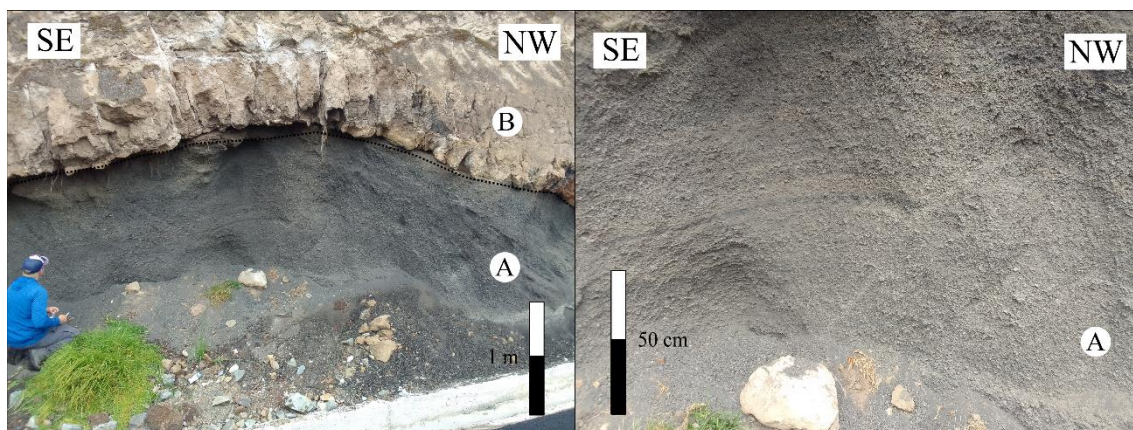


Figure 10: Sampling site 2 in Tulabug. A: Scoria layer, B: Cangahua

3.2 Scoria processing and selection of olivine crystals

Once the rocks samples, in this case scoria, were obtained the next step was to separate the samples by grain size. This process likely will separate whole olivine crystals from other rock materials from the samples like volcanic glass, which compose the matrix of the scoria itself. This is possible because due to the normal eruptive processes during magma fragmentation, the olivine crystals can be extracted, the matrix of the scoria layer is less durable compared to the olivine crystals and more likely to break when strained. Grain separation is achieved using standard sieves (200 mm in diameter) with mesh sizes of 10 (2000 μm), 18 (1000 μm), and 35 (500 μm) by manual shaking the sieves with the sample inside, and labeling each of the successive separates to ensure the reduction of the possibility of sample contamination. Olivine crystals were picked using a binocular microscope from the <18 and >35 size fractions. Selection of olivine crystals was based on certain criteria, the first criteria was that crystals with a euhedral external form were separated from the other batch that contain olivine crystals with less clearly developed crystal faces, or that have a subhedral/anhedral texture or were fractured during the eruptive event. The next step was to select olivine crystals that are not broken or do not show major fracturing within the crystal as fractures might impact the integrity of the geochemistry of the melt inclusions.

3.3 First identification of suitable melt inclusions in olivine crystals

In order to determine characteristics of the melt inclusions within the olivine crystal it is necessary to make direct observations. For this, a batch of 76 olivine crystals from the

subhedral/anhedral group were picked and mounted in a cast, using Petropoxy 154, which is a resin used to create thin sections. The mounted crystals were then ground and polished to expose the interior of the olivine crystals. Polishing was achieved using progressively finning powder grid, with each successive stage of polishing to reach a clearer surface that could be used to identify features of the olivine crystals under a petrographic microscope. This batch of olivines was used to gain a general understanding of the conditions of the olivines and if they contained melt inclusions (Figure 11).

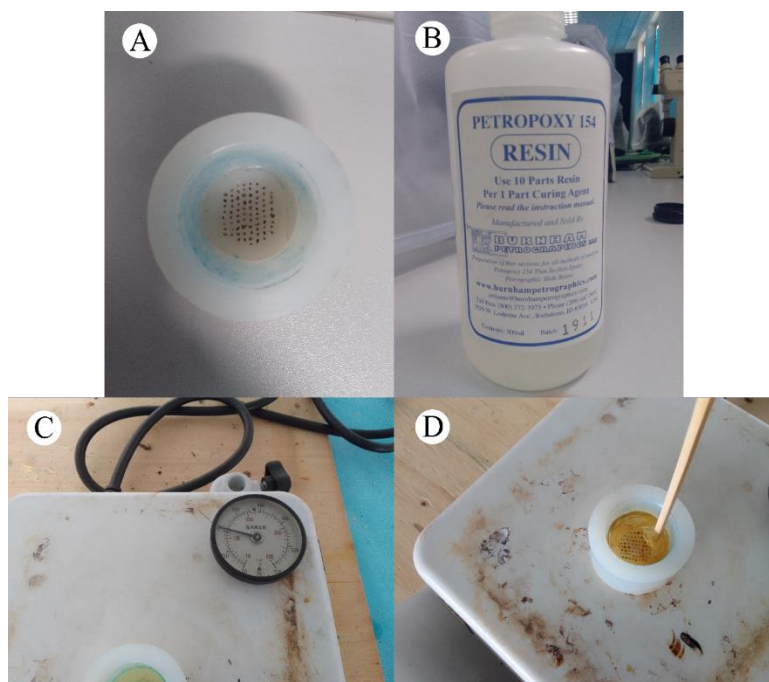


Figure 11: Mounting procedure of olivine phenocrysts. A: 76 olivines mounted in a circular vessel, B: Epoxy resin used to maintain the crystals together, C: Hot plate to ensure the solidification of the epoxy, D: Epoxy crystallized with olivines.

3.4 Melt inclusion identification/selection

Melt inclusions can be observed under a microscope if they are big enough, there is a textural difference between the olivine crystal and the inclusion inside of it. Using a petrographic microscope under polarizing light, the inclusion should have different optical properties compared to the olivine crystal. This allowed me to confirm the presence of melt inclusions within the olivine phenocrysts. Glassy olivine-hosted melt inclusions typically have a dark brown color and plane polarized light can transmit through the melt inclusion. A dark opaque coloration of the inclusion could mean that the inclusions is fully crystallized into daughter phases. In this case, it would be necessary to re-homogenize the melt inclusion using a heating stage. The primary target of the project

was to utilize glassy melt inclusions. Since these inclusions do not require re-homogenization, they can be analyzed after mounting and polishing the sample.

Host olivines of melt inclusions can be cracked due to the eruptive process in which they were deposited, this creates an open system between the entrapped inclusion and the external magma. So fractured olivines are not suitable. It is preferred to select crystals with no visible fractures. These two criteria, glassy melt inclusions and fracture free host crystals, were used in the initial selection of the olivine crystals that can contain inclusions that were used to address the different questions related to the magmatic systems that create the olivine crystals. To determine if the melt inclusion possibly was not fully enclosed, it is necessary to use further information based on obtained volatile content. In the case of the volatile contents being lower than what the melt inclusions should have, it is safe to assume that the inclusion was not fully enclosed or it has been modified after entrapment within the host. For cracked melt inclusions, if a large vapor bubble is observed it is possible that the melt inclusion was cracked during the eruption which allowed volatile to enter the inclusions increasing the size of the bubble (Rose-Koga et al., 2021). Glassy melt inclusions are suitable for the desired results of the project; they can be utilized directly because they likely are a representation of the original melt from which the olivine crystal was created. Melt inclusions with similar chemical composition can indicate that the melt inclusions were trapped at the same time or in a single phase which is the melt (Rose-Koga et al., 2021).

Due to evidence in polyhedral olivine hosts, melt inclusions are expected to have different shapes from spherical to the most common one in this type of morphology which are inclusions with curved walls and irregular shapes. This is caused by how the crystal growth progressively affects the ultimate shape and morphology of the melt inclusion.

A standard template for collecting relevant information of melt inclusions properties is applied. The information required is sample name, the deposit type from which the sample came from (for example tephra/ash fallout, lava flow, or pyroclastic flow), clast size (measured by images obtained), the crystal size, the shortest distance between the melt inclusion and the crystal edge, the shortest distance between the melt inclusion to the edge along an axis, melt inclusion size (both x and y axis), bubble size, and the presence and identity of secondary minerals (Rose-Koga et al., 2021).

From this point forward different olivines from the two sampling sites were used for different purposes. Upon initial selection of olivine crystal, it was observed that the second sampling location had the most euhedral olivine phenocrysts and was the ideal deposit for nanotomography analysis. Additionally, the only available samples to be analyzed using the EPMA and BSE (backscattered electron) imaging were from the first sampling site. Due to these considerations, scoria (olivine, melt inclusions, glasses, and other minerals encountered) from sampling site 2 were used for textural analysis using nanotomography (with volume estimations), Raman spectroscopy, and petrographic microscope analysis of thin sections of individual olivines, while scoria (olivine, melt inclusions, glasses, and other minerals encountered) from sampling site 1 were used for EPMA analysis (and all derived chemical interpretations), geochemical modeling, and vesicularity textural analysis.

3.5 Textural analysis of melt inclusions and orientation of the crystal using computed nanotomography (polyhedral olivines)

14 olivine crystals were selected that had a euhedral crystal shape. Melt inclusions can have a variety of different textures, and the aim of the first phase of the project is to constrain the shapes, sizes, and distribution of melt inclusions within the samples of olivine crystals. The second phase is focused on the petrology and geochemistry of the olivine hosted melt inclusions, and the third phase is an analysis of the pyroclasts textures. The use of the nanotomographer is presented first.

To constrain the properties of internal features of interest, in this case melt inclusions, within the minerals, an X-ray nanotomographer was used at the “Laboratorio de nanotomografía” (Universidad de Investigación de Tecnología Experimental Yachay Tech) on a Bruker SkyScan 2211 multiscale high-resolution x-ray nanotomographer. The source type of the instrument is X-ray Worx, a detector MX11002 camera with a resolution/pixel size of 9.05 μm . A source voltage of 40 kV and a current of 350 μA , and a tungsten. The distance from the sample to the detector was optimized, reducing the amount of instrumental noise. At these distances the image pixel size was between 0.9 to 2 μm . The resulting images have a 4032 x 4032 px with a 32-bit gray scale resolution. Acquisition time of the samples vary between 80 to 90 minutes, with an exposure of 1100 ms. Reconstruction was achieved using NRecon software applying post alignment,

smoothing, and ring artifact correction. Images were processed using CTan software. Images as sections of each of the 14 olivines analyzed are obtained with a distinctive code/name, for example LS2 (Licto sampling site 2), MSL (main scoria layer), 1835 (mesh size range), 5 (number of crystal), 2 (number of image of the same crystal).

3.6 Thin section of olivine crystals (polyhedral morphology)

The same 14 euhedral olivine crystals were taken out from the machine, however only 11 were suitable to create thin sections because they remained intact and did not suffer from fractures during the nanotomography analyses. The process for creating thin sections was the following: each individual crystal was placed in a glass slide; petrographic resin was used (petropoxy 154) by taking a drop of the resin to hardener mixture and placed directly on top of the olivine crystal. Each glass slide was set in a hot plate at 135°C so the resin can react and solidify. Once the resin solidified, the slide was polished with a powder grid of 320, followed by polish with a powder grid of 1200. The resulting 11 thin sections were observed in a petrographic microscope.

3.7 Raman spectroscopy (polyhedral olivines)

Raman spectroscopy has been used in recent studies to determine mainly volatile phase composition within melt inclusions. However, other applications are the rapid determination of mineral composition, specifically forsterite content of olivine crystals.

Raman spectroscopy is a non-destructive analytical technique. The basic principle is the use of electromagnetic waves generated by a laser, the electromagnetic waves interact with the covalent bonds of the sample, which reflect off the sample and are measured by a sensor. The result is a Raman spectrum, which is an intensity value of a wavenumber (Figure 12). In the case of minerals analyzed using Raman spectroscopy, the crystallographic configuration of the mineral determines the shape of the spectra (Rose-Koga et al., 2021).

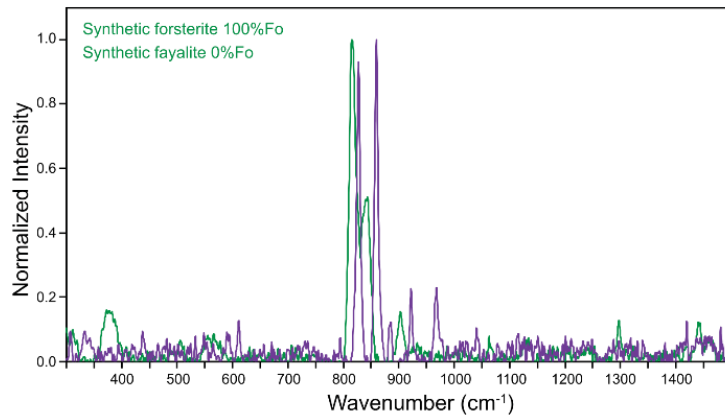


Figure 12: Example of Raman Spectra taken from olivine samples (Breitenfeld et al., 2018).

When an olivine sample is exposed to a Raman spectroscopy procedure, the resulting data, the peak positions (peak intensity values at a certain wavenumber) are a doublet of high intensity peaks in the range of 800 to 880 cm^{-1} . The centroids of these peaks can be unique depending on the olivine composition (forsterite content) (Breitenfeld et al., 2018).

Mathematical models were previously constructed to constrain the Fo content of olivine crystal using the Raman spectral peaks. This model incorporates a database of olivine compositions, their associated Fo% value (measured using EPMA), and their Raman spectra peak centroids. These data were used to create a regression model, where the input of a new peak centroid allows the user to determine a value of Fo% with a certain level of accuracy. The level of accuracy of the model is reported in the results section of the Raman approach.

A procedure to generate a Raman spectrum in olivine samples is described as follows: the samples are exposed in a glass slide, the Raman equipment uses a 532 nm laser with a microscope attachment, a laser power of 10 mW, a sample acquisition time of 10 seconds through a 20X objective (Breitenfeld et al., 2018).

So, in order to obtain these peak centroids, the 11 thin sections were analyzed under Raman spectroscopy with similar parameters as the ones described in a similar experiment. The range of wavenumber to measure was between -50 to 1300 cm^{-1} . The instrument is a LabRAM HR Evol, with a Syncerity OE detector the objective was a X20_VUS FLN. These analyses were conducted using the 532 nm laser. Plus, slide number 6 was chosen to undergo mapping of the sample with the objective to find a peak

within the sample that may contain water. The target part of the olivine crystal for each of the measurements was the olivine matrix closest to the core.

Once the results are obtained, the base of the spectra was removed using the PeakFit software. This was followed by the estimation of the peak centroids using a basic approach: all the values $x = \text{wavenumber (cm}^{-1}\text{)}$ and $y = \text{intensity (arbitrary value by the equipment and base removal procedure)}$ are set. The peaks are found by looking at the Raman spectrum, the maximum y value (along with the associated x value) are taken with the value before and after that maximum, the results will show maximum distinctive peaks, the one of interest is the one in the range of $837\text{--}857 \text{ cm}^{-1}$. Once this peak with the other two necessary points is found a linear regression using a least square method is created using these points, a polynomial regression grade 2. The centroid is estimated at the point when the slope is equal to 0 in the generated polynomial function, the x value associated at the slope of 0 is the location of the peak centroid.

3.8 Olivine composition estimation with a mathematical model

Olivine composition can be estimated using Raman spectroscopy. The general idea of the processes is that band shifts caused by the molecular structure of a material with known composition, can be correlated with Raman results from unknown samples using mathematical models created using a set of materials with established properties (Breitenfeld et al., 2018). The necessary data to make an estimation based on this model is to identify the centroid of a particular signal in the results of the Raman. This centroid is located in a doublet (DB2) formed in olivine minerals due to their particular molecular arrangement; it occurs $\sim 838\text{--}857 \text{ cm}^{-1}$ in the Raman shift (Breitenfeld et al., 2018). Once this centroid is estimated with accuracy, the value can be used in the following equation:

$$\text{Fo}\% = -0.179625x^2 + 310.077x - 133717$$

Where x is the value of the centroid in cm^{-1} . The equation was created using mathematical univariate analysis. Specifically, a second order polynomial fit that was applied in a set of samples with known olivine composition (with a range of different compositions from mafic to felsic rocks). The equation is based on comparisons with compositional measurements on the same olivines using EPMA. These comparisons demonstrate that this equation is an acceptable approximation when only peak centroids are used. Peak

centroids can be measured directly from the Raman spectra measured from the samples, and the previously published mathematical model (Breitenfeld et al., 2018).

3.9 EPMA analysis

Electron probe microanalysis is the basic and the most used procedure to measure major and certain volatile elements like S, Cl, and F for melt inclusions, matrix glasses, and minerals.

Mounting and measurements of samples using EMPA were performed by external help, due to the inaccessibility of the instrument. To make measurements of the olivine-hosts, their melt inclusions, and other mineral phases, numerous circular mounts were created containing different eruptive products. For the mounts targeting olivine-hosted melt inclusions, a circular mount containing approximately 100 hand-picked olivine crystals was created, similar to the one used to make initial observations of the olivines. Samples were sieved using a 250 and 100 mesh size. Then the crystals were hand-picked using a binocular microscope from the 250-100 mesh size fraction. The olivine crystals were then secured to a circular mounting cup using double-sided tape on the base of the cup. Epofix resin was mixed at a ratio of 15 parts resin, to 1 part hardener. The mixture was poured into the cup and placed under a vacuum for 30 minutes to remove air bubbles stuck to the bottom of the cup. The mounts were then left for 12 hours to harden. After hardening, the mounts were initially ground with a 200-grit polishing wheel until the olivine cores and their melt inclusions were exposed. Then the mount was ground using 400, 800, 1200 grit paper and 2000 μm powder grit. The mounts were finely polished with 3 and 1 μm diamond paste on a Struers LaboPol-1. The mounts were then cleaned to remove oils and coated in a thin film of carbon. Three different mountings were done, the first one with handpicked olivines (20220828-1), the second and third ones (20220828-1_C and 20220828-1_CwM respectively) were mountings with entire clasts which contained different minerals along with olivine crystals.

The microprobe used to obtain the data is a JXA-IHP200F Field Emission EPMA. The accelerating voltage was set at 10kV, a current of approximately 12 nanoamps, and 5-micron beam diameter was used in the analyses of melt inclusions and matrix glasses. For the analysis of the crystalline phases, the probe was operating at 12kV, a 12 nanoamps current, and a 2-micron beam diameter. The microprobe was standardized using Quartz

(Si), Corundum (Al), Rutile (Ti), Chromite (Cr), Hematite (Fe), Magnesite (Mn), Periclase (Mg), Wollastonite (Ca), Albite (Na), Orthoclase (K), sphalerite (S), a phosphate for (P), and an international glass standard for chlorine (Cl). Volatile species such as Na, S, and Cl were analyzed first in the analytical sequence. The ZAF correction was applied in the processing of the final results.

Prior to the chemical analysis, the polished mounts were photographed using transmitted and reflected light on a digital microscope. The photographs were stitched together to create a single image of the mount. Each crystal or clast was given a unique identification number for each mount and prospective targets for the EPMA analysis were selected under the reflected light setting (Figure 13).

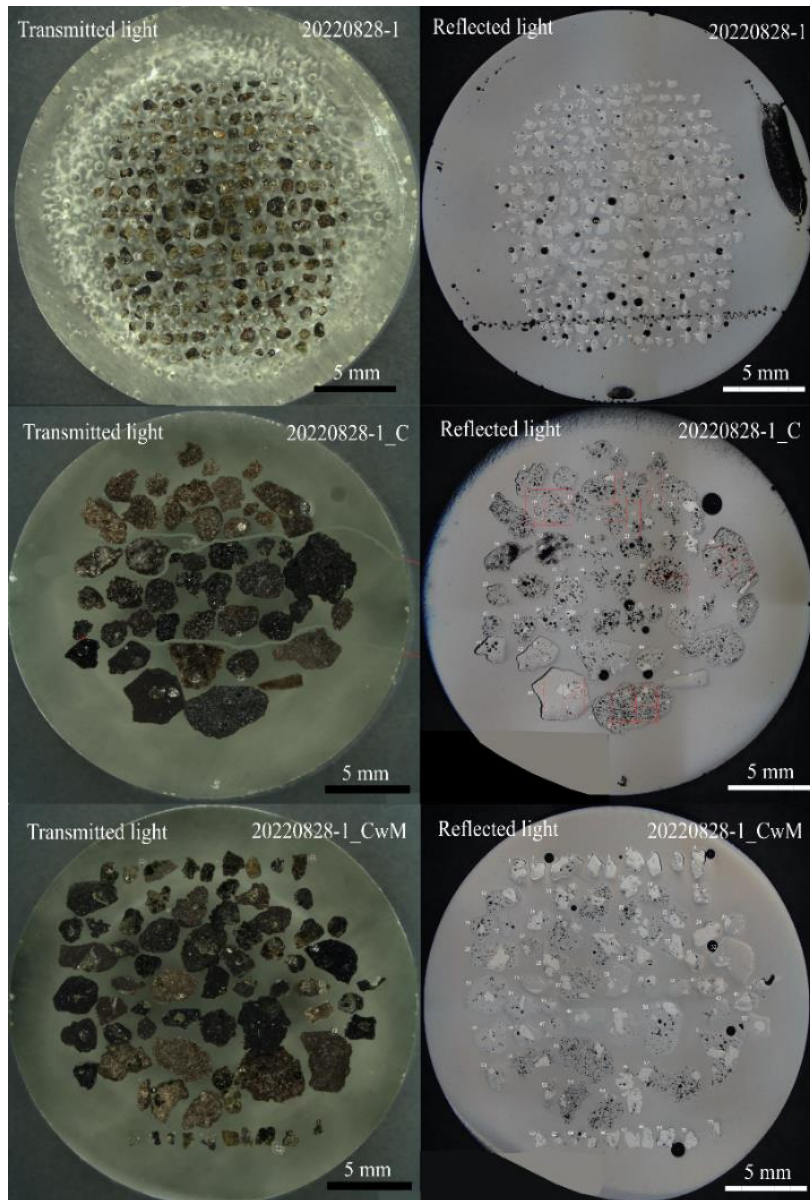


Figure 13: Images of the mounts created for EPMA analysis.

The first measurements of chemical composition are mineral data (host of the inclusions) and mineral microlites. From 20220828-1 the matrix of the crystal was targeted, a total of 51 analyses were made. 8 analyses of San Carlos olivines were made to evaluate the accuracy and reproducibility of the measurements. From 20220828-1, two spinel and one clinopyroxene microlite as accessory minerals were measured. A core measurement of an olivine microlite, a core and rim measurement of an olivine phenocryst.

From mounting 20220828-1_C the following measurements were done:

- From clast 46: 5 measurements of olivine phenocrysts (core and rim), 3 measurements of the core of clinopyroxene microlites, 1 measurement of plagioclase microlite (core), and 4 measurements of spinel as inclusions within the olivines.
- From clast 43: 6 measurements of clinopyroxene phenocrysts (core and rim), 2 measurements of clinopyroxene microlites (core), and 1 measurement of olivine microlite (core).
- From clast 44: 2 measurements of olivine phenocrysts (core and rim), and 1 spinel as an inclusion of the olivine.
- From clast 38: 4 measurements of clinopyroxene phenocrysts (core and rim).
- From clast 37: 2 measurements of olivine phenocrysts (core and rim).
- From clast 31, 24, 12, and 10: 11 measurements of plagioclase microlite (core and rim).

From mounting 20220828-1_CwM the following measurements were done:

- From clast 21: 15 measurements from core to rim of an olivine phenocryst.

Since the glasses and minerals were analyzed using different analytical conditions, the minerals were standardized and analyzed first. Then, the glass standardization was performed followed by the glass analyses (matrix glass and melt inclusions). The JDF (Juan de Fuca) reference glass was measured at the start and end of each analytical session to assess for the accuracy and precision of the standardization and for any instrumental drift. A summary of the mineral and glass standards including their accepted values are detailed in Table 1.

Sample name	Accepted values										
	SiO ₂ wt %	TiO ₂ wt %	Al ₂ O ₃ wt %	FeO wt %	MnO wt %	MgO wt %	CaO wt %	Na ₂ O wt %	K ₂ O wt %	P ₂ O ₅ wt %	NiO wt %
SC	40.81	n/a	n/a	9.55	0.14	49.42	<0.05	n/a	n/a	0.00	0.37
JDF	50.8	1.93	13.8	12.17	0.22	n/a	10.8	2.77	0.215	0.23	n/a

Table 1: Accepted values for the San Carlos olivines (SC), and Juan de Fuca glasses (JDF). n/a corresponds to values not reported or not relevant for calculations of error. (JAROSEWICH et al., 1980; Straub et al., 2004)

The idea was to measure melt inclusions (glass) within a mineral host, so the equilibrium relationship between the mineral host and melt inclusion can be established. 52 measurements of melt inclusions in the mounts with olivine phenocrysts were made, 5 matrix glass measurements (olivines), and 1 melt inclusion measurement of a clinopyroxene host.

From the first mounting of clasts a total of 20 measurements of matrix glass were performed, and 1 measurement of a plagioclase microlite core.

Finally, two measurements of matrix glass were done in samples from a different layer within the sampling site.

Using the standard San Carlos olivine composition, the possible instrument error in the mineral measurements can be calculated for the following chemical species: SiO₂, FeO, MnO, MgO, P₂O₅, and Ni. Error values are reported in the results sections of EPMA analyses.

Same procedure using standard glass compositions JDF was used to calculate the instrument error for the glass/inclusion measurements by EMPA, the error was calculated for the following chemical species: SiO₂, TiO₂, Al₂O₃, FeO, MnO, MgO, CaO, Na₂O, K₂O, and P₂O₅

3.10 Core to rim analysis

Core to rim analysis can be used to infer olivine zoning patterns while the phenocryst was formed, and in some occasions be used to infer olivine growth morphologies. The principal use of zoning patterns is the constraints of timescale information on magmatic processes. The core represents the early formation of the crystal and the rims the last stage of growth before eruption. In this case the chemical data of the path measurements from an olivine phenocryst, specifically the olivine from clast 21, was taken to create core to

rim chemical compositional diagrams where the trends of chemical composition of the olivine crystal can be observed (Salas et al., 2021).

Positional coordinates of the specific point of measurement within the olivine crystal during EMPA analysis were taken, these coordinates were transformed using trigonometry to calculate rim to core distances. These distances then were used as information in the x-axis and the Fo (mol %) and Ni (wt %) were used in two y-axes. This diagram is based on the idea that olivine compositional evolution varies depending on the melt where crystallization is occurring. Normally olivine at the core will have a higher Fo value along with Ni (this is because nickel is a compatible element with olivine).

3.11 Post-entrapment crystallization correction

It was established that melt inclusions undergo a series of processes that could modify its original composition, the chemical composition that was entrapped when the inclusion was formed. This is the case of post-entrapment crystallization correction. In Figure 1, a summary of the different types of processes that cause modification in melt inclusion composition is shown.

To achieve this correction several procedures can be done, in this case the use of the software Petrolog3 was chosen (Danyushevsky & Plechov, 2011). Petrolog is a software developed with numerical models, these numerical models were developed to describe/model fractional and equilibrium crystallization, reverse fractional crystallization with the option to vary the pressure of the system being model, different melt oxidation states, and the H₂O content of the melt measured. In this particular case the modeling of post-entrapment crystallization for melt inclusions in olivine is one of the features of the software.

One of the principal assumptions so the correction can be done is that the host olivine phenocryst chemical composition does not change, this is because the calculation assumes a fixed olivine composition and re-equilibrates this with the melt inclusion. The correction is necessary since post-entrapment processes and diffusive exchange between the melt inclusions and the host can modify the original melt inclusion composition. The diffusive loss of Fe is called Fe-loss and generally causes a decrease in FeO^t (total iron of the specific chemical species) and an increase in MgO content in the trapped volume of the inclusion (Danyushevsky et al., 2000). In other words, the MgO content of the original

melt entrapped is reduced with time since crystallization of olivine occurs along the walls of the melt inclusion, also a decrease in FeO occurs (this process is named post-entrapment crystallization). So, the objective is to apply the mathematical model to account for these post-entrapment processes and estimate the original melt composition during entrapment. In other words, the original melt is one that has higher concentrations of MgO and FeO. This is the original composition of interest to infer different magmatic processes.

The reconstruction of the trapped melt needs a value of FeO*, which is an estimation of the initial value of FeO during entrapment. The model will iteratively generate new melt compositions until the compositional value of the measured melt inclusions reaches this estimated FeO value while maintaining experimentally derived Mg-Fe olivine-melt partition coefficients.

The mathematical model will do the following procedure:

- The olivine host that contains a melt inclusion will be kept at a certain temperature; this temperature will be maintained till the inclusion reaches equilibrium with the host. Equilibrium meaning chemical equilibrium that is defined as a time where there is no exchange between reactants and products. The olivine liquidus temperature is estimated using the measured olivine and melt inclusions composition and previously described olivine-liquid thermometry techniques. At this temperature, exchange between Fe and Mg is simulated between the melt entrapped and the olivine host; this exchange occurs during the re-equilibration process. This re-equilibration can happen either by the melting or crystallization of the host olivine along the walls of the melt inclusion.
- The following step is based on the comparison between the measured FeO content of the melt at equilibrium (melt inclusion composition) and the estimated FeO content that is thought the melt had at the moment of entrapment.
- Depending on the result of this comparison, the mathematical model will do the following: 1) if the estimated FeO value introduced is higher than the FeO content of the melt at equilibrium, the model will increase the simulated temperature while keeping the melt inclusion and the host in equilibrium; 2) if the FeO estimated value is lower than the FeO content of the melt at equilibrium, the temperature is decreased and the same procedure occurs. This is done till the FeO of the melt is the same as the estimated FeO

value introduced, the melting or crystallization of olivine is what will vary till the FeO values are the same.

The results of the mathematical model that is of interest, the chemical composition when the melt inclusion is at equilibrium with the host and matches the FeO inferred value, is then saved and is defined as the estimated melt inclusions compositions at the moment of entrapment or the possible parental magma composition.

The starting melt compositions will be the 52 measurements of melt inclusions as measured by EPMA. The chemical species SiO₂, TiO₂, Al₂O₃, FeO, MnO, MgO, CaO, Na₂O, K₂O, P₂O₅, Cr₂O₃, and H₂O are used. It is important to note that the H₂O value of the melt inclusion compositions is estimated by using the deficit in total weight percentage obtained by the summation of all the species measured in the EPMA, this is based in the assumption that the deficit is a good approximation of major elements of interest such as water that cannot be directly measured by EPMA techniques (Lin et al., 2020).

The model needs the host olivine Fo% (forsterite) of each of the melt inclusions. The host compositions were measured a few microns away from the entrapped melt inclusion. The Fo% is calculated using the following formula:

$$Fo\% = \left(\frac{\frac{MgO \text{ wt}\%}{MgO \text{ mw}}}{\frac{MgO \text{ wt}\%}{MgO \text{ mw}} + \frac{FeO \text{ wt}\%}{FeO \text{ mw}}} \right) * 100$$

This formula is used in the 52 host mineral measurements taken in the EPMA, using the corresponding weight percentage of MgO and FeO. The MgO mw and FeO mw correspond to the molecular weight of each of the chemical species, 40.3044 g/mol and 71.844 g/mol respectively.

The FeO estimation necessary for the calculations which is the possible content of the chemical species when the melt was originally trapped and subsequently modified by post entrapment processes was determined as follows: a plot MgO wt% vs FeO^l wt% (Figure 38) was made with the data of the 52 measurements of melt inclusions, 8 measurements of whole rocks (lavas) from Licto obtained from other scientific research in the area (Ancellin et al., 2017; Bablon et al., 2019; Schiano et al., 2010), 5 random glass measurements of the olivine crystals, and 20 glass measurements from the clasts. The

principle was that it is necessary to have a value of FeO that represents as closely as possible the original composition of the melt prior to the formation of minerals. One of the candidates for this is the whole rock analysis. Whole rock analyses represent the chemical composition of the silicate glasses and the minerals of the rock and they do not suffer the same diffusive effects that melt inclusions can experience. Thus, whole rock analyses could represent the unmodified original FeO composition of the magma. From the suite of previously published whole rocks, the whole rock with the lower value of FeO^t (7.1 wt%) and MgO (4.75 wt%) will be used in the melt inclusions that have lower MgO wt% and FeO^t compared to this whole rock value. For the few measured melt inclusions that have greater MgO and FeO^t an average of the values of FeO^t of the whole rocks which is 8.1 wt% is used. Matrix glasses are not considered to represent the original composition since they are formed in a late stage of crystallization and by that they do not represent likely primitive compositions.

A mineral-melt equilibrium model needs to be chosen so the equilibrium can be defined between the melt and a mineral believed to be crystallizing from this melt. These models define the ratio of chemical species (for example between Fe and Mg) between a liquid (magma) and a crystal (olivine) when they are in equilibrium. The software Petrolog implements several mineral-melt equilibrium models, the one chosen is one developed by Danyushevsky (2001). This selection was based on the experimental elaboration of the model, which used basaltic compositions to create it, and since the lavas have generally a basaltic composition, it seems reasonable to use this equilibrium model.

The melt oxidation state is the proportion of Fe³⁺ and Fe²⁺ in the melt, this is set using the model of Kress & Carmichael (1988). This model determines the melt oxidation state as a function of melt composition, temperature, and oxygen fugacity. This calculation is set by using an oxygen buffer; this buffer will control the oxygen fugacity of the system, the oxygen buffer chosen to be one log unit above the Ni-NiO buffer (NNO+1) which is typical for oxidized arc magmas (Lindsley, 1991).

Density model is set as default, this is the (Bottinga & Weill, 1972).

Once the modeling has concluded with the corrected melt inclusion compositions major elements diagrams are done along with rock classification diagrams (Figure 39 and Figure 40).

3.12 Textural correlation with chemistry composition

To infer a possible correlation between the chemical composition of the corrected melt inclusions and their spatial location in two dimensions within the olivine host, measurements of the shortest distance from the edge of the crystal to the melt inclusion wall were performed. Crystal edges can be identified by the observation of the whole olivine crystal and its crystal faces, especially in BSE images since density is observed through a scale of gray colors, and the edge of the crystal usually has white color.

Back scattered electron images were taken along with the compositional measurements taken in the EPMA, the images of interest correspond to the olivine crystal which contain the melt inclusion measured and corrected. There were 52 images that were used in the program ImageJ, each of the images have a scale which was used to make accurate as possible measurements from the shortest distance of the edge of the crystal to the melt inclusion which the crystal is hosting. At this point some set-backs arose, the images in some occasions did not allow to identify the edge of the crystal making it impossible to measure the distance. In this case the images that had this problem were not taken into account. In Figure 14, an example of the distance measurements is shown.

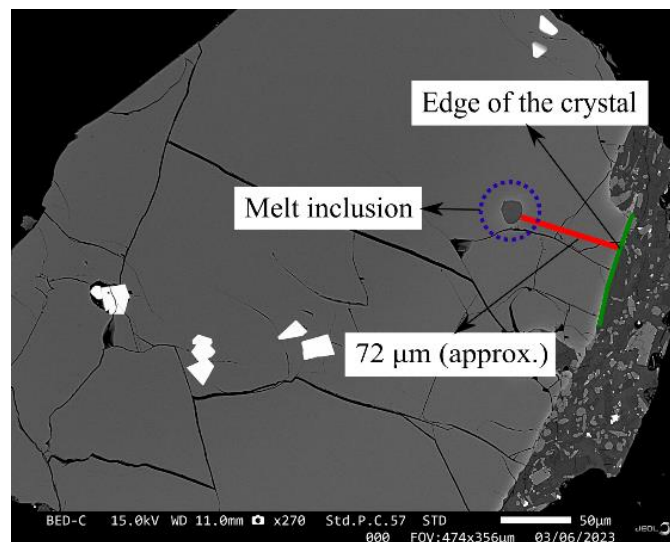


Figure 14: Measurement procedure for distance from edge of the crystal to the melt inclusion.

48 distance measurements were performed under the previous assumptions, it is important to assert that the measurements are based on observations, so there is a possible source of error with it. The melt inclusion was identified, and by criteria of the researcher the closest edge of the crystal to it was identified, followed by the distance measurement in μm . This

is a three-dimensional problem, and the observations and measurements only take into account two dimensions.

The following was creating major elements diagrams of the shortest distance between the melt inclusion and the crystal edge and the weight percentage of major elements (SiO_2 , MgO , TiO_2 , Al_2O_3 , CaO , and Na_2O), these will help to determine if there are systematic chemical variations of the melt inclusions with their location within the olivine crystal.

Olivine crystal morphology interpretation was performed using the same images of the host olivines. Only images showing the complete olivine crystal were utilized and the remainder of the crystals that were fractured and the morphology could not be assessed were disregarded. Morphology interpretation uses a basis the experiments performed by Faure & Schiano, (2005), these experiments created artificial olivines under different temperatures and cooling rates, generating olivines with distinctive morphologies depending on changes in these physical variables. The different olivine crystal morphologies are described with images, so it is possible to use these as a reference to characterize olivine crystal morphology of the samples at Licto to some degree, assuming that these experiments are an acceptable representation of natural olivines.

For an olivine crystal to be described as polyhedral it needs to meet certain characteristics, these are that the faces are very well developed and the inclusions within it can be either spherical or curvilinear. The other relevant morphology is dendritic polyhedral. In this case, dendrites grow at the edges of the crystal and in some cases have a stair-like appearance. The shape of the melt inclusions can be different in this type of morphology. If melt inclusions are seen in a particular plane of the olivine crystal (orthorhombic system plane 100) they will be elongated and parallel to the planes 010 or 021. These differences can be used to differentiate between olivine crystal morphologies in the host olivine samples.

The previously explained characteristics were applied in the 52 host olivine BSE images to make distinctions of olivine morphology, then a frequency plot was created with the relevant morphologies encountered (Figure 43).

Once the morphologies were identified the host olivines that did not meet the requirements for identification, were not considered. The rest are used to create major element compositional diagrams of the melt inclusions that the olivine with a distinctive morphology is hosting, where the crystal morphology can be seen to infer possible trends

that link olivine crystal morphology with changes in chemical composition of melt inclusions (Figure 44).

3.13 Fractional crystallization modeling and melt liquidus association

Fractional crystallization is defined as a magmatic process where minerals are formed as magma reduces its temperature and, by usually differences in density, are removed from the liquid phase. Because to form certain minerals different chemical species are necessary the melt where these minerals are formed will change its chemical composition, this is also called incongruent crystallization. If fractional crystallization actually occurred in a magmatic system, chemical changes in magmatic products can be seen. Fractional crystallization is used to determine the possible mineral phases that crystallize in a certain magmatic system. This is done by using different mineral-melt equilibrium models either alone or simultaneously, the crystallization of minerals will modify the composition of the melt each time step.

The principal idea is to generate a model that replicates the chemical variability shown on the major element variation diagrams, this will indicate that fractional crystallization could be one of the processes leading to the evolution of the melt in the Licto magmatic system. This can be rather difficult since arc volcanoes typically experience multiple episodes of magma mixing, can evolve by fractional crystallization at multiple pressures, and can crystallize numerous mineral phases. Thus, it is necessary to check all the variables in the models and vary them accordingly to identify the best possible match. Generation of multiple phases also can be done so certain minerals crystallize until a set melt composition, and then stop. That melt composition can be extracted from the output and entered as the starting composition in a new fractional crystallization model using different minerals. The chemical compositions of the melt inclusions corrected ideally represent a trend that evolves with time and the melt becomes more acidic. This trend can also be called the liquid line of descent. The objective is to generate a model that fits this trend.

Petrolog3 has an option to model fractional crystallization. This option requires the user to select which minerals will crystallize, the melt-mineral equilibrium model that the mineral will use to determine if a mineral crystallizes at a certain melt composition and temperature, the percentage of fractionation of the mineral at each time step, the melt

oxidate state, the initial pressure, gradient of pressure, melt density/viscosity, the final degree of fractionation, and the percentage of melt calculated in each time step. All these parameters need to be considered along with the initial composition of the melt using the following chemical species: SiO₂, TiO₂, Al₂O₃, Fe₂O₃, FeO, MnO, MgO, CaO, Na₂O, K₂O, P₂O₅, Cr₂O₃, and H₂O.

5 models are created each with certain changes in the parameters, however some of them maintain similar characteristics. The percentage of fractional crystallization of each of the minerals involved in the model is set to 100%, meaning that once a mineral crystallizes, the mineral is removed from the melt or fractionated. This is an ideal assumption because in natural cases, a certain percentage of a mineral after being formed is resorbed and incorporated back into parent melt. The decision was made since it can be seen that a change in this parameter did not show a major change in the resulting melt composition.

The same melt oxidate state parameters used for the post-entrapment crystallization correction were used, this is an oxygen fugacity buffer of Ni-NiO, the model of oxygen fugacity of Kress & Carmichael, (1988), the buffer shift in log₁₀ units of the oxygen fugacity is the same as the post-entrapment correction which is +1. The initial pressure for all the models was set at 2.6 kbar, this value was calculated using a clinopyroxene-melt barometer (K. D. Putirka, 2008), this assumes the fractionating minerals formed under these pressure conditions. The variable change in pressure is rather small, set at 0.014 kbar/degree (Celsius), this value was estimated by using previous work, using the average geothermal gradient of the continental crust of 25°C/km calculated between the first 3 to 5 kilometers of depth, the pressure gradient used is 0.29 kbar/km which is the average for the crust (DiPietro, 2013). This gradient may not be realistic since magma is stored at depth and reaches the surface at still higher temperatures, however for the basic purposes of this work the average global values are enough. The K_d (partition coefficient) for olivine to use in its melt-mineral equilibrium model is set as default which is approximately 0.3, this value corresponds to the partition coefficient between Fe-Mg. The water saturation option was not used, since testing of this option indicated that it did not affect positively to the results. A water content of 0.26 wt% was used in the initial composition of the melt since this is the analytical deficit in the sum of the major elements for the starting composition used. Melt density/viscosity is calculated with the models of Bottinga & Weill, (1972); Lange & Carmichael, (1987). The final degree of fractionation,

which is the percentage of the melt that became solid, is set to 100%. Finally, the amount of mineral phase that is extracted from the melt in each step of the calculation is 0.01%.

- 1st Phase Model

The model is set to crystallize olivine and spinel. The melt-mineral equilibrium model for olivine is the one created by Danyushevsky, (2001), this equilibrium model was created with values of back-arc/mid-ocean ridge magmas. In the case of spinel, the equilibrium model is the one created by Nielsen, (1985), which is applicable for a wide range of natural mafic systems. The deviation of the oxygen buffer equals 1 log units. The initial composition is as follows (in weight percentage):

SiO ₂	TiO ₂	Al ₂ O ₃	Fe ₂ O ₃	FeO	MnO	MgO	CaO	Na ₂ O	K ₂ O	P ₂ O ₅	Cr ₂ O ₃	H ₂ O
53.30	1.00	16.00	0.00	8.20	0.10	8.30	8.10	3.60	1.20	0.20	0.00	0.26

This initial composition is the whole rock with the higher value of MgO of all the data collected, which could represent the possible parental composition of the melt where the minerals crystallized. This is because MgO is one of the first compounds to be depleted at the first stages of melt crystallization due to olivine fractionation.

- Cotectic Model

The special characteristic of this model is that it simulates crystallization of olivine + plagioclase + clinopyroxene at the same time. The melt-mineral equilibrium models used were created by Danyushevsky, (2001). The deviation of the oxygen buffer equals 1 log units. The initial composition is the same as the 1st phase model.

The following second phase models are created with the basis of using a generated melt composition in the first phase, to emulate a new phase where olivine and spinel no longer crystallize.

- 54% SiO₂ Melt Composition Model (Second Phase)

The model simulates crystallization of plagioclase and clinopyroxene. The melt-mineral equilibrium models used were created by Danyushevsky, (2001). The deviation of the oxygen buffer equals 1 log units below the NNO buffer. The initial composition is as follows taken from the 1st phase model (in weight percentage):

SiO ₂	TiO ₂	Al ₂ O ₃	Fe ₂ O ₃	FeO	MnO	MgO	CaO	Na ₂ O	K ₂ O	P ₂ O ₅	Cr ₂ O ₃	H ₂ O
53.99	1.07	17.12	2.38	5.67	0.09	5.38	8.64	3.85	1.28	0.21	0.00	0.28

54% SiO₂ melt composition refers to the 1st model generated melt composition with approximately 54% of SiO₂.

- 55% SiO₂ Melt Composition Model (Second Phase)

The model simulates crystallization of plagioclase and clinopyroxene. The melt-mineral equilibrium models used were created by Danyushevsky, (2001). The deviation of the oxygen buffer equals 1 log units. The initial composition is as follows taken from the 1st phase model (in weight percentage):

SiO ₂	TiO ₂	Al ₂ O ₃	Fe ₂ O ₃	FeO	MnO	MgO	CaO	Na ₂ O	K ₂ O	P ₂ O ₅	Cr ₂ O ₃	H ₂ O
54.97	1.05	18.09	2.11	5.17	0.08	3.41	9.12	4.07	1.36	0.23	0.00	0.29

55% SiO₂ melt composition refers to the 1st model generated melt composition with approximately 55% of SiO₂.

- 56% SiO₂ Melt Composition Model (Second Phase)

The model simulates crystallization of plagioclase and clinopyroxene. The melt-mineral equilibrium models used were created by Danyushevsky, (2001). The deviation forms the oxygen buffer equals 1 log units. The initial composition is as follows taken from the 1st phase model (in weight percentage):

SiO ₂	TiO ₂	Al ₂ O ₃	Fe ₂ O ₃	FeO	MnO	MgO	CaO	Na ₂ O	K ₂ O	P ₂ O ₅	Cr ₂ O ₃	H ₂ O
56.34	0.65	18.72	1.66	4.10	0.07	2.81	9.43	4.21	1.40	0.23	0.00	0.30

56% SiO₂ melt composition refers to the 1st model generated melt composition with approximately 56% of SiO₂.

The relevant results of each of the models is the melt compositions with progressive fractional crystallization and the mineral compositions of the fractionated mineral. The melt compositions of the models are included in major element variation diagrams to see if the generated magmatic evolutionary trends fit the liquid line of descent observed in the corrected melt inclusion compositions (Figure 46). The mineral compositions generated by the models are put in diagrams of endmembers for olivine, clinopyroxene,

and plagioclase, the idea is to see if the minerals created by the plot are similar to the minerals measured by EPMA.

Melt liquidus association option within the Petrolog software calculates pseudo-liquidus temperatures (temperature at which crystallization begins and solid and liquid phases coexist) and liquidus mineral compositions, for a given selection of minerals and mineral-melt equilibrium points. In other words, this option determines the approximate composition of olivine, clinopyroxene, and plagioclase that will be in equilibrium with the calculated melt inclusions compositions, matrix glass compositions, and whole rocks. For a given chemical composition at equilibrium, a certain mineral with a fixed composition can be created depending on the specific mineral-melt model used. So, comparisons between mineral compositions measured by EPMA, mineral compositions estimated by fractional crystallization models, and mineral compositions calculated using melt liquidus association, can be made.

This comparison ensures that the fractional crystallization models reflect the realistic magmatic conditions at Licto. Melt liquidus association uses the same parameters as the fractional crystallization models. The melt compositions will be each of the measurements obtained by EMPA for matrix glasses, melt inclusions corrected by post-entrapment crystallization, and whole rock data obtained from literature. All of these compositions have been previously used in other calculations.

3.14 Vesicular analysis

Vesicle characterization of volcanic clasts can provide information in the processes that occur in the magma conduits and storage (cite jobs that use FOAMS from Shea). 2D vesicularity can be used as a representative of the 3D vesicularity using stereological corrections methods. The FOAMS software is useful for studying clast vesicularity and is the program applied to investigate the clast textural heterogeneity in the Licto deposit (Shea, Houghton, et al., 2010). This program uses grayscale images where vesicles and volcanic glass are clearly differentiated at different levels of magnification to generate essential measurements to make interpretations of the magma ascent, vesicle growth, and eruption processes.

Based on visual observations, 3 types of clasts were differentiated from the Licto sample site that were analyzed using FOAMS. These observations are color and estimated general

observed vesicularity (dense or vesicular). The visual classification developed here includes 3 groups: vesicular brown clasts (VBr), vesicular black (VB) clasts, and dense black (DB) clasts.

For the dense black clasts two clasts were selected, the first clast has 1 image at 40X magnification, 4 images at 80X magnification, 4 images at 150 X magnification, and 4 images at 250X magnification. The second clast has 1 image at 40X magnification, 4 images at 80X magnification, 4 images at 150 X magnification, and 4 images at 250X magnification.

For the vesicular black clasts two clasts were selected, the first clast has 1 image at 40X magnification, 4 images at 80X magnification, 4 images at 150 X magnification, and 4 images at 250X magnification. The second clast has 1 image at 40X magnification, 4 images at 80X magnification, 4 images at 150 X magnification, and 4 images at 250X magnification.

For the vesicular brown clasts three clasts were selected, the first clast has 1 image at 40X magnification, 2 images at 80X magnification, 2 images at 150 X magnification, and 2 images at 250X magnification. This is a modification of the nested approach by Shea in 2010, since this type of clasts were small (Figure 15). The second clast has 1 image at 40X magnification, 3 images at 80X magnification, 3 images at 150 X magnification, and 3 images at 250X magnification. The third clast has 1 image at 40X magnification, 2 images at 80X magnification, 2 images at 150 X magnification, and 2 images at 250X magnification.

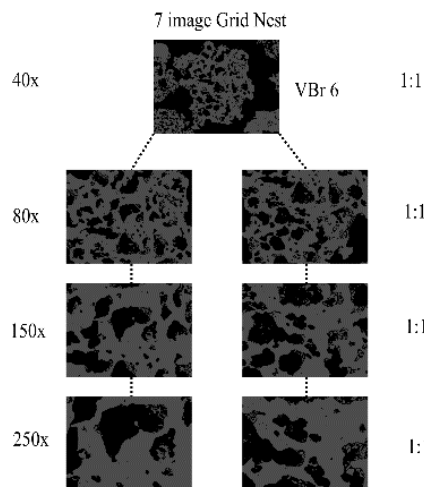


Figure 15: Example of nested approach in FOAMS, using binary generated images from BSE images of clasts (VBr/6).

Each of the images were edited following the instructions of the program FOAMS to produce binary images with two distinctive phases, vesicles in black and volcanic glass in gray.

Once the images for a certain clast is selected the scale factor for each of the magnitudes is set, which are: 40X = 800 px/mm, 80X = 1600 px/mm, 150X = 3000 px/mm, and 250X = 5000 px/mm. Generally, the parameters of the program are set as default except in the size threshold parameter which is set at 10 pixels minimum diameter since this value was previously used in scoria clasts.

3.15 Use of FOAMS to calculate estimations of volumes of melt inclusions using results from nanotomography

FOAMS software was conceived principally, as the name describes, as a fast object acquisition and measurement system for vesicular analysis of volcanic products. However, despite this, a binary image can be used not only for vesicles but the image can be used for other features such as melt inclusions. Nanotomography is a technique to obtain morphological characteristics of in other cases not directly seen features. Binary images of the possible melt inclusions obtained (white as the melt inclusions and black as the olivine crystal matrix) can be used in FOAMS to discern other measurements. In this case, volume estimates of melt inclusions. This is possible to do with tools of the same built-in software of the nanotomographer. This approach take less time to obtain volume measurements leading to quicker results and creates a first impressions of morphological elements of the melt inclusions.

Once binary images of a certain feature are obtained, they can be loaded in the FOAM software, which performs a particular important procedure that uses 2D measurements to create estimates of 3D value, this is called stereological conversion (Shea, Houghton, et al., 2010). Stereology is a statistical technique to convert 2D areas into equivalent volumes; these mathematical models now take into account intersection probabilities, cut-effects, and variations in shape (Shea, Houghton, et al., 2010).

The stereological conversion done in FOAMS generates corrected vesicle size and number distributions, by calculating the number density (number of objects/volume) of a given size class, the number density is estimated by doing successive iterations of the number density of larger objects assuming spherical geometry. However, the method is

just an estimation since the more elongated the shape being measured, the cross-section probabilities become harder to express analytically. In some melt inclusions that have a spherical shape this could be an excellent approach to estimate volumes, but in the case of more elongated shapes the results could not be as accurate. Regardless, the approach could serve as an approximation of volumes of melt inclusions which then more sophisticated methods can be used to obtain more accurate 3D measurements (Shea, Houghton, et al., 2010).

Once the binary image of each of the 14 samples is entered in the FOAMS program with a determined pixel/mm scale, which depends on each image, the same parameters used for vesicles in clasts of the previous section are set. Because we are only interested in melt inclusions of a particular size, the program will show an equivalent diameter for each melt inclusion, the equivalent spherical diameter of an irregular object (melt inclusions) is the diameter of a sphere of equivalent geometric properties, so using this diameter obtained through FOAMS with a basic simple formula of volume of a sphere, an approximation of the volume of the melt inclusions can be made.

In certain images taken from the nanotomographer, it is possible to distinguish between a bubble and the glass phase of the melt inclusions, in this case volumes for each phase were estimated using the same procedure from the binary images, and the ratio V_b/V_{MI} was calculated, where V_b is the bubble volume and V_{MI} the inclusion volume, only considering bubbles with a circular shape. This parameter can help to infer certain volatile related behavior of the magmatic system (Lowenstern, 1995).

4. Results

4.1 Olivine Morphology

The majority of olivines observed have a polyhedral morphology and a granular morphology, possibly due to being whole crystals that were formed before the magma was intruded in the magmatic chamber. These particular shapes of olivine crystals are linked to an increased level of maturity. It is common that these particular olivines in this volcanic setting (volcanic cone) also have a hopper morphology or also called skeletal (Salas et al., 2021). Particularly due to the decision to maintain the integrity of the internal features of the olivines, and use for analysis crystals with euhedral shape, some of the samples are covered with volcanic glass. It is possible to identify the usual crystallographic faces of the orthorhombic crystal system (Figure 16).

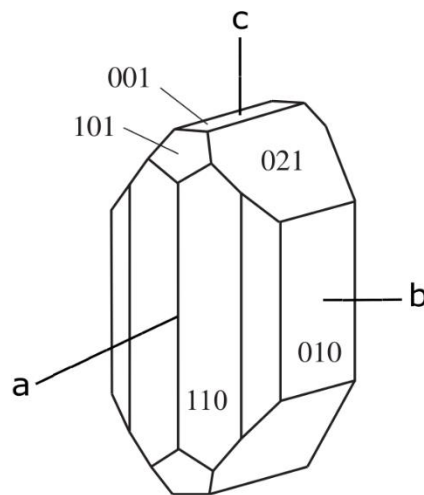


Figure 16: Crystal configuration of olivines. Image modified. (Deer et al., 2013)

At first sight it is difficult to observe internal features due to this decision. Specifically in two of the samples where thin sections were created in the 010 face, there is no clear sign of skeletal morphology within the internal structure of the olivine crystal. However, in some of the crystals it is possible to infer the possible presence of skeletal features (Figure 17).

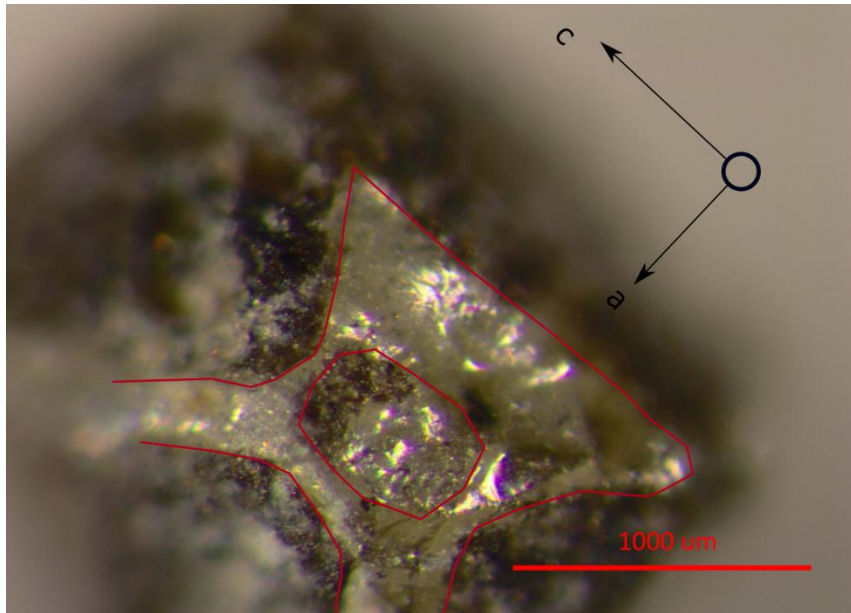


Figure 17: Polyhedral olivine with possible skeletal features.

A lack of cavities is also present in the glass slide samples. Due to normal geological factors some of the crystals have been broken, this occurs along cleavage planes. More often, these planes are the 001 and the 010. The size of the samples varies between ~1000 to 4000 μm in the bigger crystals. Planes 010, 110, and 021 are easily identified (Figure 18 and Figure 19).

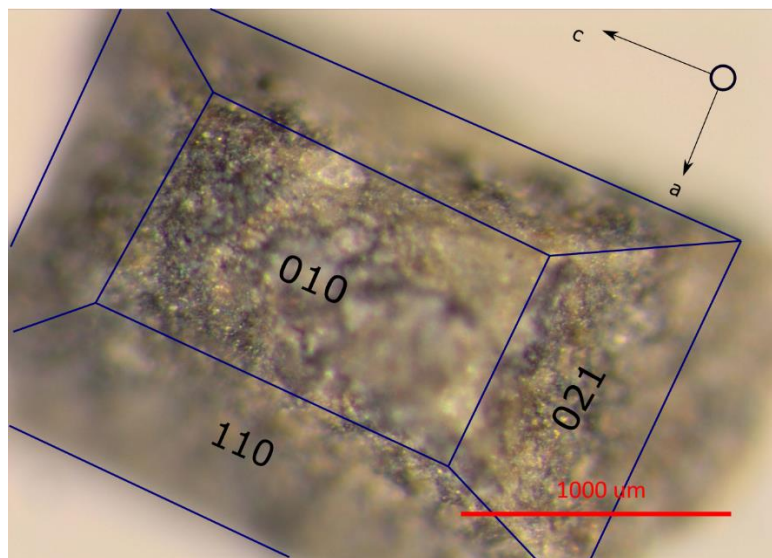


Figure 18: Example of the usual crystallographic structure of olivines observed in Licto.

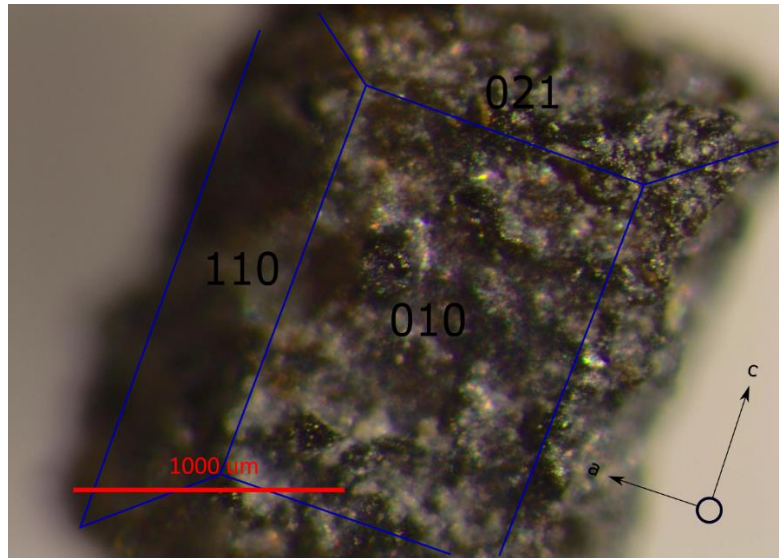


Figure 19: Different angle of an olivine from Licto covered by volcanic glass.

Depending on the orientation where planes 110 join the top of an olivine can be identified (Figure 20).

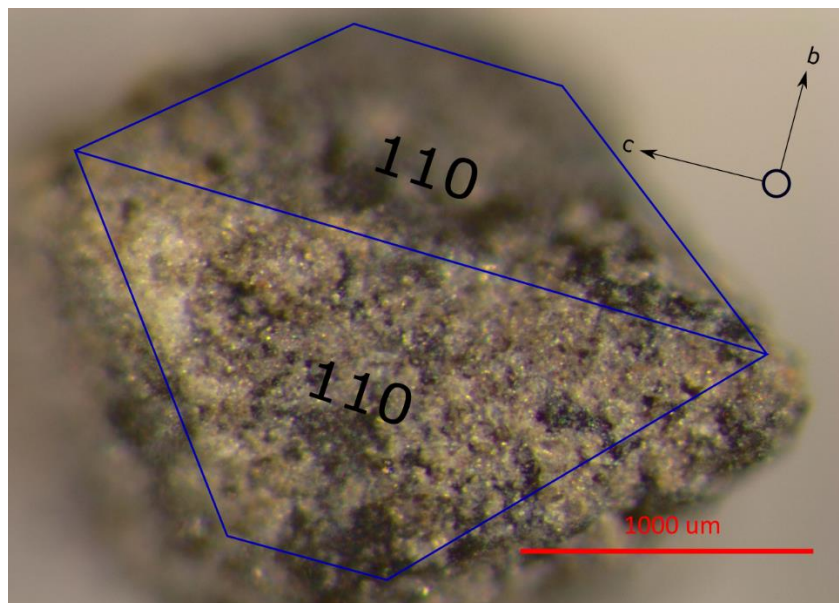


Figure 20: Different orientation of an olivine from Licto, other features of the usual orthorhombic configuration are seen.

4.2 Melt inclusion description using computed x-ray nanotomography

Results from each of the 14 olivine crystals are taken into account, followed by a brief summary and impressions of the images obtained. It is necessary to clarify that morphological values obtained from computational analysis are based on a selection of an area of interest within the crystal (just the vapor phase) and not the whole crystal itself.

However, area can be estimated using the software, using pixel size. Crystals LS2-MSL-1835-4-2 and LS2-MSL-1835-5-2 were excluded due to the apparent lack of relevant inclusions within the olivine crystal. The full section images and its results obtained from the nanotomographer are reported separately (Appendix 1).

The most remarkable characteristic that is possible to observe in the images taken by the nanotomographer is the presence of what is presumably melt inclusions within the crystal. The gray scale allows us to see empty spaces with a curve morphology; however, it does not show a spherical morphology, the denser material in the images is shown by white speckles. Melt inclusion will appear as a gray portion that wraps a spherical feature (bubble). It is possible to see a polyhedral morphology of the olivine crystal with well-developed faces. The clearest image of a melt inclusion within the olivine crystal (section LS2-MSL-1835-1/1301) shows a spherical vapor phase surrounded with a less dense phase, probably a liquid phase with an irregular shape (Figure 21).

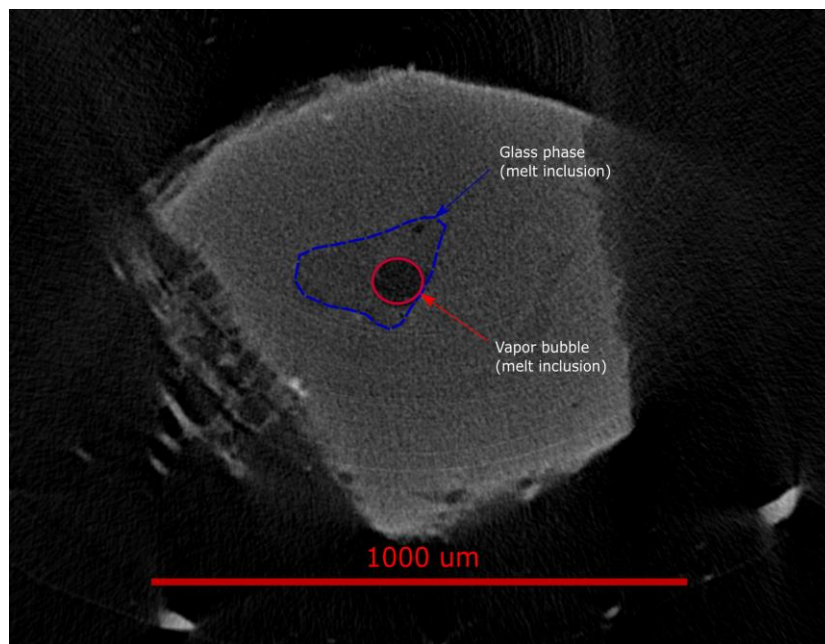


Figure 21: Section image from olivine sample LS2-MSL-1835-1/1301 taken from the nanotomographer. A large melt inclusion is seen with its associated bubble.

Binary extrapolation (done only for vapor phases) of selected portions of all the sections show that the areas of the selected empty voids (most likely vapor phases) range between 4662 and 170668 μm^2 . It is important to say that these areas taken from binary images of a selected range of grays correspond in some sections to various voids (vapor phases) within a single olivine crystal due to the lack of options to make individual measurements. That is why in some cases, the value of the area is so large. An example of a binary image

with different areas of interest measured together is shown (Figure 22). These area estimations can give us a sense of the actual size of the internal features of the olivines (vapor phase) and make assumptions based on its size.

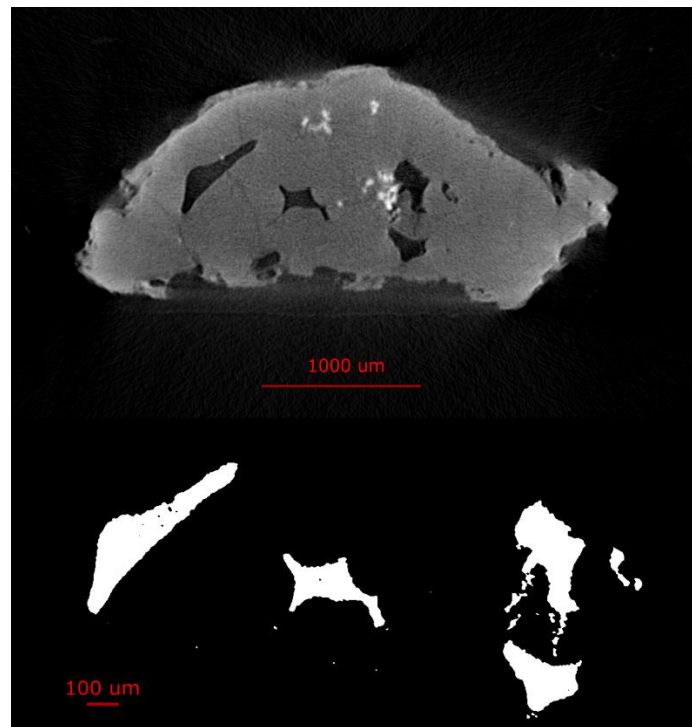


Figure 22: Section image from olivine sample LS2-MSL-1835-5-3/1862 and Binary image of a melt inclusions

It is possible to see several faces of the orthorhombic crystalline system within the sections of different olivine crystals. It is also apparent that some of the crystals have a granular morphology with poorly developed crystal faces. At the termination of the crystals, it is possible to infer that dendritic growths are developed (usually formed during rapid growth stages).

4.3 3D models of olivine crystals

It is important to constrain the three-dimensional distribution of the phases (glass, vapor, or minerals) within the olivine phenocrysts. The idea is to make computational three-dimensional reconstructions using the results in the nanotomographer observations to visualize the abundance, morphology, volume, and distribution of the phases. Accurate measurements were unfortunately not possible since the computational power load required for analyzing the results at such a small scale overloaded the computational power of the hardware. However, interactive 3D models based on voxels in a select group

of phenocrysts were created as a concept for future work that can be carried on in the instrument.

1) 3D model of LS2-MSL-1835-1

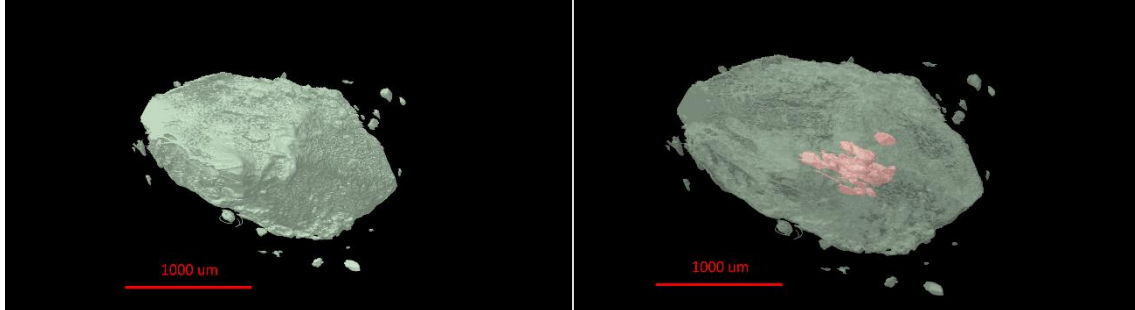


Figure 23: 3D models from olivine sample LS2-MSL-1835-1, left: model with no internal features, right: model with visible internal features.

The following images are a basic 3D representation of the olivine crystal analyzed in the nanotomographer, the green portion represents the olivine crystal, and the red portion represents possible material that could be melt inclusions or spinel inclusions near the center of the crystal (not the whole volume) (Figure 23).

2) 3D model of LS2-MSL-1835-3

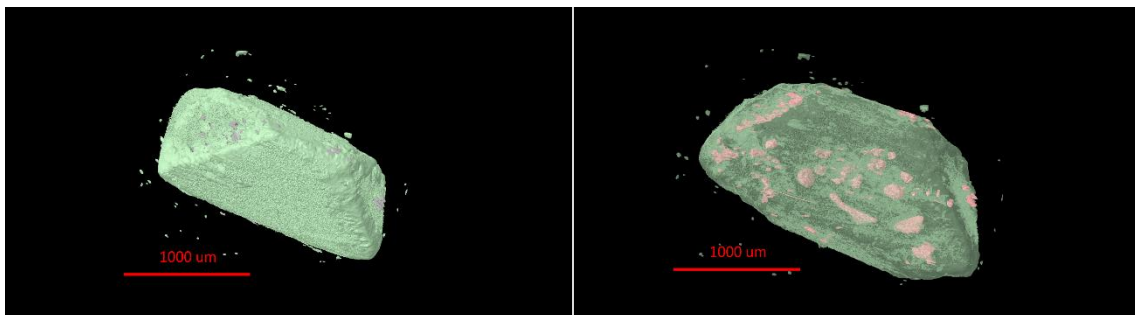


Figure 24: 3D models from olivine sample LS2-MSL-1835-3, left: model with no internal features, right: model with visible internal features.

In the next reconstruction it is possible to see more clearly the polyhedral morphology of the olivines, with an orthorhombic system and well-developed crystal faces. The melt inclusions show elongated shapes and, in some cases, almost spherical (Figure 24). The location of the melt inclusions appears not to be systematic, even more the size of the inclusions also is not systematic, and from core to rim the size of the inclusions do not vary (Figure 24).

3) 3D model of LS2-MSL-1835-5

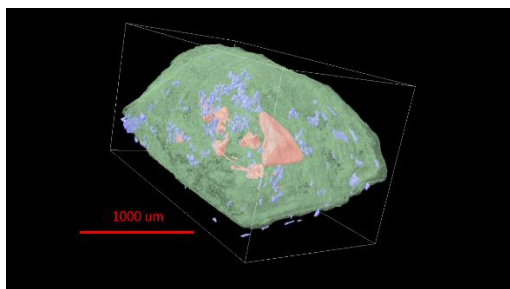


Figure 25: 3D model from olivine sample LS2-MSL-1835-5

In the last 3D model, it was possible to infer an additional phase, this is heavy mineral phase, where it was identified high-density minerals within the olivine crystal (blue portion) (Figure 25). Melt inclusions in this 3D model are mostly located in the center of the crystal host with variation in size but not a clear pattern (random), the spinel inclusions (blue color) are distributed in all different parts of the crystal and form clusters with random size (Figure 25).

4.4 Internal features within the olivine crystal

From each of the thin sections created it is possible to determine certain textural features of the olivine crystals, entrapped melt inclusions, and mineral inclusions based on their optical properties. Melt inclusions usually have a strong contrast in texture between the olivine host and the inclusion. Another feature that can be seen is a vapor bubble in some cases. The crystal plane which the thin section cuts through can be determined by comparing the general orthorhombic model with the interpreted faces in the slide. The full slide images and their interpretations are reported separate (Appendix 2).

Certain olivine crystals have a glassy texture that can be used to see internal features within the crystal, there are the presence of black spots, these can be inferred to be an opaque minerals (spinel inclusions) or melt inclusions that have been completely recrystallized. These opaque minerals are present in various parts of the crystal in a random order, with varying size. Furthermore, the olivines are colorless with a poor cleavage, high relief, with a euhedral habit, and possess abundant fractures with random orientation (Figure 26).

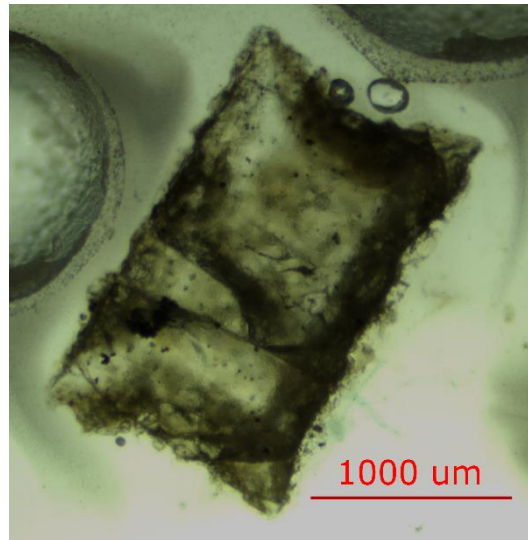


Figure 26: General image of the glass slide 3 from olivine sample (reflected light).

A closer look at the crystal faces in some of the slides helps to identify melt inclusions, the inclusion has a spherical shape with a glassy texture that contrasts with the olivine matrix, it has an approximated size of approximately 100 μm . The shape of the opaque minerals also can be seen more clearly, it does not have a clear cleavage and the habit is euhedral to subhedral, possibly the minerals that represent these opaques are spinel which generally occur in clusters or glomerocrysts (Figure 27).

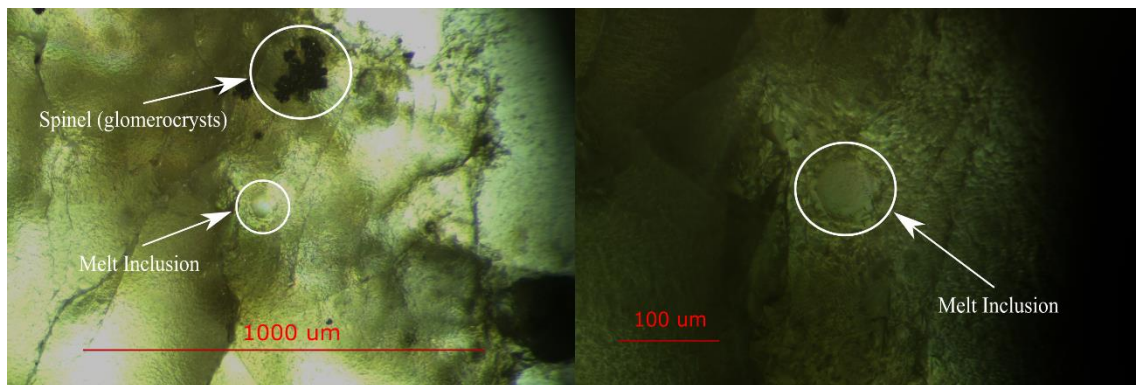


Figure 27: Left: close look to internal features within glass slide 1 (reflected light), Right: melt inclusions observed within the olivine in glass slide 1 (reflected light).

It is possible to see that within certain crystals a light brown mineral is present, this is possibly volcanic glass trapped in the olivine crystal (melt inclusion) (Figure 28).

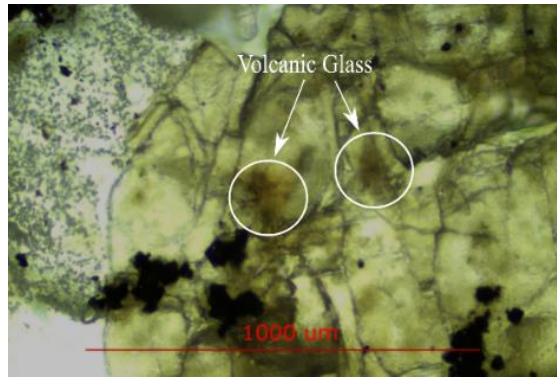


Figure 28: Volcanic glass entrapped within an olivine sample from glass slide 2 (reflected light).

In the thin section 6 there is a vapor bubble that is surrounded by a clear material (volcanic glass) that has a contrast change with the olivine mineral matrix. The inclusion is located inside the crystal. The size of the melt inclusion is approximately between 50 to 80 μm (Figure 29).

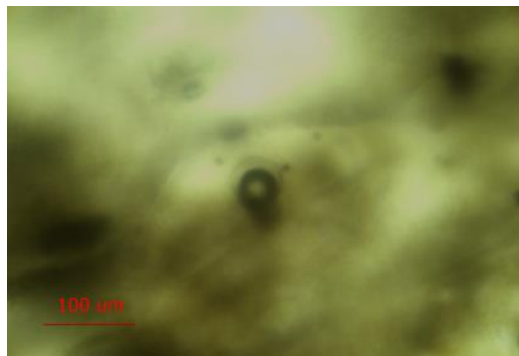


Figure 29: Close look to the melt inclusions identified in glass slide 6 (reflected light).

4.5 Olivine composition estimation using Raman spectroscopy

Eleven olivine crystals were analyzed using Raman spectroscopy to estimate the major element components Fo% of the selected crystals. Each of the samples showed distinctive peaks that correspond to the crystalline atomic structure or the silica bonds that represent certain olivine compositions. The following results for Raman spectra of the 11 samples were obtained (Figure 30).

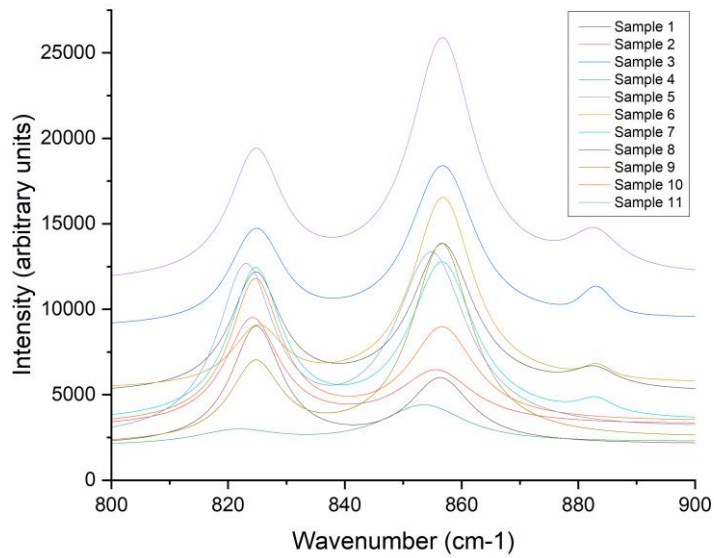


Figure 30: Raman spectra results from the 11 glass slide samples of olivines

In all the samples, a doublet of spectral peaks, which is a typical feature of olivine are observed (Figure 30). The first peak is encountered within the range of 815 to 825 cm^{-1} and the second peak within the range of 837 to 857 cm^{-1} . Peak centroids of the second peak were used in the equation for Fo% estimation (section 3.8) and the following results were obtained (Table 2):

Number of the sample	Peak Centroid (cm^{-1})	Estimated % Fo
01	854.64	87.41
02	853.44	83.5
03	854.6	87.28
04	851.6	76.47
05	854.57	87.17
06	854.57	87.19
07	854.47	86.86
08	854.39	86.63
09	854.45	86.82
10	854.44	86.78
11	852.79	81.15

Table 2: Results from estimation of Fo % using Raman spectra.

The uncertainty in composition estimations of olivines is ± 4.22 LOO RMSE-CV which is a value used to determine the accuracy of the model or a measure of how different are

the values within each other (Breitenfeld et al., 2018). These estimations of olivine composition are used for quick results when there is no possibility to use a more accurate methodology, like an EPMA. All the different estimations show similar values, except for the slide 4. It is likely that in this case, the measurement was taken from the rim rather than from the core, where the rim will have a lower Fo% value.

The methodology applied for using Raman spectroscopy to determine the Fo% of olivine phenocryst seems to be a good option when the availability of an EPMA is not possible, even if rapid chemical assessment is needed. Average Fo% for the polyhedral samples of olivine measured using the Raman approach is 86.08 (Sampling site 2 in Tulabug), compared to the average Fo% of host olivines measured by EMPA (Sampling site 1 in Tulabug) which is 81.79, the difference is 4.29 %, which is considered a significant value. This is caused because they come from different sampling sites. However, the results estimated by Raman are in agreement with the chemical composition of olivines collected at sampling site 2 measured by usual techniques (D. Weller, personal communication, 2023). The idea of the use of Raman instead of traditional methods is to ensure at least that a chemical estimation of minerals can be done with other equipment, that at least in some degree is reliable and can be used to make basic assumptions. Furthermore, the deposits located in different localities may influence the Fo content of olivines.

A similar analysis was carried with a melt inclusion observed within sample 6, the following Raman spectra was obtained (Figure 31):

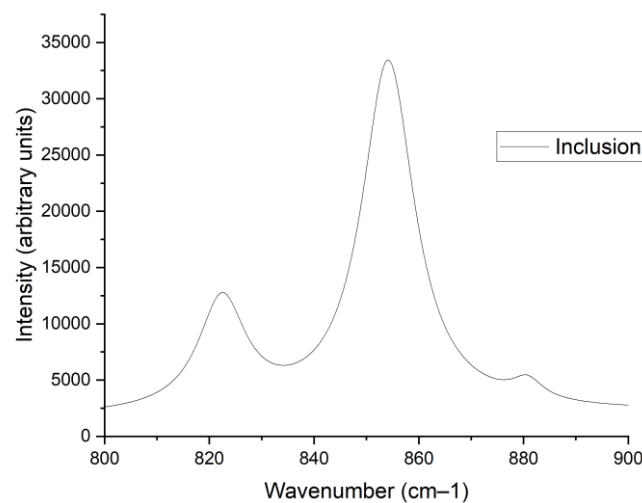


Figure 31: Raman spectra of targeted melt inclusion in glass slide 6

Even though the inclusion is composed of a glass phase and a vapor phase the characteristics doublet of olivine is encountered, the estimated % Fo in this case is 85.85 due to a peak centroid of the second peak of 854.15 cm^{-1} . The other important feature is that the Raman spectra determined another peak within the range of $3150\text{ to }3170\text{ cm}^{-1}$. This peak is related to the presence of water within the inclusion. Figure 32 shows the intensity peak for the inclusion:

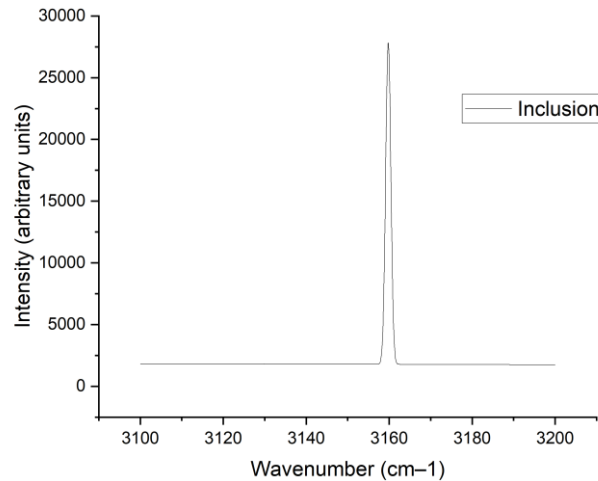


Figure 32: Raman spectra of targeted melt inclusion in glass slide 6, showing range wavenumber 3100 cm^{-1} to 3200 cm^{-1} .

The peak has an estimated amplitude of 26052.75 and a center of 3159.79 cm^{-1} . The target was a melt inclusion within the olivine crystal. Water estimation using this peak intensity was performed. However, we obtained 0.06 wt% of H_2O which is an unrealistic value. It is not realistic since the generally expected water content for arc magmas is $\sim 3\text{ wt } \%$, a possible explanation for this value is that for this measure with Raman the melt inclusions was significantly degassed. The relevant information from this peak is to probe the existence of water within the melt inclusions.

4.6 EPMA analysis

The following procedure was used to name each of the samples: first the grain number analyzed corresponding to its position in the type of grain mount being analyzed, then is followed by a unique identifying name, this is only applied for the EPMA analysis. In the case of the mineral data: no unique identifying name means a unique crystal analysis, “MI+letter” means an analysis of closest mineral host of a specific inclusion, “mic” means

a microlite analysis, “c” a core part analysis, “r” a rim part analysis, “a” or “b” a different measurement from the same crystal, “S.C” San Carlos olivines, “phe” phenocryst analysis, “ol+number” specific olivine in a clast, “l+number” line section in core to rim analysis. Same principle applies to glass data except: “H+letter” the melt inclusion mineral host that corresponds to the melt inclusion, “JDF” Juan de Fuca sample, and “number” a different measurement within the same clast. Error is calculated using the reference samples (measured values – reported values) (Table 1).

Summary of the most important results are reported in Table 3.

	SiO ₂	TiO ₂	Al ₂ O ₃	Cr ₂ O ₃	FeO	MnO	MgO	CaO	Na ₂ O	K ₂ O	P ₂ O ₅	Ni	Cl	SO ₃	Total %	Fo %
Host olv (avg)	39.68	0.01	0.02	0.02	17.04	0.24	42.95	0.14	0.00	0.00	0.02	0.17	n/a	n/a	100.29	81.79
Range	2.21	0.03	0.13	0.06	4.75	0.11	4.56	0.09	0.04	0.01	0.09	0.18	n/a	n/a	2.92	5.50
SD	0.39	0.01	0.02	0.02	0.87	0.03	0.82	0.02	0.01	0.00	0.02	0.04	n/a	n/a	0.87	0.99
olv (clasts) (avg)	38.91	0.02	0.03	0.02	19.31	0.29	42.01	0.15	0.00	0.00	0.04	0.13	n/a	n/a	100.90	79.60
Range	1.67	0.02	0.06	0.04	10.60	0.22	8.87	0.09	0.01	0.01	0.15	0.17	n/a	n/a	2.97	12.59
SD	0.51	0.01	0.02	0.01	3.39	0.07	2.72	0.03	0.00	0.00	0.04	0.05	n/a	n/a	1.04	4.05
Cpx (clasts) (avg)	51.77	0.65	3.32	0.37	7.27	0.18	16.48	20.32	0.31	0.00	0.02	0.02	n/a	n/a	100.72	n/a
Range	3.49	0.63	2.85	0.47	2.54	0.13	2.56	2.62	0.16	0.02	0.06	0.04	n/a	n/a	1.02	n/a
SD	1.26	0.22	1.05	0.15	0.83	0.03	0.94	0.91	0.05	0.01	0.02	0.01	n/a	n/a	0.29	n/a
Plg (clasts) (avg)	53.28	0.07	29.44	0.01	0.87	0.00	0.17	12.85	3.87	0.19	0.02	0.01	n/a	n/a	100.79	n/a
Range	4.11	0.15	3.46	0.02	0.66	0.02	0.22	2.93	1.38	0.33	0.03	0.03	n/a	n/a	1.82	n/a
SD	1.30	0.05	1.05	0.01	0.21	0.01	0.07	0.89	0.39	0.11	0.01	0.01	n/a	n/a	0.51	n/a
Spl (clasts) (avg)	0.09	2.08	14.09	30.48	41.83	0.34	8.33	0.05	0.01	0.00	0.00	0.10	n/a	n/a	97.38	n/a
Range	0.11	0.92	4.22	5.88	8.25	0.12	2.04	0.11	0.01	0.00	0.00	0.10	n/a	n/a	3.58	n/a
SD	0.04	0.37	1.73	2.59	3.54	0.04	0.85	0.04	0.00	0.00	0.00	0.04	n/a	n/a	1.43	n/a
Error (minerals)	±0.75	***	***	***	±0.69	±0.02	±0.6	***	***	***	±0.01	±0.02	***		***	***
MI (avg)	59.30	1.24	16.63	0.01	5.68	0.09	2.71	6.01	3.45	2.46	0.33	0.02	0.13	0.17	98.22	n/a
Range	16.35	1.81	6.55	0.06	7.61	0.12	14.39	5.97	4.25	3.63	0.40	0.08	0.17	0.44	7.83	n/a
SD	3.50	0.36	1.79	0.01	1.36	0.03	2.04	1.62	0.95	0.85	0.09	0.02	0.03	0.13	1.88	n/a
Glasses (avg)	62.05	1.52	14.20	0.00	7.17	0.11	1.98	4.45	3.56	2.70	0.41	0.01	0.10	0.01	98.28	n/a
Range	4.87	0.78	6.88	0.02	3.47	0.11	2.32	2.80	3.02	2.46	0.23	0.06	0.11	0.03	8.24	n/a
SD	1.14	0.16	1.36	0.01	0.73	0.03	0.51	0.63	0.92	0.52	0.06	0.02	0.03	0.01	1.85	n/a
Error (glass)	±0.12	±0.03	±0.11	***	±0.52	±0.001	±0.42	±0.02	±0.14	±0.06	±0.08	***	***	***	***	***

Table 3: Average values of measurement done with EPMA of host olivines (olv), olivines from clasts, clinopyroxene from clasts (Cpx), plagioclase from clasts (Plg), spinel from clasts (Spl), melt inclusions (MI), and matrix glasses from clasts. n/a (not measured), *** not possible to calculate since reference does not report values. All values in wt %.

4.7 Olivine zonation

One rim to core measurement was taken from an olivine phenocryst encountered within the clast 21 from 20220828-1_CwM mount (Figure 33 and Figure 34).

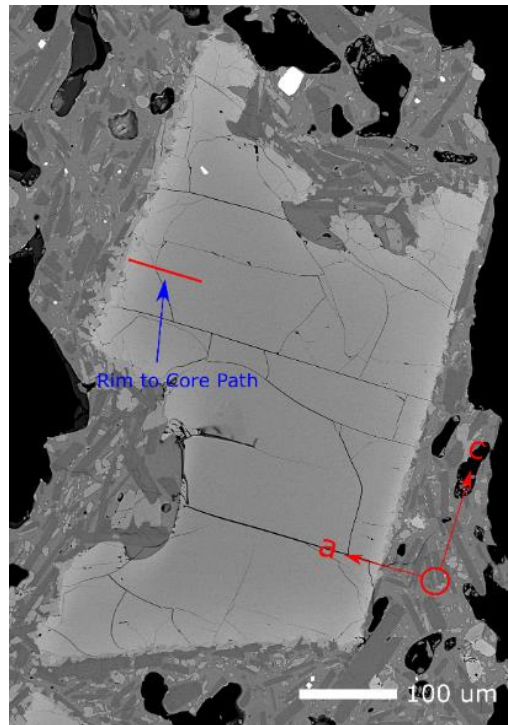


Figure 33: BSE image of olivine crystal which measurements are taken in a line from rim to core.

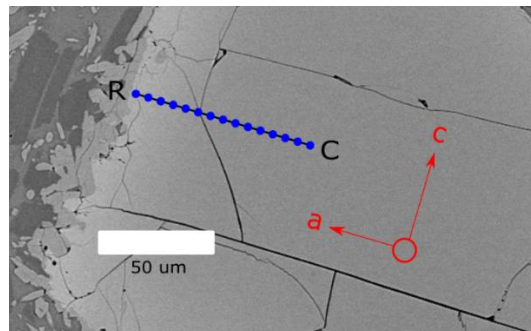


Figure 34: Zoom in the path measurements taken from specific locations of the olivine crystal.

The chemical variations of interest can be seen in the diagram of variation of Fo% and Ni wt% with distance from the rim (measurements from rim to core) (Figure 35).

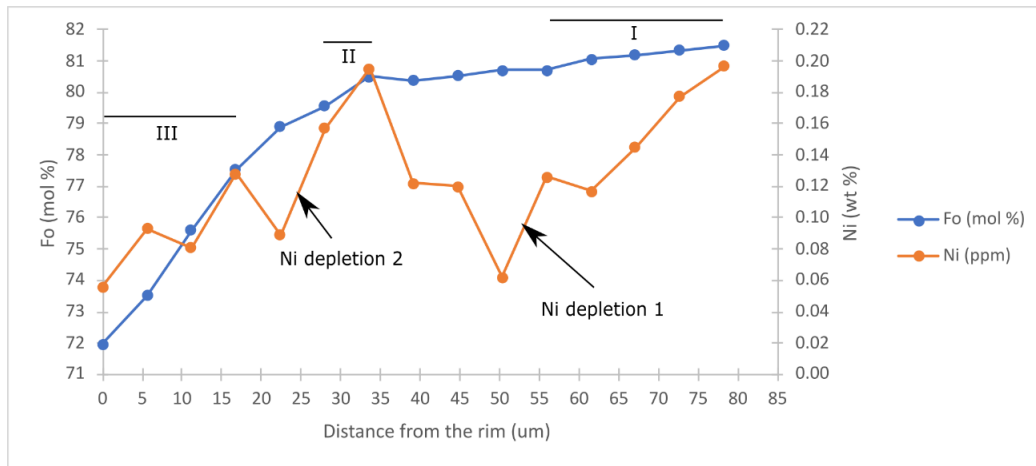


Figure 35: Diagram of distance from the rim in μm vs the Fo % and Ni wt % of the measurements from the olivine from rim to core.

The diagram represents a zoning pattern within the olivine crystal (polyhedral morphology), that has reversals in composition that are easier to see in the Ni compositional variation trend. The oscillations are estimated to occur in length scales of 10-20 μm . The measurement closer to the core of the crystal has a composition 81 Fo and 0.20 wt % of Ni or 2000 ppm. The measurement closer to the rim of the crystal has a composition of 72 Fo and 0.06 wt % of Ni or 600 ppm. The core Fo content shows a gradual decline until approximately 35 μm before it rapidly drops to the Fo of 72 at the rim. The Ni shows dramatic oscillations from the core to the rim and in some cases are out of sequence with the Fo content. Based on these observations, the crystal is divided into three discrete sections that have different petrologic implications for the history of the phenocryst. The portion of the crystal “I” has an approximated gradient of $\Delta\text{Fo} \sim 0.2$ and $\Delta\text{Ni} \sim 0.02$ wt% or 200 ppm. Portion of the crystal “II” has an approximated gradient of $\Delta\text{Fo} \sim 0.96$ and $\Delta\text{Ni} \sim 0.04$ wt% or 400 ppm. Portion of the crystal “III” has an approximated gradient of $\Delta\text{Fo} \sim 1.54$ and $\Delta\text{Ni} \sim 0.02$ wt% or 200 ppm.

Ni depletions in olivine can describe disequilibrium crystallization caused by either change in the magma (likely magma mixing) or episodes of rapid growth of the crystal. A portion of the crystal “III” Ni is quickly depleted in the melt where the crystal is being created due to the high partitioning of olivine, possibly creating a compositional boundary layer depleted in compatible elements and enriched in incompatible ones (Salas et al., 2021). Within a compositional boundary layer, Fo has a lower partition coefficient so this is why the trend in this chemical species is less sensitive to changes in the chemical composition of the melt or rapid growth episodes (creation of a compositional boundary layer) (Salas et al., 2021). Olivine zoning normally is related to magma mixing but it is

necessary to compared to other cases to infer if either the trend observed in the sample from Licto can correspond to magma mixing or an out-of-sequence growth (episodes of rapid and slow growth of the crystal) (Salas et al., 2021).

At first if there are more available olivine samples where chemical zoning analysis can be done, a uniform and uni-directional evolution of Fo and Ni trends can be related to a more likely out of sequence growth. However, in this case, there is only one sample analyzed because EPMA analysis was carried by an external consultor. Crystals record different timescale information due to mixing with chemically distinct melts during assembly of the magmas before eruption. This leads to non-uniform Fo and Ni trends among olivines (Salas et al., 2021).

Compared to other case studies where olivine zoning was carried out, the olivine at Licto is similar to normal zoning olivines from a later stage tephra expulsion from an eruption. In this case eruptions dynamics directly influence the type of zoning in olivine composition, where normal zoning is related with a more steady and laminar magma flow (Albert et al., 2020). Oscillatory patterns of Ni could be also related to changes in the magma composition caused by complex magma mixing process.

4.8 Post-entrapment corrections results and implications

As discussed in the methods section, the Peotrolog3 programs generated two outputs during the correction. The first output is when the melt inclusion and olivine host are in equilibrium (PEC-corrected) and the second output includes the correction for the diffusive loss of Fe out of the inclusion and into the host olivine (Fe-loss corrected). In some cases, the PEC-corrected inclusions might be the correct choice of compositions to use. However, in my case, the first output was determined to be not representative of the host magma and thus I needed to use the PEC-correct and Fe-loss corrected melt inclusions compositions. This is because the first output showed melt inclusion compositions with lower FeO^t compared to matrix glasses and whole rock products. Because of this, it is inferred that melt inclusions have undergone Fe-loss.

Figure 36 shows the SiO_2 vs FeO^t for the PEC-corrected melt inclusion compositions from the first output.

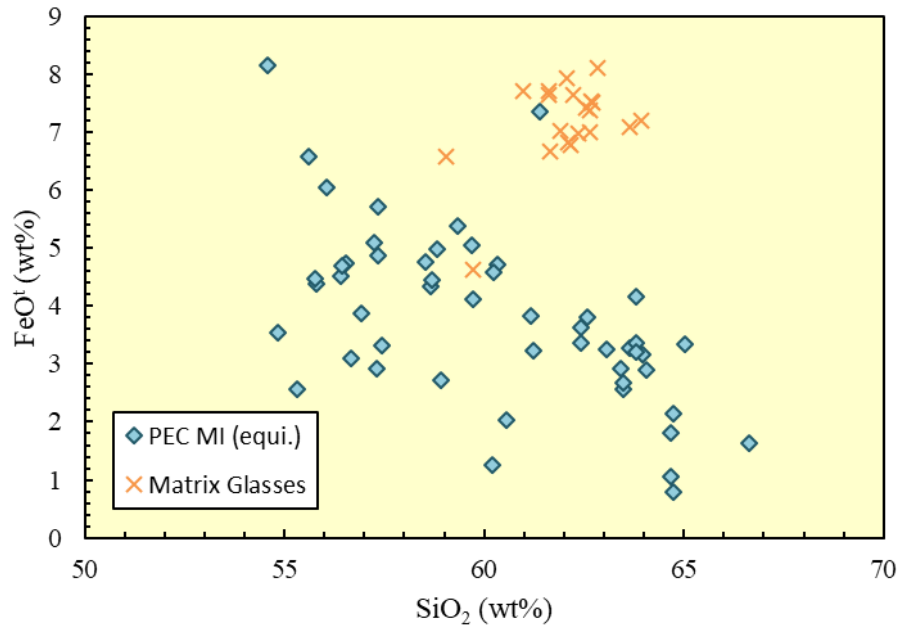


Figure 36: SiO₂ vs FeO^t diagram showing corrected melt inclusions for post-entrapment crystallization when it reaches equilibrium (first output) compared with a few glass compositions measured in EMPA

From Figure 36 the estimated FeO^t content of the melt inclusions (PEC) at equilibrium is lower compared to the FeO^t content of matrix glasses measured from clasts that contain these olivine hosts. Glass material can be a close estimation of melt compositions prior to magma ascent and late-stage crystallization of the matrix glasses. The objective is to find the compositions of melt inclusions that can be the closest representation of the melt once it was entrapped. As this process occur at equilibrium during the corrections of the melt inclusions, it means that the melt inclusions have experienced Fe-loss. Fe-loss is taken into account in the Petrolog model in the last output. This is why it considered the Fe-loss corrected melt inclusion compositions to be a fair representation of melt at the moment of entrapment. Using the PEC-corrected and Fe-loss corrected composition removes any real magmatic variation in the FeO^t contents.

After performing these calculations, it is important to evaluate other parameters included in the results such as the amount of olivine added into the melt inclusion during the PEC and Fe-loss corrections. Inclusions requiring too much olivine addition may give unrealistic results (Weller & Stern, 2018). When seen the melt inclusions that added to much olivine during PEC and Fe-loss, they were offset from the general trend that the melt inclusions create.

An arbitrary threshold of 16% olivine addition is chosen here. If one of the melt inclusions being corrected is required to add more than 16% of olivine, the inclusion will not be considered to be a representation of the melt at moment of entrapment (this change will apply for Harker diagrams). In total 3 melt inclusions were removed.

Once the following information for melt inclusions (PEC) were obtained, compositional variation diagrams were generated (Figure 37), where MI (PEC) are melt inclusions (MI) corrected for post-entrapment crystallization and Fe-loss (output 2):

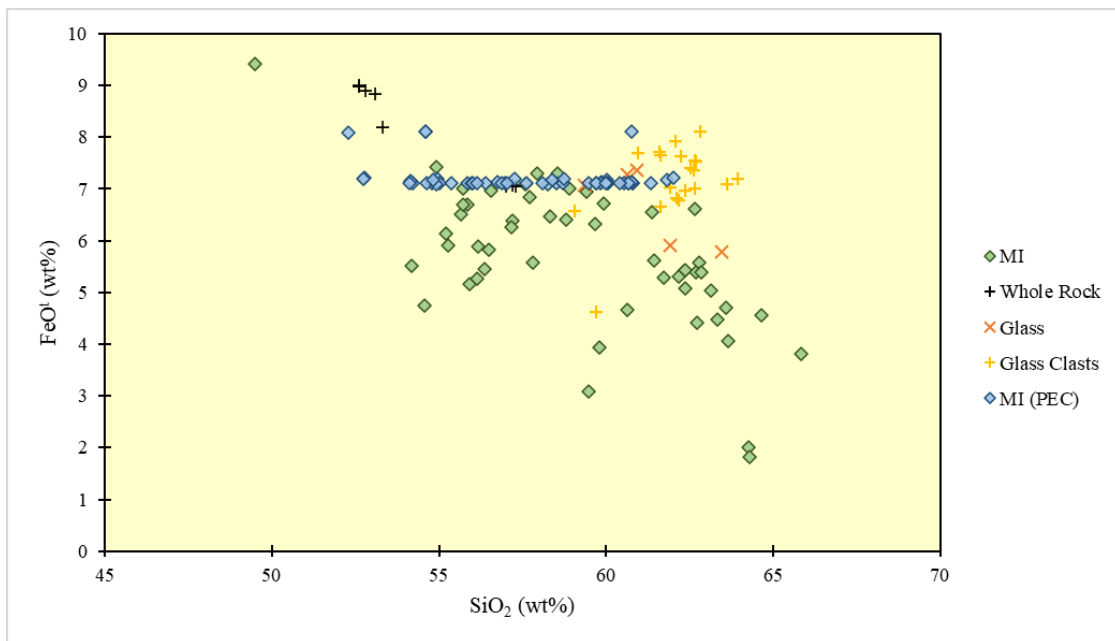


Figure 37: SiO₂ vs FeO^t diagram for uncorrected melt inclusions, whole rocks compositions, glass compositions (glass: glass within the olivine crystal, glass clasts: glass in the clasts of the scoria), and PEC and corrected Fe-loss melt inclusions.

Melt inclusions corrected (MI PEC) show a higher concentration of FeO^t to compensate Fe-loss process. However, a fixed value for all melt inclusions generates an invariant FeO^t trend. Applying the PEC-correction and Fe-loss correction produces FeO^t melt compositions that are more similar to the whole rock compositions at a similar SiO₂ content. Thus, applying both corrections seem to be the most viable option for these olivine-hosted melt inclusions. It is important to consider the invariant FeO^t trend generated by the Fe-loss correction. Although magmatic evolution as a result of late-stage fractional crystallization may impact the FeO^t liquid line of descent, it is not possible to infer these trends since FeO^t is rendered invariant. However, other major elements display characteristic patterns and are useful for interpretation (Figure 38).

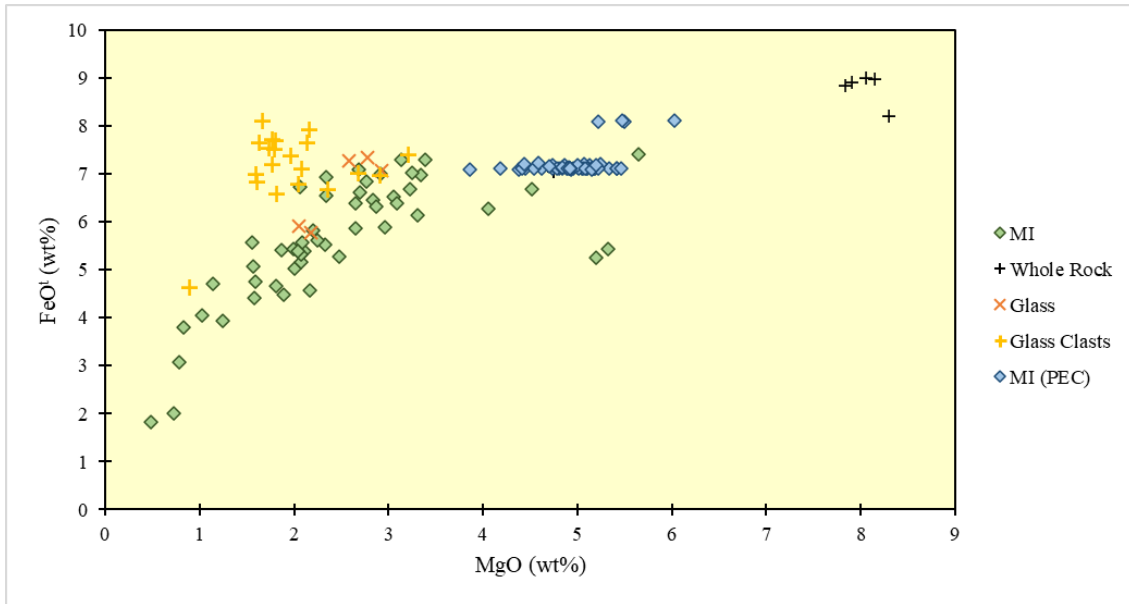


Figure 38: MgO vs FeO^t diagram melt inclusions uncorrected, whole rocks compositions, glass compositions, and PEC and Fe-loss corrected melt inclusions.

The PEC/Fe-loss corrected melt inclusions have a higher MgO and this follows the idea that parental magmas are enriched in this chemical species, which then is quickly depleted due the crystallization of olivine.

Chemical variation diagrams (Harker diagrams) for PEC and Fe-loss corrected melt inclusions are as follows (Figure 39):

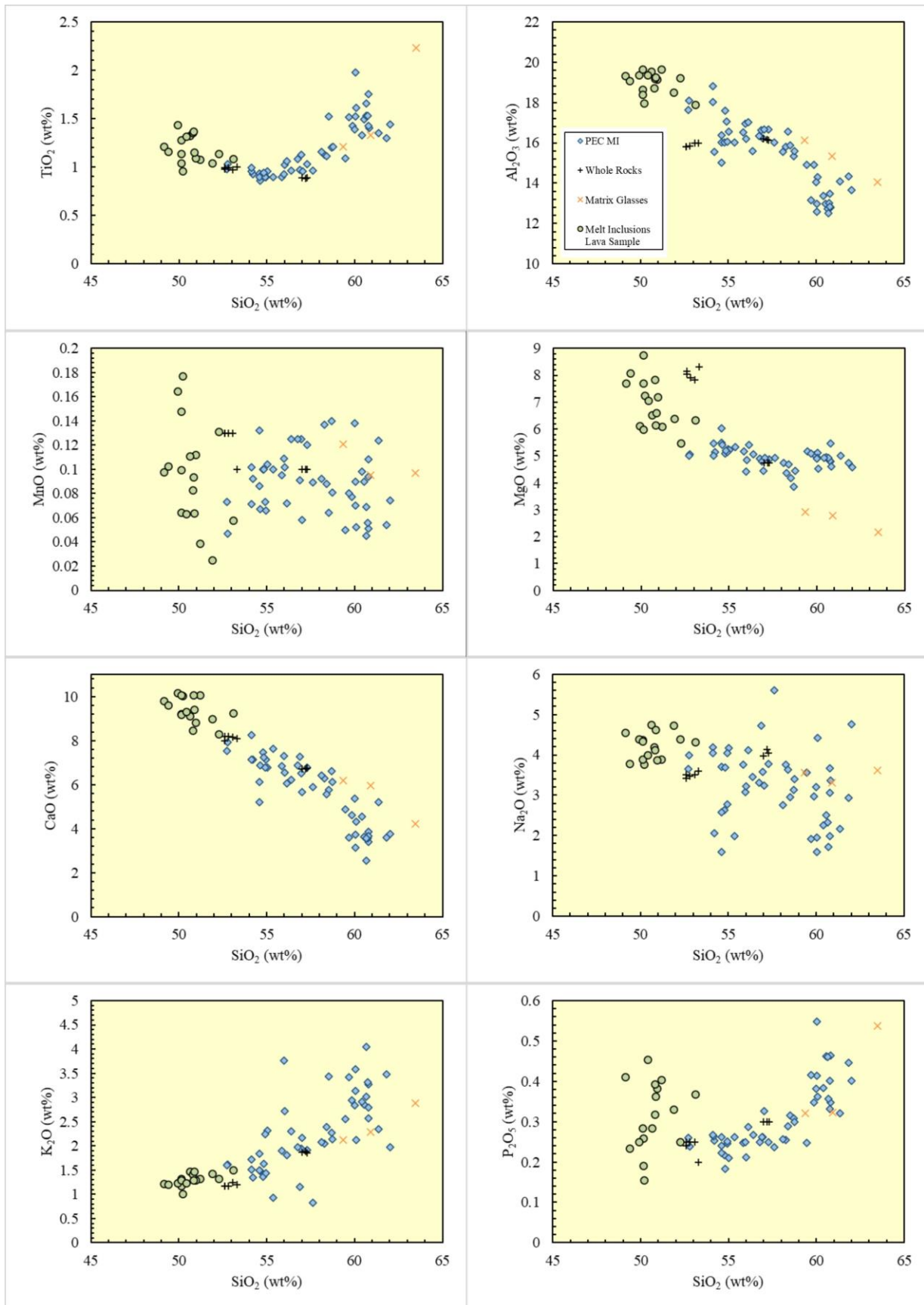


Figure 39: Harker diagrams for various major elements plotted against SiO_2 (wt%), PEC and Fe-loss corrected melt inclusions, whole rocks, a few selected matrix glasses are represented (this study). Melt inclusions obtained from a lava sample from Tulabug, green dots (D. Narváez, 2021).

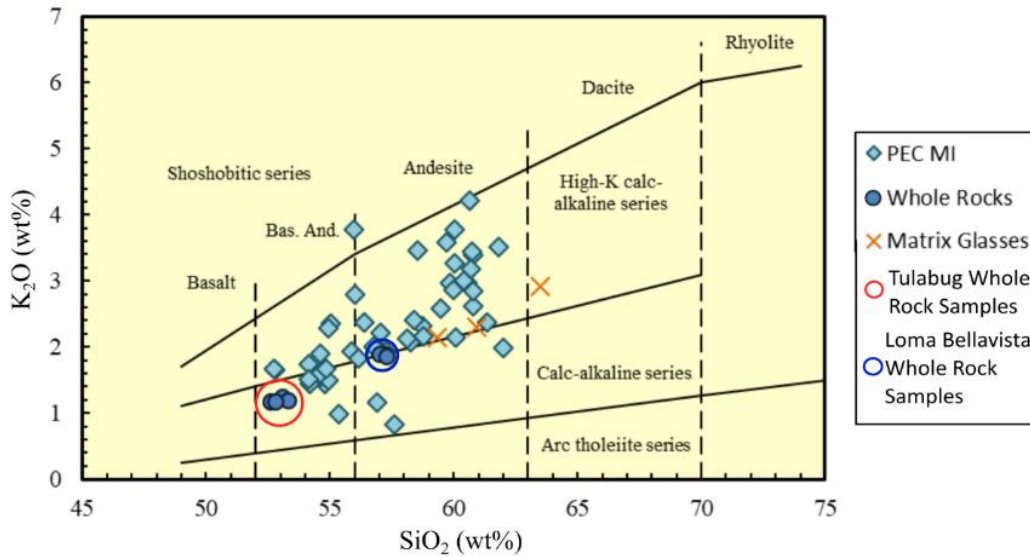


Figure 40: Rock classification diagram (Peccerillo & Taylor, 1976) for the PEC and Fe-loss corrected melt inclusions, whole rocks, and a few selected matrix glasses.

Melt inclusion compositions are basaltic andesites and andesites with a value of SiO₂ wt.% that varies from 52.73 to 62.01 (Figure 40). SiO₂ concentrations have clear negative correlation with the concentrations of Al₂O₃ and CaO. On the other hand, positive correlations between concentrations of SiO₂ are found with TiO₂, K₂O, and P₂O₅, however the dispersion is higher between SiO₂ and K₂O. There is no correlation between SiO₂ concentrations and MnO and Na₂O. In the case of the correlation between SiO₂ and MgO for the melt inclusions, the likely correlation is called invariant, where the MgO concentration seems to maintain a certain range of value as SiO₂ increases, however it is possible to assume that whole rocks samples can be the initial chemical composition of the trend and the glasses the end of the trend. In this case, the trend will have a negative correlation until an approximately 54 wt% of SiO₂, then MgO will become invariant until a value of approximately 59 wt% SiO₂.

This particular trend in MgO also can be found when the concentration of this chemical species is plotted against TiO₂ and K₂O, where there is no correlation or the trend invariant under a certain range which is MgO wt% of 3.87 to 6.03.

These chemical trends only can describe possible local magmatic evolution and behavior in Licto. For instance, the K₂O concentration of Licto melt inclusion samples is higher compared to whole rock samples of Pichincha volcano (located in the western cordillera of Ecuador, at approximately 100 km above the subducting slab and 200 km north of the

study area). In fact, Licto melt inclusion samples have a similar K_2O concentration and trend of Tungurahua volcano (located in the eastern cordillera of Ecuador, approximately 150 km above the subducting slab) (Schiano et al., 2010). There is established in previous research that a possible lack in correlation of certain chemical trends in north Andean volcanic zone is due to cross-arc variation in decreasing melt fractions cause by a decrease in the fluid that the slab inputs to the mantle wedge, or a possible change in the contribution of the continental crust and subcrustal lithosphere through assimilation (Schiano et al., 2010). In the case of Licto, the local scale lack of correlation could be related to other factors such as its small size, mantle source heterogeneity, the limited magmatic history, or the small degree of melt generated in the subarc mantle.

A comparison between melt inclusions obtained from a lava sample of basaltic-andesite at Licto can be made with the melt inclusion samples obtained from this study. The most important difference being that melt inclusions measurements presented here were obtained from tephra deposits of Licto, specifically scoria while the others were from lava (D. Narváez, 2021). The melt inclusions samples derived from the lava sample have a value of SiO_2 wt.% that varies from 49.2 to 53.1. There are no clear positive or negative correlations between SiO_2 concentration and the other chemical species in the lava samples, most of them do not show a correlation at all (increase dispersion) or they are invariant (D. Narváez, 2021) (Figure 39).

However, the value of this melt inclusion compositions derived from a lava sample could rely in its more primitive composition, since start at a SiO_2 wt% of 49.2 and the melt inclusions from the scoria analyzed in this study start at a SiO_2 wt% of 52.73, along with the available trace element concentrations and volatile elements concentrations in the melt inclusions from the lava sample (D. Narváez, 2021).

As a general comparison between olivine-hosted melt inclusions from the scoria deposit (present study) and olivine-hosted melt inclusions from the lava sample, the TiO_2 concentration in melt inclusions (lava sample) is between 1 and 1.4 wt% and it does not have a clear trend (seems invariant), while melt inclusions (scoria samples) is between 0.86 and 1.97 wt% with a clear positive correlation. Al_2O_3 concentration in melt inclusions (lava sample) is between 17.9 and 19.6 wt% and it does not have a clear trend (no correlation), while melt inclusions (scoria samples) is between 12.52 and 18.81 wt% with a clear negative correlation. MnO concentration in melt inclusions (lava sample) is between 0 and 0.2 wt% and it does not have a clear trend (no correlation), while melt

inclusions (scoria samples) is between 0.05 and 0.14 wt%, it does not have a clear trend (no correlation), Mn is very commonly difficult to interpret, however the general trend will be a decrease in concentration since Mn substitutes for Fe in olivine during crystallization. MgO concentration in the melt inclusions (lava sample) is between 5.5 and 8.7 wt%, it does have a negative correlation (disperse data), while melt inclusions (scoria samples) is between 3.87 and 6.03 wt%, with the same possible invariant correlation (or negative assuming parameters explained above). CaO concentration in melt inclusions (lava sample) is between 8.3 and 10.1 wt%, it does not have a clear correlation (invariant), while melt inclusions (scoria samples) is between 2.55 and 8.26 wt%, with a negative correlation. Na₂O concentration in melt inclusions (lava sample) is between 3.8 and 4.7 wt%, it does not have a clear correlation (invariant), while melt inclusions (scoria samples) is between 1.59 and 5.61 wt%, with no correlation (disperse data). K₂O concentration in melt inclusions (lava sample) is between 1 and 1.5 wt%, it has positive correlation, while melt inclusions (scoria samples) is between 0.82 and 4.05 wt%, with a positive correlation (disperse data). Finally, P₂O₅ concentration in melt inclusions (lava sample) is between 0.2 and 0.5 wt%, it has no correlation, while melt inclusions (scoria samples) is between 0.18 and 0.55 wt%, with a positive correlation (D. Narváez, 2021). The dispersion is evident when only the melt inclusions obtained from the lava are seen in the diagram (Figure 39), despite this for the majority of major elements these melt inclusions are located in the more mafic portion of the chemical compositions observed in Licto. The combination of these melt inclusions coming from the lava (D. Narváez, 2021) and the melt inclusions obtained from this study allows a clearer understanding of the magmatic evolution history at Licto.

4.9 Basic textural analysis and its possible link with change in chemical composition

The shortest distance between the melt inclusion the crystal edge (olivine host) was measured for the 52 melt inclusions (Table 4), using back scattered electron images (Figure 14). The idea of this approach is to find a correlation between the location of the melt inclusion (position within the olivine crystal where the melt was entrapped) and changes in the concentration of major elements exists (Figure 41).

ID	SDE (μm)	ID	SDE (μm)	ID	SDE (μm)	ID	SDE (μm)
143	28	114/MIb	150	65/MIa	177	56	19
168/MIa	9	114/MIc	129	65/MIb	243	43	81
168/MIb	24	125/MIa	190	64	n/a	45	59
191	36	125/MIb	230	62	102	32	88
190	22	101	216	61	92	15	117
175/MIa	49	102	94	46/MIa	109	27	188
175/MIb	n/a	85	75	46/MIb	92	2	110
164	72	92	200	34	110		
148	43	93	155	36	145		
155	26	97	141	49/MIa	65		
129	144	80/MIa	100	49/MIb	42		
147	5	80/MIb	245	52/MIa&b	n/a		
160	38	66/MIa	171	52/MIa&b	41		
117	296	66/MIb	307	55/MIa	165		
114/MIa	156	66/MIc	174	55/MIb	n/a		

Table 4: Measured shortest distances from crystal (host) edge to melt inclusions (SDE). ID: grain number/associated melt inclusion if applicable, n/a: not possible to measure

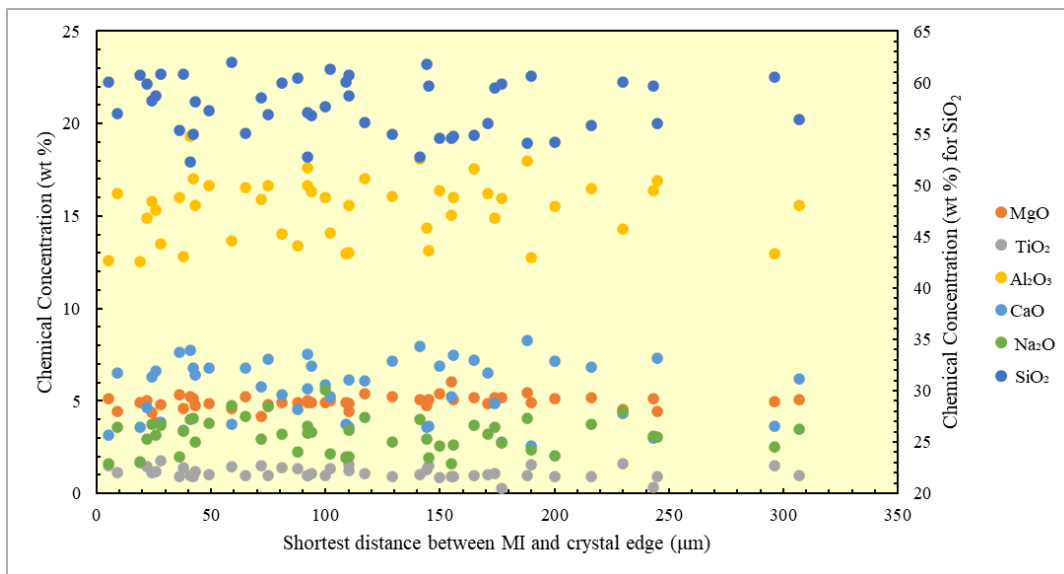


Figure 41: Major element variation depending on the shortest distance between the melt inclusion and the crystal host edge.

Based on two dimensional results, there is no clear correlation between the variables of interest. In fact, the major element within a range is invariant regardless of the position of the melt inclusion. In previous research it has been found that in the case of polyhedral morphologies, the position of the melt inclusion will not affect the chemical composition. This is because for polyhedral crystals to form, a homogeneous chemical equilibrium is maintained between melt and crystal, it is possible that the chemical compositions of the inclusions hosted in a polyhedral crystal are the compositions of the magma in

equilibrium in the liquid line of descent (Faure & Schiano, 2005). The same principle could be applied to dendritic polyhedral olivines since experimental results have shown that regardless of the position of the melt inclusion in this type of crystal morphology it also will reach equilibrium (Faure & Schiano, 2005).

Examples of the polyhedral morphology and dendritic polyhedral morphologies found in the olivine host samples are shown in Figure 42.

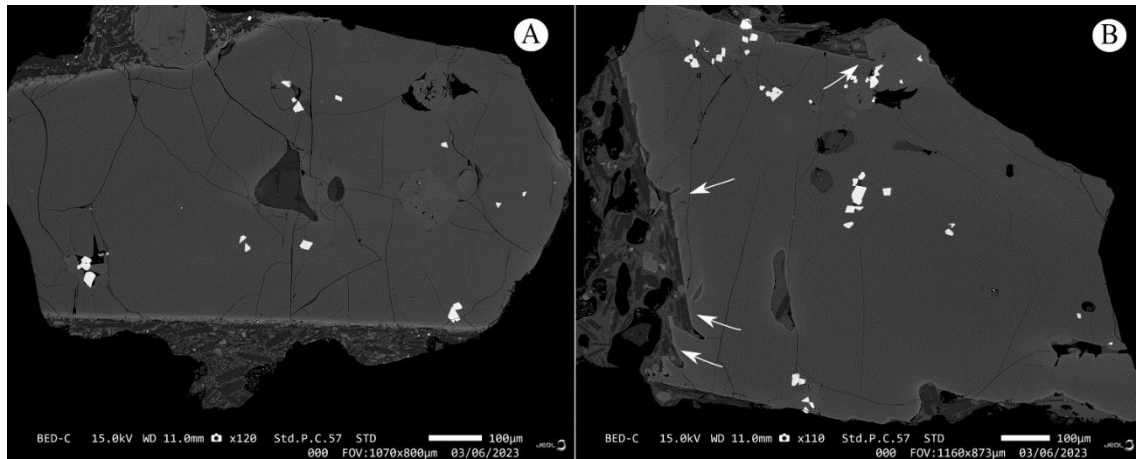


Figure 42: Images of olivine crystals obtained by BSE images. A: Example of polyhedral morphology, B: Example of dendritic polyhedral morphology (arrows showing stair like texture).

Morphology interpretation of the hosting olivine of the melt inclusions was performed, and the following recount of the all the olivines (when possible) was achieved (Figure 43):

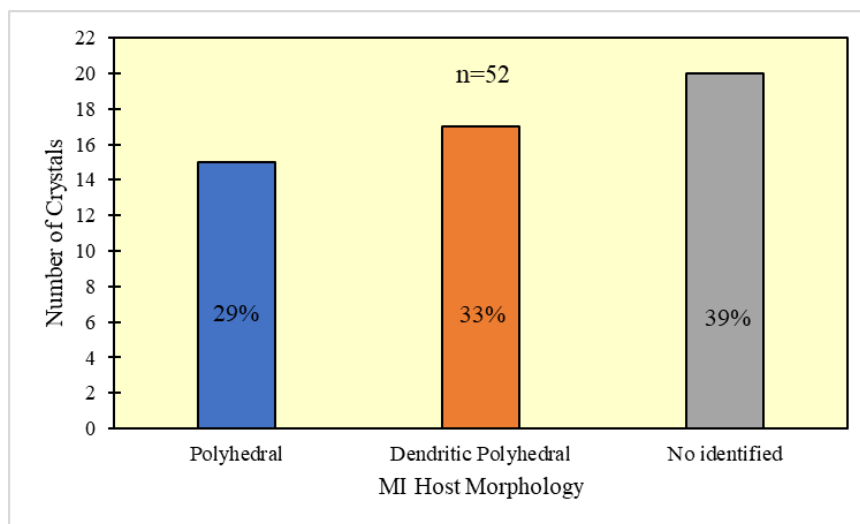


Figure 43: Frequency diagram of the different interpreted morphologies for host olivines of melt inclusions.

The next step is to observe if based on the crystal host morphology, the melt inclusions composition will vary depending on the distance where the melt inclusion is located (Figure 44).

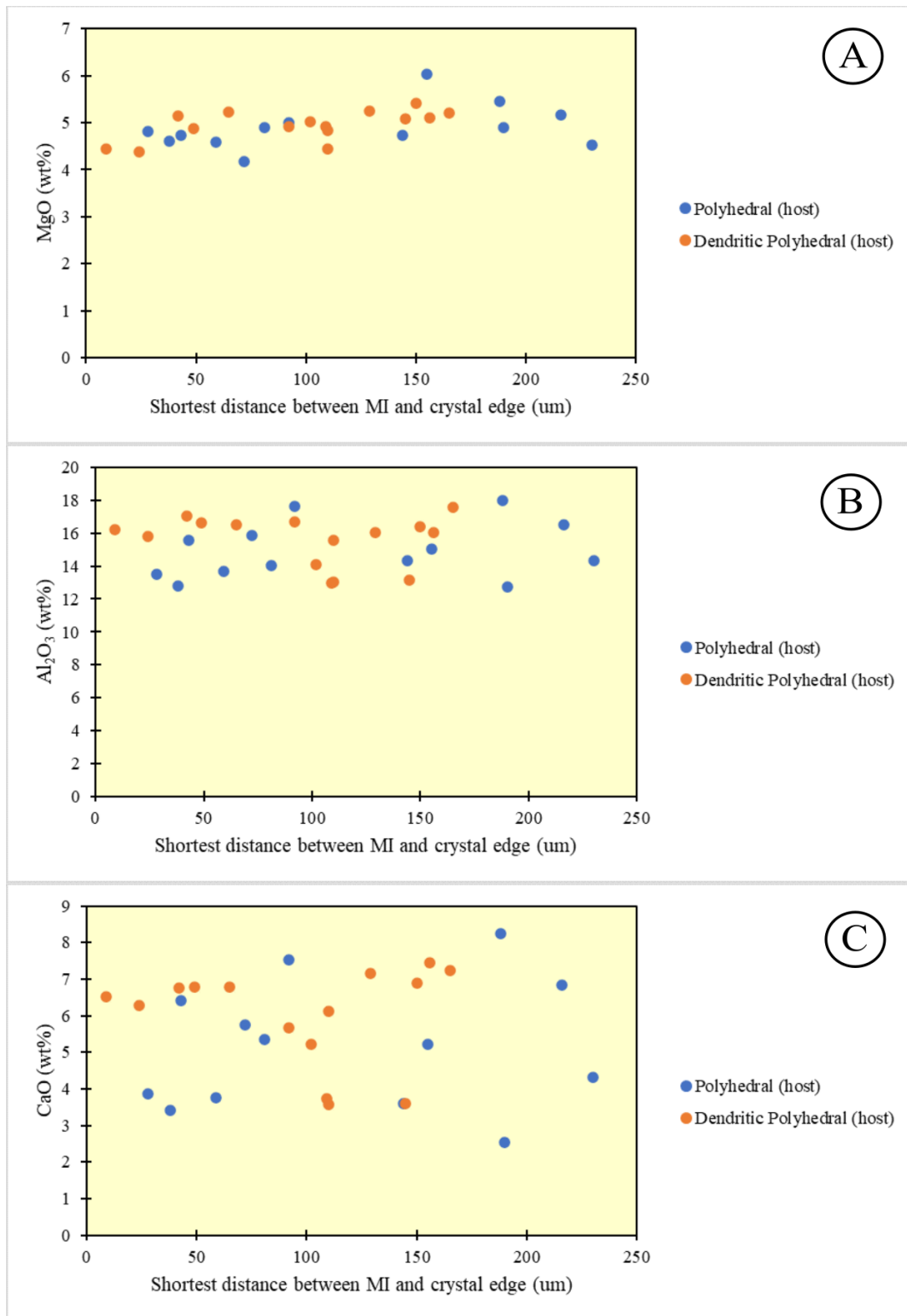


Figure 44: A: Shortest distance between melt inclusions and crystal host edge for A) MgO, B) Al₂O₃ and C) CaO (wt%) concentrations.

From the major element diagrams, it is possible to see that the lack of correlation is still present, and regardless of the morphology of the olivine crystal host, the chemical composition of the melt inclusion does not show systematic variations. It is important to clarify that the distinction between melt inclusions that were formed either in the polyhedral core or the dendritic growth was not performed. The analysis from Figure 44 only states that the presence of dendritic growths in polyhedral olivines does not influence the melt inclusions on the interior of the polyhedral core.

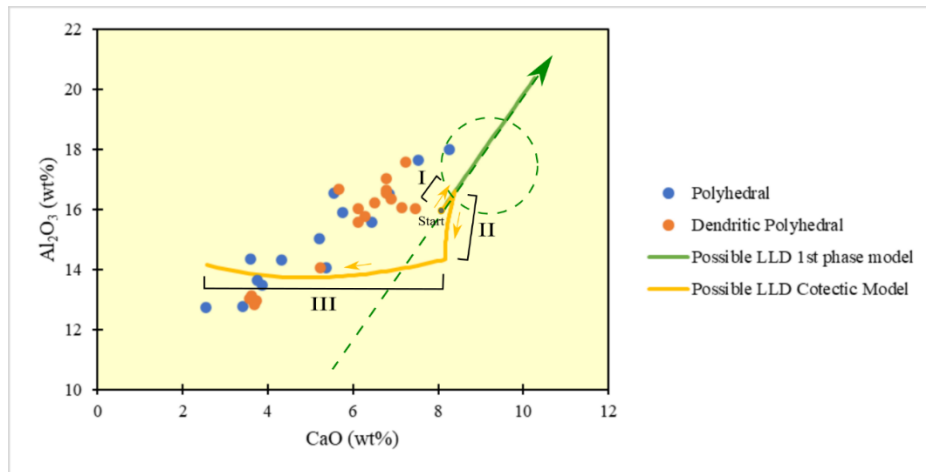


Figure 45: CaO wt % vs Al₂O₃ wt %, liquid line of descent (LLD) of 1st phase model (olivine + spinel) and cotectic model (olivine + plagioclase + clinopyroxene) that could crystallize at the set conditions.

Figure 45 displays two possible liquid lines of descent (LLD), these lines were estimated using the fractional crystallization models where multiple minerals crystallized at different periods of the magmatic evolution (explained in detail in the following section). Particularly these lines are the melt composition as minerals crystallize, the one with more use is the 1st phase model, since in this case only olivine crystallizes along with spinel in the model, the circle indicates the area where the melt composition crystallized olivine with the same Fo% than the olivine host samples from Licto.

The cotectic model (section 3.13) creates a liquid line of descent with 3 clear changes showed as portions, in the I portion the fractional crystallization model only crystallizes olivine, in the II portion it crystallizes olivine and plagioclase, and in the III portion it crystallizes olivine / plagioclase / clinopyroxene. The cotectic option does not allow the user to simultaneously fractionate the three mineral phases from the beginning of the modeling. However, it seems that when the three mineral phases crystallize at the same time the melt composition starts to generate trends more consistent with those observed

in the more evolved products at Licto. Thus, it is possible that true cotectic crystallization of olivine, plagioclase, and clinopyroxene could generate the same observed trend.

Considering that the fractional crystallization models could not perfectly replicate the real chemical trends observed from the olivine-hosted melt inclusions from Licto, the only melt composition that falls near the 1st phase model means that the chemical composition of this inclusion is the one in equilibrium magma. At least for this portion of the magmatic system evolution. This is inferred since CaO and Al₂O₃ are two cations rejected during forsterite growth (Faure & Schiano, 2005).

4.10 Fractional crystallization modeling and melt liquidus association

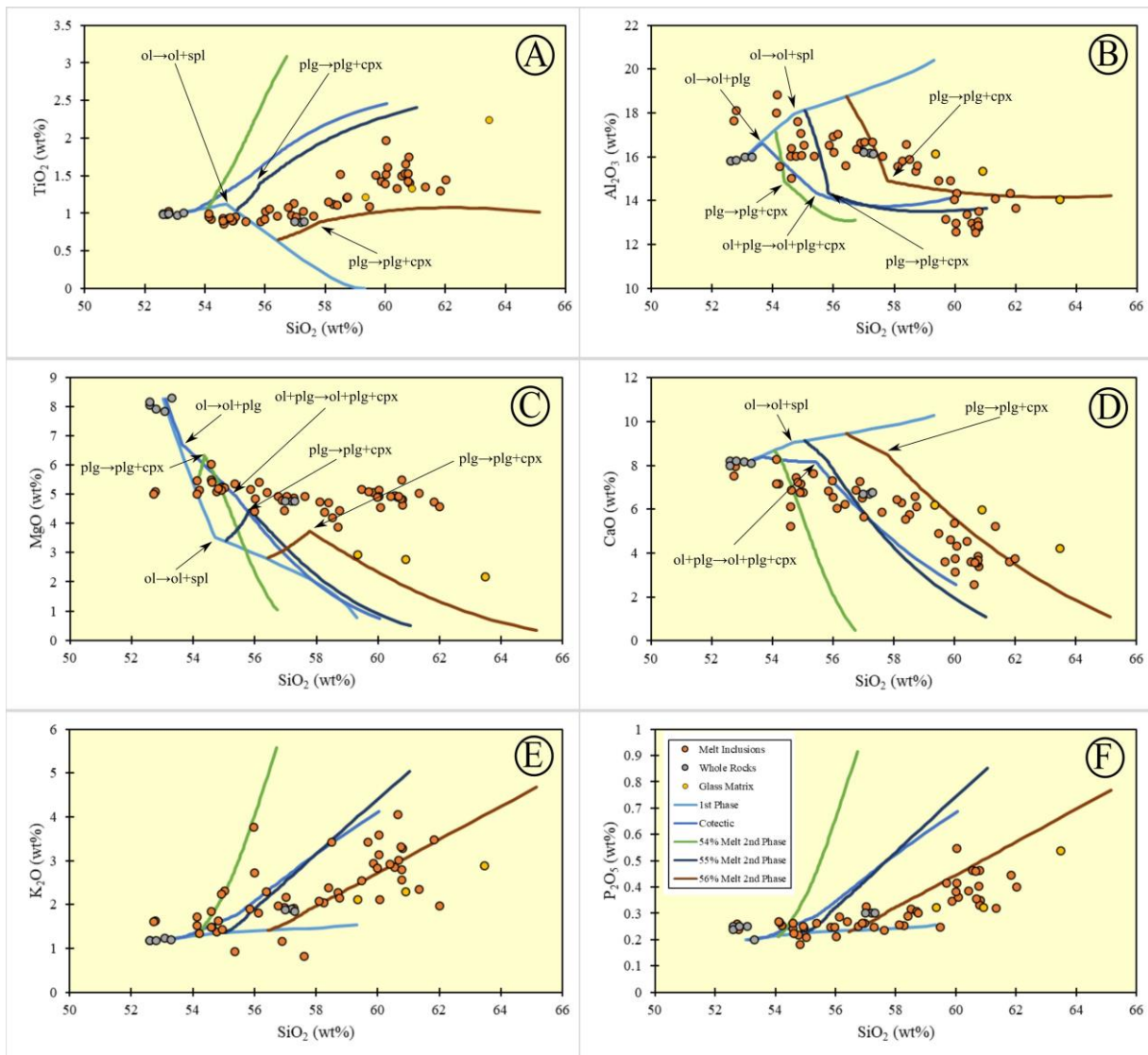


Figure 46: Calculated models of fractional crystallization for major element content plots (wt %) versus SiO₂, PEC and Fe-loss corrected melt inclusions, whole rocks, glass matrix, and fractional crystallization models developed are showed. ol: olivine, spl: spinel, plg: plagioclase, cpx: clinopyroxene

The first phase which assumes crystallization of olivine + spinel causes a depletion of TiO₂ concentration at melt SiO₂ concentration of 54.65 wt%, this probably caused by the crystallization of spinel which according to the model begins at this point, with an estimated temperature of 1052 C°. The cotectic model generates an overall positive correlation with TiO₂ since this element is not significantly incorporated in clinopyroxene or plagioclase and this positive correlation mimics the chemical trend that the melt inclusions create. However, in the cotectic model, TiO₂ starts to be enriched in melt earlier, and this is not the case of the melt inclusion trend. A possible explanation is that plagioclase and clinopyroxene start to crystallize later in the liquid line of descent (melt inclusion trend), so the enrichment in TiO₂ occurs in a more evolved melt composition. Crystallization models that start at different melt compositions generated by the 1st phase model generally cause a positive correlation for TiO₂, except for the 56% SiO₂ melt model, this is caused by only the crystallization of clinopyroxene and plagioclase, which cause enrichment in this chemical species. However, it seems that none of these models fit perfectly with the liquid line of descent defined by the melt inclusions. The best fit for these elements includes a combination of the 1st model until a melt composition of 54.97 wt% SiO₂ and the 2nd phase model that starts at this generated melt (55% melt 2nd phase) (Figure 46/A).

In the case of Al₂O₃ the liquid line of descent shows a depletion in this major element (Figure 46/B), this is possibly caused by the use of this element to crystallize spinel, clinopyroxene and most importantly plagioclase. The 1st phase model, when just olivine crystallizes, will cause an enrichment since olivine does not contain aluminum, it reaches a certain melt composition at around SiO₂ wt % of 55 when the trend bends to a negative correlation, which causes a depletion of this element. This occurs where the models of plagioclase + clinopyroxene creates better fits to the liquid line of descent, in all the 2nd phase cases, specifically the 55% melt 2nd phase, the model generates a clear bend, at around melt composition of SiO₂ wt % of 55.82. This bend is caused because the model only crystallizes plagioclase (conditions for it are met) until this point, then plagioclase and clinopyroxene start to crystallize together. The bend is not clear in the liquid line of descent created by the PEC and Fe-loss corrected melt inclusions, so it is more likely that the magmatic system at Licto crystallized cpx + plg at the same time.

For MgO concentration, 1st phase model and cotectic model generate a rapid depletion (negative correlation) (Figure 46/C), mostly promoted by the continuous crystallization

of olivine. The bend present in both models is caused by the crystallization of spinel, which at least evolved melt could not crystallize at the given conditions. 2nd phase models at the beginning show an enrichment in MgO promoted by only the crystallization of plagioclase (which does not incorporate Mg), then clinopyroxene begins to crystallize causing a change in the trend (negative correlation with a reduced slope).

The cotectic model produces better fits for the CaO variation observed in the liquid line of descent (Figure 46/D), however, this could not be realistic since plagioclase seems to be a later mineral phase based on microscopic observation (large plagioclase phenocrysts are not observed and are only encountered as small microlites or microphenocrysts in the matrix glass) (Figure 47). A depletion of this element is caused by its use in crystallization of clinopyroxene. Depending on the initial composition of the model and model parameters, it seems that clinopyroxene crystallization can be delayed to more evolved melt compositions.

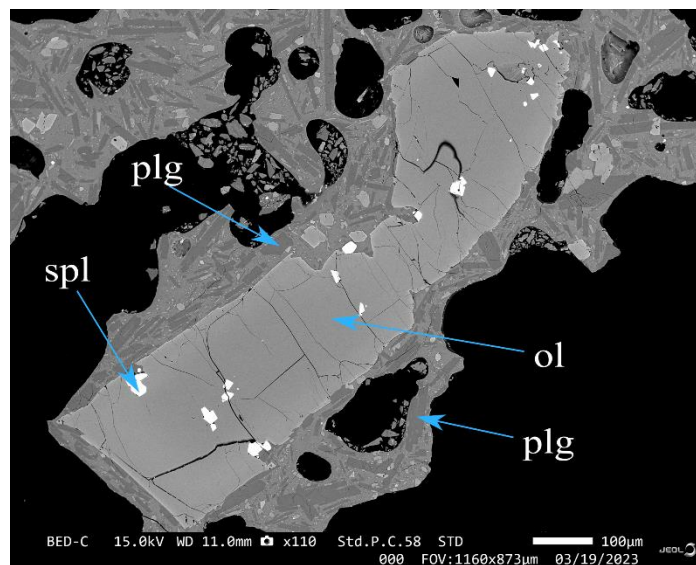


Figure 47: Small microlites or microphenocrysts of plagioclase in the matrix glass of a clast. ol: olivine, spl: spinel, plg: plagioclase, cpx: clinopyroxene

K₂O is also an incompatible element that generally creates a positive trend (enrichment) as melt evolves (Figure 46/E). The different models also produce a trend that reflects enrichment in this element. The main difference between the models and Licto eruptive products is a more rapid enrichment in the models. The difference between the models is caused by the initial melt compositions. This positive trend in the models only appears the moment that plagioclase + clinopyroxene start to crystallize. If these phases never enter into the system, the model remains invariant (1st phase model of olivine + spinel).

The same behavior of the models seen in K_2O are mimicked by P_2O_5 (Figure 46/F). So, the same principles could apply in this case.

In order to ensure that the mathematical models for fractional crystallization can reflect the real magmatic behavior at Licto, comparison between mineral compositions obtained by EMPA (measured compositions), mineral compositions from fractional crystallization modeling, and melt liquidus association are made. 10 results for the EMPA measurements, models, and melt liquids associations are selected to show mineral similarity. The following mineral classification diagrams for olivine, clinopyroxene, and plagioclase were made, along with tables summarizing their values.

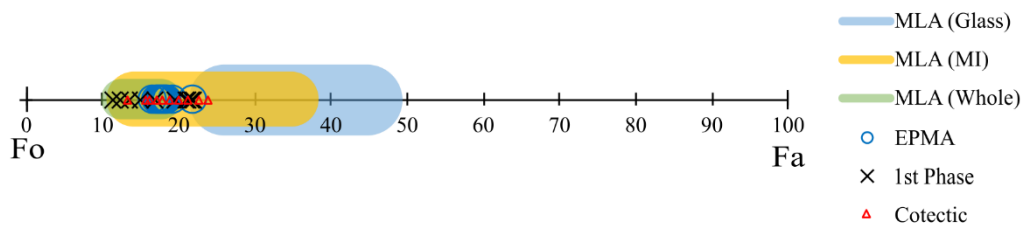


Figure 48: Forsterite % vs Fayalite % for melt liquidus association (MLA) from PEC and Fe-loss corrected melt inclusions, glasses, whole rocks, with results obtained from EMPA and fractional crystallization models. All EPMA olivines correspond to host olivines of melt inclusions.

Olivine	Range Fo %	
	Min.	Max.
EPMA	77.97	83.47
MLA (glass)	55.29	73.99
MLA (MI PEC)	65.28	85.91
MLA (whole rocks)	82.38	87.58
1 st Phase	78.08	88.69
Cotectic	76.11	86.72

Table 5: Range of Fo% values for olivines measured by EPMA, created using melt liquids association with glass compositions (MLA glass), created using melt liquids association with melt inclusions PEC compositions (MLA MI PEC), created using melt liquids association with whole rocks compositions (MLA whole rocks), created using fractional crystallization model 1st Phase, and created using fractional crystallization model cotectic.

Olivine mineral compositions from Melt Liquidus Association (MLA) that have similar chemical compositions to the real sample compositions are generated by the PEC and Fe-loss corrected melt inclusion compositions. Meaning that at equilibrium, using these melt compositions (melt inclusions) olivine minerals observed in the real world can be created. Also, the 1st model and the cotectic model for fractional crystallization can produce olivines with similar chemical compositions as the ones sampled at Licto (Figure 48 and

Table 5). Particularly interesting is that olivines produced by melt liquidus association of the matrix glass are far outside the range of the olivine composition measured in the deposit. Because of this, olivine was unlikely to be crystallizing from the matrix glass prior to the eruption and the olivine cores are out of equilibrium with the residual glasses. The host olivine measured then was either formed from a more primitive magma (in a different part of the magmatic system) or the melt underwent significant fractional crystallization since the olivine formation.

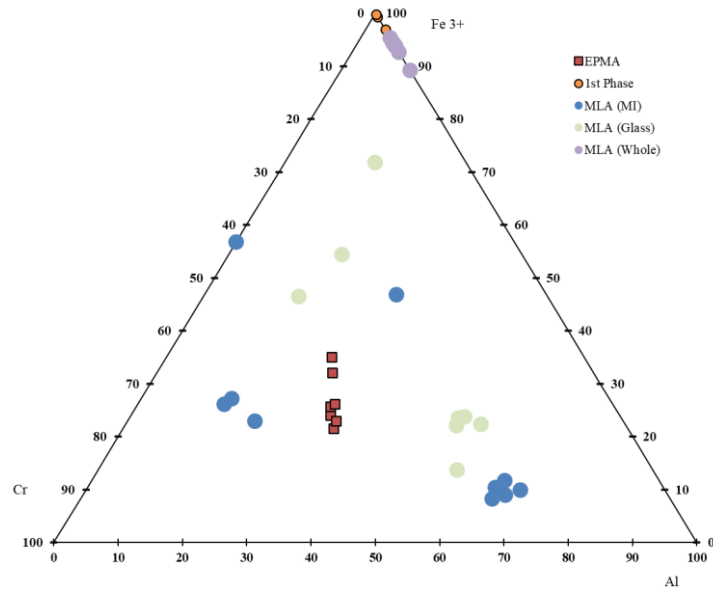


Figure 49: Triangular classification diagram for spinel for melt liquidus association from melt inclusions, glasses, whole rocks, with results obtained from EMPA and fractional crystallization models.

Spinel	Range using Fe ³⁺ as proxy for chemical variation					
	Min.			Max.		
	Fe ³⁺	Al	Cr	Fe ³⁺	Al	Cr
EPMA	21.57	32.74	45.69	35.03	25.36	39.34
MLA (glass)	13.67	55.9	30.44	71.73	14.13	14.14
MLA (MI PEC)	8.18	64.13	27.69	56.71	0.02	43.28
MLA (whole rocks)	89.15	10.85	0	95.31	4.69	0

Table 6: Range of Fe³⁺ values for spinel measured by EPMA, created using melt liquids association with glass compositions (MLA glass), created using melt liquids association with melt inclusions PEC compositions (MLA MI PEC), created using melt liquids association with whole rocks compositions (MLA whole rocks).

In this classification diagram (Figure 49 and Table 6) the sum of the cations more relevant for spinel was assumed to be an approximation of 100% of the mineral composition. Then recalculation for the % of each cation is done. Fe³⁺ is calculated based on the assumption that all cation-sites are full and the mineral has perfect charge balance. Thus, the

proportion of the Fe that is Fe^{3+} can be calculated (based on stoichiometry and charge balance), so if only FeO data is available (Fe^{2+}), estimation of Fe^{3+} can be done. None of the models or melt liquidus association could create a spinel that has similar composition from the samples obtained at Licto. So, it is possible that spinel formed from more primitive magmas. It is possible that none of the available models could replicate the composition of spinel from Licto. Or the spinel found as inclusions come from other sources and were included within the olivine crystal while forming, however the last possibility is unlikely since spinel is abundant and is located within the olivine crystals.

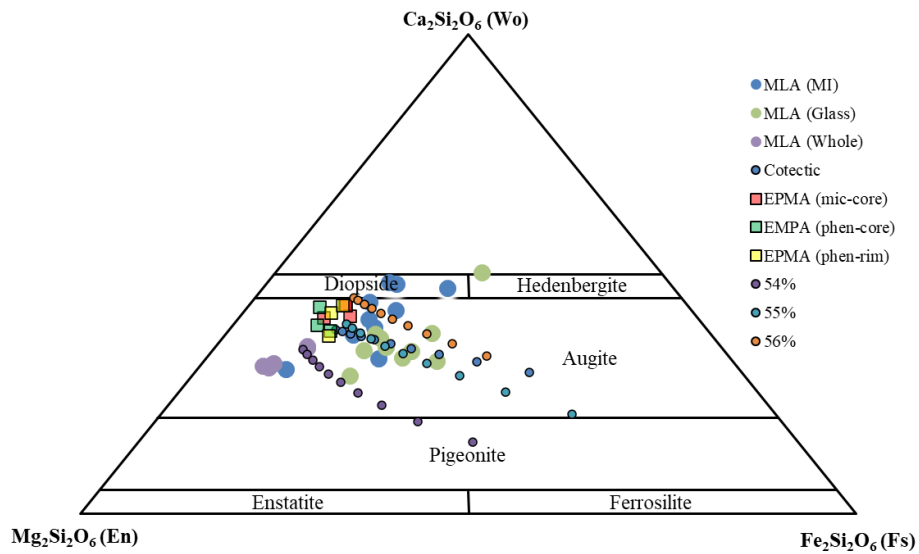


Figure 50: Triangular classification diagram for clinopyroxene for melt liquidus association from melt inclusions, glasses, whole rocks, with results obtained from EMPA (type of material and core/rim measurement) and fractional crystallization models. Mic: microlite sample, Phen: phenocryst sample.

Clinopyroxene	Range using wollastonite as proxy for chemical variation					
	Min.			Max.		
	Wo	En	Fs	Wo	En	Fs
EPMA	37.25	49.35	13.41	43.72	44.08	12.2
MLA (glass)	28.83	50.91	20.27	50.36	23.05	26.59
MLA (MI PEC)	30.23	58.44	11.33	48.31	36.01	15.68
MLA (whole rocks)	30.51	60.44	9.05	35.03	53.25	11.72
Cotectic	29.52	27.41	43.06	38.47	47.8	13.73
54% Model	14.95	41.92	43.13	34.3	54.12	11.58
55% Model	20.82	26.25	52.94	39.64	45.89	14.47
56% Model	32.92	31.12	35.96	45.09	42.94	12.73

Table 7: Range of Wo (wollastonite) values for clinopyroxene measured by EPMA, created using melt liquids association with 1) glass compositions (MLA glass), 2) melt inclusions PEC compositions (MLA MI PEC), 3) whole rocks compositions (MLA whole rocks), 4) fractional crystallization model cotectic, and using fractional crystallization model 54%, 55%, and 56%. En: Enstatite, Fs: Ferrosilite.

The most similar clinopyroxene chemical compositions to the samples encountered in the deposits are created by fractional crystallization models, these are models cotectic/55%/56%. Estimated mineral compositions from melt liquidus association using melt inclusions compositions are also similar to the measured compositions. The initial stages of the fractional crystallization modeling, where the SiO₂ concentration of the melt is less (more primitive), are probably the closest melt compositions that produce equilibrium clinopyroxene similar to the Licto clinopyroxenes. In addition, all the clinopyroxenes measured are Augite (Figure 50 and Table 7).

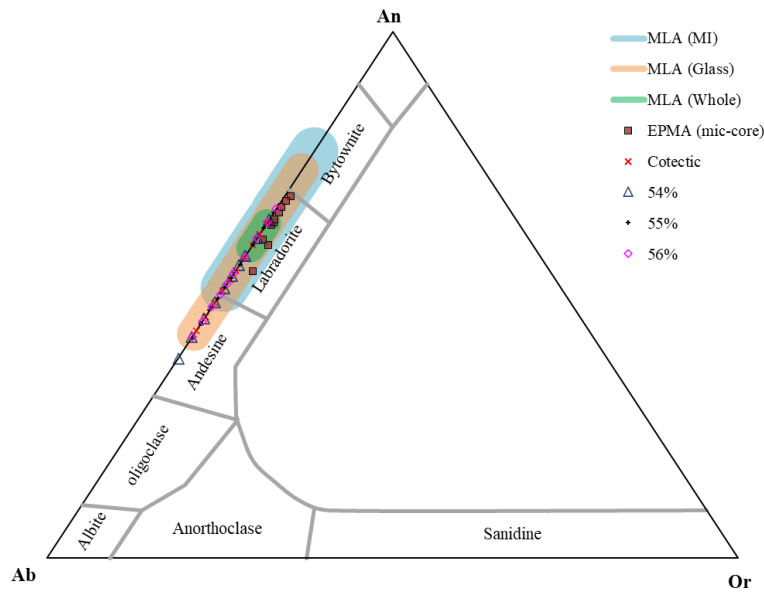


Figure 51: Triangular classification diagram for plagioclase for melt liquidus association from melt inclusions, glasses, whole rocks, with results obtained from EMPA and fractional crystallization models.

Plagioclase	Range using anorthite as proxy for chemical variation					
	Min.			Max.		
	An	Ab	Or	An	Ab	Or
EPMA	54.4	42.93	2.67	68.69	30.3	1
MLA (glass)	42.59	57.41	0	73.65	26.35	0
MLA (MI PEC)	51.3	48.7	0	77.28	22.72	0
MLA (whole rocks)	58.9	41.1	0	63.53	36.57	0
Cotectic	43.15	56.85	0	63.42	36.58	0
54% Model	37.91	62.08	0	64.25	35.75	0
55% Model	41.72	58.28	0	65.57	34.43	0
56% Model	41.96	58.04	0	66.3	33.7	0

Table 8: Range of An (anorthite) values for plagioclase measured by EPMA, created using melt liquids association with glass compositions (MLA glass), created using melt liquids association with melt inclusions PEC compositions (MLA MI PEC), created using melt liquids association with whole rocks compositions (MLA whole rocks), created using fractional crystallization model cotectic, created using fractional crystallization model 54%, created using fractional crystallization model 55%, and created using fractional crystallization model 56%. Ab: Albite, Or: Orthoclase.

The 3 melt liquidus association models can generate plagioclase similar to the real case, also the cotectic/54 %/55 %/56 % models of fractional crystallization can also generate plagioclase of similar composition. For plagioclase, also early stages of the fractional crystallization models, as for clinopyroxene, seems to be the ideal conditions and melt composition to generate the observed plagioclase samples obtained from Licto. The microlite cores measured are mostly labradorite. Melt liquidus association that uses the PEC and Fe-loss corrected melt inclusions produce more mafic plagioclase which are indicated by higher An (anorthite) value, in contrast melt liquidus association that uses matrix glass compositions overlap better with the measured plagioclase samples, this is consistent with the observation that plagioclase is only present as microlites/microphenocrysts, which is an indicative that plagioclase did not co-crystallize with olivine (Figure 51 and Table 8).

4.11 Vesicular analysis

The clasts were classified as dense black (DB clasts), vesiculated black (VB clasts), vesiculated brown (VBr clasts), as shown in Figure 52. These types of clasts were identified in the scoria layer at Tulabug.

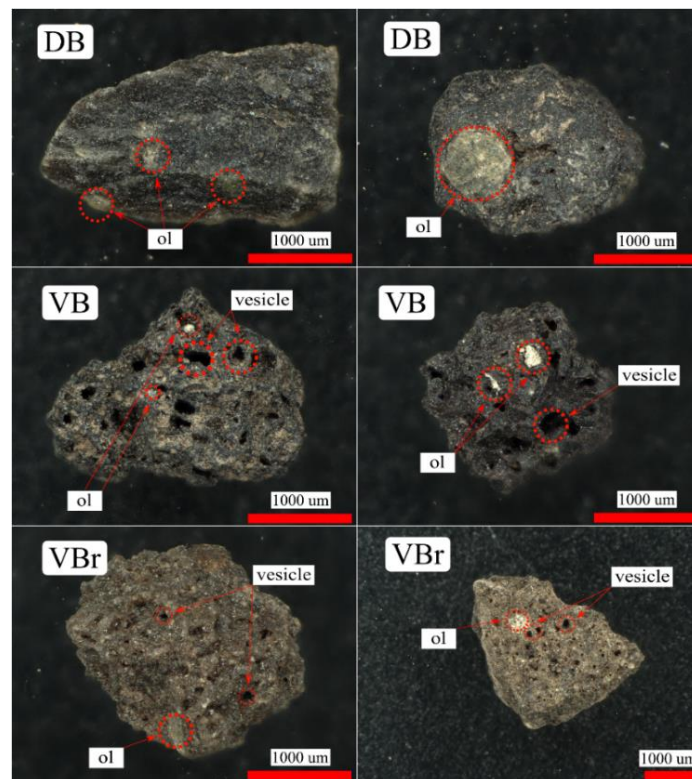


Figure 52: Images from the different clasts from the scoria layer samples at Licto. ol: olivine

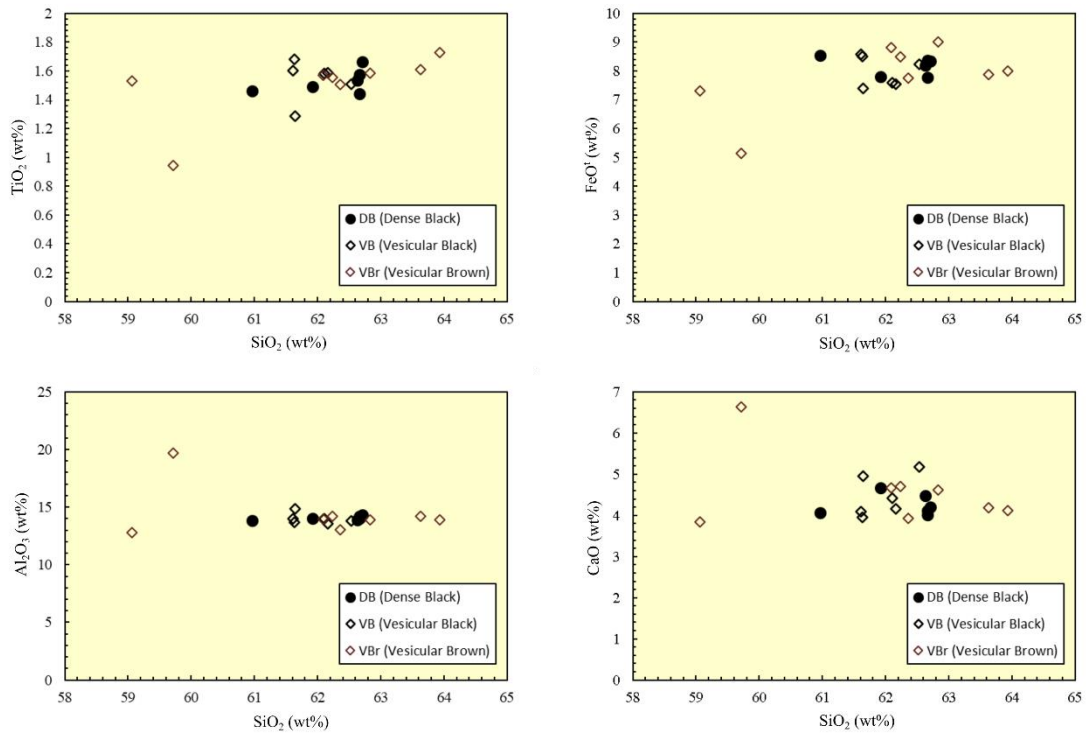


Figure 53: Major element variation diagrams (in wt%) for the different types of scoria clasts.

The diagrams show that there is no clear chemical variability between the different types of pyroclasts (Figure 53). This implies that the variability between the characteristics of each type of clast are probably not related to geochemistry but to other variables.

Each of the samples of clast obtained were subjected to the FOAMS program. The FOAMS program can allow the user to generate relevant plots to decipher the magmatic processes responsible for generating variations in pyroclast vesicle textures. These plots are: simple volume fraction (V_f) size distribution (VVD), cumulative volume fraction size distribution (CVVD), vesicle size distributions in terms of number density (VSD), and vesicle size distributions in terms of cumulative number density (CVSD). Textural characteristics can be displayed in these different plots allowing the user to interpret the different magmatic processes that could lead to these vesicle textures (Shea, Houghton, et al., 2010). As a first approach for the interpretation of the results, a comparison of these different plots created using the FOAMS program of the different types of clasts being studied was made with reference plots of ideal simulations of magmatic processes (Shea, Houghton, et al., 2010) (Figure 54).

The bubble growth and nucleation processes of interest are: continuous/accelerating nucleation and growth, coalescence, and ripening. The first process describes the steady

formation of new bubbles while they become larger in size, the second is the process where bubbles in the melt collide and become larger, and the third is described as steady diffuse transfer of gas between bubbles which is driven by an excess of pressure within bubbles (Mangan & Cashman, 1996). The foam, in this case the magma which would solidify into a clast (ripening), will become coarser and the number of bubbles will decline. In constant volume systems, ripening causes the surface area of the melt-gas interfaces to decrease, and most importantly, some bubbles will shrink as its volatile content is transmitted to other larger bubbles which will grow gradually (Mangan & Cashman, 1996).

VVD plots are used to describe possible nature of nucleation and/or coalescence events that occur during vesiculation and bubble growth upon ascent of magmas from depth to the surface, while VSDs are used to infer kinematics of nucleation density and growth rate of crystals/bubbles (Shea, Houghton, et al., 2010) (Figure 54). All plots created for each of the analyzed samples using FOAMS are included in the appendix (Appendix 3).

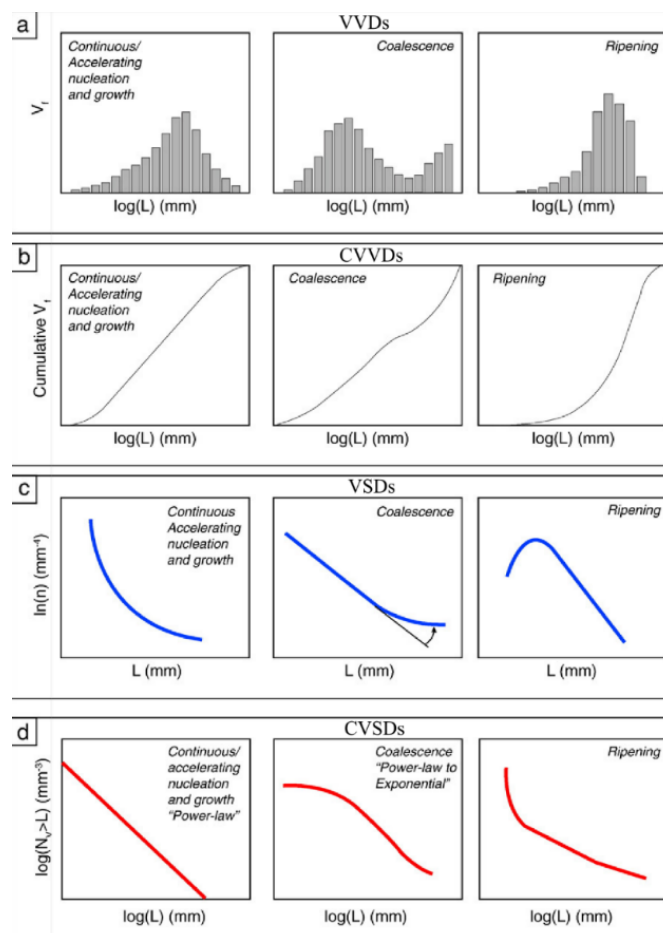


Figure 54: Modified reference diagrams for basic textural vesicle interpretation. (Shea, Houghton, et al., 2010).

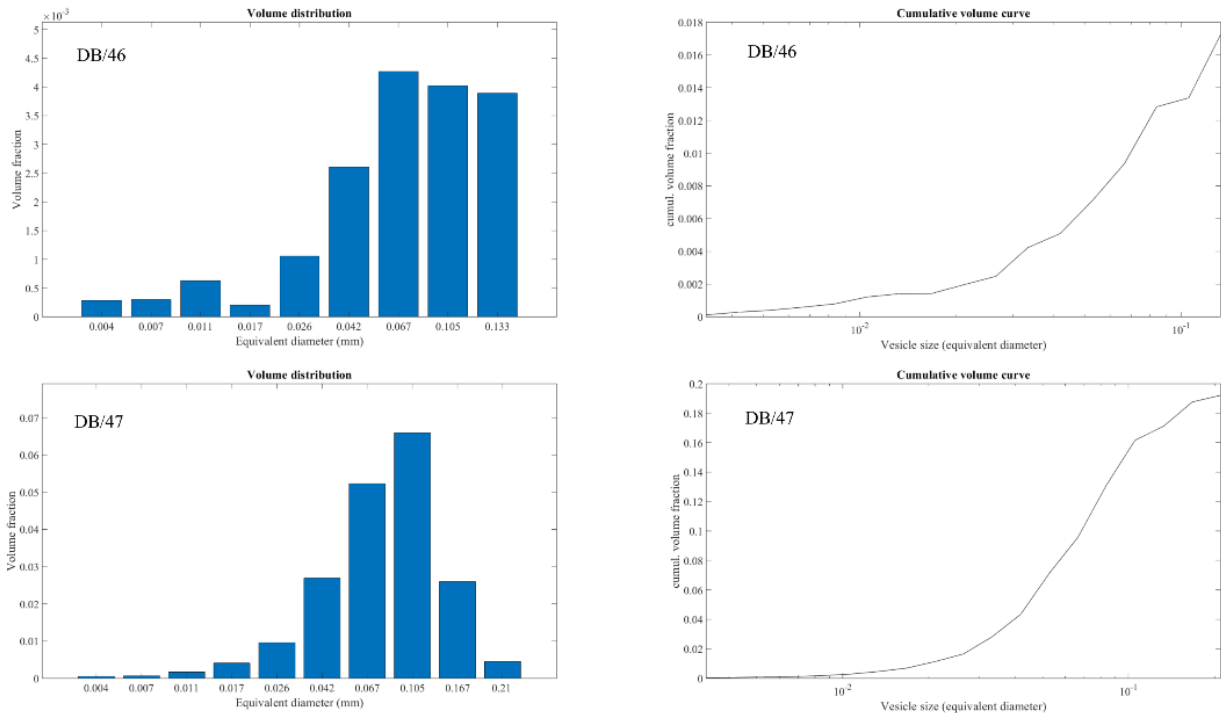


Figure 55: Left: VVD plots for dense black clast samples, Right: CVVD plots for dense black clast samples.

Both VVD plots for DB samples show similarity to a ripening process. In both dense black clasts also CVVD plots show a trend similar to those where ripening was an important process (Figure 55).

However, for the rest of the plots for dense black clasts, VSD and CVSD plots show closer similarity with a coalescence process (Figure 56).

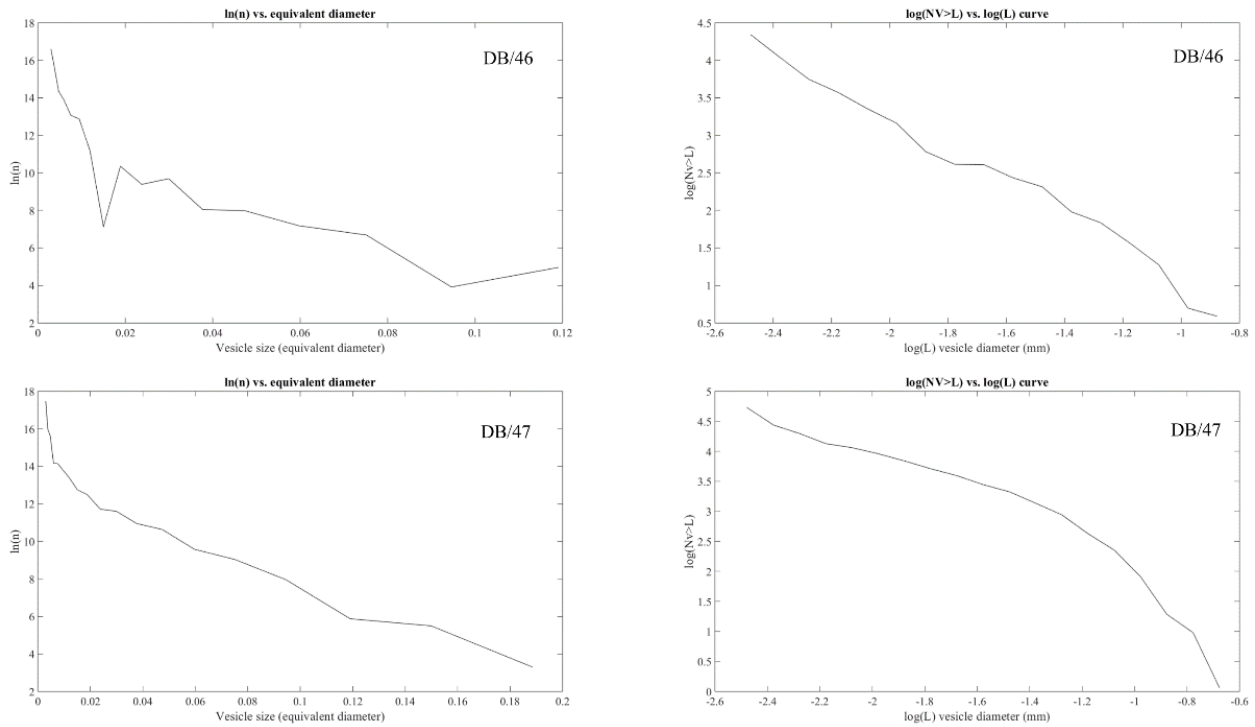


Figure 56: Left: VSD plots for dense black clast samples, Right: CVSD plots for dense black clast samples.

Because in nature, during magmatic ascent, multiple vesiculation and degassing episodes can occur simultaneously, they can overprint each other during the creation of the final texture of the clast. So, it is possible that ripening and coalescence can occur either simultaneously or after/before the other.

The 31 vesicular black sample and 12 vesicular brown sample, show more vesicularity in terms of number of vesicles and size compared to the previous samples (Figure 52). Independent of the color of the clasts, the results appear similar on the VVD plots (Figure 57).

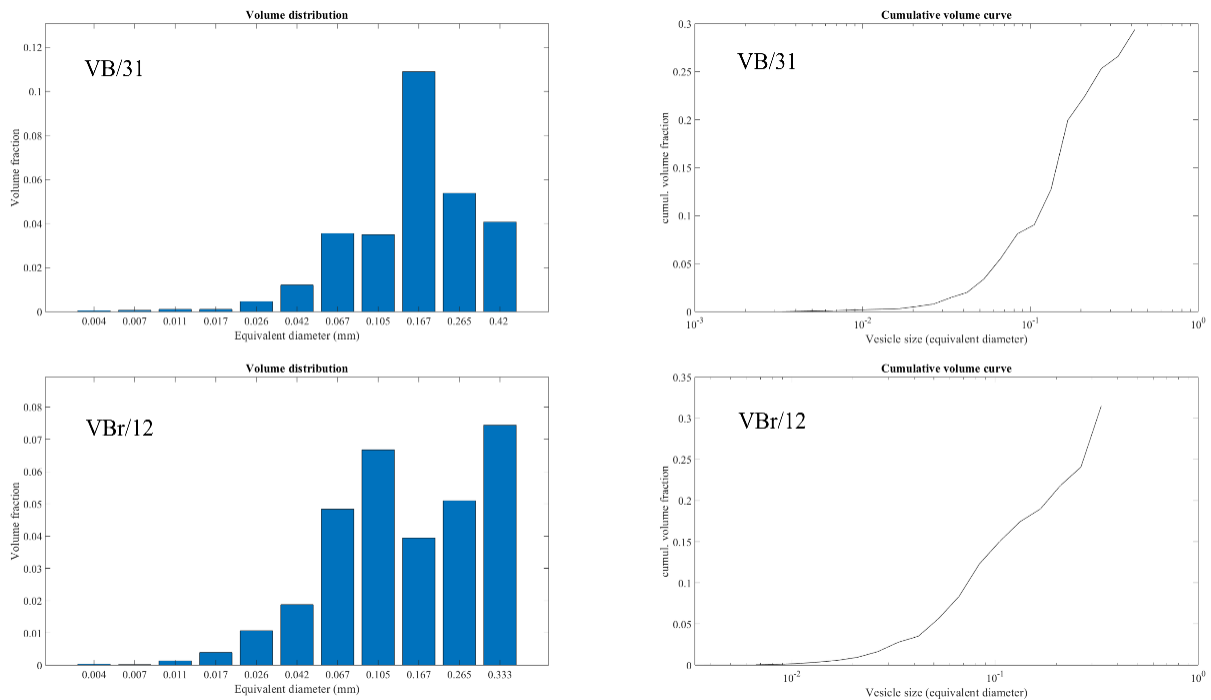


Figure 57: Left: Representative VVD plots for vesicle black and vesicle brown clast samples, Right: CVVD plots for vesicle black and vesicle brown clast samples.

VB/24 (Appendix 3, Figure 57/58) and VBr/12 show a trend that correspond to a process of coalescence, VBr/6 show a trend of ripening, VB/31 have a pattern of possible continuous/accelerating nucleation and growth of bubbles, and for VBr/10 (Appendix 3, Figure 57/58) the trend is not clear, however it can be interpreted as a coalescence process or ripening (Shea, Houghton, et al., 2010). For VB samples it is possible that a process of continuous/accelerating nucleation and growth of bubbles was followed by coalescence at a certain point. For VBr samples, a combination of coalescence with ripening could explain the vesicle textures observed in this pyroclast group.

CVVD plots of vesicular samples show (Figure 58) that for VB, stages of coalescence occur while a general trend of ripening is present. VBr/6 and VBr/10 (Appendix 3, Figure 58) show a trend similar to a process of ripening with stages of coalescence, and VBr/12 a continuous/accelerating nucleation and growth of bubbles with coalescence occurring (Shea, Houghton, et al., 2010).

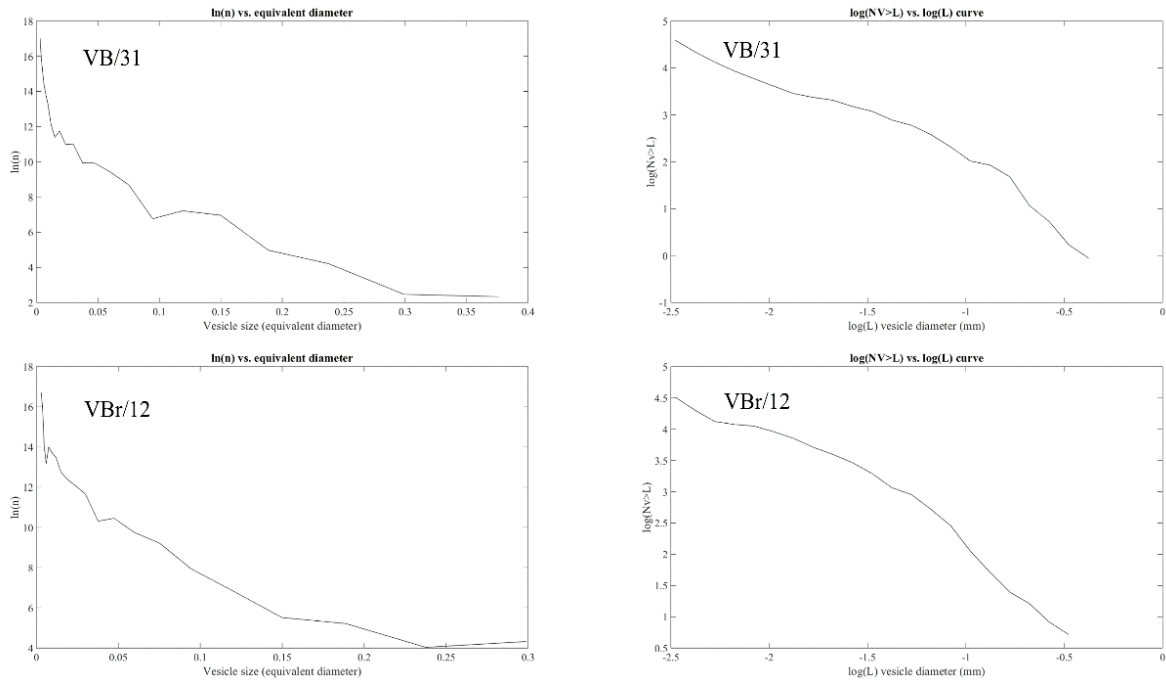


Figure 58: Left: VSD plots for vesicle black and vesicle brown clast samples, Right: CVSD plots for vesicle black and vesicle brown clast samples.

For VSD plots, small ripening stages can be observed in samples VB/24 (Appendix 3, Figure 59), VB/31, and VBr/10 (most clear example) (Appendix 3, Figure 59), coalescence can be observed in samples VB/24, VB/31, VBr/10, VBr/12. VBr/6 (Appendix 3, Figure 59) has the closest trend similar to a continuous/accelerating nucleation and growth of bubbles (Shea, Houghton, et al., 2010) (Figure 58).

Similar observations made using VSD plots can be interpreted from the CVSD plots (Figure 58) (Appendix 3, Figure 60).

4.12 Volume estimations of melt inclusions in polyhedral olivines

Volume estimates for a total of 23 voids from samples used in the nanotomographer were obtained from the grayscale images and the binary extrapolations. The voids appear as circular or irregular shaped black speckles. They likely are either a vapor phase or a melt inclusion. The results are tabulated in Table 9.

Inclusion name	Equivalent diameter (mm)	Equivalent diameter (μm)	Volume (mm^3)	Volume (μm^3)
LS2-MSL-1835-1-2-831	0.0354	35.44	2.3307E-05	23307
LS2-MSL-1835-2-1-785 (1)	0.0711	71.09	1.8812E-04	188115
LS2-MSL-1835-2-1-785 (2)	0.0895	89.50	3.7538E-04	375377
LS2-MSL-1835-2-2-461 (1)	0.0566	56.63	9.5091E-05	95091
LS2-MSL-1835-2-2-461 (2)	0.0898	89.75	3.7853E-04	378531
LS2-MSL-1835-2-3-1680	0.1127	112.67	7.4890E-04	748899
LS2-MSL-1835-2-4-1913 (1)	0.0637	63.73	1.3553E-04	135528
LS2-MSL-1835-2-4-1913 (2)	0.0802	80.24	2.7050E-04	270503
LS2-MSL-1835-3-1-1366 (1)	0.1002	100.24	5.2738E-04	527378
LS2-MSL-1835-3-1-1366 (2)	0.1589	158.87	2.0995E-03	2099541
LS2-MSL-1835-3-1-1366 (3)	0.3170	316.98	1.6676E-02	16676089
LS2-MSL-1835-3-2-1366 (1)	0.1589	158.87	2.0995E-03	2099541
LS2-MSL-1835-3-2-1366 (2)	0.2000	200.00	4.1888E-03	4188790
LS2-MSL-1835-3-2-1366 (3)	0.2518	251.79	8.3582E-03	8358225
LS2-MSL-1835-3-2-1366 (4)	0.3991	399.05	3.3272E-02	33272127
LS2-MSL-1835-4-1-1486	0.2393	239.34	7.1787E-03	7178678
LS2-MSL-1835-5-1-732 (1)	0.1002	100.24	5.2738E-04	527378
LS2-MSL-1835-5-1-732 (2)	0.1262	126.19	1.0521E-03	1052140
LS2-MSL-1835-5-3-1862 (1)	0.2000	200.00	4.1888E-03	4188790
LS2-MSL-1835-5-3-1862 (2)	0.2518	251.79	8.3582E-03	8358225
LS2-MSL-1835-5-3-1862 (3)	0.3170	316.98	1.6676E-02	16676089
LS2-MSL-1835-6-1-1810 (1)	0.1701	170.07	2.5756E-03	2575620
LS2-MSL-1835-6-1-1810 (2)	0.2141	214.10	5.1386E-03	5138645

Table 9: Results of volume estimation of melt inclusions using FOAMS.

The equivalent diameter of the voids (presumed vapor phases) range from 35.44 to 399.05 μm , and the volume range from 23307 to 33272127 μm^3 (Table 9).

From the nanotomographer images (LS2-MSL-1835-1-1-1301, LS2-MSL-1835-3-1-1366, LS2-MSL-1835-5-1-732 (1), LS2-MSL-1835-5-1-732 (2)), 4 ratios of V_b/V_{MI} where possible to construct. In these images a pair of melt inclusion glass with a bubble was possible to be identified with the following results (Table 10).

Inclusion name	Bubble			Glass			V _b /V _{MI}
	Equivalent diameter (mm)	Radius (mm)	Volume (mm ³)	Equivalent diameter (mm)	Radius (mm)	Volume (mm ³)	
LS2-MSL-1835-1-1-1301	0.11321	0.05661	0.00076	0.22589	0.11295	0.00604	0.12588
LS2-MSL-1835-3-1-1366	0.31698	0.15849	0.01668	0.50238	0.25119	0.06639	0.25119
LS2-MSL-1835-5-1-732 (1)	0.07962	0.03981	0.00026	0.12619	0.06310	0.00105	0.25118
LS2-MSL-1835-5-1-732 (2)	0.07962	0.03981	0.00026	0.31698	0.15849	0.01668	0.01585

Table 10: Ratios of volume estimation between glass and associated bubble of melt inclusions using FOAMS.

Bubble equivalent diameter ranges from 0.08 to 0.31 mm with a volume between 0.0003 to 0.01 mm³. Glass equivalent diameter ranges from 0.13 to 0.5 mm with a volume between 0.001 to 0.07 mm³. Ratios range between 0.02 to 0.25 (Table 10).

5. Discussion

5.1 Polyhedral olivine morphology and chemical composition

Because most of the olivine crystals are polyhedral, we will focus on this particular olivine morphology. Melt inclusions have a spherical or elongated shape as seen in glass slides of polyhedral olivine samples, whole crystals in stereomicroscope, and in images taken in the nanotomographer. Polyhedral olivine is defined as a crystal with well-defined or formed faces, whose habit can be equant (the length of each axis that touches with one of the faces of the crystal is equal, $c = a = b$) or tabular ($a \approx c > b$). The polyhedral morphology of these olivines based on previous models of crystal growth in olivines infer that they have been crystallizing under a low cooling rate (Donaldson, 1976). However, these experiments were carried out at ideal conditions and may not reflect the real cooling rate at which Licto olivines formed. Despite this, the implication that the olivines at Licto were formed under slow cooling rates can also be supported by the chemical composition of clinopyroxene which is thought to be a mineral that crystallizes at either the same time or later with olivine at Licto (Mollo et al., 2010). Clinopyroxene crystals that formed at basaltic compositions show that generally as cooling rate increases, the clinopyroxene crystals are continuously depleted in Ca/Mg/Fe⁺²/Si and enriched in Na/Fe³⁺/Al/Ti, which means that clinopyroxene that was formed under slow cooling rates will have higher content in Ca/Mg/Fe⁺²/Si (Mollo et al., 2010). The results of this research show that clinopyroxene with higher content of diopside has slower cooling rates.

The average composition of clinopyroxenes in Licto has a diopside % of 97.31, then supporting the idea of slow cooling for the formation of minerals at Licto. It is likely that this is not perfectly representative of the natural conditions at Licto since the study of Mollo et al. (2010) was performed with basaltic magmas, and products at Licto have either a basaltic/andesite or andesite composition. Other effects like water content and pressure should also be considered (Mollo et al., 2010) and these parameters are currently poorly constrained. Mollo et al. (2010) also demonstrated that clinopyroxene composition can be used to fit a mathematical model and estimate cooling rate. Assuming this model is viable for Licto, possible cooling rate estimated from clinopyroxene phenocrysts at Licto is of 0.17 °C/min or 10.38 °C/hour (Mollo et al., 2010).

Polyhedral olivine in magmatic ascent studies is represented by featureless surfaces in the crystal while maintaining well developed crystal faces (Jones et al., 2014). Particularly these surfaces are developed under free growth conditions from the melt, meaning that olivine grows mainly without obstructions and directly from a melt (Jones et al., 2014). These features cannot be observed with great detail with the morphological results of the Licto olivine samples, however due to the shape of the olivines it is possible that olivines were formed under free growth conditions prior to the eruption of the scoria and deposition.

Particularly, the chemical composition of the olivines at Licto and the spinel compositions may contribute to understand certain magmatic processes that lead to the deposition of the scoria cones at Licto. Research at monogenetic volcanic fields show that the products of volcanic eruptions can have a simple or more complex petrography. The cases of interest are volcanic fields that have a simple phenocryst assemblage like olivine \pm clinopyroxene with occasionally the presence of xenolith + xenocrysts (Jankovics et al., 2019). The scoria samples taken at Licto for this study show a fairly simple phenocryst assemblage within the clasts which is olivine \pm clinopyroxene \pm plagioclase and spinel as inclusions in the olivine crystals. Similarly, previous studies of lavas at Licto also showed an assemblage of olivine + orthopyroxene + plagioclase (D. F. Narváez et al., 2023). The Fekete-hegy volcanic complex (Jankovics et al., 2019) shares some similarities to that of Licto regarding volcanic deposits characteristics, however there are also differences. The volcanic complex is located in the north-eastern portion of the Alpine-Mediterranean region (Carpathians arcuate orogenic belt and the Pannonian Basin), the basin has a thin lithosphere and crust between 50-80 km and 22-30 km respectively (caused by a syn-rift phase), the post-rift phase was characterized by a thermal subsidence, the thickening of the crust, and fast sedimentation. The neotectonics is characterized by tectonic inversion (causing folding) due to the movement of the Adriatic microplate (Jankovics et al., 2019). At the Fekete-hegy volcanic complex, an eruptive stage generated lava flows followed by the formation of scoria cones. In this case, the volcanic material was lavas/scoria and was basaltic in composition and the products contained a simple phenocryst assemblage (Jankovics et al., 2019). Licto also has lavas topped by scoria at the base of the edifice and the products have relatively simple mineral assemblages. The only difference being that Licto is predominately basaltic andesite/andesite (Jankovics et al., 2019).

Based only in this comparison, and similarity of phenocryst assemblage it is possible that Licto had a stage of lava effusion, followed by a stage of activity that formed the scoria cones with explosive eruptions based on the stratigraphy sequence observed at Licto (Figure 9). This last idea is speculation and will require further investigation. Continuing the comparison with the same case study at Fekete-hegy, the scoria samples of the cones at this setting show medium-highly vesicular, porphyritic textures that mainly contain olivines, and less abundant plagioclase and clinopyroxene (Jankovics et al., 2019). The last characteristic is very typical in monogenetic/polygenetic small volume basaltic cones (Hoffer et al., 2008; Ruscitto et al., 2010). The scoria samples at Licto have almost identical characteristics as the case that is under comparison, this can lead to a more significant idea that similar magmatic processes affecting Fekete-hegy could apply for Licto. Not only the textural characteristics and mineral assemblages but the texture, zoning, and composition of olivines are similar for the case of Fekete-hegy and Licto.

Olivines at Fekete-hegy are simple and uniform with a Fo% of approximately 78 – 85, with similar compositions between each sample (Jankovics et al., 2019). The olivines used in this study are generally uniform with a clear polyhedral morphology and a Fo% between 77.97 to 83.47. Normal zoning of olivines, meaning a general gradual decrease from core to rim of Fo% and Ni (Figure 35), and increasing Ca and Mn are found in the sample analyzed at Licto. Similarly, the scoria samples at Fekete-hegy cones show normal zoning (Jankovics et al., 2019). Furthermore, spinel also can be used to infer magmatic processes, in Fekete-hegy spinel is encountered as inclusions in olivine, with a short range in chemical composition (Jankovics et al., 2019). Spinel is found similarly as inclusions in the olivine samples at Licto, the compositional range is 57.94 – 60.55 Cr# and 1.49 – 2.69 wt.% TiO₂, which also is a restricted range of compositions. The characteristic of normal zoning in olivine along with the small range of composition of spinel inclusions indicates that olivine was created during normal fractional crystallization trend (Jankovics et al., 2019). This normal trend generally suggest that simple/close-system fractional crystallization of olivine + spinel may have occurred in the magmas that later fed the explosive/effusive eruptions at Licto. The formation of a magma accumulation zone that experiences simple fractional crystallization is likely. Furthermore, the melt inclusion data measured and analyzed in this study probe that fractional crystallization was fundamental (Figure 46) (Jankovics et al., 2019).

Olivine geochemical and isotopic compositions have been used to determine the possible mantle source material of basaltic rocks, which in some cases could be peridotitic or pyroxenetic (Cao et al., 2022). As a general rule it has been shown that high concentrations of Ni and low concentrations Ca-Mn in olivine correspond to the melting of pyroxenitic mantle that did not have olivines in it.

However, this should not be applied directly since variations in these concentrations can depend on the bulk partition coefficients and these can change during mantle melting depending on temperature and pressure (Li & Ripley, 2010; Matzen et al., 2013, 2017; K. Putirka et al., 2011; Wang & Gaetani, 2008). This implies that depending on these variables the peridotitic mantle can reflect similar concentrations of Ni and Ca-Mn (Cao et al., 2022). Furthermore, not only the chemical composition of olivines can help to infer the possible source magma, but magmatic processes can leave a chemical footprint. For example, the chemical compositions of olivines can vary depending if fractional crystallization, magma mixing or diffusive re-equilibration is the dominant process leading to these variations. Thus, the olivines that crystallized directly from the mantle source when melted can change as a result of these processes (Cao et al., 2022).

By comparing the fractional crystallization models for olivine using Petrolog and the actual olivine compositions measured using EMPA in Licto it is possible to infer if other magmatic processes could have affected the chemical composition of olivines.

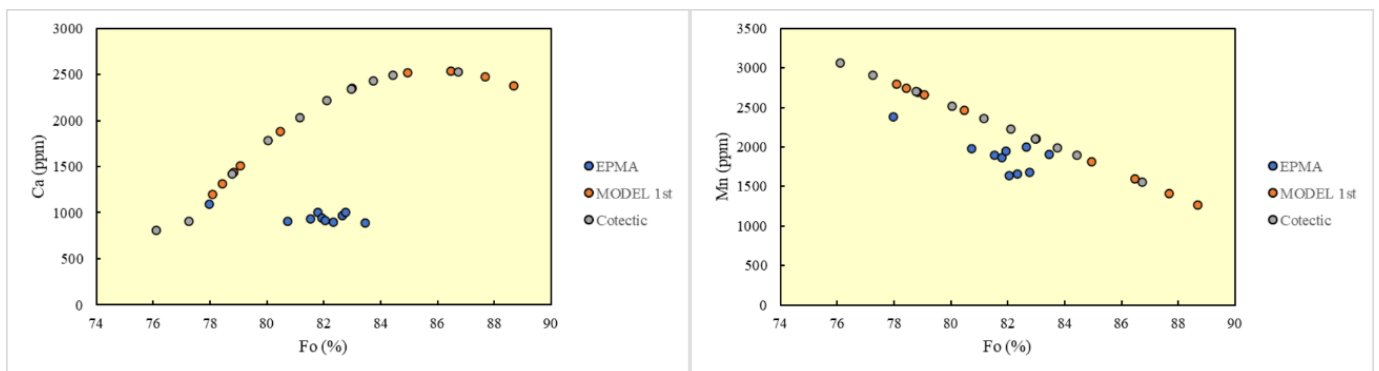


Figure 59: Left: Fo % vs Ca (ppm) of selected olivines measured by EMPA and estimated chemical compositions using mathematical models, Right: Fo % vs Mn (ppm) of selected olivines measured by EMPA and estimated chemical compositions using mathematical models.

Fractional crystallization models create olivines with higher concentration of Ca and lower concentration of Mn (Figure 59). While in previous studies (Cao et al., 2022) it has been established that lower concentration of Ca in the natural olivines compared to the olivines generated using mathematical models is a sign that other magmatic processes

have affected the composition of olivines other than fractional crystallization alone. Another requirement is that the natural olivines need to have a higher concentration of Mn (Cao et al., 2022). In our case, the olivines measured have lower Ca and Mn compared to the fractional crystallization models. This implies that other processes are operating in addition to fractional crystallization, like magma mixing (Figure 59). A way to ensure that magma mixing occurred is by analyzing the melt inclusion compositions in olivines, because these can record magma mixing processes occurring in magma chambers at higher depths. This was assessed in the melt inclusions analysis in the present study but it was unclear. However, it was demonstrated by olivine zoning analysis (Cao et al., 2022).

The composition of the melt inclusions analyzed in our study fall mainly within the high-k calc-alkaline series and the calc-alkaline series (Figure 40), while the lava samples that also contain olivines from the literature are only calc-alkaline. The greater heterogeneity observed in the melt inclusion compositions could indicate that the basaltic andesites and andesites at Licto could have undergone magma mixing processes in the magma chamber before the eruption occurred (Cao et al., 2022), and the olivines entrapped melt at various stages of the mixing process.

It is established that Ni, Mn, and Ca concentrations in olivine can be used to determine the possible mantle sources that create the magma which eventually olivine will crystallize from. These elements need to be used as a first approach of the possible mantle source, since crustal processes can also affect the olivine compositions (Cao et al., 2022; Sobolev et al., 2007).

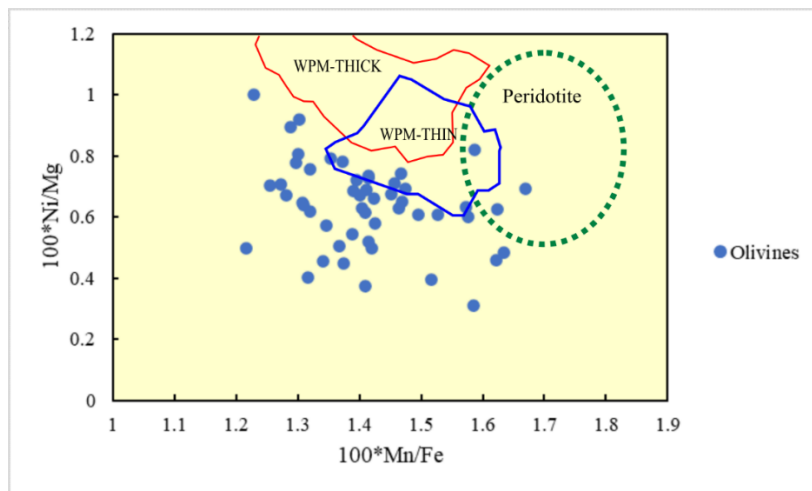


Figure 60: Mn/Fe vs Ni/Mg ratios of EMPA measured olivine compositions compared to olivines created under different tectonic settings and parental source.

Figure 60 was developed by using olivine measurements from a selection of tectonic settings (Sobolev et al., 2007). Pyroxenite can be a mantle source for magmas in subduction zones. This particular source is formed by the melting of oceanic crust at high pressure which then reacts with peridotite producing olivine-free pyroxenite (Sobolev et al., 2007). Melts that are created by pyroxenite are depleted in Mg, Ca and Mn and enriched Si and Ni compared to melts derived from peridotite. This difference occurs because in peridotite, olivine controls the composition of the melt, while pyroxene controls the composition in pyroxenite (Sobolev et al., 2007) and these two minerals have different melting behaviors during partial melting.

Based on these observations, it is possible to see if the olivines that have a certain olivine composition could have crystallized from a specific magma source. This is done by the comparison of the samples of olivine at Licto with other samples with known geological tectonic setting and mantle source rocks. Theoretical olivines crystallized from a peridotite magma source can occur within the green-dashed ellipse on Figure 60. Also, olivines from mafic rocks observed away from tectonic plate boundaries or “within” the interior of the plate, were used to create compositional fields that encompass olivines derived from mantle sources in these environments. WPM are determined as within plate magmas, these are rock samples encounter at these locations that have olivines with a particular chemical composition, THIN as ocean island basalts emplaced over thin lithosphere (<70 km thick), and THICK as ocean island basalts and large igneous provinces emplaced over thick lithosphere (>70 km thick) (Sobolev et al., 2007) The proposed pyroxenite source area is not included in the graph (high values of $100 \cdot \text{Ni}/\text{Mg}$ and low values of $100 \cdot \text{Mn}/\text{Fe}$) since none of the measured samples of olivine had these chemical proportions.. The data from olivines are plotted as ratios of Mn/Fe and Ni/Mg since these ratios show no significant variation during olivine fractionation. So, it is more likely that this data will reflect the possible rock source of the magma (Sobolev et al., 2007). Recycled oceanic crust and its interactions with other materials during melting and ascending (in subduction zones) are also described in Sobolev’s work. This is important because Licto magma most certainly had undergone this process, and the graphs described in here also take into account this tectonic setting. Figure 60 shows that the vast majority of olivines used in our study in Licto are not compatible with a peridotite source of magma. Samples that do not fall exactly at determined areas of peridotite or pyroxenite could be related to a binary mixture between peridotite and pyroxenite (Sobolev et al.,

2007). This model assumes that the recycled crust did not fully mix with peridotite during subduction and mantle convection so the olivine free lithology could form. However, the homogenization of the crust material with the peridotite in the mantle can create ultramafic lithologies that have variable amounts of olivine. This seems to be the case for the melt source at Licto since they do not fall in a complete pyroxenite or peridotite source (Sobolev et al., 2007). Another possibility described in Sobolev's work is that in subduction, oceanic crust material (basalts and gabbros) is transformed into eclogite with a free SiO₂ phase. The free SiO₂ phase will be relevant during recycling of the upper mantle because it can create a high silica melt. This melt reacts with peridotite (olivine portion) which produces pyroxenes and garnet, the final product will be a refertilized peridotite enriched in pyroxene (Sobolev et al., 2007). This last explained interaction can lead to variable mixing proportions of eclogite/high-Si melt/peridotite which can be the source of melt at Licto since the olivines generated do not fall in an exclusive peridotite or pyroxenite source. However, the inferred magma source requires more studies specially regarding trace elements to confirm the proposed source rock magma in Licto. Meanwhile, these are working hypotheses as their resolution requires further trace element and isotope analysis.

As it was estimated based on the chemical composition of clinopyroxenes, which were formed at the same time as olivines, the estimated cooling rate was 0.17 °C/min or 10.38 °C/hour. This slow cooling rate could be related to a simple close-system magmatic chamber, where olivines crystallized at slow cooling rate allowing the formation of mainly polyhedral morphologies. The degree of undercooling also has shown a direct relationship with olivine morphology in experimental studies. A small degree of undercooling is related with equant habits in olivine phenocrysts (Donaldson, 1976). To understand this, a small degree of undercooling means that the difference in temperature between the liquidus (boundary that separates the liquid phase and the olivine + melt) and the temperature when crystallization starts is small. The size of the crystal along the b axis also changes with cooling rate variation and degree of undercooling. The size of the crystal along the b axis decreases normally with an increase in cooling rate and degree of undercooling. Based on these general properties, olivine morphology varies depending on the cooling rate and degree of undercooling. Thus, it is possible to assume that the polyhedral olivine crystals that were analyzed form at a slow cooling rate, and also from a small degree of undercooling, since we obtained a slow cooling rate from

clinopyroxenes and experimental results show that undercooling also is low at this cooling rate (Donaldson, 1976). A low degree of undercooling will mean for olivine that as soon as crystallization of olivine temperatures are reach, crystallization starts rapidly so the equilibrium temperature at which olivines crystallizes is almost the same as the actual temperature at which olivine solidifies. The possible implications of this are that at low degrees of undercooling, olivine has an equilibrium composition. This means that the chemical composition of the olivine is similar to those expected from thermodynamic equilibrium calculations, or in other words, that olivine crystals form under conditions where the melt composition is in equilibrium with the crystal composition. To illustrate the conditions that lead to the polyhedral olivine morphology to form at ideal conditions, the next diagram develop by Faure et al. (2003) is used to determine the general conditions of cooling rate and undercooling, where our values of slow cooling rate will have a relationship with low undercooling values (Figure 61).

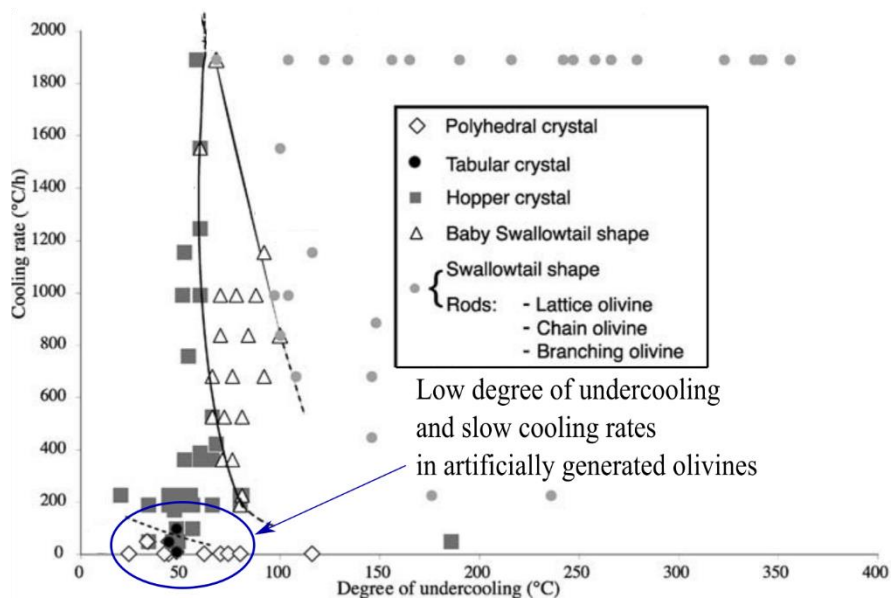


Figure 61: Modified image where ideal conditions olivines were created under specific conditions of degree of undercooling and cooling rate (Faure et al., 2003).

5.2 Melt inclusions morphology and chemical analysis

The morphology of melt inclusions along with its geometry can be used to establish details of the magmatic behavior in which they were formed. The ratios of bubble volume and melt inclusions glass vary between 0.02 to 0.25. The vapor bubbles based on this ratio can range from shrinkage bubbles (V_b/V_{MI} between 0.2 to 5) to bubbles with higher inclusion volumes ($V_b/V_{MI} > 5$) which in order to form require additional post-entrapment

processes (Gennaro et al., 2018; Lowenstern, 1995). In sample LS2-MSL-1835-1/1301 (Figure 21) the V_b/V_{MI} ratio is 0.13. Bubbles with this ratio could imply that the olivine crystal suffer post-entrapment mechanisms (like rapid decompression), thermal shock (cracking of the host) or depressurization-vesiculation (Gennaro et al., 2018; Lowenstern, 1995). Larger volume ratios also could be created due to the simultaneous entrapment of melt and a different vapor/fluid phase (Gennaro et al., 2018; Lowenstern, 1995).

In sample LS2-MSL-1835-3-1/1366 (Figure 62) the V_b/V_{MI} ratio of volume is 0.25. Again, the explained procedures could have affected this olivine crystal.

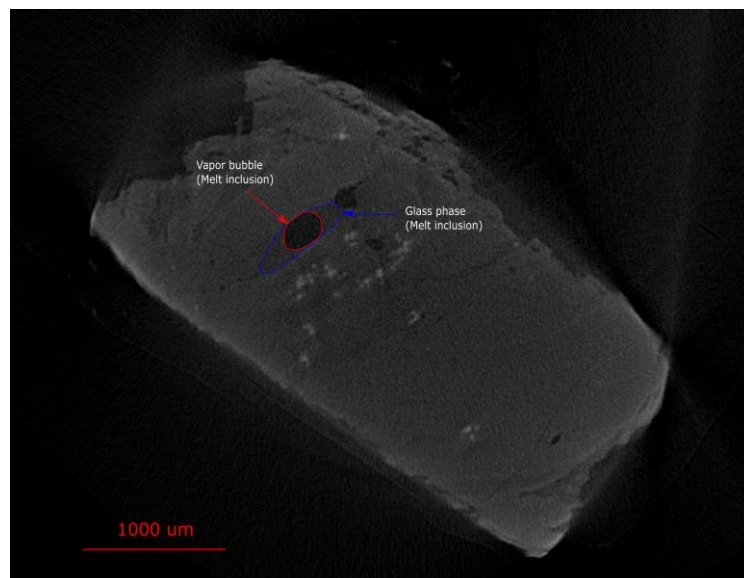


Figure 62: Section taken from the nanotomographer of one olivine crystal, a larger bubble is seen compared to its associated glass phase.

The larger glass phase with the bubble (Figure 63) creates a ratio of 0.02. In this case, the bubbles are called shrinkage, the other pair of glass/bubbles again falls within the later description.

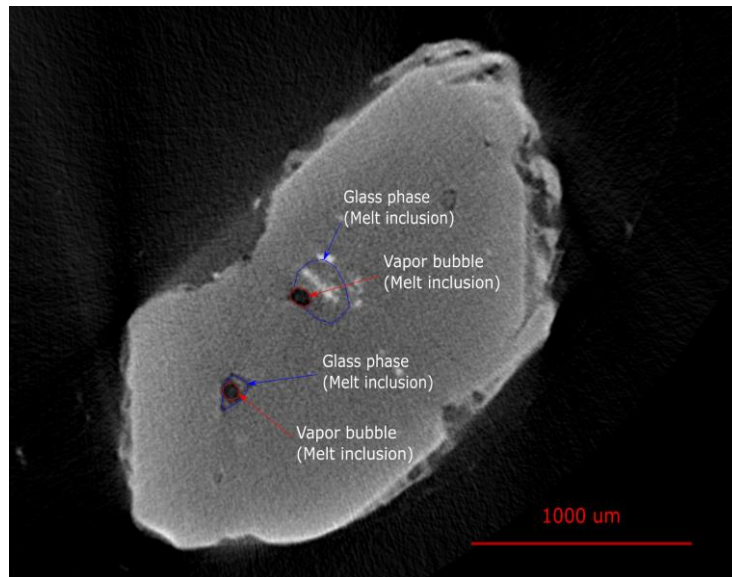


Figure 63: Section taken from the nanotomographer of one olivine crystal, smaller bubbles compared to its associated glass phase.

Melt inclusions that have similar vapor/melt ratios usually will have similar origins, or the melt inclusions are formed at the same time in a particular magmatic stage (Lowenstern, 1995). From these results, it is likely that all the melt inclusions from these polyhedral olivines share the same origin. However, the last ratio ($V_b/V_{MI} = 0.02$) is different compared to the other (melt inclusion with shrinkage bubble, $V_b/V_{MI} = 0.13$ or 0.25). Either the melt inclusion in this case had a different origin or there is some erroneous interpretation. A larger bubble also can be interpreted to be formed in a volatile rich magmatic system (Frezzotti, 2001). So, it is possible that the olivines formed at Licto were formed in a magma rich in volatiles which are reflected in the size of the bubbles. The presence of small and large ratios of V_b/V_{MI} in a single olivine crystal could mean that the magma evolved, at a certain stage had more volatiles, then it was depleted in them, since shrinkage bubbles are common in volatile poor magmas (Frezzotti, 2001).

The polyhedral morphology and the shape of the inclusions in the olivines observed have also other implications related to thermodynamic processes, especially the idea that particularly these inclusions contain melts that are in thermodynamic equilibrium with their host minerals (Faure & Schiano, 2005).

The various images obtained from the nanotomographer and BSE images show that from the identifiable olivines (52 host olivines), 47% are polyhedral and 53% are dendritic polyhedral. It is found that the shape of experimentally entrapped melt inclusions can be spherical/subspherical/void. However irregular curvilinear shapes also can be observed.

In our case, the shape of the melt inclusions is mostly irregular with curvilinear shapes. But in some instances, it is possible to see spherical inclusions, confirming the relationship between polyhedral olivines and the usual melt inclusions morphologies (Figure 64).

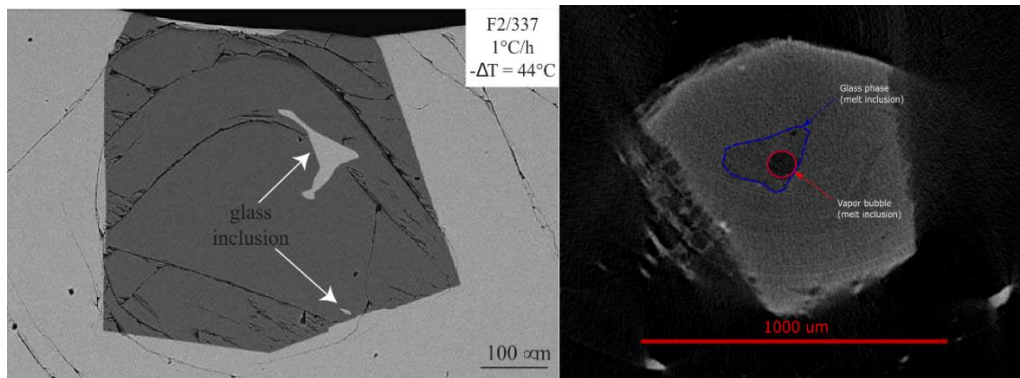


Figure 64: Comparison between melt inclusions from artificially created polyhedral olivines (left) and melt inclusions observed in olivine samples at Licto (right) (Faure & Schiano, 2005).

The size is highly variable from 126 – 502 μm in diameter from the samples measured in the nanotomographer, this is the same as experimental results. On the other hand, the diameter of the melt inclusions are higher in the Licto samples compared to experimental results. This suggests that other processes are possibly affecting the size of the inclusions (Faure & Schiano, 2005). The idea that melt inclusions compositions are independent from their host crystal morphology could mean that minerals other than olivine co-crystallized at later stages in the magmatic evolution. This is seen in the CaO vs Al₂O₃ diagrams of melt inclusions composition regarding host morphology (Figure 45). Melt inclusion compositions that fall near the liquid lines of descent in Figure 45 mean that they are in equilibrium with the olivines crystallized in these fractional crystallization models (Faure & Schiano, 2005).

In the case of observed dendritic polyhedral olivines, laboratory experiments in ideal conditions have shown that an initial low cooling rate followed by a high cooling rate is necessary to form this type of morphology (Faure & Schiano, 2005). The presence of dendritic polyhedral olivines in Licto analyzed in this study can be a product of an increase in the cooling rate of the magmatic system. An increase in cooling rate can happen due to magma mixing which has been proven to be a magmatic process that occurred in Licto.

It was estimated that indeed a low cooling rate could have formed the olivines (polyhedral) and overall mineral phases encountered in some of the samples, the possible explanation for a sudden/short increase in the cooling rate could be related to the mixing episode. Mixing increased the cooling rate and olivines began to form dendritic morphologies (dendritic polyhedral). Other possibilities are contact with a cold medium such as cold country rock, rapid ascent, mixing of two thermally contrasting magmas or volatile loss. In the case of dendritic polyhedral morphologies (created during faster cooling rates), it is expected that the chemical compositions of their melt inclusions do not fall within the liquid line of descent and they are enriched in Al_2O_3 (Figure 65), this is due the presence of a boundary layer (change in growth mechanism) (Faure & Schiano, 2005).

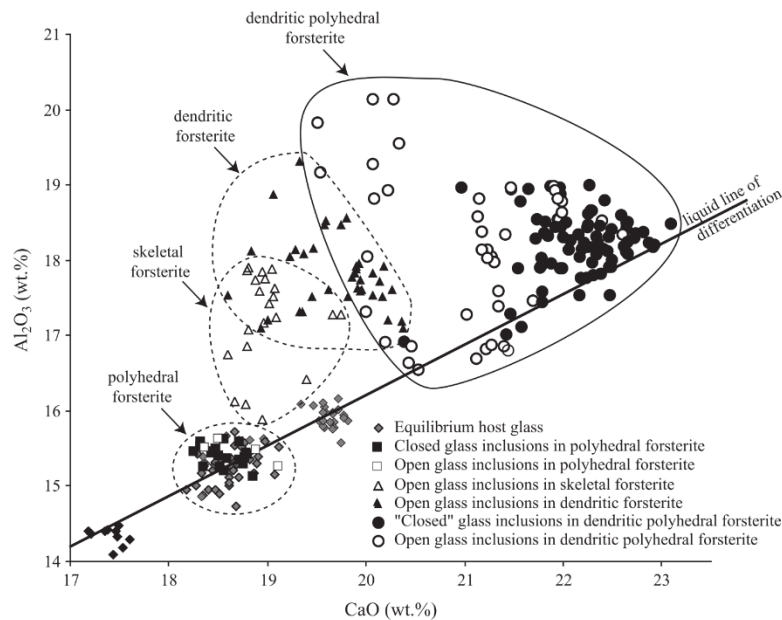


Figure 65: Plot of CaO vs Al_2O_3 of melt inclusions compositions from specific morphology olivines created in ideal conditions (Faure & Schiano, 2005).

In our case there is enrichment in Al_2O_3 for both polyhedral and dendritic polyhedral melt inclusions and also the compositions do not fall near the liquid line of descent (Figure 45). Although the characteristics for dendritic polyhedral hosted melt inclusions are the same as the experimental melt inclusions, these were created with crystallization of only olivine and, in our case, it is known that olivine was not the only mineral phase crystallizing. It is possible that in fact the dendritic growths influence the chemical composition of the melt inclusions. In this case, it is difficult to assess this since the

analysis of distance of the melt inclusion from the olivine interface does not clearly show evidence for the presence of boundary layer (Faure & Schiano, 2005).

Another particular observation from the geochemical results from the melt inclusions is the distance of the melt inclusion and a possible variation in chemical composition. Our results show that the melt inclusion compositions corrected for post-entrapment crystallization do not vary depending on the spatial location of the melt inclusions within the olivine crystal. It is necessary to clarify that these results are based on 2D slices, and the distances are from the shortest distance of the melt inclusion to the olivine crystal rim. 3D spatial distributions could reflect different results. However, these results can be used for certain interpretations regarding the formation of the melt inclusions. A possible explanation for this is that when olivine crystallization began, whole olivine crystals started to form along with entrapment of melt inclusions. Crystallization and entrapment advances until there was a change in cooling rate (caused by mixing) which created the dendritic growths in the polyhedral crystals (created during slow cooling rates). Based on this melt inclusion compositions will not vary depending on its distance from the polyhedral rim if the melt inclusion is located in the polyhedral portion of the crystal. A future analysis of melt inclusions located in the dendritic growths is necessary to establish if in fact there is a correlation between melt inclusion composition and its distance from the crystal rim.

Some of the most relevant characteristics of the melt inclusions in the polyhedral experimental olivines are random distribution, curvilinear shape, and in some cases the occurrence of open inclusions (as embayments). These features are believed to be formed by a process called spiral growth interaction (Faure & Schiano, 2005). This process can also be defined as a growth process that is mainly controlled by screw dislocations. These dislocations appear in the solid-liquid interface of the crystal boundary. The growth process is also characterized by occurring at a lower degree of undercooling. Screw dislocation can be defined as a defect in the lattice of a crystal which is parallel to the slip direction (Faure & Schiano, 2005). There are several similarities between the polyhedral olivines from Licto and the experimental model of polyhedral olivines. These are similar morphologies, shape of melt inclusions, and random distribution of the inclusions within the olivine crystals. Because of this, it is also probable that the main mechanism that led to the formation of these melt inclusions in the Licto olivines is also based in the spiral growth interaction.

Focusing on the chemistry of the melt inclusions, the first comparison is that the majority of melt inclusions have a higher concentration of SiO_2 compared to the whole rock samples (lavas) from the Tulabug Cone, and some of the melt inclusions compositions match the composition of the whole rock samples from the more evolved cone Loma Bellavista (Figure 40). A lower SiO_2 for the melt inclusions compared to lavas or tephra can suggest that the magmas of the cinder cones were contaminated by crustal material after the crystallization and entrapment of more primitive melt inclusions within the olivines (Walowski et al., 2019), or that fractional crystallization was occurring in the magmatic system. For the case of the Tulabug lava samples (whole rock analyses), the observation that the SiO_2 concentrations are similar or higher in the melt inclusions of our study compared to the lava samples could mean that there was no crustal contamination prior to the entrapment of the inclusions and eruption of the lavas. However, the melt inclusion compositions obtained from lava samples at Tulabug (D. F. Narváez et al., 2023) have a lower SiO_2 concentration than the whole rock samples from the same lavas, which is evidence that crustal contamination occurred before the eruption of lavas at Tulabug. Now for the case of the Loma Bellavista lavas (more andesitic in composition). The concentration of SiO_2 from the melt inclusions from Tulabug are lower compared to the lavas of Loma Bellavista. Since the analyzed olivine-hosted melt inclusions came from scoria samples from Tulabug, a direct comparison is difficult. However, based on the proximity of the cones, it is possible and likely the two cones of Licto once shared a magmatic plumbing system. When Tulabug initially formed, the plumbing system contained predominantly primitive basaltic andesite magma and there was evidence for crustal contamination. When Loma Bellavista started to form, crustal contamination became even more significant. Another possibility is that magma was formed and erupted at Tulabug, and a portion of this magma traveled to a different location, was still in a shallower position assimilating crustal material mixing with other magma, and then Bellavista was formed from this new more contaminated magma. The last is a common process of magmatic evolution documented in the region (Schiano et al., 2010). The only age constraints from lavas at Licto are from Tulabug (Bablon et al., 2019) so the chronology of emplacement is still uncertain. However, the chemical composition difference of lavas between the two cones can be used to infer different emplacement times, with the most primitive lava being from Tulabug (first to be formed) and the more evolved lava being from Loma Bellavista (the second to be formed). This is only a theory and it is important to know that this easily could not be the case, since

chemical composition is not a definitive tool to infer times of deposition of a particular volcanic material (more evolved material can be expelled first and then less evolved later), but this is a first approach to solve this issue.

Olivine could have either mainly grown and melt inclusions were trapped during the eruption of Tulabug, or the crystal could have formed before the eruption, stayed at the bottom of the magmatic chamber and then disrupted by the movement of magma during the eruption (this is the most likely scenario since some melt inclusions have a high degree of post-entrapment crystallization). Then crustal contamination of the overall magmatic system increased due to mixing with a shallower magmatic system that was assimilating crustal material, generating the most chemically evolved compositions from Bellavista. However, there is a problem with the previous statement, the estimated Fo% of olivines using the lava composition from Tulabug does not match the Fo% measured from the olivines of the scoria samples. In other words, the olivine crystals from the scoria at Tulabug are not in Fe-Mg equilibrium with the lava from the same site, which could make sense if the olivines from the scoria deposits crystallized from more evolved liquids. On the other hand, estimated Fo% of olivines using the lava composition of Bellavista match the Fo% of the olivine scoria samples at Tulabug, this could mean that there was a shared magmatic plumbing system for Tulabug and Bellavista and that similar magmatic processes operated during the evolution of the magmas. Thus, a plausible explanation could be that: 1) the lava flows were first erupted at Tulabug; 2) then crustal contamination started to occur, which created new magma composition and the olivines that fractionated from this more evolved melt were later deposited as scoria at Tulabug; 3) the more evolved magma migrated and reach the surface at a new location in Bellavista (Walowski et al., 2019).

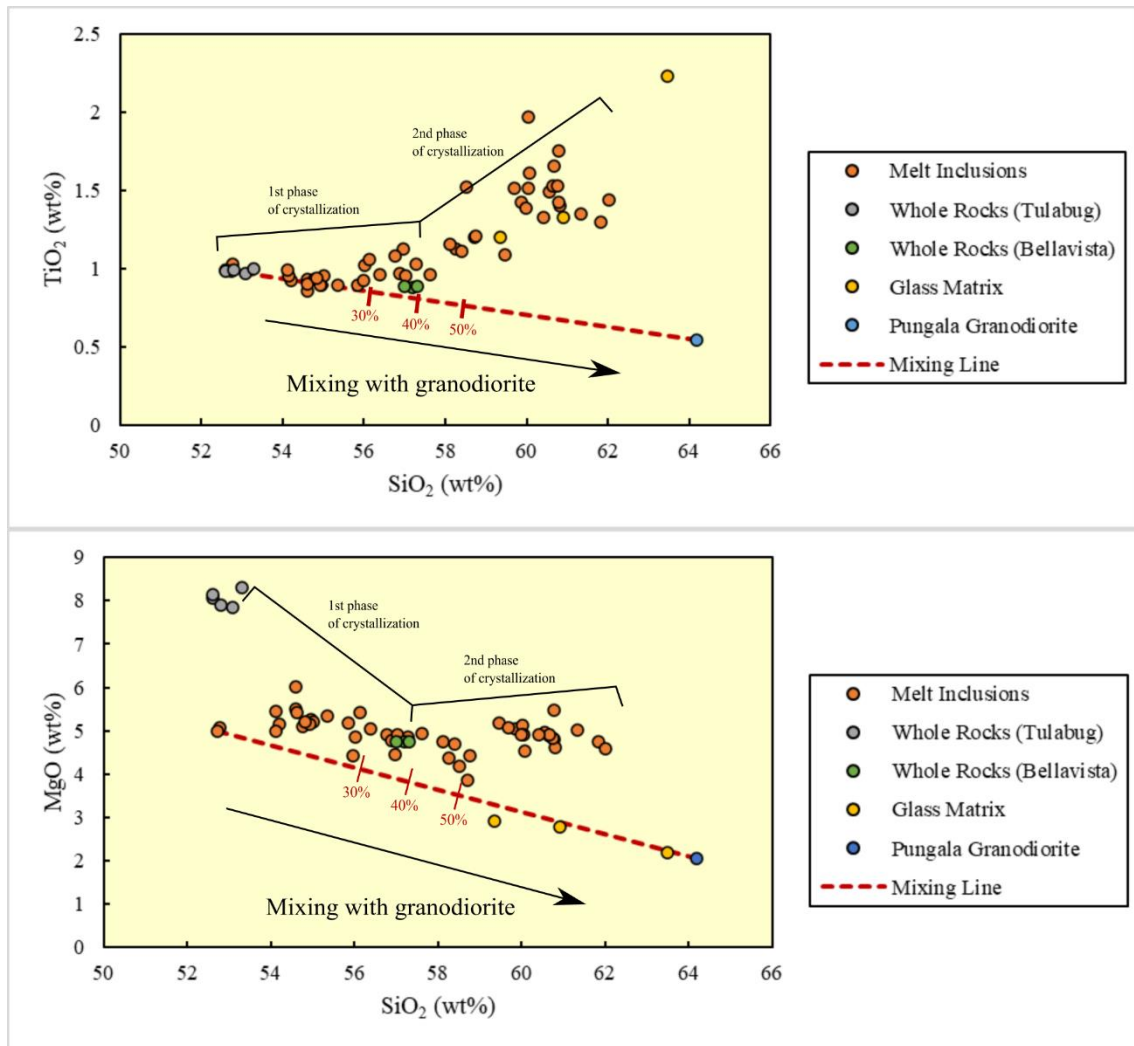


Figure 66: Top: SiO_2 wt % vs TiO_2 wt % of PEC and Fe-loss corrected melt inclusions, identified lava samples (whole rocks from Tulabug and Bellavista), glass from clasts, the composition of the Pungala granodiorite (Guerrero & Vallejo, 2020), and the possible mixing line between the most primitive magma observed and the granodiorite. Bottom: SiO_2 wt % vs MgO wt %, same measurements as before.

Complementary explanation to the theory of magma mixing is supported by the idea of plotting the likely extent of mixing between the composition of the melt inclusion with crustal rocks compositions (Figure 66) (Walowski et al., 2019). Pungala is a plutonic intrusion that outcrops east of Licto, and based on tectonic and geomorphological information can be inferred to be located below the volcanic deposits of Licto (Guerrero & Vallejo, 2020). In this case, the extent of mixing is calculated between the lowest SiO_2 melt inclusion composition and the closest source of granodiorite near Licto, this last is called Pungala granodiorite (Guerrero & Vallejo, 2020). The chemical composition of the granodiorite is given in appendix 4. We hypothesize that Tulabug lava deposits were created with a magma contaminated by assimilated melts of this granodiorite. Then, mixing and changing the chemical composition of the overall magmatic system along

with the usual change due to crystallization of minerals. This theory could be possible since the lava sample compositions from Bellavista fall within the theoretical mixing line between the initial magma compositions of lavas in Tulabug (the lower SiO₂ melt inclusion composition from the scoria) and the Pungala granodiorite composition (Guerrero & Vallejo, 2020). Particularly the mixing percentage between the initial magma at Licto and the granodiorite from Pungala that fits the chemical composition of lavas in Bellavista (and the magma composition that creates olivines with Fo% similar to the olivines in the scoria deposits in Tulabug) is approximately 38% Pungala granodiorite and 62% initial magma composition at Licto. The mixing percentages can be unrealistic since this is a very basic approach to infer mixing in this setting and a more in-depth analysis is required.

From these results it is also possible to infer changes in magmatic evolution at Tulabug. There was an initial stage characterized by an effusive eruption. After this stage, the shallow magma chamber started to assimilate crustal material (presumably granodiorites from Pungala), and the magmatic chamber that was feeding the lavas at Tulabug mixed with the shallower magma. The new chemical composition of the magmas led to a change in eruption-style to a more explosive style, depositing the volcanic scoria material (layer were the olivines of the present study come from). While this was happening at Tulabug, just to the east, another eruption was occurring which led to the formation of Loma Bellavista. This led to the lower Fo% olivines in the scoria deposits at Tulabug which were likely formed during or right after the assimilation episode. Further geological analysis is necessary to give more strength to this theory.

Fractional crystallization modeling done in the present study does not take into account the possible change in composition of the magma due to other processes such as assimilation or mixing which is likely in this system, this is because the software used does not allow to model this processes. However, the models can be used to constrain trends showing general evolutionary pathways caused by the fractional crystallization of different mineral phases. The changes in the patterns observed in the chemical variation diagrams, change in trend around ~57% SiO₂ (Figure 39), can be also tightly related with the episode of mixing presumably happening during the eruption of the volcanic material. Each of the models represent a possible path for the magmatic evolution to vary based on crystallization of certain minerals. For instance, it is possible to divide the magmatic evolution in two phases, marked by changes in the overall melt inclusion compositional

trends. That are not considered in the fractional crystallization models but could be attributed to magmatic assimilation. The first phase is likely involving the crystallization of olivine, plagioclase, and pyroxenes within the magmatic system, this is the cotectic model (ol (olivine) + plg (plagioclase) + cpx (clinopyroxene)), spinel is not considered in this fractional crystallization phase, since the models do not form spinel with the same chemical compositions as the samples found in the scoria deposits in Tulabug. However, the ubiquity and size of the spinel inclusions suggest that they must have formed along with olivine. The explanation to this is that the equilibrium models used for fractional crystallization models of these phases are not appropriate for the Licto system or our parameters such as pressure and oxygen fugacity are not representative of the environment where they form.

Mineral crystallization of the first phase occurred while one of the magmatic chambers, that was assimilating crustal material (granodiorite), began to mix with the magma that was feeding the effusive stage at Tulabug. This happened until crystallization of this particular assemblage (controlled mainly by olivine fractionation) stopped at around a magmatic SiO₂ wt% composition of 57.

Elements that support this theory is the observed mineral assemblages in lava samples in Tulabug (presumably being the first volcanic deposits at the initial stage of eruption in Tulabug, where the observed mineral assemblages are ol + plg + opx (orthopyroxene) (D. Narváez, 2021), and the broadly similar trends between the cotectic model and the trend created by the melt inclusions (scoria samples). Again, the fractional crystallization models do not account for the assimilation of crust material. The scoria deposits at Tulabug erupted during this first phase. Even though crystallization with this mineral assemblage stopped, olivines created at the end of the first phase remained as cumulate deposits near the base of a reservoir and were remobilized and expelled within the scoria along with the other minerals.

The second phase of fractional crystallization is likely again to be crystallization of ol + plg + cpx, with the particularity that this time the geochemical trend is controlled mainly by cpx + plg fractionation. This is based on the chemical trend observed in the melt inclusions and the fractional crystallization models that only take into consideration fractionation of just cpx+plg and the cotectic model. The crystallization of a significant fraction of olivine at this second phase could have shown a steady depletion in MgO in the melt inclusions which is not observed (Figure 46/C). We consider that olivine kept

crystallizing at this second phase but it was not the dominant mineral phase controlling chemical evolution. Scoria deposits of Tulabug may have minerals formed during this second phase of fractional crystallization along with minerals from the end of the first phase. Bellavista lava samples have similar chemical composition as the melt inclusions of this second phase of fractional crystallization and it also may have minerals formed during these previously described stages.

Magma mixing episodes also can be related to depletion of Ni within the zoning of the olivine (Figure 35), which is observed in one of the olivine samples of the scoria deposits at Tulabug. This supports the idea of magma mixing during the initial phase of magmatic evolution (after eruption) or more events of mixing during later stages (Salas et al., 2021).

Olivine-hosted melt inclusions are an important tool for petrological or geochemical studies. It is shown that the melt inclusion compositions are not systematically biased based on their spatial arrangement within the host crystal while being faithful recorders of melt composition.

5.3 Textural analysis of clasts from the Tulabug cinder cone

Clasts samples taken from sampling site 1 in Tulabug (Figure 9) did not show internal layering meaning that the clasts with different textures (Figure 52) were mixed. Assuming that there were no post-depositional changes in the deposit it means that all the different clasts came out of the vent at the same time.

Chemical analysis from the clast samples of the scoria layers at Tulabug did not show a correlation between the type/color of the clast and chemical composition (Figure 53).

A few analyses from the vesicular brown clasts have different chemical composition compared to the other types (Figure 53). However, this is not a clear indication that the chemical composition is controlling the clast textural variability since other analyses from the vesicular brown clasts overlap with the other clast types. Based on this, it is likely that the clasts have a similar magmatic origin. In other words, they were deposited at the same time and the variation in texture and coloration depend on other factors. While the chemical composition does not show clear causal relationship with the clast texture, coloration may indicate changes in the oxygen fugacity (controls the $\text{Fe}^{2+}/\text{Fe}^{3+}$ ratio) which is mainly controlled by sulfur degassing (Moussallam et al., 2016). Iron rich

minerals such as olivine can give a darker coloration, so it is possible that this mineral can be found in more abundance within the dense black and vesicular dark clasts along with other minerals such as plagioclase and pyroxenes. While in the case of clast with a brown coloration, the prominent mineral assemblage could be clinopyroxene and plagioclase. It is important to notice that the chemical composition of the glass present in these different types of clasts fall within the chemical trend generated by the melt inclusions compositions.

The idea is that the textural vesicular analysis carried out with FOAMS can give insights into how the eruption behaved during the explosive period in Tulabug, being that each of the clast types were caused by dynamics in the magmatic system and are related to the kinetics of vesicle nucleation and growth mechanisms. This discussion will begin with the dense black clasts. The eruption period where this type of clast was expelled based on VVDs plots shows that bubbles behave during vesiculation following a process called ripening, this occurs during a period of magmatic degassing (Mangan & Cashman, 1996; Shea, Houghton, et al., 2010). Ripening will cause an increase in bubble size which at the same time will promote degassing in the magmatic system, leading to explosive eruptions. Vesicularity in rocks where ripening was an important process is low which is the same case in our samples. The vesicularity in the dense black samples is low compared to the other type of clasts (Figure 67) (Lautze et al., 2011).

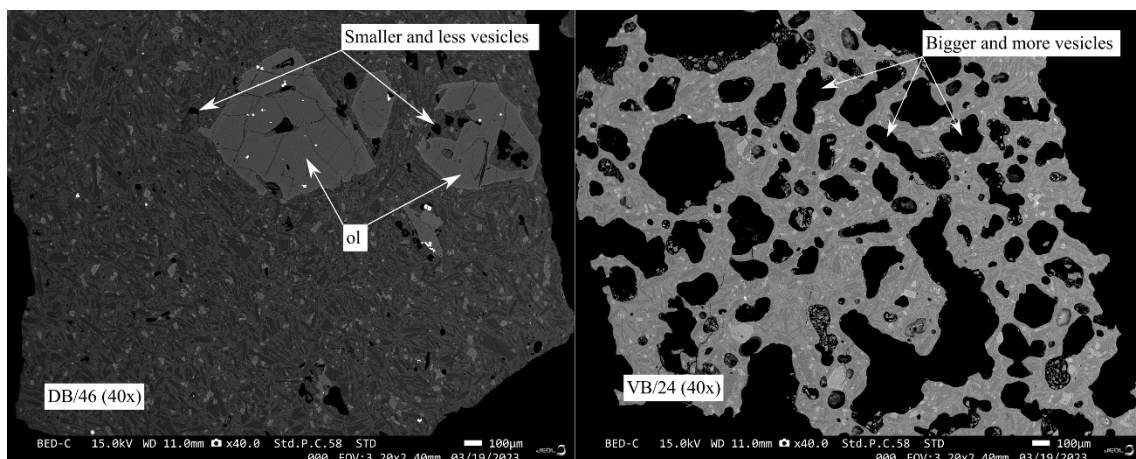


Figure 67: Comparison between dense black clast and a vesicular black clast. Similar mineral assemblages with larger olivines in dense black clasts. Microphenocrysts of plagioclase, clinopyroxene, and olivine occur in the matrix glass of both samples. ol: olivine

Particularly this type of clast seems to be expelled during the explosive period in Tulabug as the rest of the types, ripening causes generally that bubbles become coarser, while the number density decreases (number of bubbles of a certain size) (Lautze et al., 2011).

Ripening will create coarser vesicles, but these are not generally seen in the dense black samples. A possible explanation for this is that in the more vesicular samples signs of ripening, coalescence, and continuous nucleation and growth of bubbles are seen. While in dense black samples continuous nucleation and growth of bubbles is not clearly seen. This difference could have created the textural difference in the clasts. The nature of the scoria deposits which again suggest deposition at the same time of the different clasts indicate that all the different types of clasts were expelled contemporaneously. A possible explanation of this is a model consisting of multiple reservoirs at top each other or near each other, each reservoir due to its magmatic characteristics could have produced scoria with different vesicularity/color. We hypothesize that during the eruption all the different materials from each reservoir were deposited as one scoria layer, the layer were this textural analysis is carried. This last theory is also supported by the similar signs of coalescence, ripening, and continuous nucleation and growth of bubbles that are seen in the VVD and VSD plots of all the different clast types.

As bubbles become larger, ascent rates of magma increase. Fast ripening is attributed to magmas degassing richer in H₂O compared to CO₂ (Lautze et al., 2011). There is an indication that the magmas at Licto indeed were richer in H₂O compared to other types of volatiles, this is due to the sudden jump in diameter size in VVDs plots for dense black clasts (Figure 55). CVVDs plots for dense black clasts also show a similar trend caused by ripening. In the case of VSD and CVSD plots for dense black clasts coalescence is a process that can be inferred (Figure 56), so it is possible that both coalescence and ripening were the dominant processes for bubble growth in the system.

Focusing on the clasts with higher vesicularity, coalescence and ripening seems to be operating, with high ascent rates based on an increase in bubble size. However, the vesicularity in these types of clasts is higher compared to the dense black clasts, and the same mechanisms for bubble growth are potentially operating based on the vesicular analysis. A possible explanation for this is based on observations in the VVDs of vesicular clasts, where a continuous and accelerating bubble nucleation was occurring. In this particular case, bubble nucleation seems to be higher compared to the first type of clast (dense black clasts). Nucleation of bubbles could have been lower at the reservoir where dense black clasts came from and is consistent with their origin in a higher-pressure environment. This could have led to the lower vesicularity in the dense black samples, as the bubbles grow dominantly through ripening and coalescence, there was not enough

new bubbles to ensure that the number density for all sizes of bubbles was maintained. This can be explained by an increase in degassing in the reservoir where these clasts came from. While the reservoir hosting the magma that would eventually form the black dense clast at Tulabug also indicates that degassing was occurring but it was not as intense compared to the other stages. VSDs for the more vesicular clasts also show the presence of coalescence, ripening, and continuous/accelerating nucleation of bubbles (Figure 58). It is important to notice that within the eruption of the scoria, the clasts vesicularity evolved in stages with just coalescence and ripening. Meaning that these two types of mechanisms for bubble growth could have occurred at the same time or were alternating between each other. A summary for the possible vesicularity evolution is shown (Figure 68).

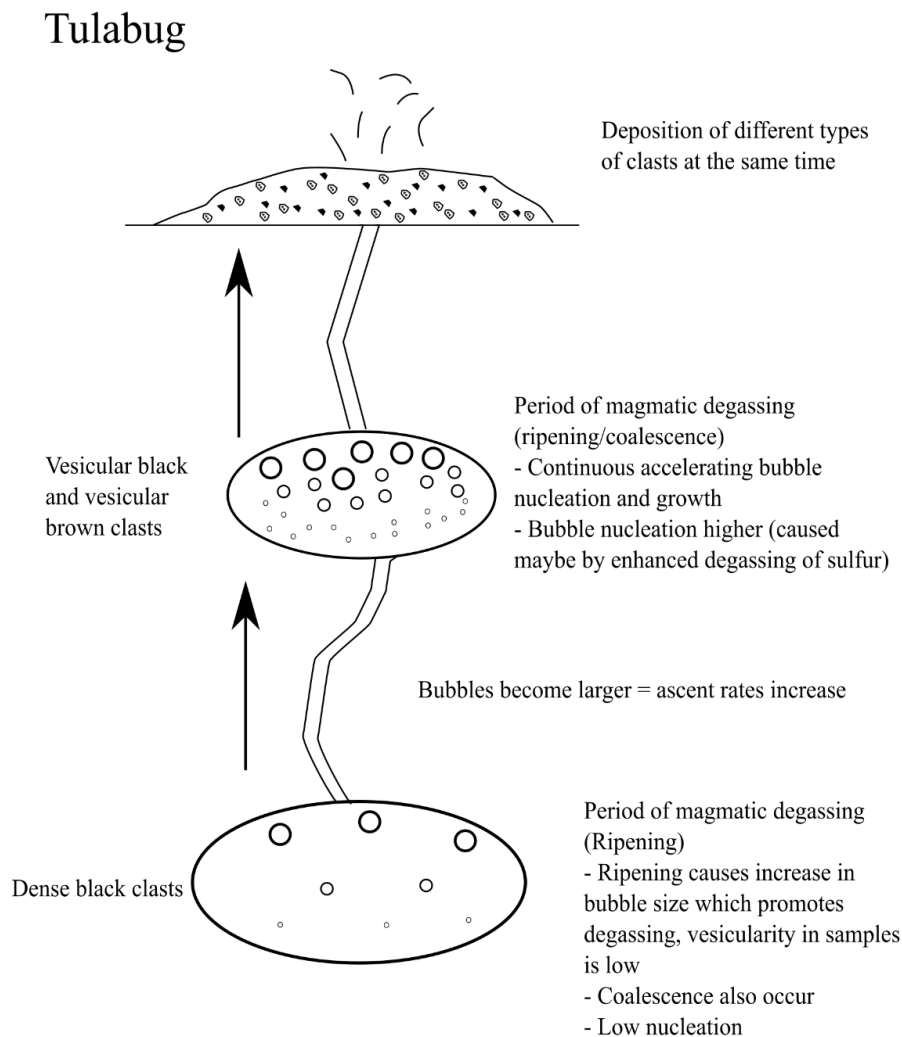


Figure 68: Theory of vesicularity evolution of clast during the explosive eruption of Licto inferred from texture analysis.

5.4 Theory of magmatic evolution and eruption at Licto

The reconstruction of the magmatic evolution and eruption processes at Licto is hypothesized with previous studies and the present information in this work. Lavas from Tulabug were estimated to have an age of 183 ± 9 ka (Bablon et al., 2019).

Fault activity is another precursor in the increase or initiation of volcanic activity. However, compared to other volcanic edifices which seem to be closely correlated with faulting systems in the southern portion of the volcanic arc in Ecuador, no correlation is readily apparent at Licto. For example, the Calpi cones and their spatial association with fractures led Bablon et al. (2019) to postulate that their eruptions were favored by fractures opening along the Pallatanga fault activity. As a first idea Licto's eruptive activity does not seem to be greatly affected by faulting or fractures (Bablon et al., 2019). However, this can be studied more in detail.

The following discussion is to evaluate the mantle source material from where the magma was created beneath Licto. Previous studies attempted to determine the influence of the slab components in the creation of magmas at Licto. The idea is that hydrous siliceous melts (product of the physical melting of oceanic crust/subducted sediments of the subducting plate) have the ability to easily mobilize certain trace elements, compared to aqueous fluids driven off the slab that liberate different trace elements. Measurements of these trace elements can be used to infer the likely contribution of either hydrous silicate melts or aqueous fluids in the initial melting of the mantle (D. F. Narváez et al., 2023). The southern portion of the volcanic arc in Ecuador is enriched in fluid mobile elements (thermal regime colder) which is indicative of an aqueous fluid and not a hydrous silicate melt (D. F. Narváez et al., 2023). Along with the conditions that promote melting caused by the geotectonic context, aqueous fluids addition promote the melting under Licto. The magmas migrated, evolved and erupted in the area of study. Melt inclusion compositions in Ecuador represent different melts produced by the mixing between melts derived from amphibole bearing clinopyroxenites with peridotites/phlogopite-peridotites (D. F. Narváez et al., 2023). Our results are in agreement with the last statement since olivines at Licto do not have a composition that falls within the exclusive peridotite magma source or the pyroxenite source (Figure 60). The compositions are near the area of exclusive peridotite source (this establishes the peridotite was an important component), so the

melting of peridotite along with other mixed ultramafic lithologies, produced the initial magmatic composition under Licto.

This magma ascent reaches approximately a pressure of 2.6 kbar, which using the average geobaric gradient (0.3 kbar/km) is approximately a depth of 8.7 km. It is important that this depth constraint was obtained using clinopyroxene barometry, and is not an absolute indicator of where olivine in equilibrium with melt existed. However, since clinopyroxene seems to be a mineral phase that crystallizes along with olivine the depth at which olivine crystallizes could be the same. This initial magma was emplaced and began to erupt in an effusive manner. This happened while another magmatic emplacement interacted with the Pungala granodiorite. Both magmatic chambers at some point interacted with each other. This assimilation (shallower magmatic chamber) and mixing process did not solely control the entirety of the chemical variability at Licto, since more evolved melt inclusion compositions are observed, and they do not fall within the theoretical two component mixing line between the more primitive melt and the granodiorite assimilated magma.

This initial phase of the magmatic evolution is reflected in the lava deposits in Tulabug which is the most primitive material expelled during this magmatic event. The magmatic chamber that fed the eruptions at Tulabug was located near another magmatic chamber that interacted with the Pungala granodiorite.

At some point during mixing between the two magmatic chambers the configuration at Licto changed. For instance, a new vent was developed, from this new vent lavas were expelled and deposited which form part of the Loma Bellavista cone, located near Tulabug (theory supported by chemical trends but needs dating of deposits in Loma Bellavista for confirmation). The explosive activity and related deposits at Tulabug marked the last eruption, at least from the volcanic deposits examined in this study.

Based on all the previous information, Licto, despite being considered a small volcanic system, has proven that it had a complex magmatic system possibly similar to larger volcanoes with very complex systems (Cannata et al., 2018; Ruth & Costa, 2021).

A schematic diagram showing the theoretical general evolution at Licto is shown (Figure 69).

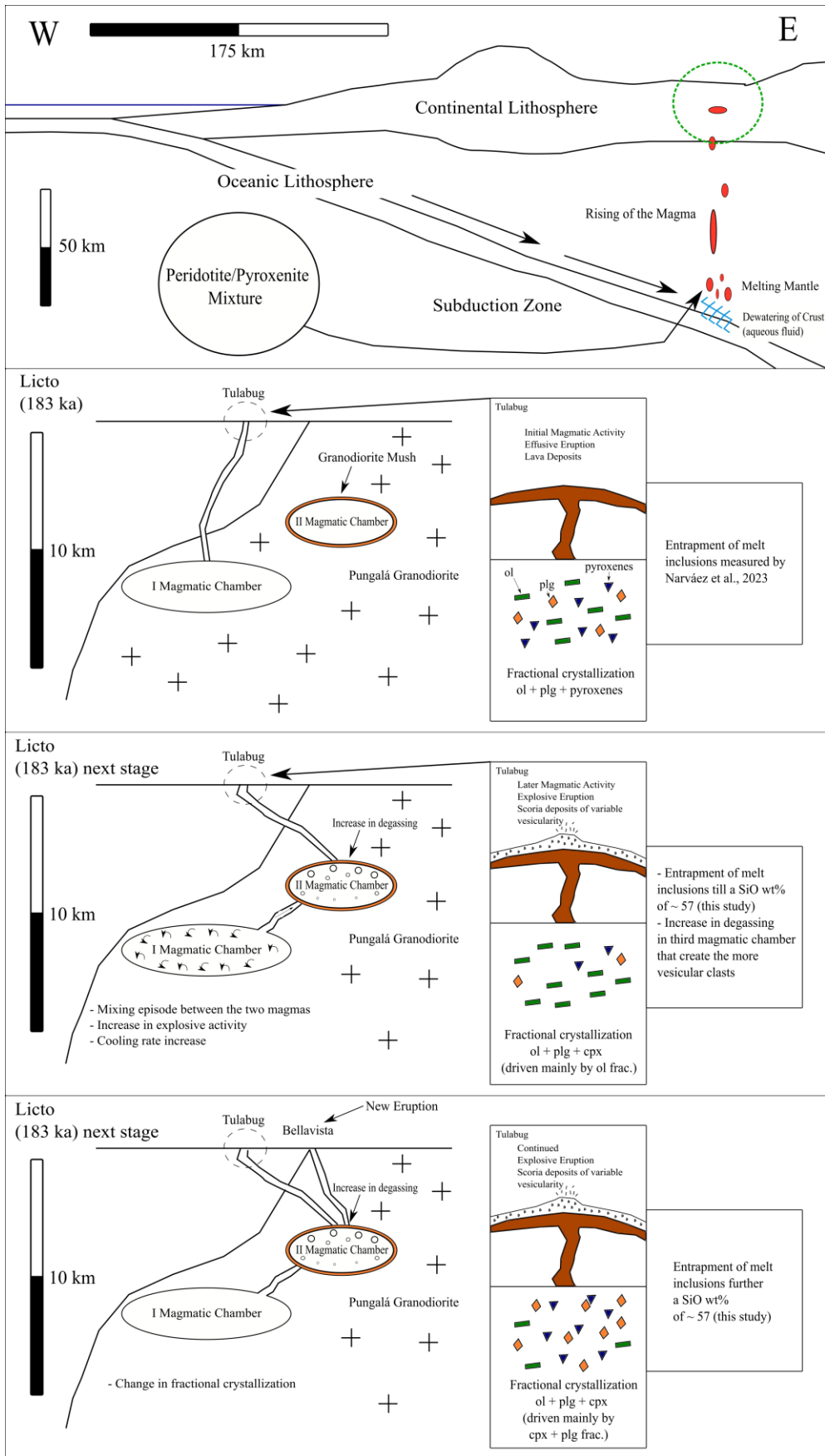


Figure 69: Theory of magmatic evolution at Licto based on the chemical information, olivine + melt inclusion morphology and textural analysis of the scoria clasts.

6. Conclusions and Future Work

The present study is conceived to understand magmatic processes that led to the formation of volcanic deposits in this case a scoria cones. This work integrated numerous techniques in different parts of the magmatic system at Licto to address the pertinent hypothesis related to volcanism at Licto. The techniques chosen for this particular work are focused on studying the morphology and chemical composition of different products formed during magma genesis, magma evolution and volcanic eruptions. The study of the Licto deposits involved field sampling, sample preparation for laboratory activities, petrological observations, spatial visualization and measurements using the nanotomography techniques, the application of Raman spectroscopy to constrain the compositions of mineral phenocrysts, major element measurements with an EPMA, use of mathematical models to correct for natural processes, and textural analysis of the volcanic products. These techniques/approaches allowed me to constrain the magmatic processes related to the formation, evolution, and eruption of small volume subduction-related basaltic cones in the southern portion of the north Andean volcanic zone of Ecuador.

While different eruptive products have been used in the present work, the principal focus was on olivine-hosted melt inclusions. They are established as one, if not the only, direct source of information regarding primitive magma compositions and pre-eruptive volatile contents of magmas. Lavas, tephra, and minerals formed due to crystallization of magma are all important sources of information. However, if the focus of the study is primary melt evolution, melt inclusions are the best option compared to other volcanic materials since these previously mentioned products undergo a series of geological processes that modify the original compositions of the magma. Melt inclusions are not perfect, but carefully applying corrections ensure that their compositions can be reliably be used in volcanic/petrological interpretations.

Polyhedral and dendritic polyhedral olivines are the predominant morphology of the minerals host of melt inclusions encountered at Licto. More specifically, olivines found within scoria deposits of Tulabug. This particular morphology, supported with chemical data, shows that olivine at the magmatic chamber formed at slow cooling rates. Furthermore, the morphology also suggests a development under free growth conditions prior to the eruptive process.

The mineral assemblage encountered in the studied samples show similarities with other eruptions at cinder cones. The stratigraphy observed at Licto is similar to other cinder cones that have an initial effusive activity followed by a more energetic explosive phase. The textural characteristics from the volcanic products at Tulabug also share similar characteristics to other basaltic cones. The normal chemical zoning in the olivine samples with a small range of spinel inclusions compositions are characteristics of a simple/close-system fractional crystallization process that formed the olivines at Licto. The chemical composition and core to rim characteristics of Licto's olivines suggest magma mixing was an important process that was happening prior to the eruptions at Licto. The olivine compositions also indicate the magma source rock can be a mixture of a series of materials that interact in subduction systems, likely a mix of ultramafic lithologies. However, its proportions or even presence require additional work.

The magmatic and eruptive interpretation obtained from the morphology and chemical composition of the olivines that host melt inclusions is important. Interestingly different characteristics of melt inclusions give similar interpretations, which support the previous findings. Regardless the size/shape of melt inclusions studied from olivines from Tulabug (Licto), which actually have the expected values for melt inclusions formed during slow cooling rates and small degrees of undercooling, the vapor/melt volume ratios estimated show that melt inclusions shared the same origin with only minor exceptions. The size of the bubbles measured also can be a sign of a volatile-rich magma that varies as degassing becomes an important process. The chemical variations of the melt inclusions are independent of the host crystal morphology when the melt inclusions analyzed are located in the polyhedral portion of the crystal. The melt inclusions have trends indicating that: minerals other than olivine crystallize during magmatic evolution (supported also by the presence of other minerals in the eruptive products and the fractional crystallization models), the distance of the melt inclusion within the host crystal does not influence the chemical composition of the inclusions, that chemical characteristics of the melt inclusions compared to lavas or tephra can suggest that the magmas of the cinder cones were contaminated by crustal material, magma mixing between primary magmas (melt inclusions with most primitive chemical composition) and a more evolved country rock (Pungala granodiorite) is supported by simple binary mixing relationships. Similarity the melt inclusion chemical variations and fractional crystallization models imply the likely identity and timing of fractionating minerals.

The vesicular analysis of the dense and vesicular clasts from the scoria at Tulabug provides insight into the eruption and magma ascent dynamics. The explosive stage of the eruption at Licto includes clasts with textural differences and show signs of degassing with peculiar changes in the bubble growth mechanisms from ripening to coalescence. Potential changes in the explosivity and the types of gas predominant in the magma (H₂O) are also inferred from this approach.

The previous information, morphological/chemical characteristics of melt inclusions, crystal hosts, whole rock samples, glass samples, and scoria vesicles are used to infer a basic model of magmatic evolution under Licto that led to its formation. From the tectonic setting that led to the generation of the magma, the evolution of this magma as it traveled through the crust, its crystallization in the plumbing system and eventual eruption. The different results support the idea of a particular cinder cone eruption with unique characteristics caused by its location in the north Andean volcanic zone of Ecuador (southern portion).

Magmatic processes are considered as the first step to create new rocks and minerals in the rock cycle. Understanding these processes that occurred in the past is to understand the evolution of a certain geological setting, the geomorphology, and possible resources that are emplaced in the area. How a magmatic system evolves can be used for volcanic eruption modeling in order to ensure a more accurate prediction of volcanic hazard. All this information is a valuable resource for future studies regarding various branches of geology like petrology, resource exploration, and the general understanding of the earth's history, especially the volcanic history of Ecuador.

Future research at Licto should consider an extensive geological stratigraphic study of the volcanic deposits in the area, the assessment of volatile concentrations in the magma pre-syn-eruptive, and a tectonic/structural research where the eruption at Licto was relevant. All of these approaches can help to advance our understanding of both small and large volcanic systems, why and how they erupt, and how these eruptions have an impact on population of nearby areas. All of this with the idea to improve our understanding of the geological history of Ecuadorian volcanoes.

References

- Albert, H., Larrea, P., Costa, F., Widom, E., & Siebe, C. (2020). Crystals reveal magma convection and melt transport in dyke-fed eruptions. *Scientific Reports*, *10*(1). <https://doi.org/10.1038/s41598-020-68421-4>
- Ancellin, M. A., Samaniego, P., Vlastélic, I., Nauret, F., Gannoun, A., & Hidalgo, S. (2017). Across-arc versus along-arc Sr-Nd-Pb isotope variations in the Ecuadorian volcanic arc. *Geochemistry, Geophysics, Geosystems*, *18*(3), 1163–1188. <https://doi.org/10.1002/2016GC006679>
- Bablon, M., Quidelleur, X., Samaniego, P., Le Pennec, J. L., Audin, L., Jomard, H., Baize, S., Liorzou, C., Hidalgo, S., & Alvarado, A. (2019). Interactions between volcanism and geodynamics in the southern termination of the Ecuadorian arc. *Tectonophysics*, *751*, 54–72. <https://doi.org/10.1016/j.tecto.2018.12.010>
- Barth, A., & Plank, T. (2021). The Ins and Outs of Water in Olivine-Hosted Melt Inclusions: Hygrometer vs. Speedometer. In *Frontiers in Earth Science* (Vol. 9). Frontiers Media S.A. <https://doi.org/10.3389/feart.2021.614004>
- Bottinga, Y., & Weill, D. F. (1972). The viscosity of magmatic silicate liquids; a model calculation. *American Journal of Science*, *272*(5), 438–475. <https://doi.org/10.2475/ajs.272.5.438>
- Bowen, N. (1922). The Reaction Principle in Petrogenesis. *The Journal of Geology*, *30*(3), 177–198. <http://www.jstor.org/stable/30080767>
- Breitenfeld, L. B., Dyar, M. D., Carey, C. J., Tague, T. J., Wang, P., Mullen, T., & Parente, M. (2018). Predicting olivine composition using Raman spectroscopy through band shift and multivariate analyses. *American Mineralogist*, *103*(11), 1827–1836. <https://doi.org/10.2138/am-2018-6291>
- Bucholz, C. E., Gaetani, G. A., Behn, M. D., & Shimizu, N. (2013). Post-entrapment modification of volatiles and oxygen fugacity in olivine-hosted melt inclusions. *Earth and Planetary Science Letters*, *374*, 145–155. <https://doi.org/10.1016/j.epsl.2013.05.033>
- Cajamarca-Zuniga, D., Kabantsev, O. V., & Marin, C. (2022). Macroseismic intensity-based catalogue of earthquakes in Ecuador. *Structural Mechanics of Engineering Constructions and Buildings*, *18*(2), 161–171. <https://doi.org/10.22363/1815-5235-2022-18-2-161-171>
- Cannata, A., Di Grazia, G., Giuffrida, M., Gresta, S., Palano, M., Sciotto, M., Viccaro, M., & Zuccarello, F. (2018). Space-Time Evolution of Magma Storage and Transfer at Mt. Etna Volcano (Italy): The 2015-2016 Reawakening of Voragine Crater. *Geochemistry, Geophysics, Geosystems*, *19*(2), 471–495. <https://doi.org/10.1002/2017GC007296>
- Cao, G., Tong, Y., Li, X., & Wang, L. (2022). *Insights from olivine chemistry into crustal magmatic processes and the mantle source lithology of basalts from Hainan Island, China*. <https://ssrn.com/abstract=4105366>
- Chiaradia, M., Müntener, O., & Beate, B. (2020). Effects of aseismic ridge subduction on the geochemistry of frontal arc magmas. *Earth and Planetary Science Letters*, *531*. <https://doi.org/10.1016/j.epsl.2019.115984>

- Chiaradia, M., Müntener, O., Beate, B., & Fontignie, D. (2009). Adakite-like volcanism of Ecuador: lower crust magmatic evolution and recycling. *Contributions to Mineralogy and Petrology*, 158(5), 563–588. <https://doi.org/10.1007/s00410-009-0397-2>
- Conte, A. M., Perinelli, C., & Trigila, R. (2006). Cooling kinetics experiments on different Stromboli lavas: Effects on crystal morphologies and phases composition. *Journal of Volcanology and Geothermal Research*, 155(3–4), 179–200. <https://doi.org/10.1016/j.jvolgeores.2006.03.025>
- Cressey, G., & Howie, R. A. (2005). Minerals - Olivines. *Encyclopedia of Geology*, 557–561.
- Danyushevsky, L. V. (2001). The effect of small amounts of H₂O on crystallisation of mid-ocean ridge and backarc basin magmas. *Journal of Volcanology and Geothermal Research*, 110(3–4), 265–280. [https://doi.org/10.1016/S0377-0273\(01\)00213-X](https://doi.org/10.1016/S0377-0273(01)00213-X)
- Danyushevsky, L. V., Della-Pasqua, F. N., & Sokolov, S. (2000). Re-equilibration of melt inclusions trapped by magnesian olivine phenocrysts from subduction-related magmas: Petrological implications. *Contributions to Mineralogy and Petrology*, 138(1), 68–83. <https://doi.org/10.1007/PL00007664>
- Danyushevsky, L. V., Leslie, R. A. J., Crawford, A. J., & Durance, P. (2004). Melt inclusions in primitive olivine phenocrysts: The role of localized reaction processes in the origin of anomalous compositions. In *Journal of Petrology* (Vol. 45, Issue 12, pp. 2531–2553). <https://doi.org/10.1093/petrology/egh080>
- Danyushevsky, L. V, Sokolov, S., & Falloon, T. J. (2002). Melt Inclusions in Olivine Phenocrysts: Using Diffusive Re-equilibration to Determine the Cooling History of a Crystal, with Implications for the Origin of Olivine-phyric Volcanic Rocks. In *JOURNAL OF PETROLOGY* (Vol. 43).
- Deer, W. A. (William A., Howie, R. A. (Robert A., & Zussman, J. (2013). *An introduction to the rock-forming minerals*.
- DiPietro, J. A. (2013). Keys to the Interpretation of Geological History. In *Landscape Evolution in the United States* (pp. 327–344). Elsevier. <https://doi.org/10.1016/B978-0-12-397799-1.00020-8>
- Donaldson, C. H. (1976). An Experimental Investigation of Olivine Morphology. In *Contrib. Mineral. Petrol* (Vol. 57).
- Faure, F., & Schiano, P. (2005). Experimental investigation of equilibration conditions during forsterite growth and melt inclusion formation. *Earth and Planetary Science Letters*, 236(3–4), 882–898. <https://doi.org/10.1016/j.epsl.2005.04.050>
- Faure, F., Schiano, P., Trolliard, G., Nicollet, C., & Soulestin, B. (2007). Textural evolution of polyhedral olivine experiencing rapid cooling rates. *Contributions to Mineralogy and Petrology*, 153(4), 405–416. <https://doi.org/10.1007/s00410-006-0154-8>
- Faure, F., Trolliard, G., Nicollet, C., & Montel, J. M. (2003). A developmental model of olivine morphology as a function of the cooling rate and the degree of undercooling. *Contributions to Mineralogy and Petrology*, 145(2), 251–263. <https://doi.org/10.1007/s00410-003-0449-y>
- Frezzotti, M. L. (2001). Silicate-melt inclusions in magmatic rocks: Applications to petrology. *Lithos*, 55(1–4), 273–299. [https://doi.org/10.1016/S0024-4937\(00\)00048-7](https://doi.org/10.1016/S0024-4937(00)00048-7)

- Genareau, K., Valentine, G. A., Moore, G., & Hervig, R. L. (2010). Mechanisms for transition in eruptive style at a monogenetic scoria cone revealed by microtextural analyses (Lathrop Wells volcano, Nevada, U.S.A.). *Bulletin of Volcanology*, 72(5), 593–607. <https://doi.org/10.1007/s00445-010-0345-z>
- Gennaro, E., Iacono-Marziano, G., Paonita, A., Rotolo, S., Martel, C., Rizzo, A., Pichavant, M., & Liotta, M. (2018). Melt inclusions track melt evolution and degassing of Etnean magmas in the last 15 ka. *LITHOS*, #pagerange#. <https://doi.org/10.1016/j.lithos.2018.11.023>
- Guerrero, E., & Vallejo, C. (2020). *GEOCRONOLOGÍA Y GEOQUÍMICA DE LOS INTRUSIVOS DE PUNGALÁ, AMALUZA, SAN LUCAS E INTRUSIÓN PORFIRÍTICA VÍA ALAO*.
- Hoffer, G., Eissen, J. P., Beate, B., Bourdon, E., Fornari, M., & Cotten, J. (2008). Geochemical and petrological constraints on rear-arc magma genesis processes in Ecuador: The Puyo cones and Mera lavas volcanic formations. *Journal of Volcanology and Geothermal Research*, 176(1), 107–118. <https://doi.org/10.1016/j.jvolgeores.2008.05.023>
- Hoffstetter, R. (1956). *Lexique stratigraphique international: Vol. 5. Amérique latine. Ecuador - Equateur - (incl. Galapagos)*.
- Iacovino, K., Matthews, S., Wieser, P. E., Moore, G. M., & Bégué, F. (2021). VESICAL Part I: An Open-Source Thermodynamic Model Engine for Mixed Volatile (H₂O-CO₂) Solubility in Silicate Melts. *Earth and Space Science*, 8(11). <https://doi.org/10.1029/2020EA001584>
- Jankovics, M. É., Sági, T., Astbury, R. L., Petrelli, M., Kiss, B., Ubide, T., Németh, K., Ntaflos, T., & Harangi, S. (2019). Olivine major and trace element compositions coupled with spinel chemistry to unravel the magmatic systems feeding monogenetic basaltic volcanoes. *Journal of Volcanology and Geothermal Research*, 369, 203–223. <https://doi.org/10.1016/j.jvolgeores.2018.11.027>
- JAROSEWICH, E., NELEN, J. A., & NORBERG, J. A. (1980). Reference Samples for Electron Microprobe Analysis*. *Geostandards and Geoanalytical Research*, 4(1), 43–47. <https://doi.org/10.1111/j.1751-908X.1980.tb00273.x>
- Jones, T. J., Russell, J. K., Porritt, L. A., & Brown, R. J. (2014). Morphology and surface features of olivine in kimberlite: Implications for ascent processes. *Solid Earth*, 5(1), 313–326. <https://doi.org/10.5194/se-5-313-2014>
- Kent, A. J. R. (2008). Met inclusions in basaltic and related volcanic rocks. *Reviews in Mineralogy and Geochemistry*, 69, 273–331. <https://doi.org/10.2138/rmg.2008.69.8>
- Kress, V. C., & Carmichael, I. S. E. (1988). Stoichiometry of the iron oxidation reaction in silicate melts. *American Mineralogist*, 73(11–12), 1267–1274.
- Lange, R. A., & Carmichael, I. S. E. (1987). Densities of Na₂O-K₂O-CaO-MgO-FeO-Fe₂O₃-Al₂O₃-TiO₂-SiO₂ liquids: New measurements and derived partial molar properties. *Geochimica et Cosmochimica Acta*, 51(11), 2931–2946. [https://doi.org/10.1016/0016-7037\(87\)90368-1](https://doi.org/10.1016/0016-7037(87)90368-1)
- Lautze, N. C., Sisson, T. W., Mangan, M. T., & Grove, T. L. (2011). Segregating gas from melt: An experimental study of the Ostwald ripening of vapor bubbles in magmas. *Contributions to Mineralogy and Petrology*, 161(2), 331–347. <https://doi.org/10.1007/s00410-010-0535-x>

- Lavenu, A., Winter, T., & Dávila, F. (1995). A Pliocene-Quaternary compressional basin in the Interandean Depression, Central Ecuador. *Geophysical Journal International*, 121(1), 279–300. <https://doi.org/10.1111/j.1365-246X.1995.tb03527.x>
- Li, C., & Ripley, E. M. (2010). The relative effects of composition and temperature on olivine-liquid Ni partitioning: Statistical deconvolution and implications for petrologic modeling. *Chemical Geology*, 275(1–2), 99–104. <https://doi.org/10.1016/j.chemgeo.2010.05.001>
- Lin, Y., Hui, H., Xia, X., Shang, S., & Westrenen, W. (2020). Experimental constraints on the solidification of a hydrous lunar magma ocean. *Meteoritics & Planetary Science*, 55(1), 207–230. <https://doi.org/10.1111/maps.13425>
- Lindsley, D. (1991). *Oxide Minerals: Petrologic and Magnetic Significance* (Vol. 25). Reviews in Mineralogy. <https://doi.org/10.1017/S0016756800023876>
- Lloyd, A. S., Plank, T., Ruprecht, P., Hauri, E. H., & Rose, W. (2013). Volatile loss from melt inclusions in pyroclasts of differing sizes. *Contributions to Mineralogy and Petrology*, 165(1), 129–153. <https://doi.org/10.1007/s00410-012-0800-2>
- Lowenstern, J. B. (1995). Applications of silicate-melt inclusions to the study of magmatic volatiles. In *Mineralogical Association of Canada Short Course Volume* (Vol. 23, Issue in Magmas, Fluids and Ore Deposits, pp. 71–79).
- Mangan, M. T., & Cashman, K. V. (1996). The structure of basaltic scoria and reticulite and inferences for vesiculation, foam formation, and fragmentation in lava fountains. In *Journal of Volcanology and Geothermal Research* (Vol. 73).
- Matzen, A. K., Baker, M. B., Beckett, J. R., & Stolper, E. M. (2013). The Temperature and Pressure Dependence of Nickel Partitioning between Olivine and Silicate Melt. *Journal of Petrology*, 54(12), 2521–2545. <https://doi.org/10.1093/petrology/egt055>
- Matzen, A. K., Baker, M. B., Beckett, J. R., Wood, B. J., & Stolper, E. M. (2017). The effect of liquid composition on the partitioning of Ni between olivine and silicate melt. *Contributions to Mineralogy and Petrology*, 172(1), 3. <https://doi.org/10.1007/s00410-016-1319-8>
- Mollo, S., Del Gaudio, P., Ventura, G., Iezzi, G., & Scarlato, P. (2010). Dependence of clinopyroxene composition on cooling rate in basaltic magmas: Implications for thermobarometry. *Lithos*, 118(3–4), 302–312. <https://doi.org/10.1016/j.lithos.2010.05.006>
- Moore, G. (2008). Interpreting H₂O and CO₂ contents in melt inclusions: Constraints from solubility experiments and modeling. *Reviews in Mineralogy and Geochemistry*, 69(1928), 333–361. <https://doi.org/10.2138/rmg.2008.69.9>
- Moore, L. R., Gazel, E., Tuohy, R., Lloyd, A. S., Esposito, R., Steele-MacInnis, M., Hauri, E. H., Wallace, P. J., Plank, T., & Bodnar, R. J. (2015). Bubbles matter: An assessment of the contribution of vapor bubbles to melt inclusion volatile budgets. *American Mineralogist*, 100(4), 806–823. <https://doi.org/10.2138/am-2015-5036>
- Moussallam, Y., Edmonds, M., Scaillet, B., Peters, N., Gennaro, E., Sides, I., & Oppenheimer, C. (2016). The impact of degassing on the oxidation state of basaltic magmas: A case study of Kīlauea volcano. *Earth and Planetary Science Letters*, 450, 317–325. <https://doi.org/10.1016/j.epsl.2016.06.031>

- Narváez, D. (2021). *Arc magma sources: Contribution of primitive olivine-hosted melt inclusions from Ecuadorian volcanoes* [Université Clermont].
<https://theses.hal.science/tel-03554073>
- Narváez, D. F., Samaniego, P., Koga, K. T., Rose-Koga, E. F., Hidalgo, S., & Ratzov, G. (2023). Two types of slab components under Ecuadorian volcanoes supported by primitive olivine-hosted melt inclusion study. *Lithos*, 442–443, 107049.
<https://doi.org/10.1016/j.lithos.2023.107049>
- Newman, S., & Lowenstern, J. B. (2002). VolatileCalc: a silicate melt–H₂O–CO₂ solution model written in Visual Basic for excel. *Computers & Geosciences*, 28(5), 597–604.
[https://doi.org/10.1016/S0098-3004\(01\)00081-4](https://doi.org/10.1016/S0098-3004(01)00081-4)
- Nielsen, R. L. (1985). EQUIL: a program for the modeling of low-pressure differentiation processes in natural mafic magma bodies. *Computers & Geosciences*, 11(5), 531–546.
[https://doi.org/10.1016/0098-3004\(85\)90084-6](https://doi.org/10.1016/0098-3004(85)90084-6)
- Peccerillo, A., & Taylor, S. R. (1976). Geochemistry of eocene calc-alkaline volcanic rocks from the Kastamonu area, Northern Turkey. *Contributions to Mineralogy and Petrology*, 58(1), 63–81. <https://doi.org/10.1007/BF00384745>
- Putirka, K. D. (2008). Thermometers and Barometers for Volcanic Systems. *Reviews in Mineralogy and Geochemistry*, 69(1), 61–120. <https://doi.org/10.2138/rmg.2008.69.3>
- Putirka, K., Ryerson, F. J., Perfit, M., & Ridley, W. I. (2011). Mineralogy and Composition of the Oceanic Mantle. *Journal of Petrology*, 52(2), 279–313.
<https://doi.org/10.1093/petrology/egq080>
- Qin, Z., Lu, F., & Anderson, A. (1992). Diffusive reequilibration of melt and fluid inclusions. In *American Mineralogist* (Vol. 77).
- Richard, A., Morlot, C., Créon, L., Beaudoin, N., Balistky, V. S., Pentelei, S., Dyja-Person, V., Giuliani, G., Pignatelli, I., Legros, H., Sterpenich, J., & Pironon, J. (2019). Advances in 3D imaging and volumetric reconstruction of fluid and melt inclusions by high resolution X-ray computed tomography. *Chemical Geology*, 508(June), 3–14.
<https://doi.org/10.1016/j.chemgeo.2018.06.012>
- Roedder, E. (1984). *Fluid Inclusions* (Vol. 12).
- Rose-Koga, E. F., Bouvier, A. S., Gaetani, G. A., Wallace, P. J., Allison, C. M., Andrys, J. A., Angeles de la Torre, C. A., Barth, A., Bodnar, R. J., Bracco Gartner, A. J. J., Butters, D., Castillejo, A., Chilson-Parks, B., Choudhary, B. R., Cluzel, N., Cole, M., Cottrell, E., Daly, A., Danyushevsky, L. V., ... Zhou, T. (2021). Silicate melt inclusions in the new millennium: A review of recommended practices for preparation, analysis, and data presentation. *Chemical Geology*, 570(March).
<https://doi.org/10.1016/j.chemgeo.2021.120145>
- Ruscitto, D. M., Wallace, P. J., Johnson, E. R., Kent, A. J. R., & Bindeman, I. N. (2010). Volatile contents of mafic magmas from cinder cones in the Central Oregon High Cascades: Implications for magma formation and mantle conditions in a hot arc. *Earth and Planetary Science Letters*, 298(1–2), 153–161. <https://doi.org/10.1016/j.epsl.2010.07.037>
- Ruth, D. C. S., & Costa, F. (2021). A petrological and conceptual model of Mayon volcano (Philippines) as an example of an open-vent volcano. *Bulletin of Volcanology*, 83(10), 62.
<https://doi.org/10.1007/s00445-021-01486-9>

- Salas, P., Ruprecht, P., Hernández, L., & Rabbia, O. (2021). Out-of-sequence skeletal growth causing oscillatory zoning in arc olivines. *Nature Communications*, *12*(1).
<https://doi.org/10.1038/s41467-021-24275-6>
- Schellart, W. P. (2023). Subduction Zones: A Short Review. In *Dynamics of Plate Tectonics and Mantle Convection* (pp. 321–355). Elsevier. <https://doi.org/10.1016/B978-0-323-85733-8.00009-3>
- Schiano, P. (2003). Primitive mantle magmas recorded as silicate melt inclusions in igneous minerals. *Earth-Science Reviews*, *63*(1–2), 121–144. [https://doi.org/10.1016/S0012-8252\(03\)00034-5](https://doi.org/10.1016/S0012-8252(03)00034-5)
- Schiano, P., Monzier, M., Eissen, J. P., Martin, H., & Koga, K. T. (2010). Simple mixing as the major control of the evolution of volcanic suites in the Ecuadorian Andes. *Contributions to Mineralogy and Petrology*, *160*(2), 297–312. <https://doi.org/10.1007/s00410-009-0478-2>
- Shea, T., Gurioli, L., Larsen, J. F., Houghton, B. F., Hammer, J. E., & Cashman, K. V. (2010). Linking experimental and natural vesicle textures in Vesuvius 79AD white pumice. *Journal of Volcanology and Geothermal Research*, *192*(1–2), 69–84.
<https://doi.org/10.1016/j.jvolgeores.2010.02.013>
- Shea, T., Houghton, B. F., Gurioli, L., Cashman, K. V., Hammer, J. E., & Hobden, B. J. (2010). Textural studies of vesicles in volcanic rocks: An integrated methodology. *Journal of Volcanology and Geothermal Research*, *190*(3–4), 271–289.
<https://doi.org/10.1016/j.jvolgeores.2009.12.003>
- Shea, T., Lynn, K. J., & Garcia, M. O. (2015). Cracking the olivine zoning code: Distinguishing between crystal growth and diffusion. *Geology*, *43*(10), 935–938.
<https://doi.org/10.1130/G37082.1>
- Sobolev, A. V. (1996). Melt Inclusions in Minerals as a Source of Principle Petrological Information. *Petrology*, *4*(3), 209–220.
- Sobolev, A. V., Hofmann, A. W., Kuzmin, D. V., Yaxley, G. M., Arndt, N. T., Chung, S.-L., Danyushevsky, L. V., Elliott, T., Frey, F. A., Garcia, M. O., Gurenko, A. A., Kamenetsky, V. S., Kerr, A. C., Krivolutskaya, N. A., Matvienkov, V. V., Nikogosian, I. K., Rocholl, A., Sigurdsson, I. A., Sushchevskaya, N. M., & Teklay, M. (2007). The Amount of Recycled Crust in Sources of Mantle-Derived Melts. *Science*, *316*(5823), 412–417.
<https://doi.org/10.1126/science.1138113>
- Straub, S. M., Layne, G. D., Schmidt, A., & Langmuir, C. H. (2004). Volcanic glasses at the Izu arc volcanic front: New perspectives on fluid and sediment melt recycling in subduction zones. *Geochemistry, Geophysics, Geosystems*, *5*(1), n/a-n/a.
<https://doi.org/10.1029/2002GC000408>
- Wallace, P. J. (2005). Volatiles in subduction zone magmas: Concentrations and fluxes based on melt inclusion and volcanic gas data. *Journal of Volcanology and Geothermal Research*, *140*(1–3), 217–240. <https://doi.org/10.1016/j.jvolgeores.2004.07.023>
- Wallace, P. J., Plank, T., Bodnar, R. J., Gaetani, G. A., & Shea, T. (2021). *Olivine-Hosted Melt Inclusions: A Microscopic Perspective on a Complex Magmatic World*.
<https://doi.org/10.1146/annurev-earth-082420>
- Walowski, K. J., Wallace, P. J., Cashman, K. V., Marks, J. K., Clynne, M. A., & Ruprecht, P. (2019). Understanding melt evolution and eruption dynamics of the 1666 C.E. eruption of Cinder Cone, Lassen Volcanic National Park, California: Insights from olivine-hosted melt

inclusions. *Journal of Volcanology and Geothermal Research*, 387.
<https://doi.org/10.1016/j.jvolgeores.2019.106665>

Wang, Z., & Gaetani, G. A. (2008). Partitioning of Ni between olivine and siliceous eclogite partial melt: experimental constraints on the mantle source of Hawaiian basalts. *Contributions to Mineralogy and Petrology*, 156(5), 661–678.
<https://doi.org/10.1007/s00410-008-0308-y>

Weller, D. J., & Stern, C. R. (2018). Along-strike variability of primitive magmas (major and volatile elements) inferred from olivine-hosted melt inclusions, southernmost Andean Southern Volcanic Zone, Chile. *Lithos*, 296–299, 233–244.
<https://doi.org/10.1016/j.lithos.2017.11.009>

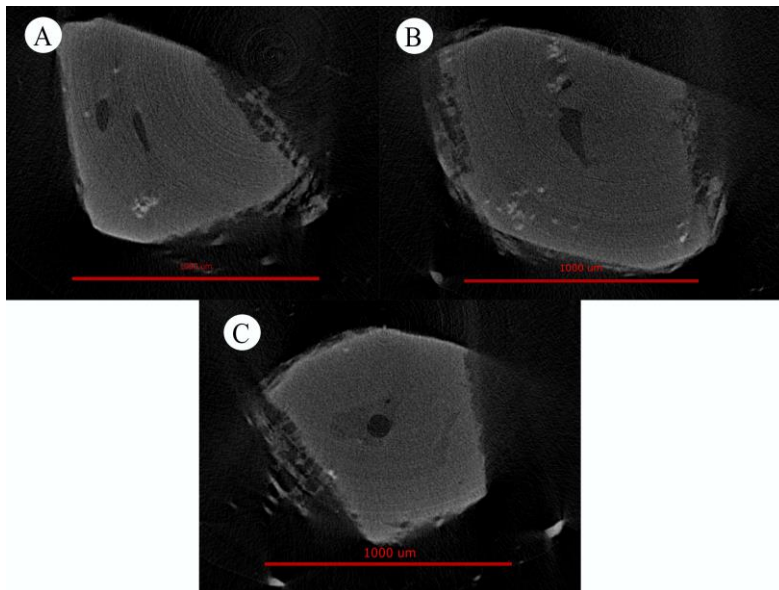
Appendix

Appendix 1: Section Images from the nanotomographer

1) LS2-MSL-1835-1-1

The most remarkable characteristic that is possible to observe in the images taken by the nanotomography is the presence of what is presumably melt inclusions within the crystal, voids that could represent vapor phases, or denser material (spinel inclusions). The gray scale allows to see empty spaces with a curve morphology; however, it does not show a spherical morphology (Appendix 1/Figure 1 (A)), the denser material in the images is shown by white speckles. These empty spaces at the edges likely are defects in crystal growth. Melt inclusion will appear as a gray portion that wraps a spherical feature (bubble).

It is possible to see a polyhedral morphology of the olivine crystal with well-developed faces. Crystalline properties of an orthorhombic system are clear from the images that are taken by one of the faces of the crystal (which change based on the orientation of the crystal), along with the presence of voids near the center of the crystal (Appendix 1/Figure 1). The clearest image of a melt inclusion within the olivine crystal shows a spherical vapor phase surrounded with a less dense phase, probably a liquid phase with an irregular shape (Appendix 1/Figure 1 (C)).



Appendix 1/Figure 1: Section images from olivine samples LS2-MSL-1835-1/1301 (A), LS2-MSL-1835-1/1012 (B), and LS2-MSL-1835-1/1301 (C) taken from the nanotomograph.

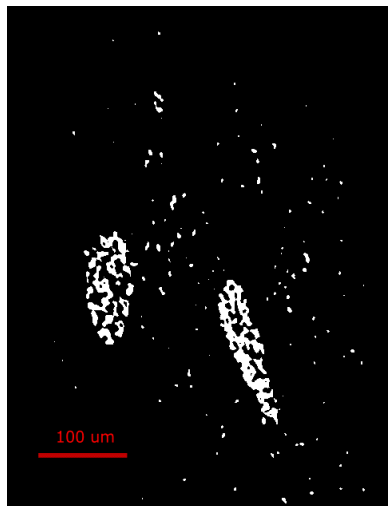
In order to take measurements of areas of possible vapor phases, the most rounded empty spaces (black voids) that likely are bubbles are selected for a 2D analysis in all the next images, the selection is shown as white pixels in binary images.

Binary extrapolation based on a gray scale for section LS2-MSL-1835-1/649 takes into account gray index values in an interval of 7 to 32, which correspond to 3.31% of the total image approximately and an area of 6339 μm^2 .

For section LS2-MSL-1835-1/1012 gray index values are taken in an interval of 0 to 32, which correspond to 14.95% of the total image approximately and an area of 20356 μm^2 .

For section LS2-MSL-1835-1/1301 gray index values are taken in an interval of 0 to 35, which correspond to 10.27% of the total image approximately and an area of 8190 μm^2 .

Morphometry analysis gives a surface area of the selected object of 9703 μm^2 and a peripheral object surface of 3243 μm^2 for section LS2-MSL-1835-1/649, a particle size range from 0 to 1.15 μm establishes an approximated area of 6426 particles. For section LS2-MSL-1835-1/1012 it gives a surface area of the selected object of 30858 μm^2 and a peripheral object surface of 10124 μm^2 , a particle size range from 0 to 1.15 μm establishes an approximated area of 20597 particles. For section LS2-MSL-1835-1/1301 it gives a surface area of the selected object of 10833 μm^2 and a peripheral object surface of 2550 μm^2 , a particle size range from 0 to 1.15 μm establishes an approximated area of 8246 particles. Binary images which correspond to the gray scale selection of empty voids used to make calculations of area are shown (Appendix 1/Figure 2).



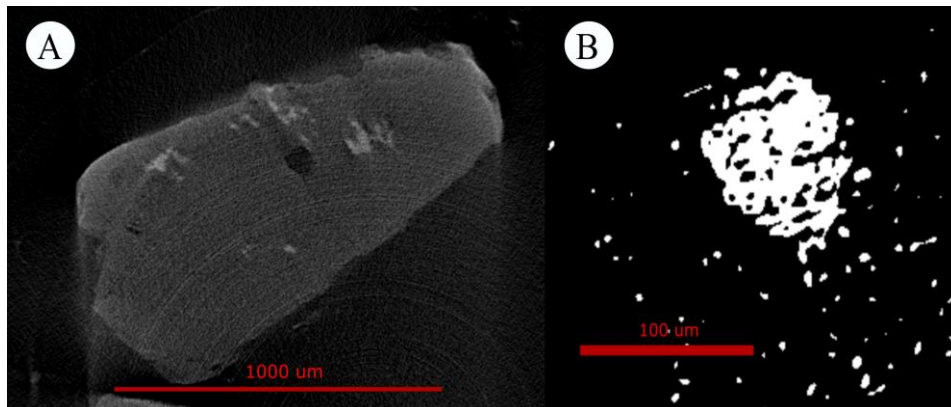
Appendix 1/Figure 2: Binary image of a melt inclusions in section sample LS2-MSL-1835-1/649

2) LS2-MSL-1835-1-2

It is possible to identify a vapor phase with a spherical shape presumably surrounded by a less dense material that could correspond to the glass phase of the melt inclusion.

Located at the center of the olivine crystal, the presence of denser material again is shown at random places of the crystal, last crystal faces again can be seen due to the polyhedral nature of the olivine crystals (Appendix 1/Figure 3 (A)).

Binary extrapolation based on a gray scale for section LS2-MSL-1835-2/831 takes into account gray index values in an interval of 1 to 31, which correspond to 13.78% of the total image approximately and an area of $4662 \mu\text{m}^2$. Morphometry analysis gives a surface area of the selected object of $6497 \mu\text{m}^2$ and a peripheral object surface of $1765 \mu\text{m}^2$ for section LS2-MSL-1835-2/831, a particle size range from 0 to $1.4 \mu\text{m}$ establishes an approximated area of 4711 particles. Binary images which correspond to the gray scale selection of empty voids used to make calculations of area are shown (Appendix 1/Figure 3 (B)).

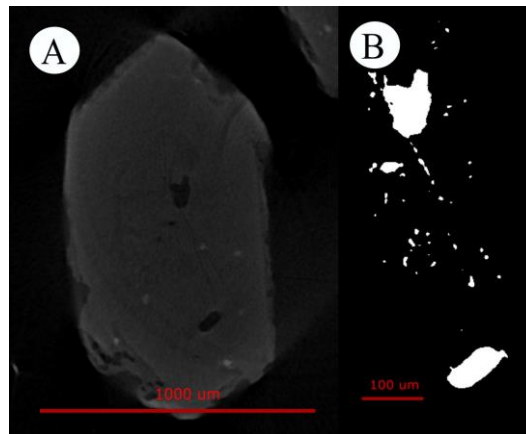


Appendix 1/Figure 3: Section image from olivine sample LS2-MSL-1835-2/831 (A), Binary image of a melt inclusions in section sample LS2-MSL-1835-2/831 (B), taken from the nanotomograph.

3) LS2-MSL-1835-2-1

It is possible to see several faces of the orthorhombic crystalline system in this particular olivine seen by an upper view of the crystal. The black portion at the bottom can be considered as a possible vapor phase, the upper one has an irregular shape so likely is a vapor bubble adjacent to a mineral phase; it is possible to identify less dense phases with an irregular shape at different places within the crystal which can be glass phases of the melt inclusions (Appendix 1/Figure 4 (A)).

Binary extrapolation based on a gray scale for section LS2-MSL-1835-2-1/785 takes into account gray index values in an interval of 1 to 27, which correspond to 8.56% of the total image approximately and an area of $11832 \mu\text{m}^2$. Morphometry analysis gives a surface area of the selected object of $14449 \mu\text{m}^2$ and a peripheral object surface of $2523 \mu\text{m}^2$ for section LS2-MSL-1835-2-1/785, a particle size range from 0 to $91 \mu\text{m}$ establishes an approximated area of 11893 particles. Binary images which correspond to the gray scale selection of empty voids used to make calculations of area are shown (Appendix 1/Figure 4 (B)).



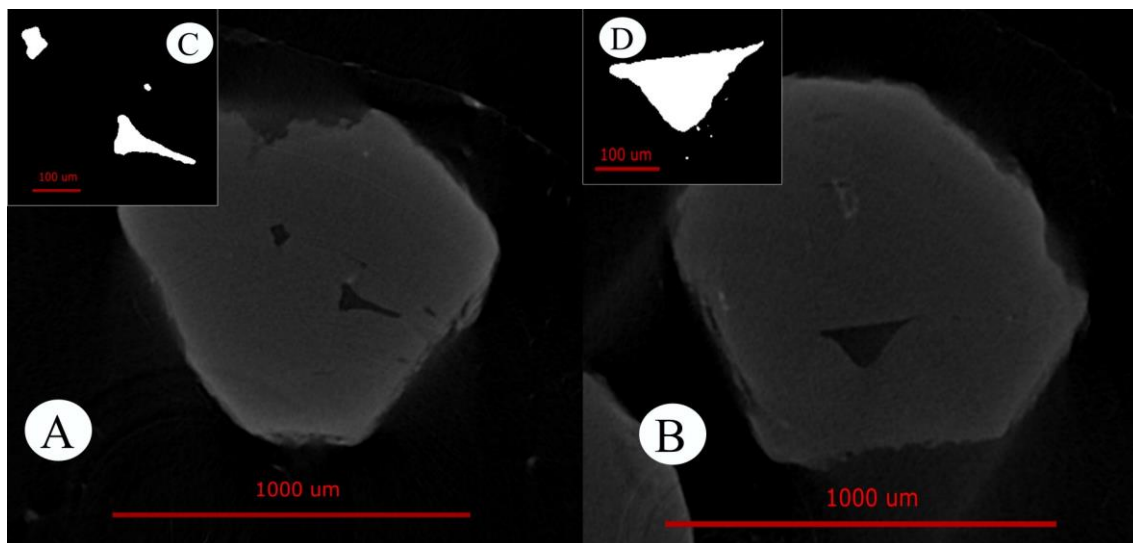
Appendix 1/Figure 4: Section image from olivine sample LS2-MSL-1835-2-1/785 (A), Binary image of a melt inclusions in section sample LS2-MSL-1835-2-1/785 (B), taken from the nanotomograph.

4) LS2-MSL-1835-2-2

In this case voids are shown with the usual curve shape within the innermost part of the crystal, however a less dense phase that can be explained as a liquid phase of the melt inclusion is difficult to observe. Crystal faces are present so the crystal has a polyhedral morphology (Appendix 1/Figure 5 (A, B)).

Binary extrapolation based on a gray scale for section LS2-MSL-1835-2-2/461 takes into account gray index values in an interval of 1 to 27, which correspond to 6.86% of the total image approximately and an area of $7140 \mu\text{m}^2$. For section LS2-MSL-1835-2-2/700 gray index values are taken in an interval of 1 to 26, which correspond to 29.74% of the total image approximately and an area of $11905 \mu\text{m}^2$. Morphometry analysis gives a surface area of the selected object of $8180 \mu\text{m}^2$ and a peripheral object surface of $997 \mu\text{m}^2$ for section LS2-MSL-1835-2-2/461, a particle size range from 0 to $91 \mu\text{m}$ establishes an approximated area of 7180 particles. For section LS2-MSL-1835-2-2/700 it gives a surface area of the selected object of $12883 \mu\text{m}^2$ and a peripheral object surface of 940

μm^2 , a particle size range from 0 to 182 μm establishes an approximated area of 11941 particles. Binary images which correspond to the gray scale selection of empty voids used to make calculations of area are shown (Appendix 1/Figure 5 (C, D)).



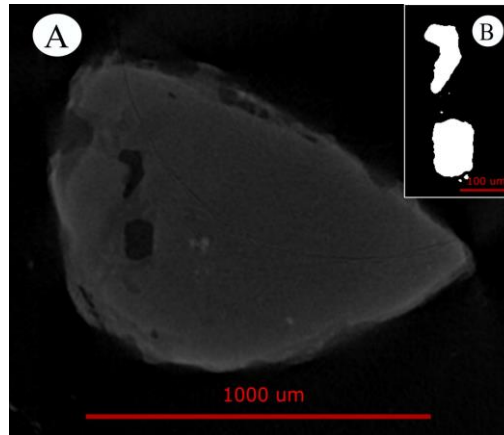
Appendix 1/Figure 5: Section images from olivine sample LS2-MSL-1835-2-2/461 (A) and LS2-MSL-1835-2-2/700 (B), Binary images of a melt inclusions in section sample LS2-MSL-1835-2-2/461 (C) and LS2-MSL-1835-2-2/700 (D), taken from the nanotomograph.

5) LS2-MSL-1835-2-3

Empty voids are located in this case closer to the edges of the crystal, it is possible to distinguish a liquid phase with an irregular shape that covers these voids; however, the shape of the voids does not appear as bubbles, denser material is seen at some portion of the crystal. The shape of the olivine crystal is granular compared to the polyhedral morphology of the previous seen cases (Appendix 1/Figure 6 (A)).

Binary extrapolation based on a gray scale for section LS2-MSL-1835-2-3/1680 takes into account gray index values in an interval of 1 to 29, which correspond to 21.41% of the total image approximately and an area of 15387 μm^2 . Morphometry analysis gives a surface area of the selected object of 16688 μm^2 and a peripheral object surface of 1254 μm^2 for section LS2-MSL-1835-2-3/1680, a particle size range from 0 to 182 μm establishes an approximated area of 15427 particles.

Binary images which correspond to the gray scale selection of empty voids used to make calculations of area are shown (Appendix 1/Figure 6 (B)).

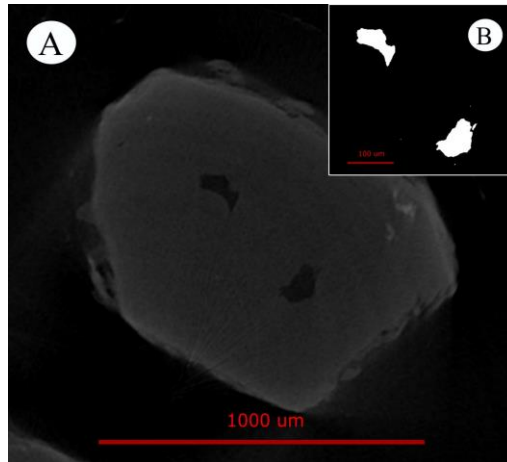


Appendix 1/Figure 6: Section image from olivine sample LS2-MSL-1835-2-3/1680 (A), Binary image of a melt inclusions in section sample LS2-MSL-1835-2-3/1680 (B), taken from the nanotomograph.

6) LS2-MSL-1835-2-4

The olivine crystal has a polyhedral morphology with clear crystal faces, empty voids are located close to the center of the crystal with an irregular shape and curve morphology. Denser material which also can be called a solid phase is located near the edge of the crystal (Appendix 1/Figure 7 (A)).

Binary extrapolation based on a gray scale for section LS2-MSL-1835-2-4/1913 takes into account gray index values in an interval of 1 to 25, which correspond to 8.55% of the total image approximately and an area of $14218 \mu\text{m}^2$. Morphometry analysis gives a surface area of the selected object of $15567 \mu\text{m}^2$ and a peripheral object surface of $1294 \mu\text{m}^2$ for section LS2-MSL-1835-2-4/1913, a particle size range from 0 to $182 \mu\text{m}$ establishes an approximated area of 14270 particles. Binary images which correspond to the gray scale selection of empty voids used to make calculations of area are shown (Appendix 1/Figure 7 (B)).

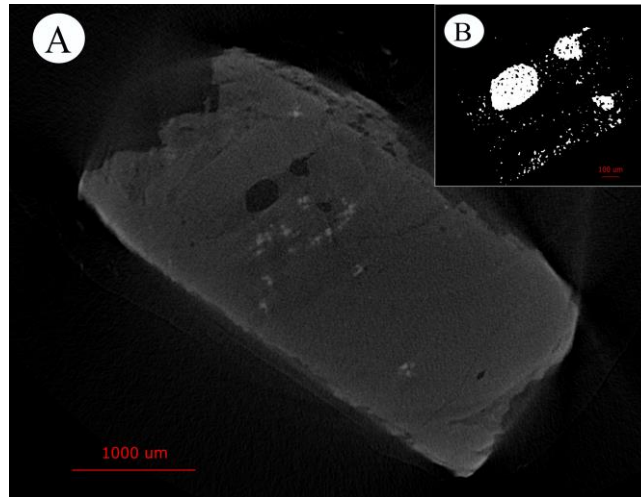


Appendix 1/Figure 7: Section image from olivine sample LS2-MSL-1835-2-4/1913 (A), Binary image of a melt inclusions in section sample LS2-MSL-1835-2-4/1913 (B), taken from the nanotomograph.

7) LS2-MSL-1835-3-1

Olivine crystal has a polyhedral morphology; however, the usual faces of an orthorhombic system are less developed. Vapor phase of the inclusions have a generic spherical morphology, surrounded in one of the cases with an irregular glass phase, solid phase denser material is present with more abundance in this case. At the termination of the crystals, it is possible to infer that dendritic growths are developed (usually formed during rapid growth stages) (Appendix 1/Figure 8 (A)).

Binary extrapolation based on a gray scale for section LS2-MSL-1835-3-1/1366 takes into account gray index values in an interval of 0 to 31, which correspond to 11.56% of the total image approximately and an area of $87224 \mu\text{m}^2$. Morphometry analysis gives a surface area of the selected object of $108480 \mu\text{m}^2$ and a peripheral object surface of $20472 \mu\text{m}^2$ for section LS2-MSL-1835-3-1/1366, a particle size range from 0 to $256 \mu\text{m}$ establishes an approximated area of 87760 particles. Binary images which correspond to the gray scale selection of empty voids used to make calculations of area are shown (Appendix 1/Figure 8 (B)).

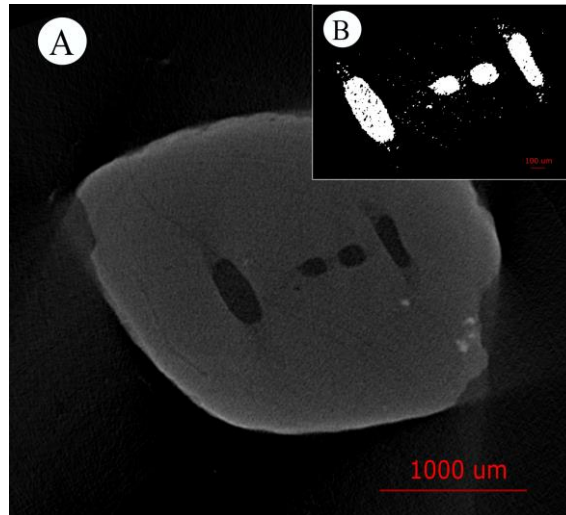


Appendix 1/Figure 8: Section image from olivine sample LS2-MSL-1835-3-1/1366 (A), Binary image of a melt inclusions in section sample LS2-MSL-1835-3-1/1366 (B), taken from the nanotomograph.

8) LS2-MSL-1835-3-2

The crystal has a granular morphology with poorly developed crystal faces, inclusions seem to be located in the center of the crystal, empty voids have an ellipsoidal/spherical morphology. It is possible to distinguish glass phases around a vapor phase. Denser material is less in this particular section (Appendix 1/Figure 9 (A)).

Binary extrapolation based on a gray scale for section LS2-MSL-1835-3-2/1366 takes into account gray index values in an interval of 0 to 32, which correspond to 14.29% of the total image approximately and an area of $170668 \mu\text{m}^2$. Morphometry analysis gives a surface area of the selected object of $192520 \mu\text{m}^2$ and a peripheral object surface of $20940 \mu\text{m}^2$ for section LS2-MSL-1835-3-2/1366, a particle size range from 0 to $512 \mu\text{m}$ establishes an approximated area of 171420 particles. Binary images which correspond to the gray scale selection of empty voids used to make calculations of area are shown (Appendix 1/Figure 9 (B)).



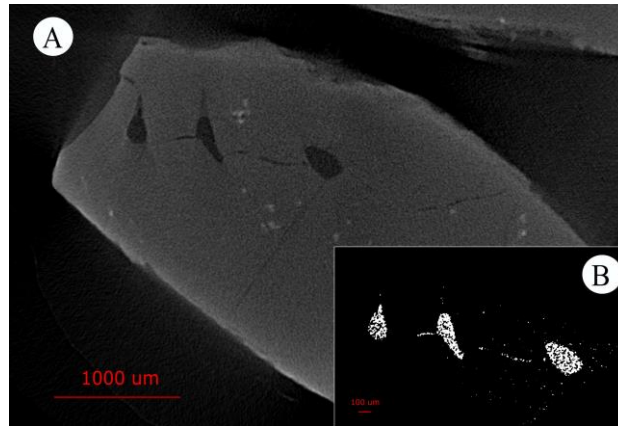
Appendix 1/Figure 9: Section image from olivine sample LS2-MSL-1835-3-2/1366 (A), Binary image of a melt inclusions in section sample LS2-MSL-1835-3-2/1366 (B), taken from the nanotomograph.

9) LS2-MSL-1835-4-1

The crystal has a polyhedral morphology where faces can be distinguished, inclusions can be seen in the form of a vapor phase (black features) with a curved almost spherical morphology and in some cases covered by a glass phase with a similar morphology. It is possible to see fractures between the inclusions which could be developed during the formation of the inclusions or later (Appendix 1/Figure 10 (A)).

Binary extrapolation based on a gray scale for section LS2-MSL-1835-4-1/1486 takes into account gray index values in an interval of 0 to 33, which correspond to 4.71% of the total image approximately and an area of 75110 μm^2 .

Morphometry analysis gives a surface area of the selected object of 101460 μm^2 and a peripheral object surface of 25261 μm^2 for section LS2-MSL-1835-4-1/1486, a particle size range from 0 to 243 μm establishes an approximated area of 76066 particles. Binary images which correspond to the gray scale selection of empty voids used to make calculations of area are shown (Appendix 1/Figure 10 (B)).

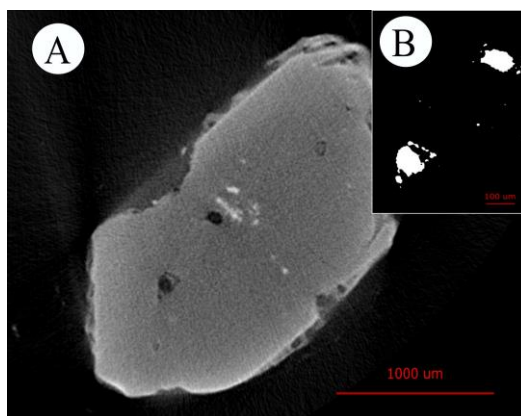


Appendix 1/Figure 10: Section image from olivine sample LS2-MSL-1835-4-1/1486 (A), Binary image of a melt inclusions in section sample LS2-MSL-1835-4-1/1486 (B), taken from the nanotomograph.

10) LS2-MSL-1835-5-1

Olivine shows a polyhedral morphology where it is possible to see faces of the usual orthorhombic system of olivines; there is a solid phase within the crystal of denser material in the center of the crystal. Inclusions are characterized by clear vapor phases (bubbles) with a spherical morphology; however, their size is small compared to previous inclusions, and the glass phase is difficult to distinguish. One of the inclusions is shown by a spherical vapor phase, a glass phase around it, that also is covered by a less dense material (almost similar to a vapor phase) (Appendix 1/Figure 11 (A)).

Binary extrapolation based on a gray scale for section LS2-MSL-1835-5-1/732 takes into account gray index values in an interval of 0 to 68, which correspond to 6.65% of the total image approximately and an area of $17880 \mu\text{m}^2$. Morphometry analysis gives a surface area of the selected object of $21222 \mu\text{m}^2$ and a peripheral object surface of $3215 \mu\text{m}^2$ for section LS2-MSL-1835-5-1/732, a particle size range from 0 to $128 \mu\text{m}$ establishes an approximated area of 17976 particles. Binary images which correspond to the gray scale selection of empty voids used to make calculations of area are shown (Appendix 1/Figure 11 (B)).

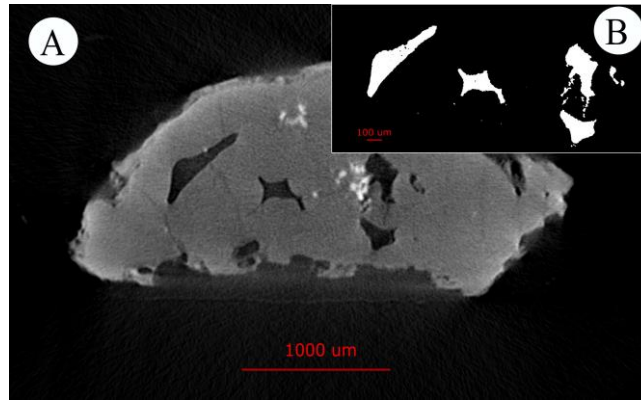


Appendix 1/Figure 11: Section image from olivine sample LS2-MSL-1835-5-1/732 (A), Binary image of a melt inclusions in section sample LS2-MSL-1835-5-1/732 (B), taken from the nanotomograph.

11) LS2-MSL-1835-5-3

Olivine has a polyhedral morphology, possibly showing half of an orthorhombic system. Empty voids have an irregular curvilinear shape, small black circles near the edges can be bubbles, glass phase can be present covering these bubbles but it is difficult to ensure this. Inclusions are located in the center of the crystal, with denser material around them. Likely dendritic morphology can be seen at the edges of the crystal (Appendix 1/Figure 12 (A)).

Binary extrapolation based on a gray scale for section LS2-MSL-1835-5-3/1862 takes into account gray index values in an interval of 0 to 61, which correspond to 12.31% of the total image approximately and an area of $159800 \mu\text{m}^2$. Morphometry analysis gives a surface area of the selected object of $173970 \mu\text{m}^2$ and a peripheral object surface of $13552 \mu\text{m}^2$ for section LS2-MSL-1835-5-3/1862, a particle size range from 0 to $512 \mu\text{m}$ establishes an approximated area of 160380 particles. Binary images which correspond to the gray scale selection of empty voids used to make calculations of area are shown (Appendix 1/Figure 12 (B)).

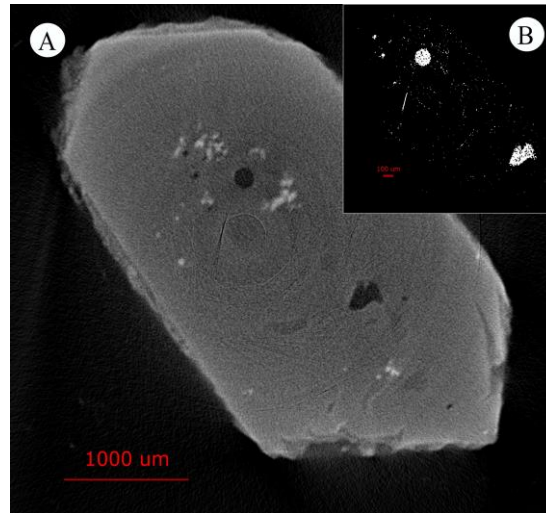


Appendix 1/Figure 12: Section image from olivine sample LS2-MSL-1835-5-3/1862 (A), Binary image of a melt inclusions in section sample LS2-MSL-1835-5-3/1862 (B), taken from the nanotomograph.

12) LS2-MSL-1835-6-1

Crystal a polyhedral morphology with well-developed orthorhombic crystal faces. It is possible to see inclusions in a liquid and vapor phase due to differences in the grayscale. Vapor phase has a clear spherical shape, while the liquid phase has an irregular morphology and curvilinear features. Denser material also is present within the crystal (Appendix 1/Figure 13 (A)).

Binary extrapolation based on a gray scale for section LS2-MSL-1835-6-1/1810 takes into account gray index values in an interval of 0 to 42, which correspond to 2.28% of the total image approximately and an area of $60896 \mu\text{m}^2$. Morphometry analysis gives a surface area of the selected object of $86235 \mu\text{m}^2$ and a peripheral object surface of $24524 \mu\text{m}^2$ for section LS2-MSL-1835-6-1/1810, a particle size range from 0 to 218 μm establishes an approximated area of 61387 particles. Binary images which correspond to the gray scale selection of empty voids used to make calculations of area are shown (Appendix 1/Figure 13 (B)).



Appendix 1/Figure 13: Section image from olivine sample LS2-MSL-1835-6-1/1810 (A), Binary image of a melt inclusions in section sample LS2-MSL-1835-6-1/1810 (B), taken from the nanotomograph.

Appendix 2: Glass slides images

Slide 1)

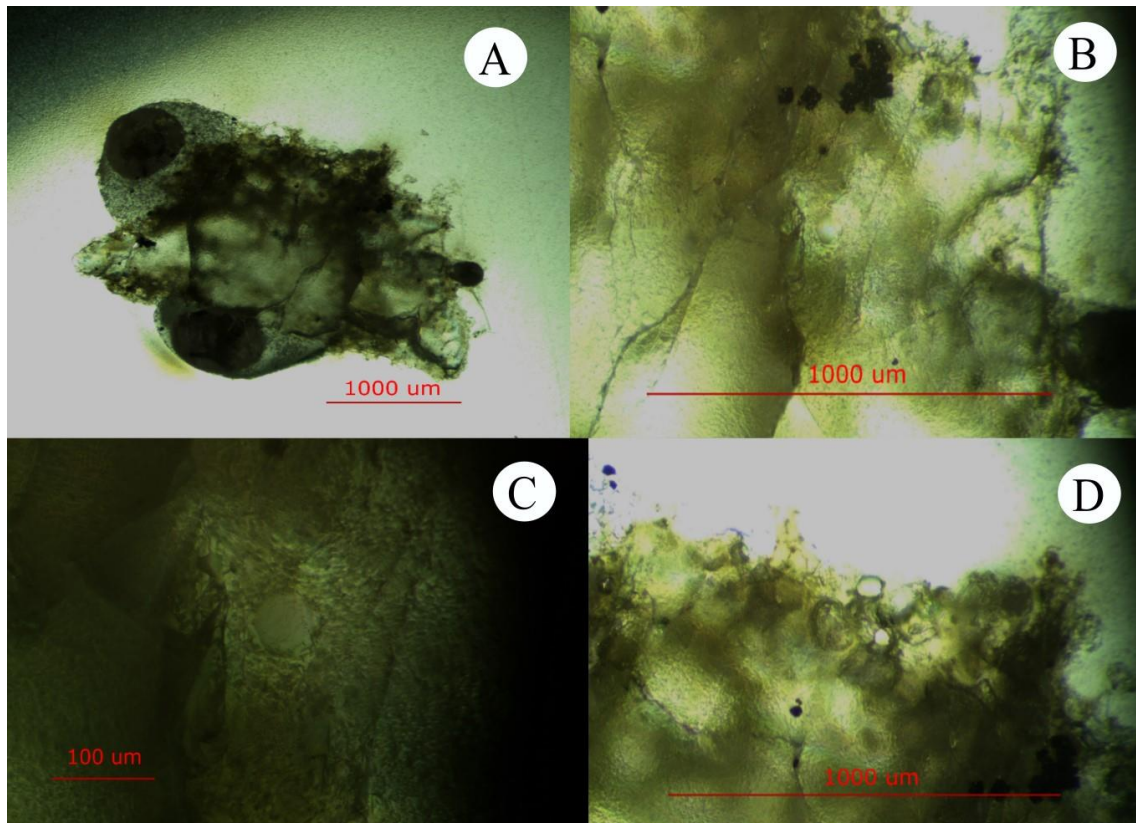
The thin section cuts the olivine crystal in the plane 001, the crystal has a glassy texture that can be used to see internal features within the crystal, there is the presence of black spots, these can be inferred to be opaque minerals (spinel inclusions) or a melt inclusion that has been completely recrystallized. These opaque minerals are present in various parts of the crystal in a random order, with varying size (Appendix 2/Figure 14 (A)).

The olivine is colorless with a poor cleavage, high relief, with a euhedral habit. There are abundant fractures with random orientation.

A closer look at the crystal face helps to identify melt inclusions, in this particular case the inclusion has a spherical shape with a glassy texture that contrasts with the host olivine, it has an approximated size of approximately 100 μm . The shape of the opaque mineral also can be seen more clearly, it does not have a clear cleavage and the habit is euhedral to subhedral. Possibly the minerals that represent these opaques are oxides, magnetite, ilmenite, spinel and chromite which last two generally occur in clusters (Appendix 2/Figure 14 (B)). The opaque minerals are likely spinel inclusions, they occur as clumps or glomerocrysts within the olivine host (Appendix 2/Figure 14 (B)).

The melt inclusion composed of volcanic glass is colorless with no distinctive cleavage, the habit has a groundmass appearance (Appendix 2/Figure 14 (C)).

It is possible that certain glassy melt inclusions are located in the edges of the olivine crystal, due to how mineral growth and defects are the principal mechanism through which inclusions are formed (Appendix 2/Figure 14 (D)).

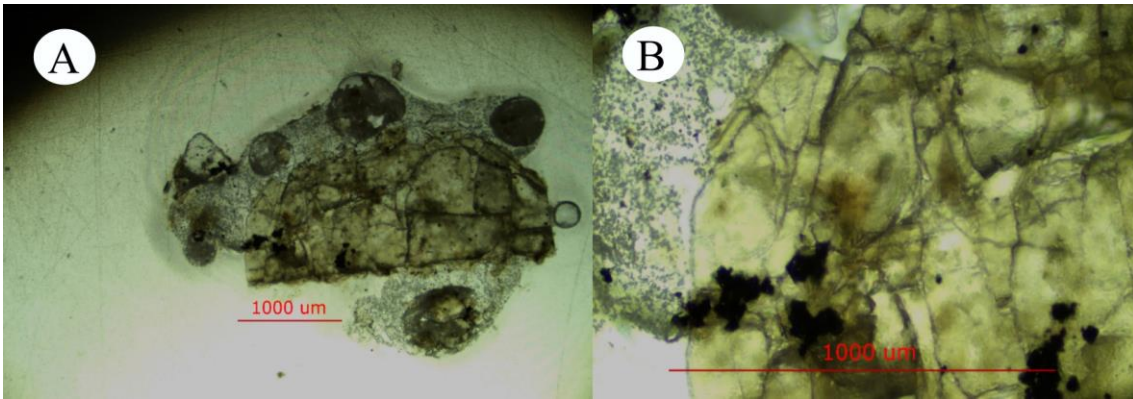


Appendix 2/Figure 14: General image of the glass slide 1 from olivine sample (A). Close look to internal features within glass slide 1 (B). Melt inclusions observed within the olivine in glass slide 1 (C). Possible melt inclusions in the edges of the olivine sample in glass slide 1 (D).

Slide 2)

The thin section cuts the olivine crystal in the plane 001, the olivine has a high relief with a euhedral habit, it does not have color, and maintains a poor cleavage. Abundant fractures are present (Appendix 2/Figure 15 (A)).

Opaque minerals are also present, in this case their pattern matches with spinel, which common co-crystallizes within olivine in mafic magmas. It is possible to see that within the crystal a light brown mineral is present, this is possibly volcanic glass trapped in the olivine crystal (melt inclusion) (Appendix 2/Figure 15 (B)).

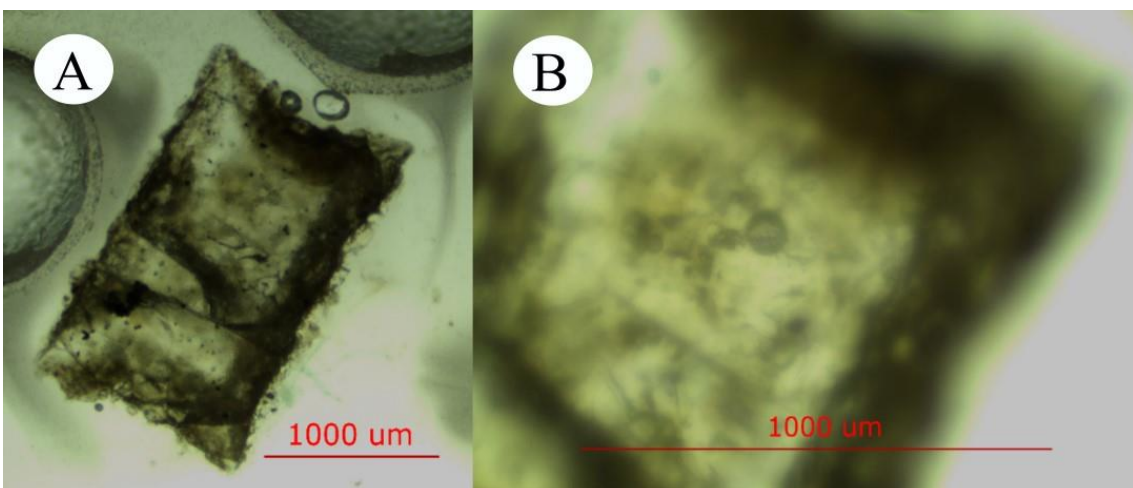


Appendix 2/Figure 15: General image of the glass slide 2 from olivine sample (A). Volcanic glass entrapped within an olivine sample from glass slide 2 (B).

Slide 3)

In this thin section the olivine crystal is present along the 010 plane. It matches the same listed characteristics previously established in the other cases; however, it has a more developed euhedral habit with not a characteristic texture. Fractures in this case also are less common (Appendix 2/Figure 16 (A)).

One of the principal indicators of a melt inclusion is the presence of a bubble, in this case it was possible to identify it. The bubble is colorless with no cleavage, and the habit is spherical. In most cases the presence of a bubble is accompanied by volcanic glass, which surrounds the bubble since the bubble likely formed by exsolution of a vapor from the entrapped melt inclusion (Appendix 2/Figure 16 (B)).

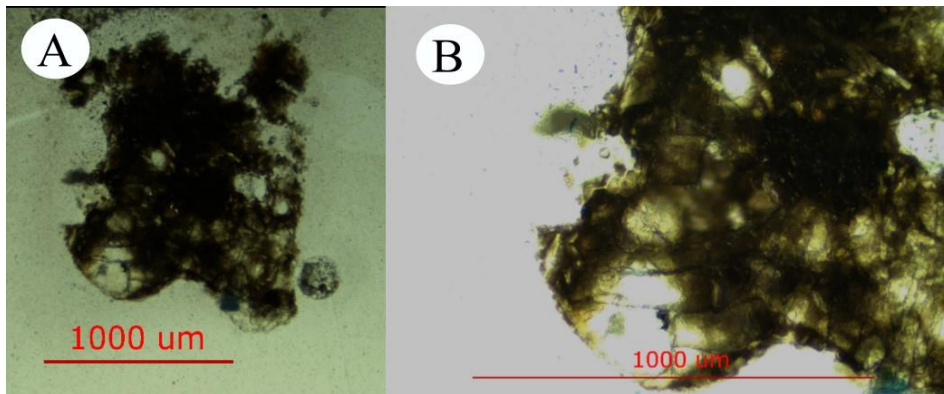


Appendix 2/Figure 16: General image of the glass slide 3 from olivine sample (A). Bubble entrapped within the olivine crystal from glass slide 3 (B).

Slide 4)

In this case it is not possible to infer the plane in which the thin section was created, the olivine crystal suffered from significant fractures and was likely plucked from the epoxy during the thin section preparation. The apparent dark material is dark matrix glass that was once adhering to the margin of the crystal (Appendix 2/Figure 17 (A)).

It is possible that melt inclusions are located in this highly fractured olivine crystal. There is the presence of plagioclase microphenocrysts with no color, again located at the edges of the crystal (Appendix 2/Figure 17 (B)).

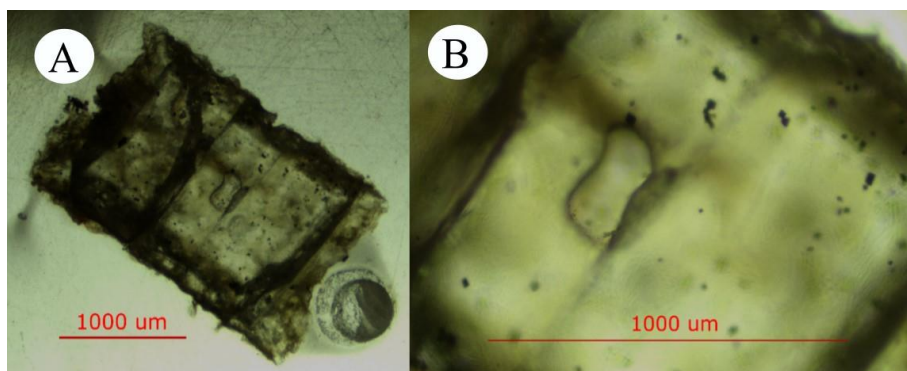


Appendix 2/Figure 17: Highly fractured olivine from glass slide 4 (A). Edges from olivine crystal of glass slide 4 (B).

Slide 5)

The thin section is made in the 010 plane. The crystal is a highly euhedral habit with well-developed crystal faces (Appendix 2/Figure 18 (A)).

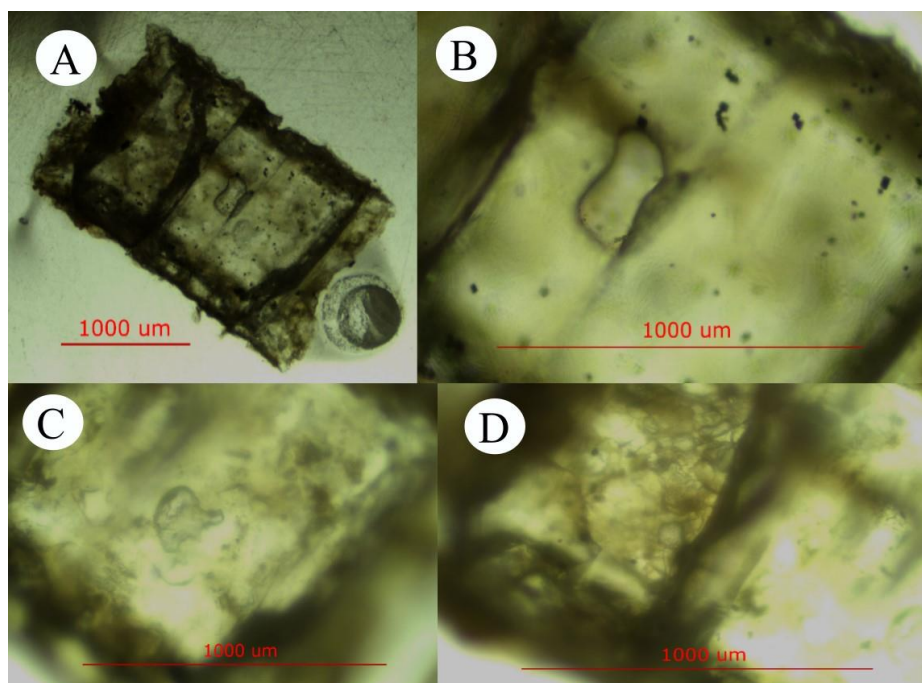
The relief between the olivine mineral matrix and certain features, in this case possibly volcanic glass, can be an indicator of a melt inclusion. The inclusion in this case has a curvilinear shape with a size approximately of 300 μm. Spinel also is present in small portions (Appendix 2/Figure 18 (B)).



Appendix 2/Figure 18: General image of the glass slide 5 from olivine sample (A). Melt inclusion in olivine from glass slide 5 (B).

Other melt inclusions were identified again with curvilinear shapes, melt inclusions formed in polyhedral olivines usually have this shape, however in some cases the features can be classified as something different like transparent plagioclase (Appendix 2/Figure 18 (C)).

Certain areas present in the clearest parts of the thin section show abundance of melt inclusions that are packed together. Other interpretations is possible vesicles within the matrix glass (Appendix 2/Figure 18 (D)).



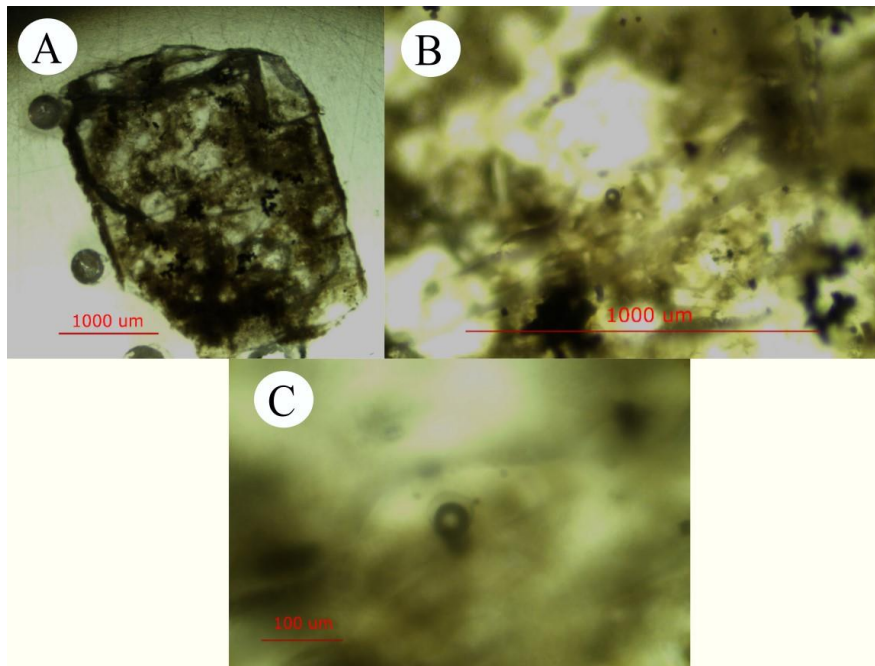
Appendix 2/Figure 18: General image of the glass slide 5 from olivine sample (A). Melt inclusion in olivine from glass slide 5 (B). Melt inclusion near the edge of the crystal of olivine from glass slide 5 (C). Melt inclusions packed together at the edge of the crystal from glass slide 5 (D).

Slide 6)

The probable orientation of the thin section is 001. Pieces of spinel are dispersed around the crystal. Fracturing appears to be most prominent across the 001 plane of the olivine crystal. The presence of volcanic glass in the crystal is characterized by the light to dark brown portions inside the crystal (Appendix 2/Figure 19 (A)).

As stated, before the presence of different phases within a melt inclusion are a common feature. In this thin section there is a clear vapor bubble that is surrounded by a clear material (volcanic glass) that has a contrast change with the olivine mineral matrix, the inclusion is located inside the crystal (Appendix 2/Figure 19 (B)).

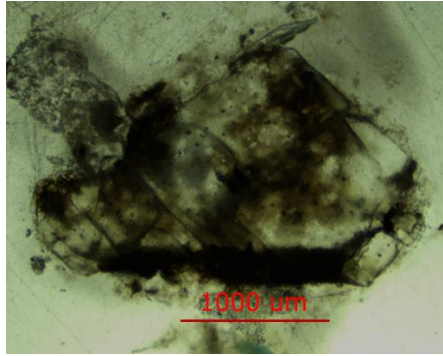
The size of the melt inclusion is approximately between 50 to 80 μm (Appendix 2/Figure 19 (C)).



Appendix 2/Figure 19: General image of the glass slide 6 from olivine sample (A). Presence of a clear melt inclusion within the olivine crystal from glass slide 6 (B). Close look to the melt inclusions identified in glass slide 6 (C).

Slide 7)

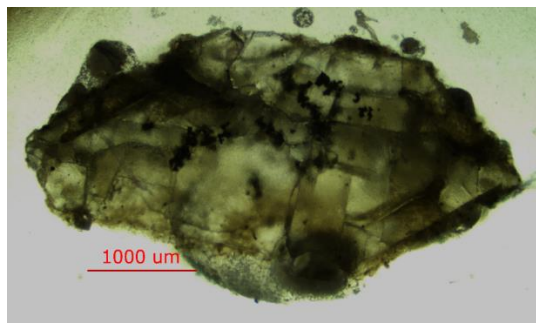
The thin section cuts the crystal in the 001 plane, fracturing is present with no particular order across the plane. Light to dark brown volcanic glass is present with small portions of magnetite compared to other of the samples (Appendix 2/Figure 20).



Appendix 2/Figure 20: General image of the glass slide 7 from olivine sample.

Slide 8)

The thin section crosses along the 001 plane, similar features of other observed crystals are present with few differences, the most important one is that the spinel forms a particular continuous pattern (Appendix 2/Figure 21).

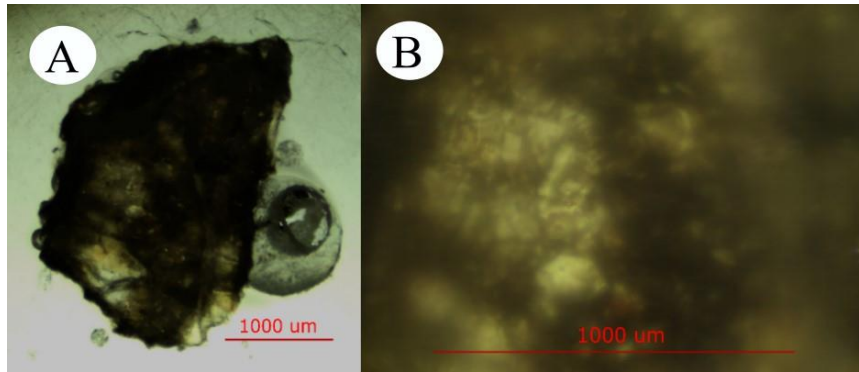


Appendix 2/Figure 21: General image of the glass slide 8 from olivine sample.

Slide 9)

The crystal has a subhedral habit, the thin section was made along the 001 plane. A significant portion of the crystal is difficult to see, the black material could be adhering matrix glass (Appendix 2/Figure 22 (A)).

In one of the clearest parts of the section it is possible to see either volcanic glass or olivine with certain euhedral habits. Particularly a portion that has almost a perfect orthorhombic 001 plane. It is also likely that smaller olivine crystals begin to crystallize with a tabular morphology (Appendix 2/Figure 22 (B)).

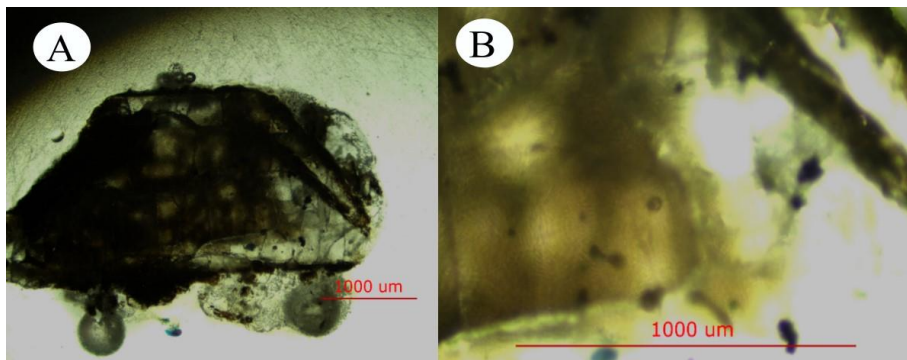


Appendix 2/Figure 22: General image of the glass slide 9 from olivine sample (A). Olivine with tabular morphology crystallizing within the olivine host from glass slide 9 (B).

Slide 10)

The thin section occurs along the 001 plane. Fracturing is present with pockets of opaque material. Magnetite mineralization in small portions also is present, volcanic glass pockets also occur in this section (Appendix 2/Figure 23 (A)).

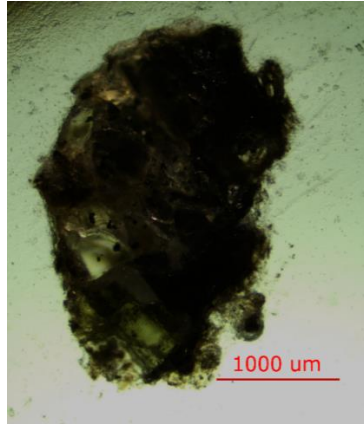
Volcanic glass (in the form of melt inclusions) is abundant in this section. It is possible to see spherical bubbles inside pockets of glass, whose color varies between colorless to light to dark brown. The approximate size of these inclusions are between 50 to 100 μm (Appendix 2/Figure 23 (B)).



Appendix 2/Figure 23: General image of the glass slide 10 from olivine sample (A). Different melt inclusions within the olivine crystal of glass slide 10 (B).

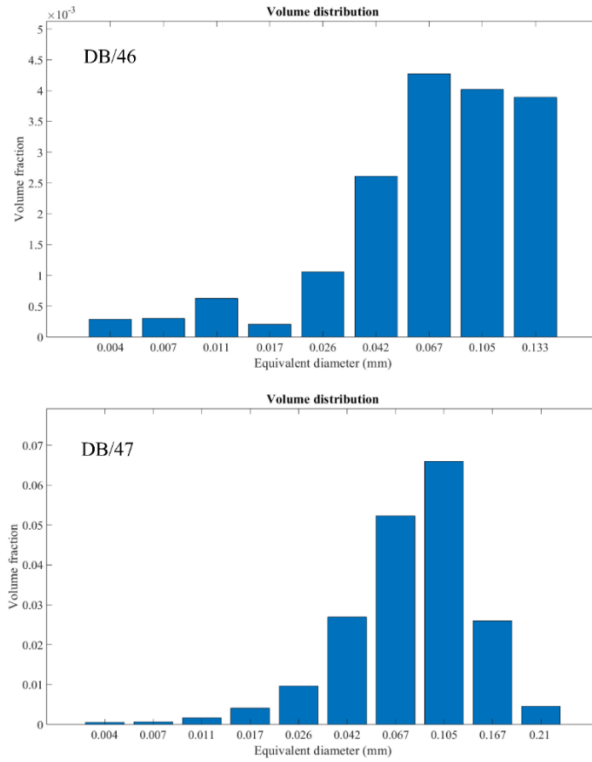
Slide 11)

The crystal has an anhedral habit, and because it is highly fractured it is difficult to see the orientation of the crystal. The crystal is largely opaque which origin is likely due adhering dark matrix glass on base of the olivine mineral restricting light from transmitting through the mineral (Appendix 2/Figure 24).

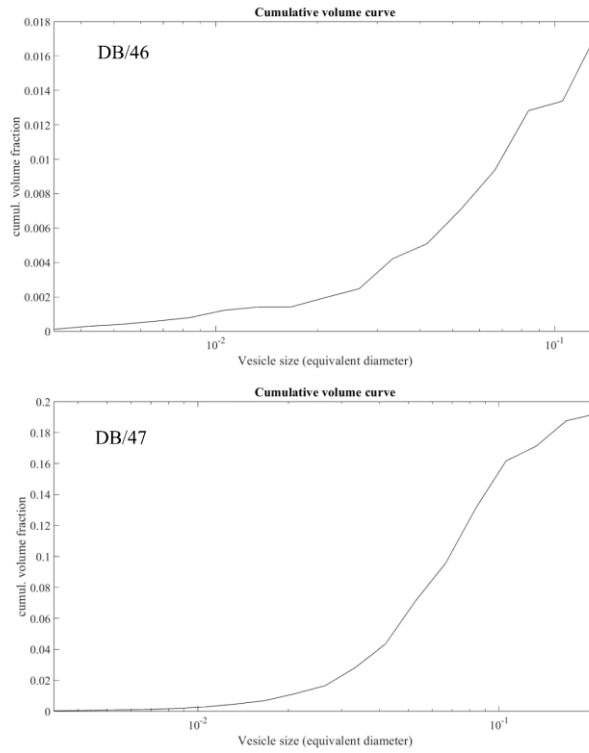


Appendix 2/Figure 24: General image of the glass slide 11 from olivine sample.

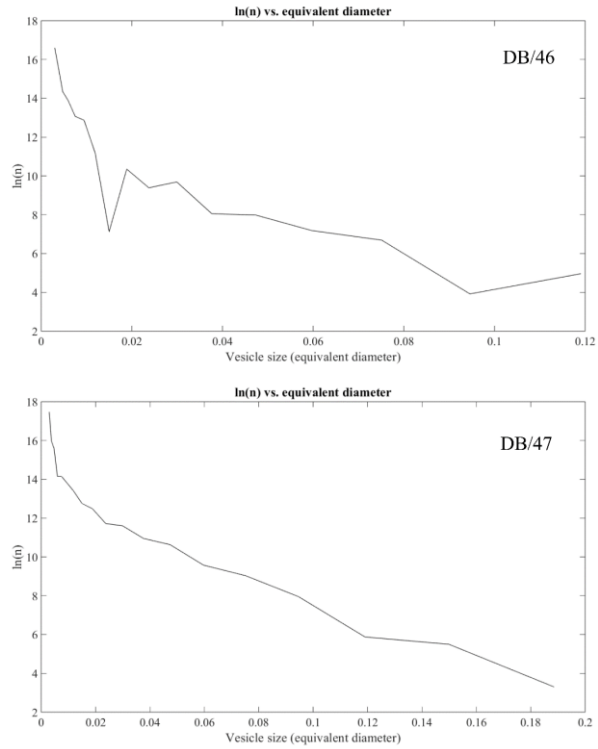
Appendix 3: Foams results in diagrams for all the clasts analyzed



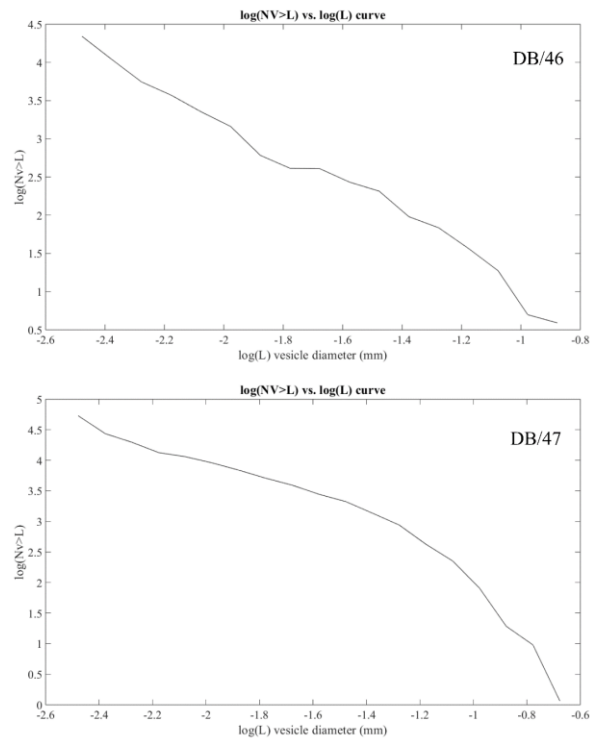
Appendix 3/Figure 53: VVD plots for dense black clast samples.



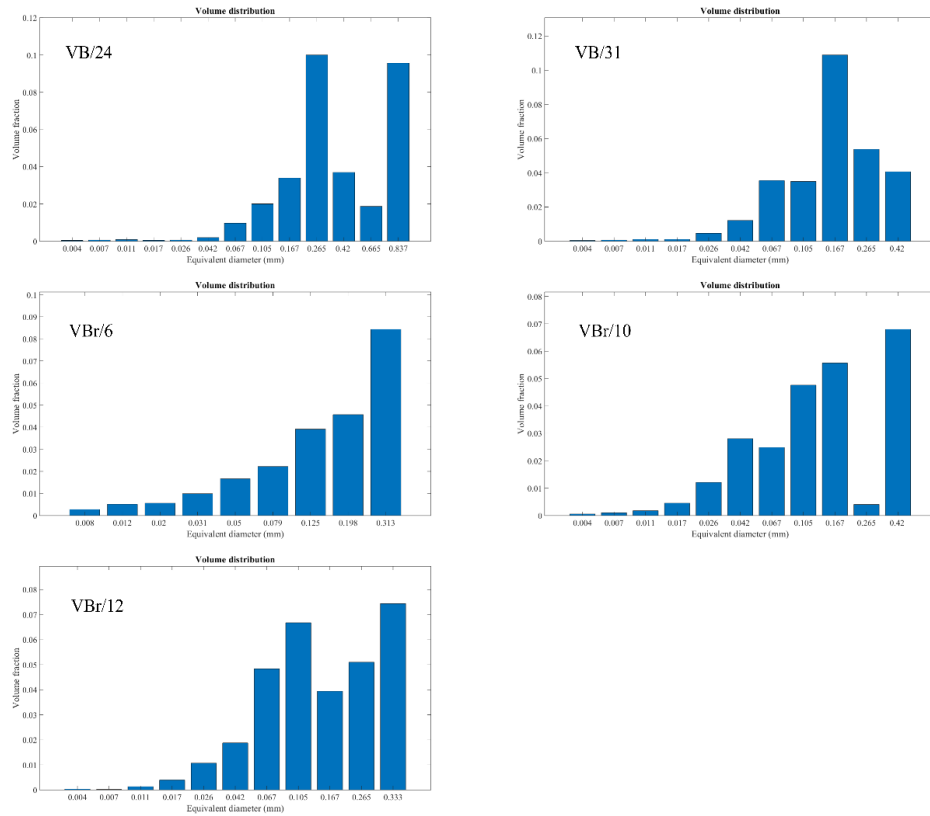
Appendix 3/Figure 54: CVVD plots for dense black clast samples.



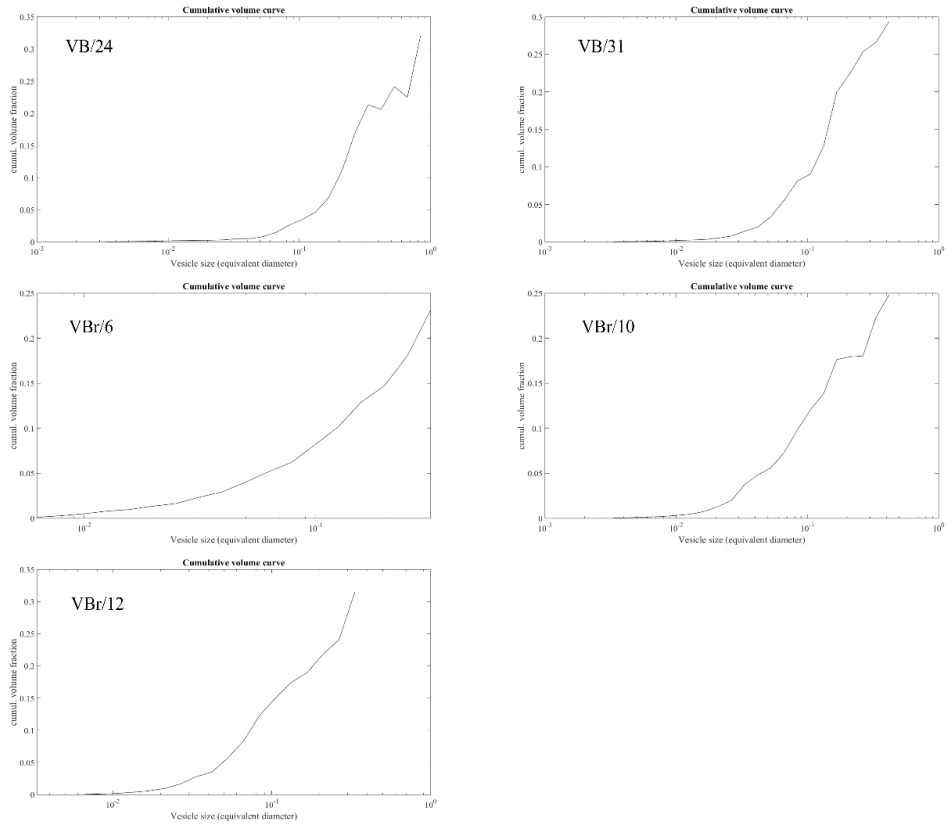
Appendix 3/Figure 55: VSD plots for dense black clast samples.



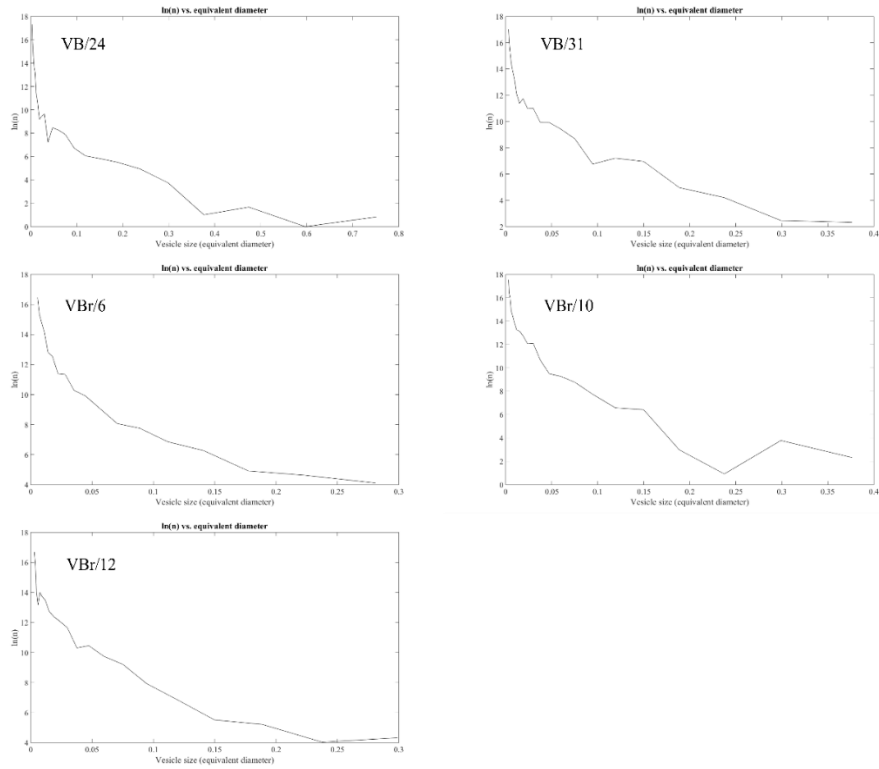
Appendix 3/Figure 56: CVSD plots for dense black clast samples.



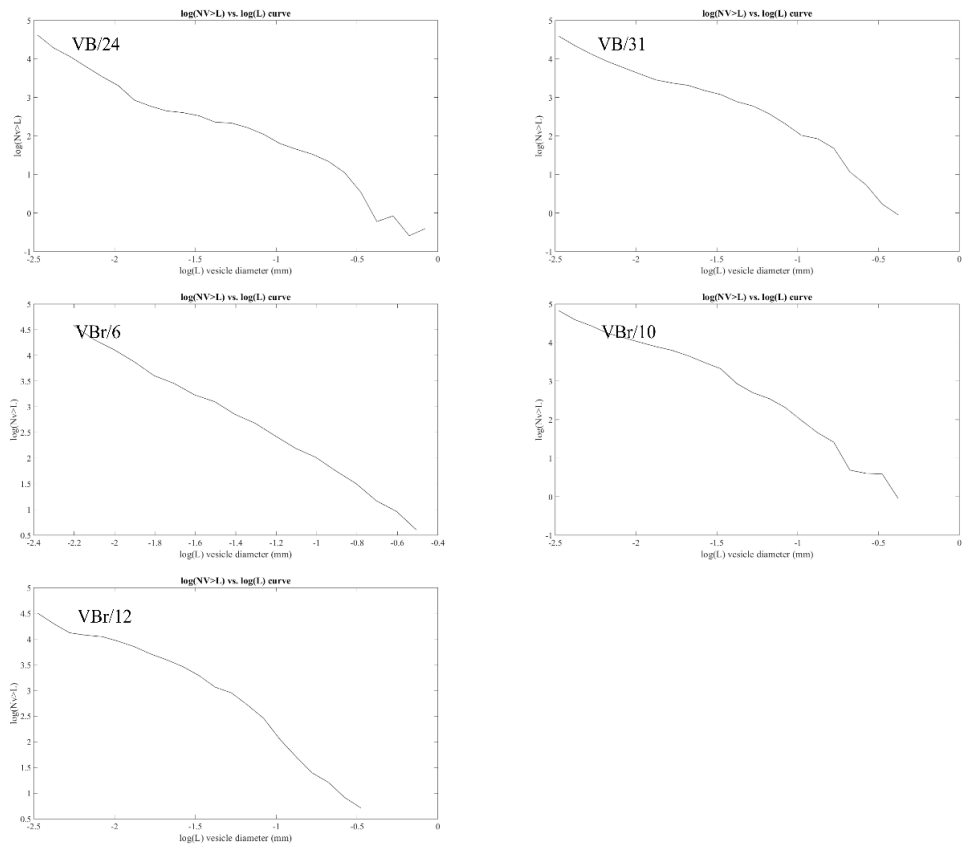
Appendix 3/Figure 57: VVD plots for vesicle black and vesicle brown clast samples.



Appendix 3/Figure 58: CVVD plots for vesicle black and vesicle brown clast samples.



Appendix 3/Figure 59: VSD plots for vesicle black and vesicle brown clast samples.



Appendix 3/Figure 60: CVSD plots for vesicle black and vesicle brown clast samples.

Appendix 4: Pungalá Granodiorite Sample whole rock composition

Intrusion name	Pungalá
Sample Name	EG19-PU
Type of rock	Granodiorite
Al₂O₃	13.96
CaO	1.63
Cr₂O₃	<0.01
Fe₂O₃	2.83
K₂O	3.08
MgO	0.59
MnO	0.05
Na₂O	4.06
P₂O₅	0.06
SiO₂	71.75
TiO₂	0.24
LOI	0.45
Total	98.7

Appendix 4/Table 1: Pungalá granodiorite composition (Guerrero & Vallejo, 2020).